



# **Dynamic and Thermal Modelling of Induction Machine with Non-Linear Effects**

Ogbonnaya Inya Okoro

Die vorliegende Arbeit wurde vom Fachbereich Elektrotechnik - der Universität Kassel als Inaugural-Dissertation zur Erlangung des akademischen Grades eines Doktor-Ingenieurs (Dr.-Ing.) angenommen.

Erster Gutachter: Prof. Dr.-Ing. Bernd Weidemann  
Zweiter Gutachter: Prof. Dr.-Ing. Heinz Theuerkauf

Tag der mündlichen Prüfung

20. September 2002

Gedruckt mit der Unterstützung des Deutschen Akademischen Austauschdienstes

Bibliografische Information Der Deutschen Bibliothek  
Die Deutsche Bibliothek verzeichnet diese Publikation in der Deutschen Nationalbibliografie; detaillierte bibliografische Daten sind im Internet über <http://dnb.ddb.de> abrufbar

Zugl.: Kassel, Univ., Diss. 2002  
ISBN 3-89958-003-6

© 2002, kassel university press GmbH, Kassel

Das Werk einschließlich aller seiner Teile ist urheberrechtlich geschützt. Jede Verwertung außerhalb der engen Grenzen des Urheberrechtsschutzgesetzes ist ohne Zustimmung des Verlags unzulässig und strafbar. Das gilt insbesondere für Vervielfältigungen, Übersetzungen, Mikroverfilmungen und die Einspeicherung und Verarbeitung in elektronischen Systemen.

Umschlaggestaltung: 5 Büro für Gestaltung, Kassel  
Druck und Verarbeitung: Zentraldruckerei der Universität Kassel  
Printed in Germany

To my beloved **mother**,  
Mrs Obila Inya Okoro whose love saw me to adulthood.

To all my respectable **teachers**,  
Who emptied their brains to enrich mine.

*“Concern for man himself and his fate must always form the chief interest of all technical endeavours—in order that the creations of our mind shall be a blessing and not a curse to mankind.”*

-----Albert Einstein

## ACKNOWLEDGEMENT

To claim total responsibility for the success of this work will be tantamount to indirectly expressing my ingratitude to people who in one way or the other contributed in one hand to make this work a huge success and in other hand to see that my stay in Germany is financially guaranteed and socially conducive. To these people—too numerous to mention, I wish to sincerely reserve my thanks.

My *Doktorvater*, Herrn Prof.Dr.-Ing. B.Weidemann is unique in several ways. His consistent encouragement has made the work easier. His day-to-day elaborate but useful discussions on problems encountered have made attainment to solutions faster. I thank him immensely. Again for accepting me as his doctoral student, I owe him my gratitude! I thank Herrn Prof.Dr.-Ing. H. Theuerkauf , who at my *Doktorvater's* behest has willingly accepted to act as my second *Gutachter*.

I am indeed grateful to DAAD for granting me the opportunity to pursue this programme in Germany and for supporting me financially. I also thank Prof.Dr.-Ing. H. Grostellen who honoured my letter and expressed his readiness to supervise my work at University of Paderborn. That it did not work out, is purely a matter of divine providence.

My special thanks go to my co-workers(*Mitarbeiter*): Adzic, Andreas, Aziz, Baral, Brand, Djauhari, Gier, Schönweiß, Tom, Thomas, and Vesna for their invaluable encouragement and assistance. I shall be guilty of great ingratitude if I fail to put on record the excellent services rendered to me by the secretary of my department: Frau Bleckwenn and Frau Heyber—which I heartily appreciate.

I would like to acknowledge with thanks Dr. Matthias Wesseler and wife , Frau Heinen, Frau Erichson, Frau Weidemann, Herr Borys, Holger, Karen, Markus, Robert, Tim, Annegret, Melanie, Ayako, Herr Breitel, Lady Monika and Lady Carola whose friendly disposition I count in no small measure.

My beloved uncle, late Chief Uduma Inya and my dear father, late Chief Inya Okoro have been instrumental to this academic journey. They committed all that they had –in love and in finance to see that my desire for western education is not hindered. Unfortunately, they could not live to see this day. I thank God their dreams, aspirations and efforts were not in vain.

I am grateful to my wife and son who have been with me all this time in prayers and in understanding. My son has been doing everything possible to help. Understandably he couldn't because of his age—8months! I appreciate.

The University of Nigeria for granting me study leave in order to pursue this programme is highly acknowledged. Worthy of mention is the then head of department of Electrical Engineering, Engr.Dr.M.U.Agu who had to shortcut all the official protocol in order to smoothen my departure to Germany. I reserve my gratitude to him.

I would also like to thank the following people for their encouragement and prayers:

Dr.&Mrs. E.E. Nkama, Mr.&Mrs. M.I. Okoro, Beatrice, Ada, Uduma, Alu, Ogechi, Albert, Boniface, Toby, Mr. O., Parker, Johnson, Amicable, Chief A.U. Aka, Elder Kenneth I. Ndukwe, Chief Augustine A. Inya, Mr. Eze Ibiam, Dr. Osu Otu, Mrs. M.N. Agu, the Boys and Mr. Nick Idoko.

Lastly, I would like to express my thanks to every other person whose name I failed to mention here, but who supported me morally and materially. I am happy they know themselves!

## **ABSTRACT**

The dynamic modelling of induction machines involves the development of accurate and reliable models that can adequately account for the machine's non-linearities as a result of saturation effect, skin-effect and thermal effect with the view of realising the actual machine performance in transient conditions.

The work presents the modelling of the Squirrel-cage rotor bar. To effectively account for Skin-effect in the rotor bar, a T-network lumped parameter model is developed. An optimisation algorithm which provides a good correlation between the actual bar impedance and the model impedance for varying frequency at approximately 6% error is achieved. The work also develops mathematical models which include saturation effect or /and Skin-effect –features that are usually neglected in the development of the conventional model. The non-linear differential equations governing the transient behaviour of the test machine are derived and expressed in state variable form. The machine parameters are determined by carrying out D.C. measurement test, No-Load test, Blocked-Rotor test and Retardation test on the machine. MATLAB Programs are developed and used to solve the steady and transient mathematical models of the machine. A comparison between the predicted transient torque and speed in the conventional model and that with Skin or/and Saturation effects shows a remarkable difference. The simulated machine model with both skin-effect and saturation effect included gives a better result than the other models when compared with the measured machine transient performances at run-up condition and can therefore be conveniently used to predict the actual machine performances.

The study also investigates the estimation of induction machine mean temperatures at different parts. Thermal network model is developed and the resulting algebraic and differential equations solved in order to determine the thermal behaviour of the machine under steady and transient conditions respectively. It is observed that the computed mean temperatures of the machine parts at No-load, rated load and blocked rotor operations compare satisfactorily well with the measured temperatures.

## **ABSTRACT(German)**

Die dynamische Modellierung von Asynchronmaschinen schließt die Entwicklung von genauen und zuverlässigen Modellen ein, die Nichtlinearitäten der Maschine wie Sättigung, Stromverdrängung und Erwärmung berücksichtigen. Die nichtlinearen Effekte beeinflussen das tatsächliche Maschinenverhalten bei nichtstationären Betriebszuständen ganz wesentlich.

Die Arbeit präsentiert die Modellierung der Stromverdrängung des Rotorstabs. Um effektiv den Stromverdrängungseffekt im Rotorstab zu erfassen, wird ein T-Netzwerk mit konzentrierten Parametern entwickelt. Ein Optimierungsalgorithmus erzielt eine gute Korrelation zwischen dem tatsächlichen Stabwiderstand und der Modellimpedanz. Der Fehler der Modellimpedanz beträgt bei einer Rotorfrequenz von 4 kHz etwa 6 %.

Die Arbeit enthält ein mathematisches Modell, das neben der Stromverdrängung auch die Sättigungseffekte berücksichtigt. Diese nichtlinearen Effekte werden normalerweise bei konventionellen Maschinenmodellen vernachlässigt.

Die nichtlinearen Differentialgleichungen, die das transiente Verhalten der Asynchronmaschine beschreiben, werden in der Zustandsvariablen- Form ausgedrückt. Die Maschinenparameter der Testmaschine wurden durch DC-Messung, Leerlauf-, Kurzschluss- und Auslauftest der Maschine ermittelt.

Die statischen und transienten mathematischen Modelle der Maschine wurden mit Hilfe von MATLAB entwickelt. Ein Vergleich von transientem Drehmoment und Drehzahl des konventionellen Maschinenmodells mit dem Modell, das Stromverdrängung und Sättigung berücksichtigt, zeigt einen bemerkenswerten Unterschied. Das Maschinenmodell mit Stromverdrängung und Sättigung liefert deutlich genauere Ergebnisse als das einfache Standardmodell, wie Messungen des Anlaufverhaltens der Testmaschine am starren Netz bestätigen. Mit diesem Modell lässt sich das tatsächliche Maschinenverhalten gut simulieren.

Die Arbeit gibt auch ein Modell zur Schätzung der mittleren Betriebstemperaturen der verschiedenen Maschinenteile an. Aus diesem thermischen Netzwerkmodell resultieren algebraische und Differentialgleichungen, deren Lösung das thermische Verhalten der Maschine unter stationären und nichtstationären Betriebszuständen ermittelt. Es wird festgestellt, dass die berechneten mittleren Temperaturen der verschiedenen Maschinenteile bei Leerlauf-, Nennlast- und Kurzschlussbetrieb zufriedenstellend mit den gemessenen Temperaturen übereinstimmen.

## Zusammenfassung

Die Hauptzielsetzung dieser Arbeit ist die Entwicklung von Maschinenmodellen, die das dynamische und thermische Verhalten eines Kurzschlussinduktionsmotors relativ genau auch mit seinen nichtlinearen Effekten nachbildet. Um diese Zielsetzung zu realisieren, wurde in vier Schritten vorgegangen:

1. Identifikation der Maschinenparameter durch DC-Messung, Leerlauftest, Kurzschlusstest mit blockiertem Rotor und Auslaufversuch einer Testmaschine.
2. Entwicklung von Maschinenmodellen unter Einbeziehung der Stromverdrängung, der Sättigung und der Erwärmung.
3. Entwicklung eines Rechenprogramms mit Hilfe des kommerziellen Softwarepaketes MATLAB.
4. Validierung der simulierten Resultate mit Messungen an der Versuchsmaschine.

Bei der Modellierung der Maschine mit Stromverdrängung wurde nur der Stromverdrängungseffekt im Rotorstab berücksichtigt. Es wurde ein T-Netzwerk mit konzentrierten Parametern verwendet, um den Rotorstab zu modellieren. Ein Optimierungsalgorithmus, der eine Fehlerfunktion beinhaltet, wurde entwickelt. Bei einer Frequenz von 4 kHz war der Fehler des entwickelten Rotormodells zu dem des tatsächlichen Stabes etwa 6 %. Dieser Fehler kann durch Erhöhung der Zahl der Parameter des Rotor-Kettenleitermodells reduziert werden. Die Testergebnisse von Leerlauf-, Kurzschluss-, DC-Messung und Auslauftest wurden verwendet, um Parameter für die konventionellen und nichtlinearen Maschinenmodelle zu erhalten, und um das Verhalten der Testmaschine unter stationären und dynamischen Bedingungen zu studieren. Ein Vergleich der Resultate zeigte einen großen Unterschied im entwickelten Drehmoment im stationären und transienten Zustand. Beim Modell mit Sättigungseffekt wurden nur geringe Unterschiede des Betriebsverhaltens beobachtet. Dass der Sättigungseffekt nicht sehr wahrnehmbar ist, ist darauf zurückzuführen, dass der magnetische Kreis der Maschine im Nennpunkt nur schwach gesättigt ist. Der Einfluss auf das Maschinenverhalten wird bei stark gesättigter Maschine bedeutend höher.

Es besteht jedoch ein erheblicher Unterschied im Betriebsverhalten zwischen dem konventionellen Maschinenmodell und dem Modell mit Stromverdrängungseffekt. Das entwickelte Drehmoment ist beim Stromverdrängungsmodell im Anlauf ungefähr dreimal höher als beim konventionellen Maschinenmodell. Entsprechend sind während des Anlaufs auch Statorstrom, Leistungsfaktor und die aufgenommene Leistung wesentlich größer als beim konventionellen Maschinenmodell.

Vergleichsrechnungen zwischen dem Maschinenmodell mit Stromverdrängung und dem konventionellen Modell zeigen bei den Hochlaufrechnungen große Abweichungen im berechneten Drehmoment und in der Drehzahl. Die größte Drehmomentspitze ist beim Maschinenmodell mit Stromverdrängung ungefähr 40 % höher als beim konventionellen Maschinenmodell. Die Hochlaufzeit auf synchrone Drehzahl ist beim Maschinenmodell mit Stromverdrängung wesentlich geringer als beim konventionellen Modell. Das Maschinenmodell mit Stromverdrängung und Sättigungseffekt liefert die besten Ergebnisse bei den Hochlaufrechnungen im Vergleich zu den Simulationen mit anderen Maschinenmodellen. Dieses Modell ist gut geeignet, um das tatsächliche Maschinenverhalten zu simulieren.

Zur Berechnung der Erwärmung wird ein thermisches Modell der Maschine entwickelt, das auf einem diskreten Masse-Wärmewiderstands-Netzwerk basiert. Thermische Netzwerke sind zur thermischen Modellierung von elektrischen Maschinen sehr effizient.

Die unterschiedlichen Maschinenkomponenten (Wicklungen, Isolation, Eisen etc.) sind einfach zu modellieren. Die Berechnung erfordert keine extrem schnellen Hochleistungsrechner.

Vorgegeben werden für die Erwärmungsrechnungen mit einem MATLAB-Programm die Maschinengeometrie, die thermischen Materialdaten und die Verlustleistungen der Maschine. Das Programm berechnet die Temperaturverteilung der Maschine im stationären und nichtstationären Betrieb. Wegen der angenommenen thermischen Symmetrie des Motors wurde nur eine Hälfte der Maschine nachgebildet. Diese Näherung führt bei großen und längsbelüfteten Maschinen wegen der thermischen Asymmetrie zu größeren Ungenauigkeiten. In diesem Fall müsste das thermische Netzwerk der kompletten Maschine nachgebildet werden.

Die berechneten Übertemperaturen der Maschinenteile wurden im Leerlauf, bei Nennlast und bei Kurzschluss im Stillstand ermittelt. Die berechneten Temperaturverläufe stimmen gut mit den gemessenen Werten überein. Die Temperaturfehler betrugen weniger als 10 % C im stationären und nichtstationären Betrieb. Diese Fehler resultieren auch aus der Tatsache, dass das entwickelte thermische Modell die durchschnittlichen Temperaturen innerhalb der Stator- und Rotorwicklungen und innerhalb der Eisenmassen berechnet, während die auf der Oberfläche installierten Thermoelemente nur jeweils die Außentemperaturen messen.

Insgesamt trägt diese Arbeit zur Modellierung von Induktionsmaschinen folgendes bei:

- eine relativ einfache Modellierung der Stromverdrängung im Rotorstab, die auch für beliebige Stabformen oder Mehrfachkäfige angewendet werden kann.
- ein tieferes Verständnis des Betriebsverhaltens der Induktionsmaschine im stationären und nichtstationären Betriebszustand aufgrund der Stromverdrängung, der Sättigung und der Erwärmung.
- ein thermisches Netzwerkmodell, das die gemittelten Temperaturen in den Maschinenteilen verlässlich schätzt.
- ein interaktives MATLAB-Programm, das das Betriebsverhalten der Induktionsmaschine gut nachbildet.

Das entwickelte nichtlineare Maschinenmodell kann auch vorteilhaft bei der Auslegung von Drehzahl- und Drehmomentreglern angewendet werden, z.B. bei der Regelung der Induktionsmaschine auf konstante Rotorflussverkettung.

---

<b>Contents</b>	<b>Pages</b>
<b>Abstract</b>	<b>vi</b>
<b>Abstract(German)</b>	<b>vii</b>
<b>Zusammenfassung</b>	<b>viii</b>
<b>List of symbols and abbreviations used</b>	<b>xii</b>
<b>1      Introduction</b>	<b>1</b>
1.1. Dynamic modelling of induction machines.....	1
1.2. Thermal modelling of induction machines.....	2
1.3. Purpose and overview of the research.....	3
<b>2      Modelling , simulation tools and machine data</b>	<b>5</b>
2.1 State-variable method.....	5
2.2 Program structure.....	6
2.3 Machine data .....	8
2.3.1 No-load test .....	8
2.3.2 Blocked rotor test .....	9
2.3.3 Retardation test.....	10
2.3.4 Induction machines characteristic curves .....	10
<b>3      Rotor-bar modelling for skin-effect</b>	<b>17</b>
3.1 Theory of Skin-effect .....	17
3.2 Derivation of impedance equation for rectangular rotor bar .....	18
3.3 Temperature effect .....	23
3.4 Derivation of the model impedance equation.....	25
<b>4      Model modification, optimisation and computer simulation</b>	<b>33</b>
4.1 Model modification .....	33
4.2 Algorithm for model optimisation.....	35
4.3 Methods of solution and simulation results.....	37
<b>5      Conventional machine model</b>	<b>40</b>
5.1 D-Q axis transformation.....	40
5.1.1 Reference frames voltages.....	41
5.2 Conventional machine model development .....	42
5.3 Electrical model of the machine .....	43
5.4 Mechanical model of the machine.....	45
5.4.1 Mechanical model of the machine without coupling .....	45
5.4.2 Mechanical model of the machine with coupling .....	47
5.4.3 Determination of the shaft system stiffness constant .....	49
5.5 Steady-state machine model .....	50
5.6 Computer simulation and results.....	51
<b>6      Machine models with skin-effect and saturation effect</b>	<b>54</b>
6.1 Development of the equivalent circuit .....	54
6.2 The machine D-Q model equations.....	56
6.3 Motor sets of differential equations.....	59
6.4 Model equations in state variable form .....	60
6.5 Model development with saturation effect.....	62
6.6 Steady-state machine model .....	65
6.7 Computer simulation and results.....	69
6.8 Models simulation results comparison .....	77

---

	<b>Pages</b>
<b>7      Induction machine thermal modelling</b>	<b>82</b>
7.1 Losses in induction machine.....	82
7.1.1 Losses calculations.....	82
7.2 Heat transfer theory.....	88
7.3 Thermal network model theory.....	91
7.4 Developed thermal model for the test machine .....	94
7.5 Mathematical representation of the proposed thermal model.....	95
7.5.1 Transient state thermal model equations.....	95
7.5.2 Steady-state thermal model equations.....	99
7.6 Computer simulation and results .....	100
<b>8      Measurements</b>	<b>105</b>
8.1 Test machine .....	105
8.2 Measurement of electrical and mechanical quantities of the motor.....	107
8.3 Temperature measurements .....	108
8.4 Simulation and experimental results.....	110
8.4.1 Run-up transient measurements and simulation results.....	110
8.4.2 Temperature measurements and simulation results .....	117
8.4.3 Comments on the results.....	129
<b>9      Conclusion</b>	<b>130</b>
<b>Appendix</b>	<b>132</b>
Calculated thermal resistances and capacitances .....	132
<b>References</b>	<b>133</b>

**List of symbols and abbreviations used**

$R_T$	total resistance of rectangular bar[ $\Omega$ ]
$Z$	impedance[ $\Omega$ ]
$L_s$	length of rotor bar[m]
$\chi_{cu}$	conductivity of copper conductor[Sm/mm <sup>2</sup> ]
$h_L$	height of rotor conductor[mm]
$b_L$	width of rotor conductor[mm]
$n$	total number of bar sections
$B$	magnetic flux density[T]
$\phi, \psi$	magnetic flux[Weber]
$\underline{U}$	complex bar voltage[V]
$\underline{I}$	complex bar current[A]
$R_L$	resistance of each of the bar section[ $\Omega$ ]
$\alpha$	temperature coefficient for copper[1/K]
$R_\theta$	resistance at $0^\circ\text{C}$ [ $\Omega$ ]
$R_{20}$	resistance at $20^\circ\text{C}$ [ $\Omega$ ]
$\rho_\theta$	resistivity at $0^\circ\text{C}$ [ $\Omega\text{-m}$ ]
$\rho_{20}$	resistivity at $20^\circ\text{C}$ [ $\Omega\text{-m}$ ]
$\Delta\theta$	change in temperature[ $^\circ\text{C}$ ]
$U_E$	input model voltage[V]
$\mathbf{I}$	identity matrix
$S$	complex angular frequency[rad/s]
$f$	frequency[Hz]
$\omega$	angular frequency[rad/s]
$L$	bar inductance[H]
$i_{sd}$	d-axis stator current[A]
$i_{sq}$	q-axis stator current[A]
$i_o$	null current[A]
$i_{sa}, i_{sb}, i_{sc}$	stator phase currents[A]
$V_{qs}$	q-axis stator voltage[V]
$V_{ds}$	d-axis stator voltage[V]
$\omega_r$	electrical angular velocity[rad/s]
$\theta_r$	electrical rotor angular position[ $^\circ$ ]
$P$	number of pole pairs
$\theta_m$	rotor angular position[ $^\circ$ ]
$\omega_m$	rotor mechanical speed[rad/s]
$\lambda$	flux linkages[Vs]
$T_e$	electromagnetic torque[N-m]
$T_L$	load torque[N-m]
$\mathbf{i}$	current matrix
$\mathbf{V}$	voltage matrix
$\mathbf{R}$	resistance matrix
$\mathbf{L}$	inductance matrix
$\mathbf{G}$	rotational inductance matrix
$s$	machine slip
$V_{qso}, V_{dso}$	steady-state q- and d-axis stator voltages[V]
$i_{qso}, i_{dso}$	steady-state q- and d-axis stator currents[A]

---

$i_{qro}, i_{dro}$	steady-state q-and d-axis rotor currents[A]
$\mu_0$	permeability of free space[H/m]
$k$	transformation ratio
$m_1$	number of phases on the stator
$m_2$	number of phases on the rotor
$k_{w1}$	stator winding factor
$k_{w2}$	rotor winding factor
$N_1$	number of series-connected turns per phase of the stator
$N_2$	number of series-connected turns per phase of the rotor
$V_{as}, V_{bs}, V_{cs}$	stator phase voltages[V]
$\theta_0$	room temperature[°C]
$\theta$	temperature[°C]
$V$	volume[m <sup>3</sup> ]
$\Delta_{Fe}$	thickness of the lamination sheet[m]
$K$	thermal conductivity[W/m.°C]
$c_p, c_f$	specific heats[J/kg.°C]
$Q$	heat generation rate[W/m <sup>3</sup> ]
$q$	heat flux[w/m <sup>2</sup> ]
$R_{th}$	thermal resistance[K/W]
$A$	area[m <sup>2</sup> ]
$h_c$	heat transfer coefficient[W/m <sup>2</sup> .K]
$\mu$	fluid dynamic viscosity[kg/ms]
$\nu$	kinematic viscosity[m <sup>2</sup> /s]
$g$	acceleration due to gravity[m/s <sup>2</sup> ]
$\beta$	thermal expansion coefficient[1/°C]
$U_f$	fluid velocity[m/s]
$\epsilon$	emissivity of surface
$\delta$	Stefan-Boltzmann constant[W/m <sup>2</sup> .K <sup>4</sup> ]
$C_{th}$	thermal capacitance[J/K]
$C_i$	node thermal capacitance[J/K]
$\theta_i$	node temperature rise[°C]
$R_{ij}$	thermal resistance between adjoining nodes i,j[K/W]
$\Theta_t$	temperature rise matrix
$C_t$	thermal capacitance matrix
$P_t$	loss matrix
$G_t$	thermal conductance matrix
<b>PWM</b>	pulse-width-modulation
<b>FEA</b>	finite element analysis
<b>TNM</b>	thermal network model
<b>SCIM</b>	squirrel-cage induction machine
<b>DC</b>	direct current
<b>AC</b>	alternating current
<b>KVA</b>	kilo-volt ampere
<b>X</b>	state variable vector
<b>U</b>	input vector
<b>B</b>	control matrix
<b>n</b>	system order
<b>A</b>	system matrix
<b>pi</b>	number of inputs
<b>ODE</b>	ordinary differential equation

<b>R<sub>Wi</sub></b>	a.c. rotor bar resistance[ $\Omega$ ]
<b>X<sub>Wi</sub></b>	inner rotor bar conductor reactance[ $\Omega$ ]
<b>UOI</b>	user-optimisation-index
<b>CMO</b>	Conventional model only
<b>SEMO</b>	Skin-effect model only
<b>CMPS</b>	Conventional model plus saturation effect
<b>SEMPS</b>	Skin-effect model plus saturation effect
<b>FEM</b>	finite element method
<b>V<sub>o</sub></b>	Steady-state voltage matrix with skin-effect
<b>Z<sub>o</sub></b>	Steady-state impedance matrix with skin-effect
<b>i<sub>o</sub></b>	Steady-state current matrix with skin-effect
P <sub>Fe1Y</sub>	Iron losses in the machine Yoke[W]
P <sub>Fe1T</sub>	Iron losses in the stator teeth[W]
P <sub>Fe2R</sub>	Iron losses in the rotor[W]
$\sigma_H$	Hysteresis loss coefficient
$\sigma_E$	Eddy-current loss coefficient
P <sub>FeT</sub>	total iron losses[W]
$\psi_N$	rated magnetic flux[Wb]
K <sub>S</sub> ,K <sub>T</sub> ,H <sub>Y</sub> ,H <sub>T</sub> ,H <sub>R</sub>	constant iron losses distribution factors
$\omega_d$	undamped natural frequency[rad/s]
$\theta_{mL}$	angular position of the load[rad]
$\omega_{mL}$	mechanical speed of the load[rpm]
J <sub>m1</sub>	moment of inertia of the induction motor[kgm <sup>2</sup> ]
J <sub>L</sub>	moment of inertia of the load motor[kgm <sup>2</sup> ]
c <sub>w</sub>	shaft system stiffness constant[Nm/rad]
M <sub>w</sub>	shaft torque[Nm]
d <sub>w</sub>	damping factor
J <sub>m</sub>	combined rotor and load inertia coefficient[kgm <sup>2</sup> ]
<b>T1..T28</b>	Installed J-Type thermoelements

## 1 Introduction

### 1.1 Dynamic modelling of induction machines

The increased use of variable frequency in induction motor drive systems has generated enormous interest on the computer simulation of induction machines[1,2,16,17,18,19]. In recent years,due to advances in the development of high speed computers and Power electronics technology with associated high speed microcontrollers, AC drive systems have become a viable alternative to DC machines for variable speed applications[3,4]. This increased interest in induction motor is mainly because of its merits over other industrial motor types. These advantages include: Lightness, simplicity, ruggedness,less initial cost, higher torque-inertia ratio, capability of much higher speed, ease of maintenance,etc. Moreover, for instance, the most important feature which makes the induction motor a viable alternative to D.C. drive system is its cost per KVA which is approximately one fifth of that of the D.C. motor and its suitability in hostile environment[15,20].

For the past 30years, the dynamic behaviour of induction machines has received a considerable attention in most researched works[1,2,16,17,18,19,20]. However, the analyses are based on the simple idealised machine model without skin-effect or/and saturation. These works were also analysed based on the assumption that the rotor resistance is constant at the d.c. value. Pertinently, this method of analysis usually lead to a very large error in the torque developed at certain speeds and applied frequencies for squirrel-cage rotors with deep rotor bars[80]. Consequently, the need for the development of accurate models for induction machine becomes highly imperative. This is so because in an induction machine, the lower portions of the bars of the rotor cage are linked by more slot leakage flux than the upper portions of the bar. Under dynamic conditions, the lower section of the rotor bar experiences a higher inductance than the upper section of the rotor bar due to non-uniform flux distribution, thereby causing the current to flow primarily in the upper portion of the bar. Also, the re-distribution of the current flowing in the rotor bar effectively increases the resistance of the bar. This phenomenon of decrease in inductance and increase in resistance of rotor conductors is known as the deep-bar effect or the skin-effect[5,6,7,8,9,11,14,59,81,83]. This effect is highly noticeable in motors with rotor bars that have a large bar depth to bar width ratio and in motors operated over a wide frequency ranges—such as induction motors fed by PWM inverters.

The dynamic modelling of induction machines therefore, involves the development of accurate and reliable models that can adequately account for the machines' non-linearities such as saturation effect, skin-effect and thermal effect with the view of realising the actual machine performance in transient conditions. The model analysis gives rise to a set of differential equations which are usually expressed in state-space variable form for computer simulation purpose[13]. Where the rotor speed is constant, the solution of the resulting set of differential equations could be obtained analytically as the equations are linear. However, in most induction machine's dynamic problems, the rotor speed is usually varying and as such the machine's dynamic differential equations are non-linear. Consequently, a numerical method such as Runge-Kutta, Euler, Adams, Predictor-Corrector,etc is usually applied in arriving at a solution. The fourth-order Runge-Kutta methods are widely used in computer solutions to transient studies of A.C. machines[66,67]. The dynamic models of a squirrel-cage induction machine,SCIM which take into account saturation or/and skin-effect are developed and presented in this work.

## 1.2 Thermal modelling of induction machines

Generally, rotating electrical machines convert electrical energy to mechanical energy, or vice versa. This is made possible by the interaction of electric circuits and magnetic fields across an air gap. The electric and magnetic circuits require materials of low resistivity and high permeability respectively. These two circuits are usually separated by insulating materials of good thermal properties. The electric and magnetic circuits must be capable to withstand the mechanical loads imposed upon them by transfer of energy across the airgap. The transfer of energy across the airgap necessitates the dissipation of heat by ohmic losses in the electric circuit, and by eddy current and hysteresis losses in the magnetic circuit. The performance of the insulating materials which separate the electric and magnetic circuits is highly dependent on temperature and deteriorates rapidly as temperature increases. From the foregoing, it is seen that the electric circuit, the magnetic circuit and the insulating part of the electrical machines are affected by the heating process in the machine emanating from the transfer of energy across the air gap. Consequently, the main limiting factor, among others, on how long an electrical machine can be operated continuously on load remains the temperature of the various circuit elements that constitute the machine. Undesirable effects result when the thermal limit of an electrical machine is exceeded:

- Loss of dielectrical property of the insulating material
- Thermal bending of the rotor and consequent loss of eccentricity
- Bearing wear and vibration
- Deterioration of bearing lubricants
- Thermal stresses and changes in geometry of the machine elements due to thermal expansion.

Due to these problems, the temperatures in electrical machines must be properly monitored and specified within certain limits to reflect the mechanical, electrical and environmental conditions in which the machine will operate. In order to predict the temperatures in electrical machines, thermal models are used. Thermal models of electrical machines vary in degree of complexities depending on areas of applications and the level of accuracy to which the models are expected to give when compared to the physical temperature measurements of the test machine. Most thermal models are based on the similarity between Ohm's law of electrical conduction and Fourier's law of heat conduction. A thermal model can be used to determine allowable short-time overloads of a machine. Thermal model therefore forms a key element for motor protection and condition monitoring.

The Lumped-parameter models[39,40,41,42,43,44] and the Finite-element method,FEM[45,46,47] are the most frequently used thermal models. The lumped parameter model, otherwise known as the thermal network model has been used for a very long time in calculation of the temperature rises in electrical machines. Soderberg[48] applied thermal networks for temperature calculations of turbine-generators in 1931. In the 1950s, Hak[41,49,50] made elaborate contribution to thermal networks as applicable to electrical machines. Several researchers have made their dissertation on thermal modelling and networks[40,51]. On the other hand, Finite-element method is relatively new. [52] and [53] among others have used the FEM in studying the thermal behaviour of electrical machines.

The merit of the thermal network model,TNM lies on the fact that the network parameters can be derived from entirely dimensional information, the thermal properties of the materials used in designing the machine, and the constant heat transfer coefficients. This feature makes the model to be easily adapted to a range of machine sizes. The draw-back of the thermal model is that the calculation of the model

parameters can be complex and involving. However, once the model parameters are known, the resulting set of thermal algebraic and differential equations, which completely describe the machine steady and transient states thermal performances respectively can be computed with ease. Again, although the TNM predicts average temperatures quite accurately, the method fails in predicting hot spot temperatures.

Heat conduction problems can be solved more accurately using a finite element method. The finite element method is particularly well suited for solving transient or steady state problems of large electrical machines where thermal asymmetries are common features. The demerit of the finite element method is that three-dimensional and time-dependent problems are generally involving both in software development and hardware implementation[40,47,54]. Also, even though the method predicts hot spot temperatures accurately, it lacks in flexibility in handling complex boundary conditions and geometry[57]. For normal operation of small machines, the finite element method is less suited because the temperature gradients within distinct machine parts are small, which makes the thermal network method more appropriate[40].

In this work, a thermal network model for a 7.5KW SCIM is developed. A step-by-step thermal network model strategy as proposed by[43,55,56] is adopted:

- Modelling the thermal network of the machine
- Determination of the thermal resistances
- Calculation of the thermal capacitances
- Determination and calculation of the losses in the machine
- Writing the system algebraic and differential equations for steady and transient state studies respectively
- Computer simulation of the thermal model
- Experimental verification

### 1.3 Purpose and overview of the research

The main objectives of the research are:

- To model a squirrel-cage rectangular rotor bar to account for the deep-bar effect(skin-effect)
- To develop suitable transient models that account for saturation,or/and skin-effect phenomenon
- To develop thermal-analysis model for SCIM
- To validate the developed models with experimental measurements for a 7.5KW SCIM

In chapter two, an introduction to the modelling and simulation tools as used in the work as well as the machine data is presented.

Chapter three describes briefly the theory of skin-effect. The derivation of the rectangular bar impedance equation as well as the development of the T-network model is also presented in this chapter.

Chapter four presents the optimisation technique used in the optimisation of the model and the methods used to arrive at the results.

In chapter five, the D-Q axis transformation is presented and subsequently used to develop the conventional machine model. The equations that completely describe the steady and transient behaviour of the machine are derived and the response curves also depicted.

The machine model with saturation effect and skin-effect is developed in chapter six. Chapter six also presents the model equations and the computer simulation results. The chapter also highlights the comparison between the machine models: conventional/-

saturation, conventional/skin-effect, saturation/skin-effect, and both skin-effect and saturation/conventional.

Chapter seven focuses on the thermal modelling of a squirrel-cage induction machine. Here, losses in induction machine and its determination are elucidated. The chapter continues with the introduction of thermal network and heat transfer theories. The analysis and computational procedures on the developed thermal network model together with the simulation results are also discussed.

The measurements carried out on the test machine are described in chapter 8. The chapter also presents the comparison between the measured and simulated results with relevant comments on the results.

Chapter nine concludes the thesis by giving a summary of the important results.

## 2 Modelling, simulation tools and machine data

### 2.1 State-variable method

The differential equations of a lumped linear network can be written in the form[13,27].

$$\dot{\mathbf{X}}(t) = \mathbf{AX}(t) + \mathbf{BU}(t) \quad (2.1)$$

where,

$\mathbf{A} = n \times n$  System matrix

$\mathbf{B} = n \times m$  Control matrix

$\mathbf{X}(t) = n \times 1$  State variable vector

$\mathbf{U}(t) = p_i \times 1$  Input vector

$p_i$  = Number of inputs

$n$  = System order

Equation(2.1) is known as the state variable equation of the system. The merit of the State-variable method is that it results easily to the form amenable to digital and/or analog computer methods of solution. It can also be extended to analysis of non-linear systems. This method has therefore been used extensively to represent electrical machine connected to a source as:

$$\dot{\mathbf{V}} = \mathbf{Ri} + \dot{\mathbf{L}}\mathbf{i} \quad (2.2)$$

Putting equation(2.2) in its State-variable form result to equation(2.3)

$$\dot{\mathbf{i}} = \mathbf{L}^{-1}\mathbf{V} - \mathbf{L}^{-1}\mathbf{Ri} \quad (2.3)$$

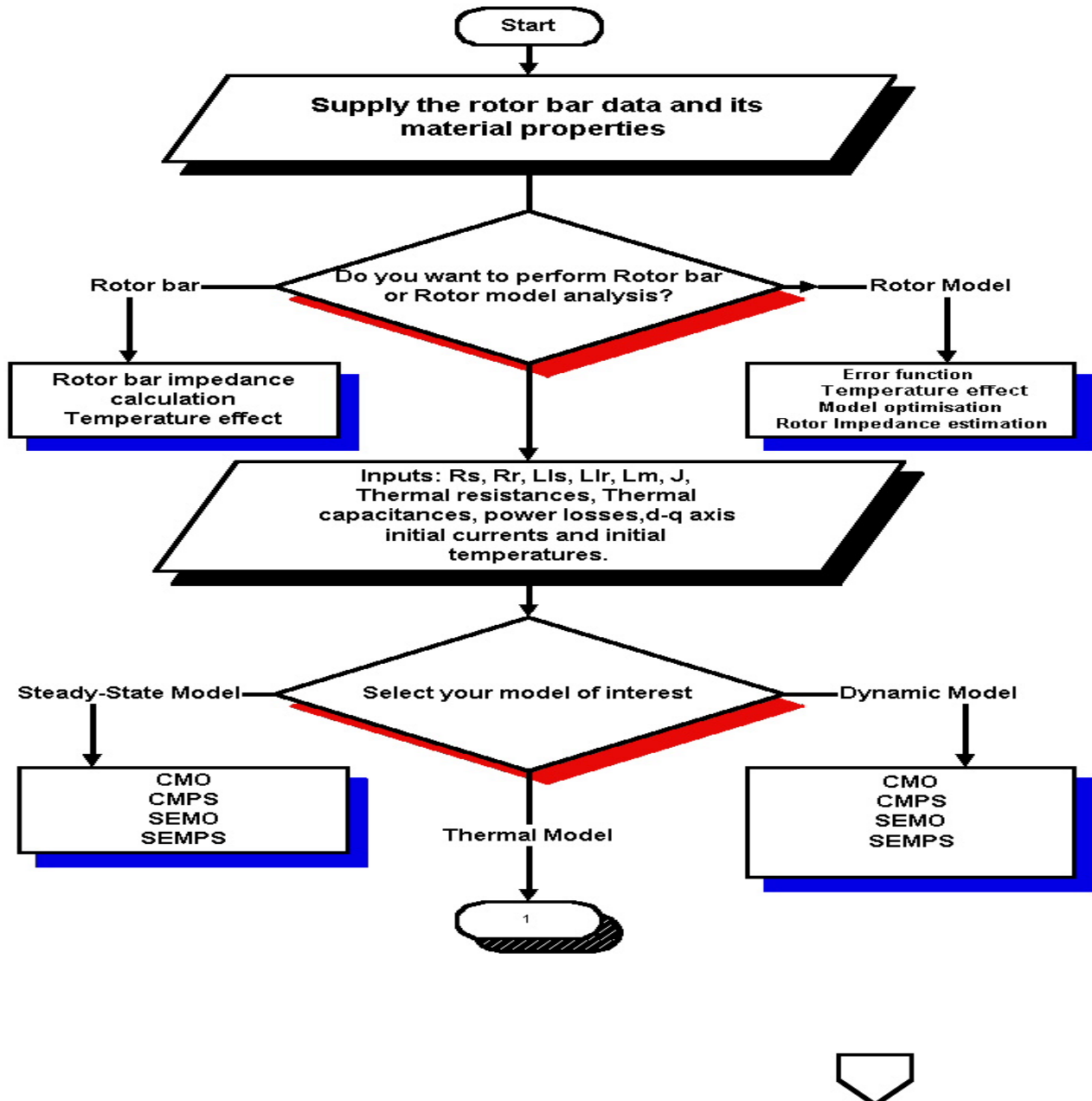
Equation(2.3) represents the State equations with current as state variables. In order to calculate the variables for a given condition of operation, the state equations are used in conjunction with the control variables(Excitation or Torque) applied externally, as well as the relevant initial conditions. For a physical machine where the rotor speed changes with time, analytical solution for equation(2.3) is not possible. Therefore, an efficient and a suitable numerical method becomes imperative.

MATLAB, licensed by MathWorks[10] provides a powerful matrix analysis environment, the basis of state-space modelling of dynamic systems, for systems identification, engineering graphics, modelling and algorithm development. MATLAB has an open system environment which provides access to algorithms and source code and allows the user to mix MATLAB with FORTRAN or C language, and generates code to be used in an existing program.

In the work, several function and script m-files were developed. These developed m-files were used to solve the rotor bar and model optimisation impedances for skin-effect; the machine algebraic and differential system of equations with and /or without saturation and skin effects under steady state and dynamic condition respectively and to solve for the thermal behaviour of the test machine in both steady and transient states. The developed m-files could be executed interactively by loading same in MATLAB command window.

## 2.2 Program Structure

The Program structure is depicted as shown in figure 2.1. The rectangular blocks represent processes that lead to the development of MATLAB m-files.



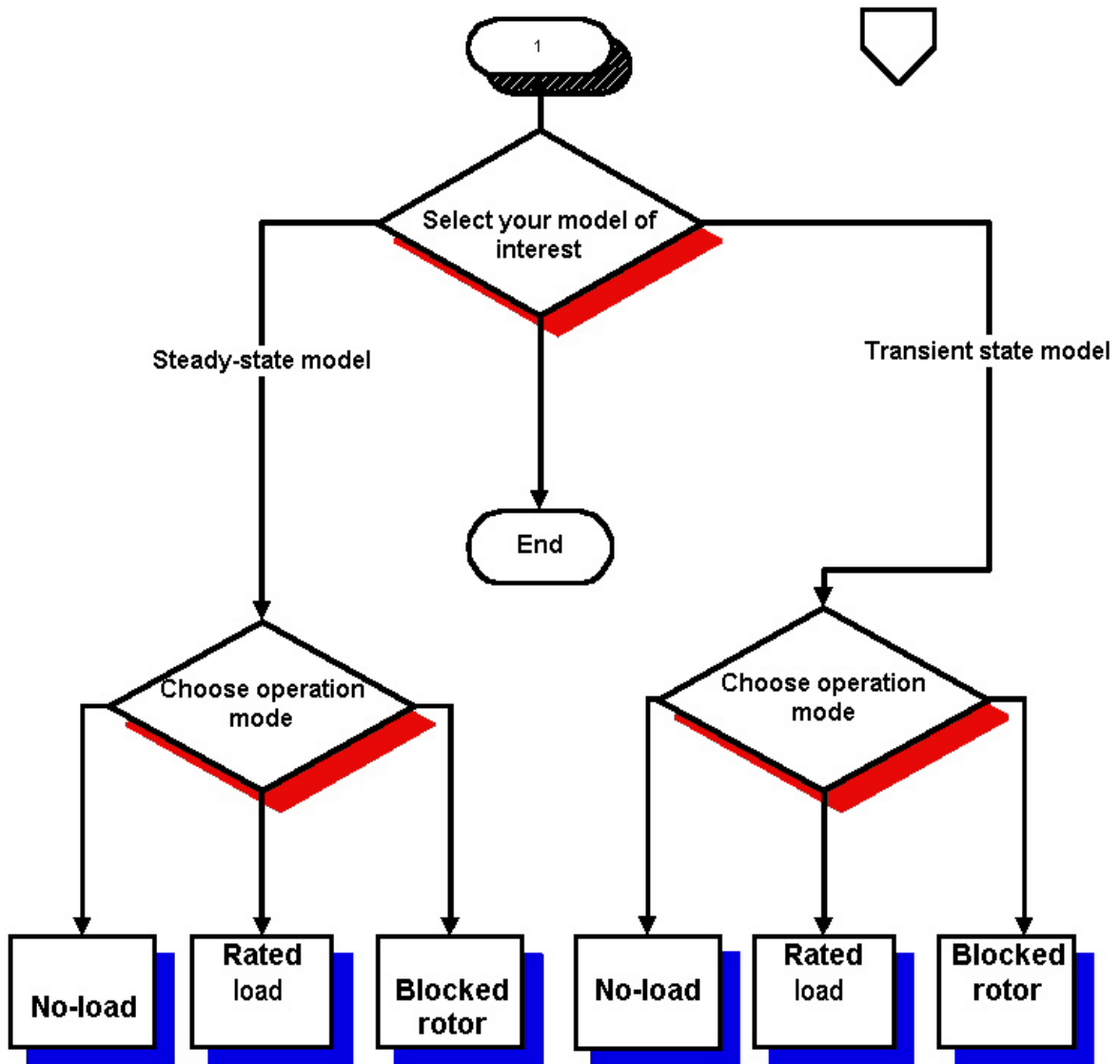


Figure 2.1.: Program structure

### 2.3. Machine data

In order to carry out the complete computer simulation of the 7.5KW Squirrel-cage induction machine, it becomes necessary to determine experimentally the machine data via No-load test, Blocked-rotor test, Retardation test and by the measurements of the d.c. resistances of the stator windings.

#### 2.3.1. No-load test

The aims of the No-load test are to determine:

- Stator ohmic/Copper losses,  $P_r$
- Stator core losses due to hysteresis and Eddy current,  $P_c$
- Rotational losses due to friction and windage,  $P_{rot}$ .
- Magnetizing inductance,  $L_m$

Mathematically, the No-load input power of the machine is expressed as

$$P_o = mI_o^2 r_1 + P_c + P_{rot} \quad (2.16)$$

where,

$m$ =number of stator phases

$r_1$ =effective stator resistance per phase

$P_o$ =No-load input power

$I_o$ =current per phase

The test is carried out at rated frequency and with balanced polyphase voltages applied to the stator terminals. Readings were taken at rated voltage, after the motor has been running for a considerable long period of time necessary for the bearings to be properly lubricated. At No-load, the machine slip and the rotor current are very small thereby resulting to a negligible No-load rotor loss. Figure 2.2 shows the No-load characteristic curves of the test machine.

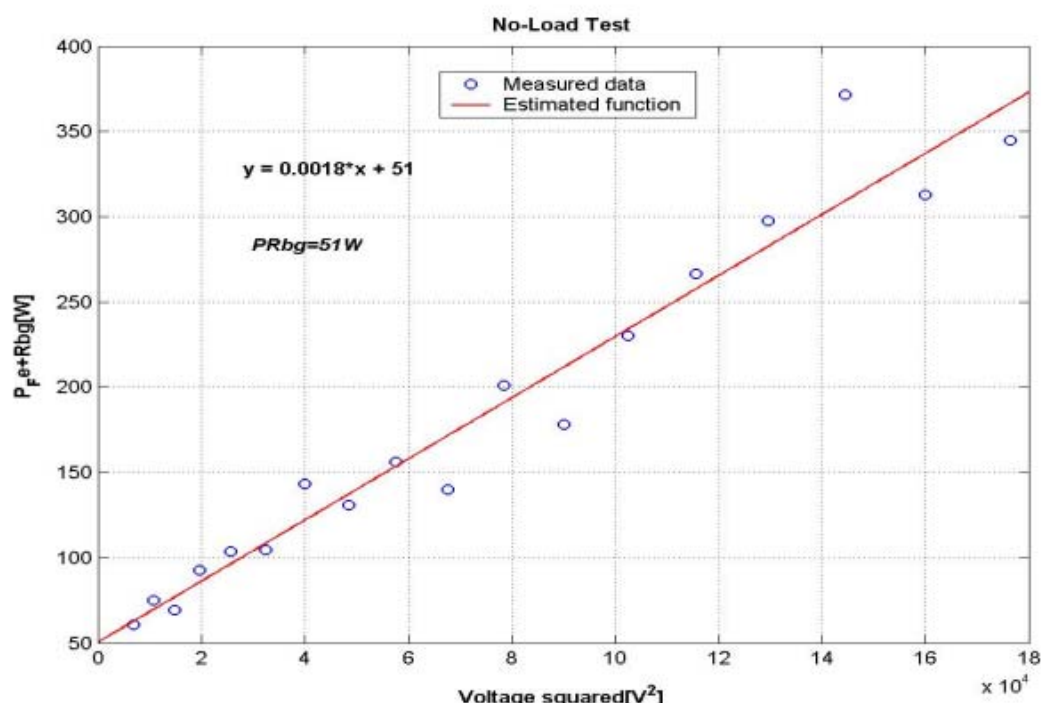


**Figure 2.2.:** Power Losses against Voltage squared at No-Load test.

### 2.3.2. Blocked-rotor test

The blocked-rotor test provides information necessary to determine:

- the winding resistances
- the leakage reactances

In this test, the rotor was blocked by external means to prevent rotation. In blocked-rotor test, the slip is unity ( $s \geq 1$ ). And the mechanical load resistance,  $R_m$  is zero; thereby resulting in a very low input impedance of the equivalent circuit.

The characteristic curve of the test machine at blocked-rotor test is depicted in figures 2.3.

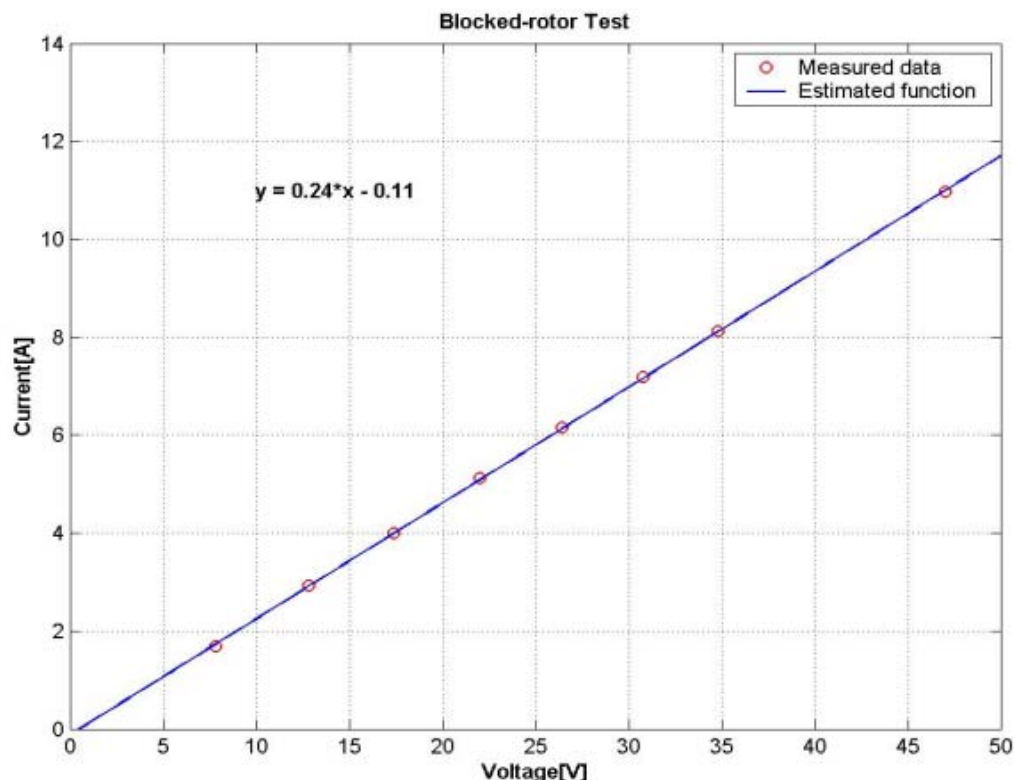


**Figure 2.3.:** Current against Voltage at Blocked-rotor test.

### 2.3.3. Retardation test

The retardation test was carried out to determine the test motor moment of inertia. In this test, a No-load test was carried out with and without additional standard mass. Figure 2.4 shows the test curve when the machine is stopped and the rotor freely allowed to deaccelerate to zero speed with and without additional standard mass respectively.

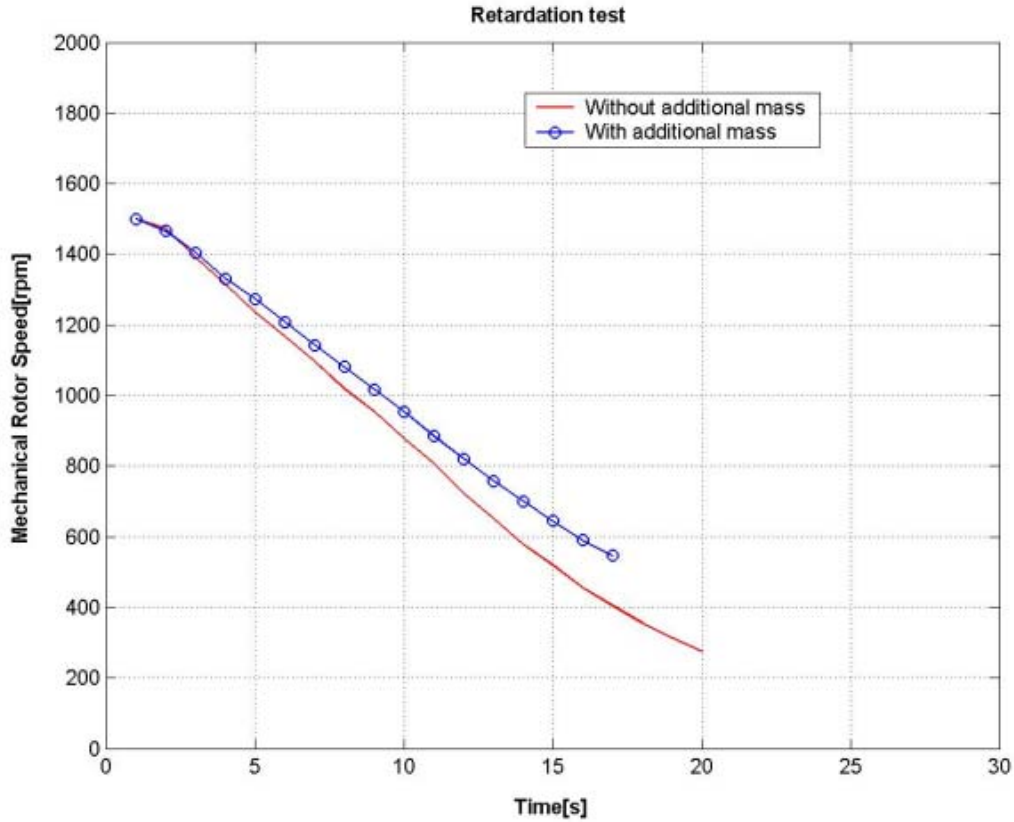


**Figure 2.4.:** Speed against time at retardation test.

### 2.3.4. Induction machines characteristic curves

Generally, other than the above-mentioned tests, parameters of standard induction machines can be obtained from manufacturer's data as well as from the Finite-Element-Analysis(FEA) calculation results.

By using the manufacturer's data(**SCHORCH**), the induction machines characteristic curves with the number of poles as a parameter are shown in figures 2.5, 2.6, 2.7 and 2.8. Figure 2.9 and figure 2.10 show the characteristic curves of reactances and resistance of a 4-Pole induction machine respectively. In figures 2.5 and 2.6, it is seen that due to the large air-gap of high-pole machines, their efficiency and power factor lie below designs with low number of poles. Figure 2.5 also shows that irrespective of the number of poles, at rated output power above 500KW, the efficiency of standard induction machines remains fairly the same. In figure 2.8, it can be seen that the moment of inertia for a high pole induction machine is more than that of a low pole induction machine of the same rated output power. This is because the relative mass of an induction machine increases with increase in size—or the number of poles.

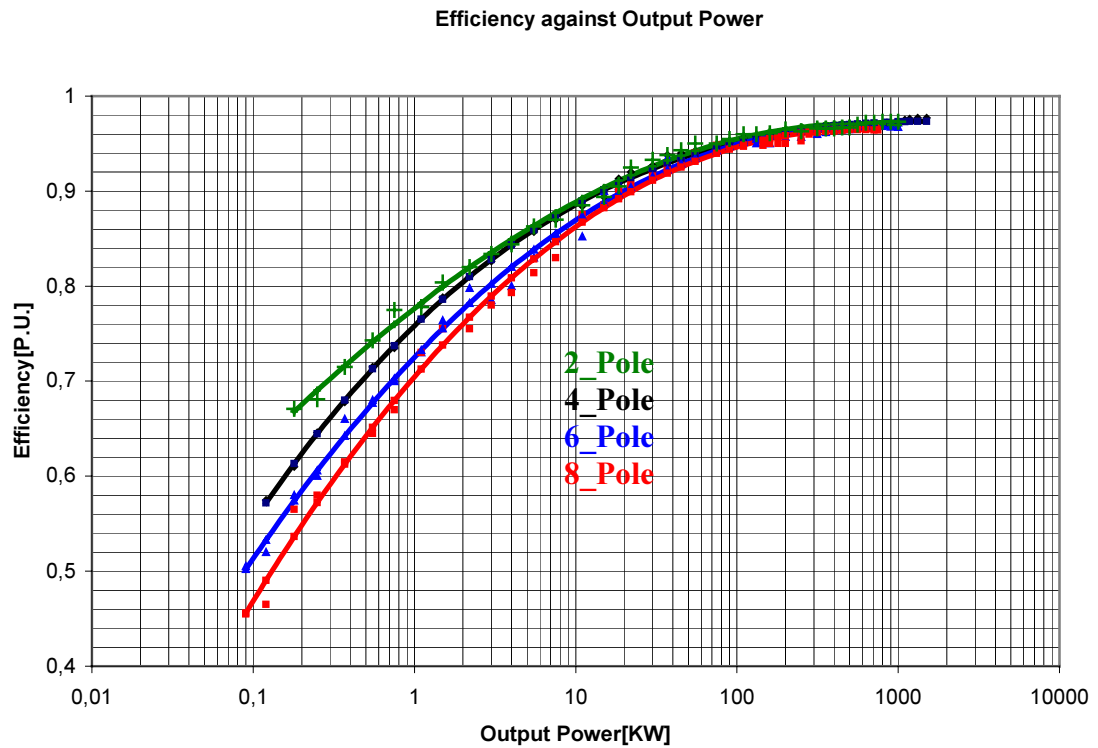


**Figure 2.5:** Efficiency of Induction machine

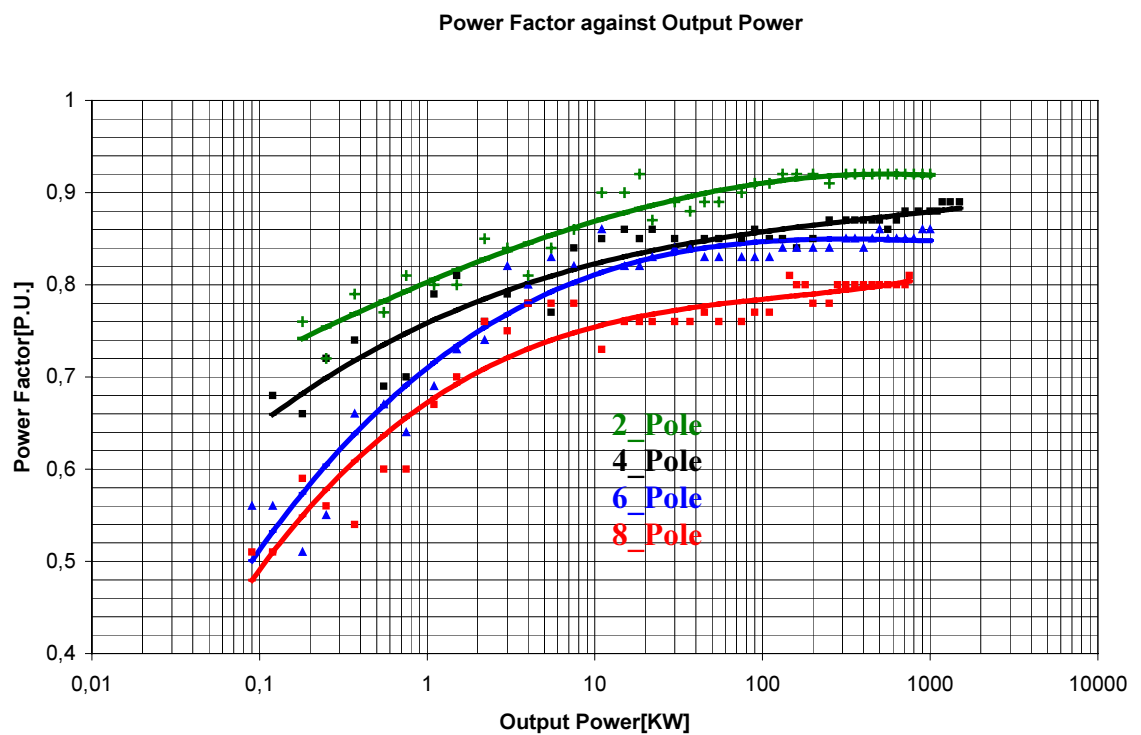


**Figure 2.6:** Power factor of Induction machine

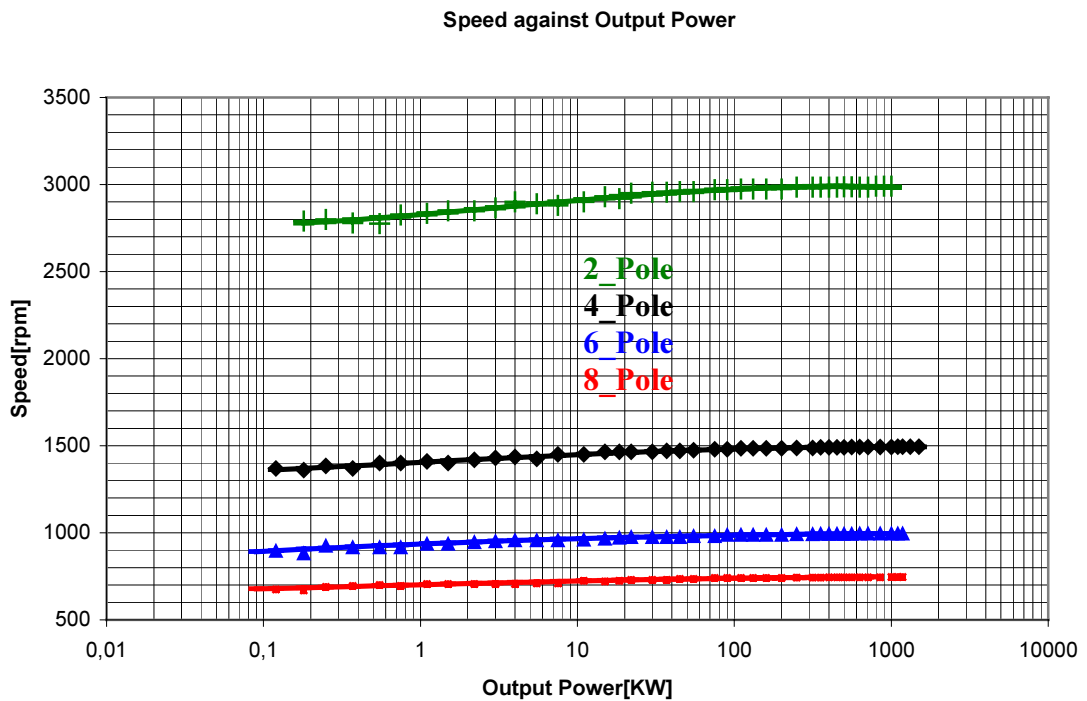


**Figure 2.7:** Speed of Induction machine

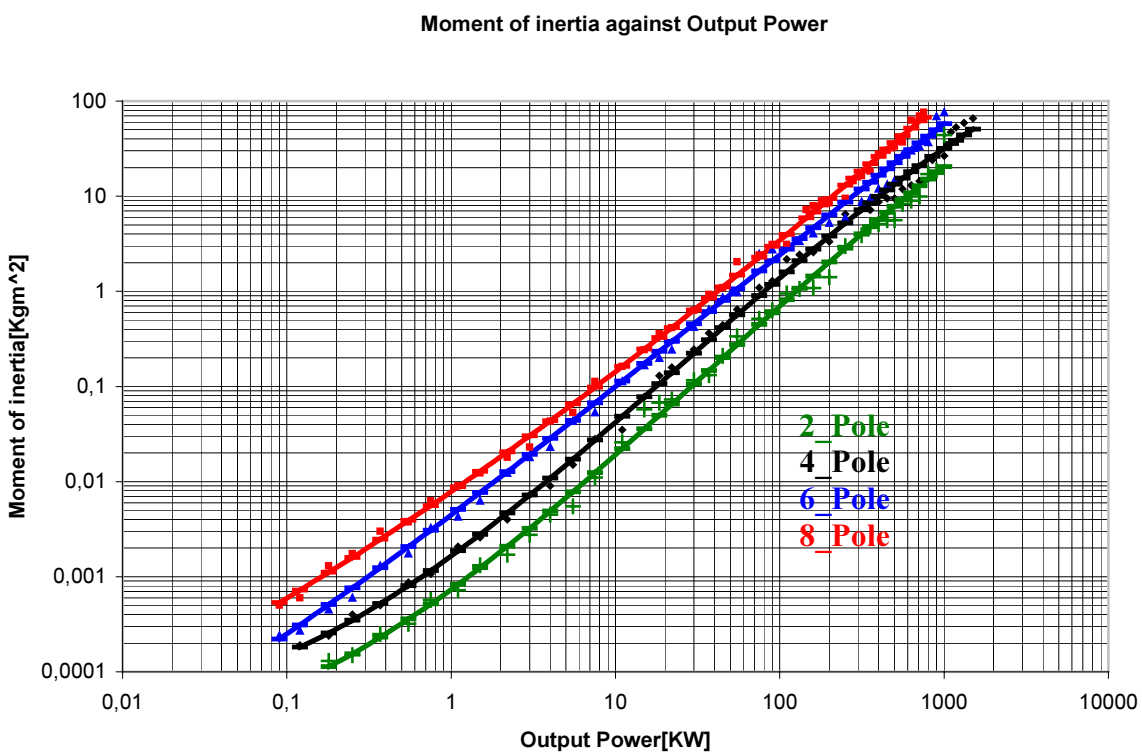


**Figure 2.8:** Moment of inertia of Induction machine

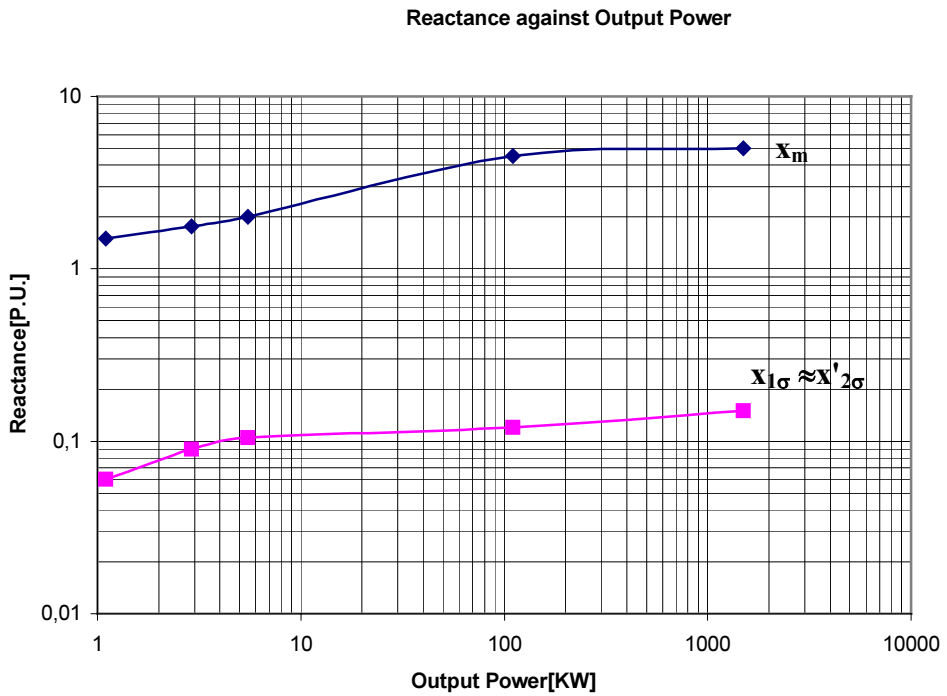


**Figure 2.9:** Reactances of a 4-pole Induction machine

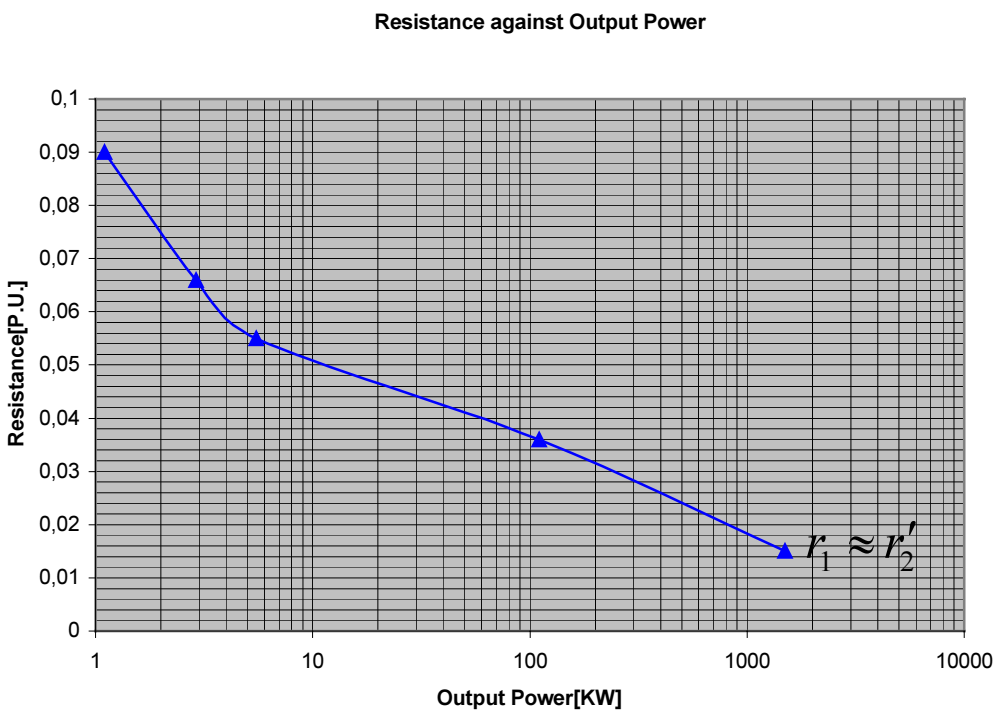


**Figure 2.10:** Resistance of a 4-pole Induction machine

Figures 2.11, 2.12 and 2.13 are the numerical FEA calculation results for the 7.5KW induction machine at 50Hz rated frequency—computed using the finite-element analysis, FEA program[87].

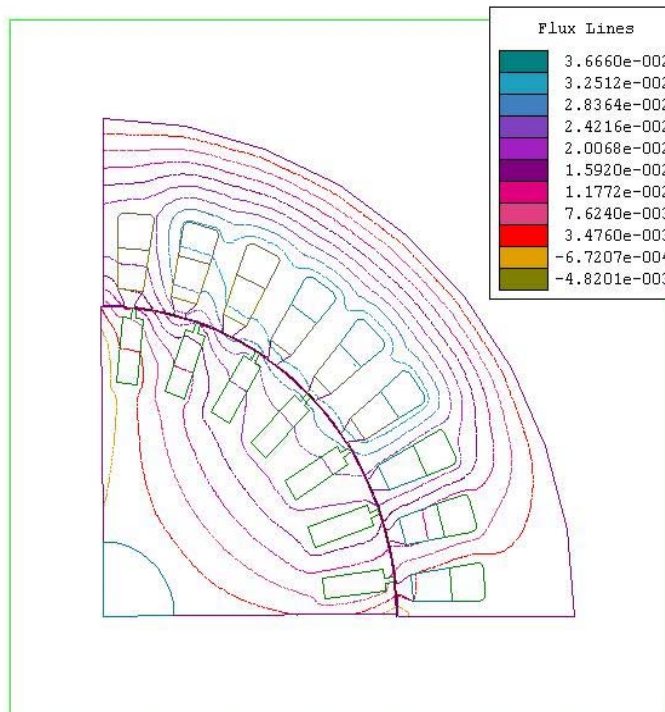


**Figure 2.11:** FEA solution of the flux distribution in the test induction machine at No-Load( $t=6\text{ms}$ )

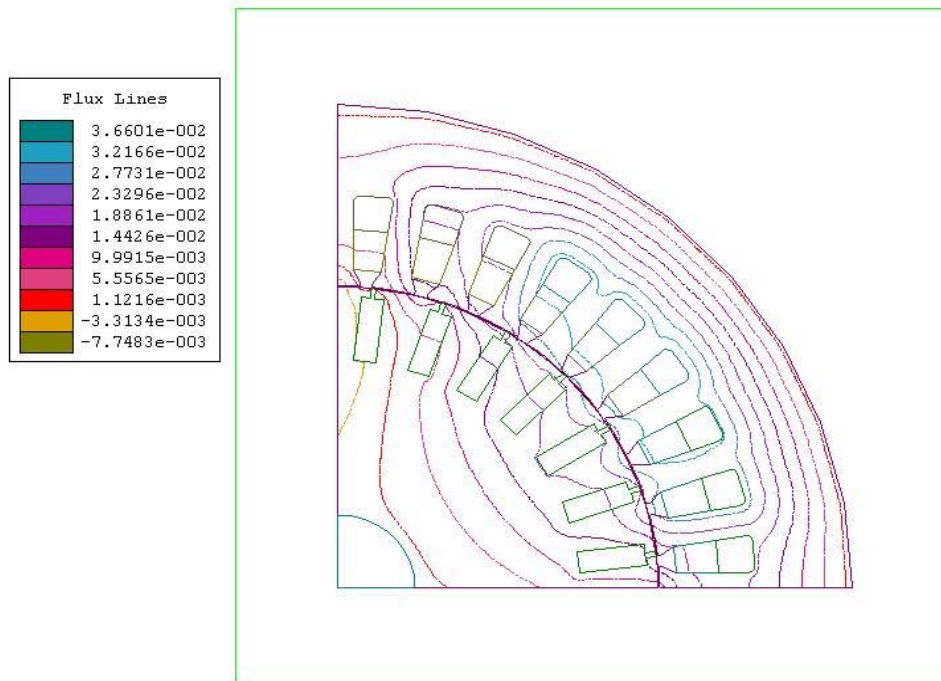


**Figure 2.12:** FEA solution of the flux distribution in the test induction machine at rated load( $t=3\text{ms}$ )

Table 2.1 shows the data for the test 7.5KW Squirrel-cage induction machine.

Output Power	7.5KW
Rated voltage	340V
Winding connection	Delta
Number of Poles	4
Rated speed	1400rpm
Rated frequency	50Hz
Number of Stator slots	36
Outer diameter of stator	200mm
Inner diameter of stator	125mm
Coil pitch	12
Wire diameter	0.71mm
Slot insulation thickness	0.3mm
Number of rotor slots	28
Air gap	0.3mm
Inner diameter of rotor	30mm
Height of end ring	13.2mm
Width of end ring	4.4mm
Half-turn length of stator winding	39.667mm
Iron core length	170mm
Bar length	239mm
Stator resistance	2.52195ohm
Stator leakage reactance	1.95145ohm
Rotor resistance	0.976292ohm
Rotor leakage reactance	2.99451ohm
Magnetizing reactance	55.3431ohm
Mechanical shaft torque	51.2636Nm
Equivalent stator stacking factor	0.95
Equivalent rotor stacking factor	0.95
Estimated rotor inertia moment	0.1173939Kgm^2
Type of rotor cage	Steel(cast copper)
Conductivity of rotor bars	56Sm/mm^2
Permeability of free space	$4\pi \times 10^{-7}$ H/m
Relative permeability of copper	1000
Temperature coefficient of copper at 20°C	0.0039/K
End ring resistance	4.49386e-6ohm
End ring leakage inductance	3.01401e-9H
Number of parallel branches	1
Number of turns in the stator winding	174
Rated current	19.2A

**Table 2.1:** The machine data

The name plate description of the load machine is:

IEC 132 VDE 0530

Rated voltage 230V

Rated speed 1490rpm

Rated current 33.5A  
Rated power 7.6KW  
Field current 1.60A  
Field voltage 180V  
Thermal insulation class F  
Estimated moment of inertia 0.10958Kgm<sup>2</sup>

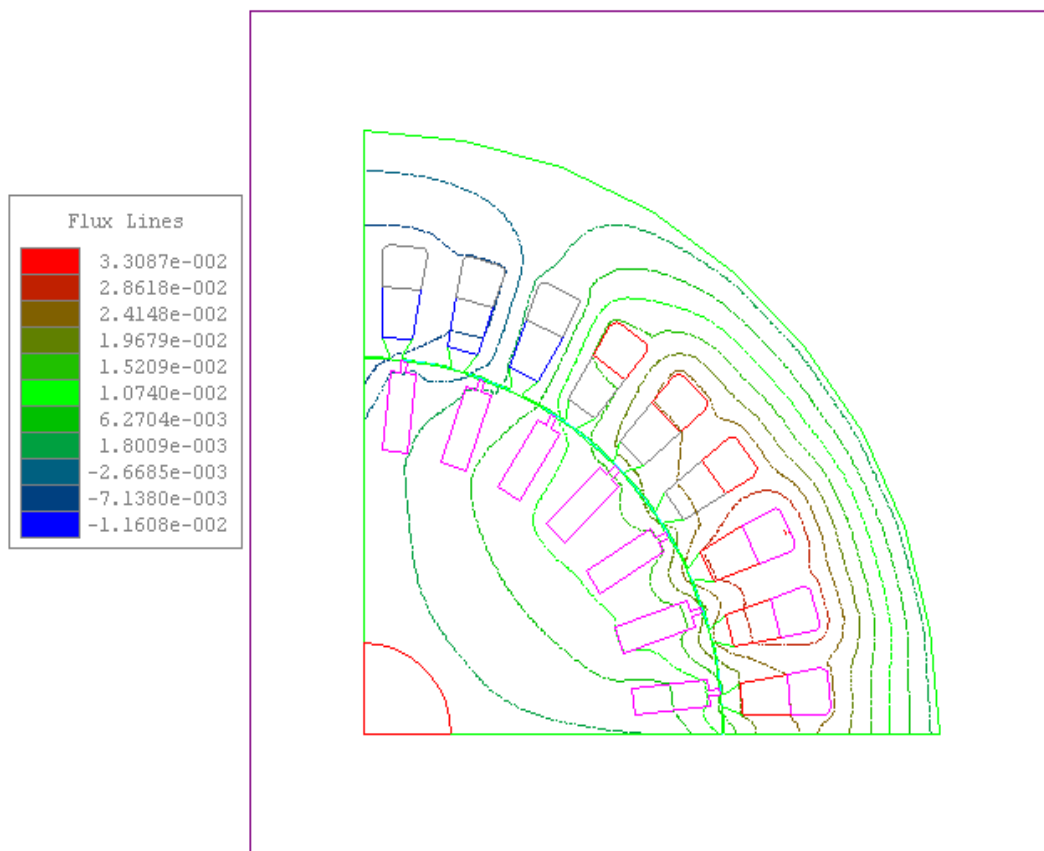


**Figure 2.13:** FEA solution of the flux distribution in the test induction machine at blocked rotor( $t=21\text{ms}$ )

### 3 Rotor-bar modelling for skin-effect

#### 3.1 Theory of Skin-effect

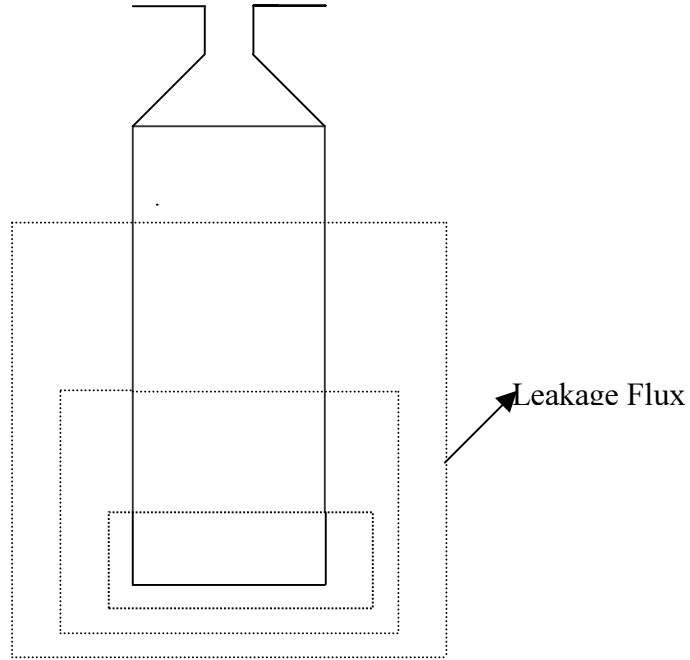


**Figure 3.1.:** Deep rectangular rotor bar

If the squirrel-cage bar is made very deep and narrow as shown above, the bottom parts of the rotor bar are linked by more slot leakage flux than the top parts. Under transient conditions, the bottom part of the rotor bar experiences a higher inductance than the top part of the bar due to non-uniform flux distribution; resultantly causing the current to flow primarily in the top part of the bar. The aftermath of this current migration is to decrease the apparent inductance of the rotor conductors and to increase their effective resistance[4]. The magnitude of these changes on the effective rotor conductor's resistance and inductance is very much dependent on the design of the rotor bars. This phenomenon of decrease in inductance and increase in resistance of rotor conductors is known as the deep bar effect or the skin-effect.

This effect is highly noticeable in motors with rotor bars that have a large bar depth to bar width ratio and in motors operated over a wide frequency ranges—such as in induction motors fed by PMW inverters. Consequently, large squirrel-cage machines are often designed to exhibit predominant skin effect at the higher rotor frequencies to achieve a high starting torque and a relatively low starting current. In this work, the rotor bar of the test machine is of the rectangular type.

### 3.2 Derivation of impedance equation for rectangular rotor bar

The skin-effect phenomenon in rectangular rotor bar as shown in figure 3.2 can be determined through the conductor inner impedance,  $Z_i$ . This can be achieved through the lumped-parameter network method. In this method, the rotor bar conductor is divided into  $n$ -equal number of sections[8,9]. By so doing, the current distribution within each section can be considered uniform. The height of the section,  $h_{sec}$  must be smaller than the skin-depth,  $\delta$ .

$$h_{sec} \ll \delta$$

and

$$\delta = \sqrt{\frac{\rho}{\pi f \mu_0}} \quad (3.1)$$

The skin-depth as a function of frequency for copper and aluminium rotor bar is shown in figure 3.3. It is seen that  $\delta$  is dependent on temperature and also on the material of which the rotor bar is made. At a working frequency of 4000Hz,  $\delta$  is approximately 1.04mm which informed the basis for the bar divisions.

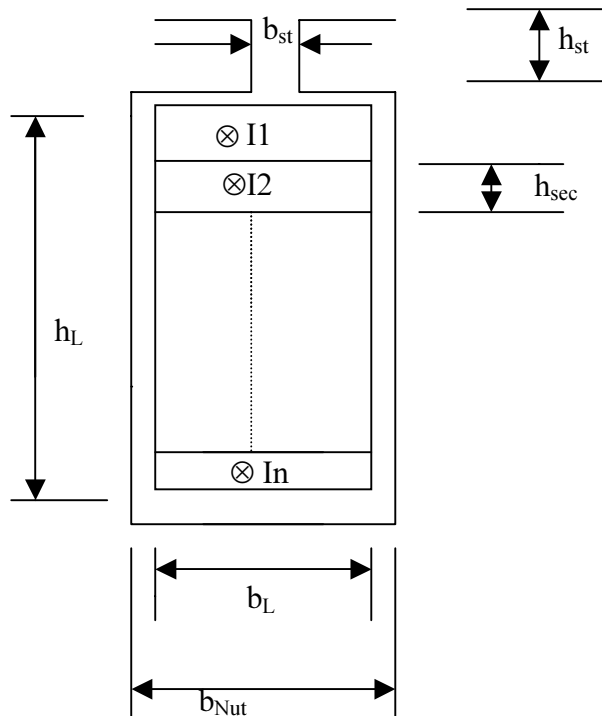


**Figure 3.2:** n sections of rectangular rotor bar

Total resistance of the rectangular bar is,  $R_T$

$$R_T = \frac{L_s}{\chi_{cu} h_L b_L} \quad (3.2)$$

Where,

$L_s$  = length of the rotor bar

$\chi_{cu}$  = conductivity of copper conductor

$h_L$  = height of rotor conductor

$b_L$  = width of rotor conductor

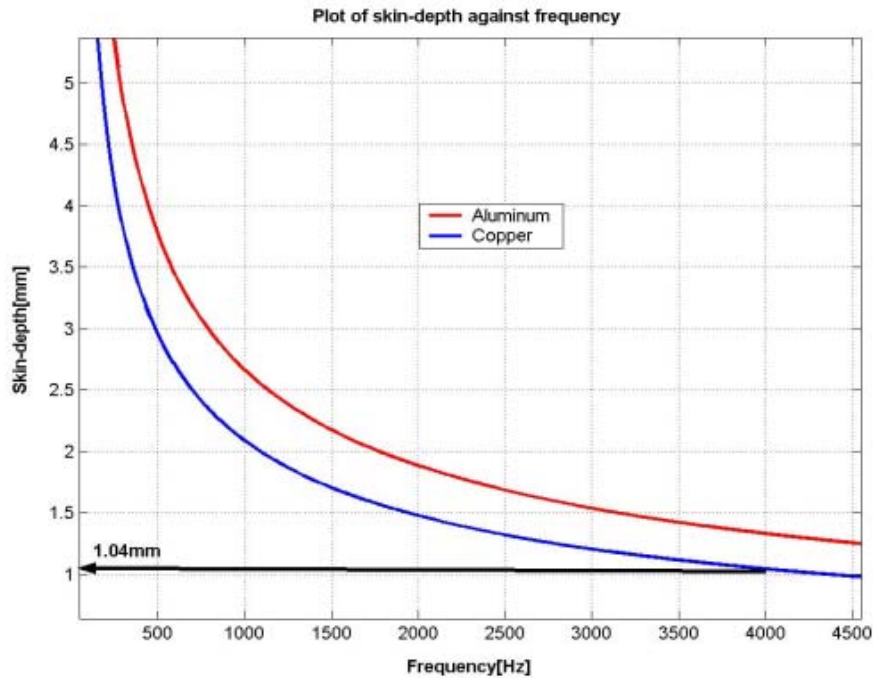


**Figure 3.3:** Graph of skin-depth against frequency.

The resistance of each section is therefore given by

$$R_L = (L_s) / (\chi_{cu} h_{sec} b_L) \quad (3.3)$$

$$\text{And, } h_{sec} = h_L/n \quad (3.4)$$

where

$n$  = total number of sections

The magnetic flux density in section one of the bar is

$$\underline{B}_1 = \frac{\mu_o \underline{I}_1}{b_{Nut}} \quad (3.5)$$

Therefore, the magnetic flux between the first and fictitious section becomes

$$\underline{\Phi}_1 = \underline{B}_1 L_s h_{sec} = \mu_o L_s \underline{I}_1 / (n b_{Nut}) \quad (3.6)$$

where  $\underline{I}_1$  is the current vector that flows in section one of the bar.

In analogy, the magnetic flux between section 2 and section 3, becomes

$$\underline{\Phi}_2 = \left( \mu_o L_s h_L / n b_{Nut} \right) (\underline{I}_1 + \underline{I}_2) \quad (3.7)$$

In general, the magnetic flux between the sections  $n$  and  $n+1$  of the rotor bar is,

$$\underline{\Phi}_n = \left( \mu_o L_s h_L / nb_{Nut} \right) \sum_{v=1}^n \underline{I}_v \quad (3.8)$$

where,

$\underline{I}_v$  =the current vector in each of the sections.

It can be observed from figure 3.2 that a loop results between the nth and (n+1)th sections. Therefore Kirchhoff's voltage equation could be applied.

$$U = 0 = iR + \frac{d\phi}{dt} \quad (3.9)$$

Between the nth and (n+1)th section, we have

$$0 = \underline{I}_n R_L - \underline{I}_{n+1} R_L + j\omega \underline{\phi}_n \quad (3.10)$$

Combining equations (3.3),(3.8) and (3.10), and with little manipulation, the total bar current is

$$\underline{I}_{n+1} = \underline{I}_n + j \left( \omega \mu_o h_L^2 b_L \chi_{cu} / n^2 b_{Nut} \right) \sum_{v=1}^n \underline{I}_v \quad (3.11)$$

From equation(3.11), let define

$$d = \left( \omega \mu_o h_L^2 b_L \chi_{cu} / n^2 b_{Nut} \right) \quad (3.12)$$

It therefore clearly shows that if the number of the bar section, n is five, the loop currents from equation(3.11) become,

$$\underline{I}_2 = \underline{I}_1 + jd \underline{I}_1 \quad (3.13a)$$

$$\underline{I}_3 = \underline{I}_2 + jd(\underline{I}_1 + \underline{I}_2) \quad (3.13b)$$

$$\underline{I}_4 = \underline{I}_3 + jd(\underline{I}_1 + \underline{I}_2 + \underline{I}_3) \quad (3.13c)$$

$$\underline{I}_5 = \underline{I}_4 + jd(\underline{I}_1 + \underline{I}_2 + \underline{I}_3 + \underline{I}_4) \quad (3.13d)$$

The vector diagram showing the currents for a 5-section rotor bar is shown in figure 3.4. The total voltage drop in the rotor bar is,

$$\underline{U} = R_L \underline{I}_5 \quad (3.14a)$$

The a.c resistance and the inner reactance of the rotor bar can be calculated from the voltage drop and the total bar current as,

$$\underline{U} = R_L \underline{I}_5 = R_{Wi} \underline{I} + jX_{Wi} \underline{I} \quad (3.14b)$$

Also the total bar current can generally be expressed as,

$$\underline{I} = \underline{I}_1 + \sum_{v=2}^n \left( \underline{I}_{v-1} + jd \sum_{\mu=1}^{v-1} \underline{I}_{\mu} \right) \quad (3.15)$$

The value of the bar voltage, $\underline{U}$  to the total bar current, $\underline{I}$  gives the inner impedance, $\underline{Z}_i$ :

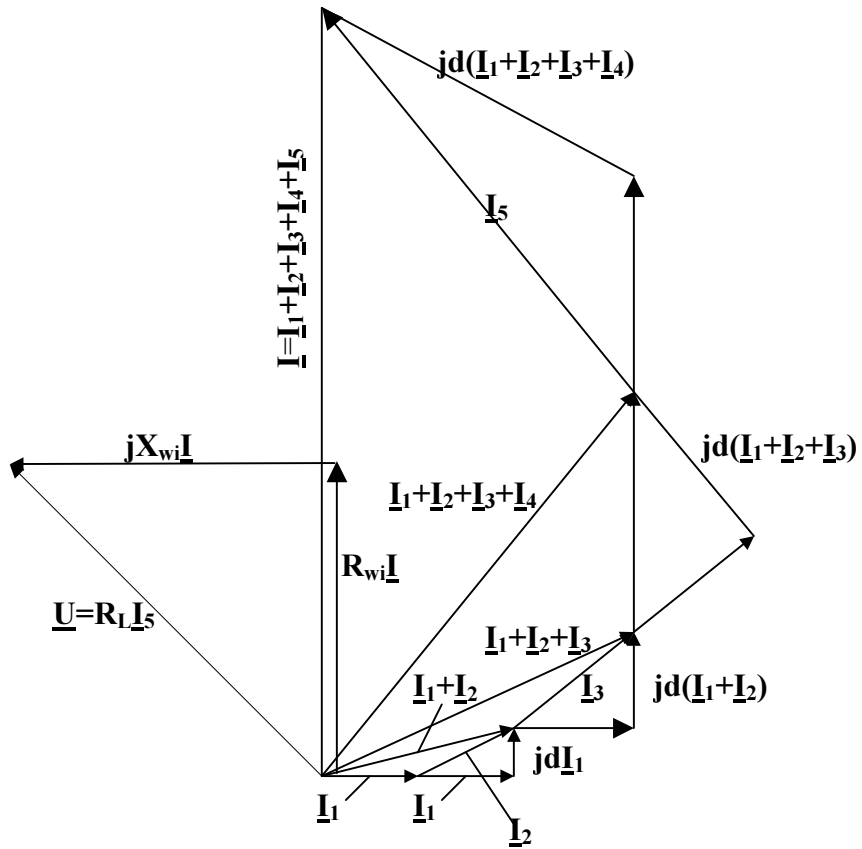


**Figure 3.4:** Vector diagram for a 5-section rotor bar

$$\underline{Z}_i = \frac{\underline{U}}{\underline{I}} \quad (3.16)$$

MATLAB program is developed and used to evaluate the complex impedance,  $\underline{Z}_i$  of the rotor bar. Because of the linearity of the equations, the bar current,  $\underline{I}_1$  can be optionally assumed to take any value.

The outside bar reactance,  $X_a$  as well as the impedance of the end ring parts,  $Z_r$  can be computed thus:

$$\underline{Z} = \underline{Z}_i + jX_a + \underline{Z}_r \quad (3.17)$$

The value of the outside reactance,  $X_a$  is however, independent of the skin-effect influence on the rotor inner bar. It has been shown by Weidemann[51] that the computational numerical difficulties involve in determining the effect of skin effect on the impedance of the outside bar reactance and the end ring parts can be neglected since the magnitude of their values have minimal influence on the total bar impedance at high frequency. Figures 3.5 and 3.6 show the computed rotor bar impedance for varying rotor frequency.

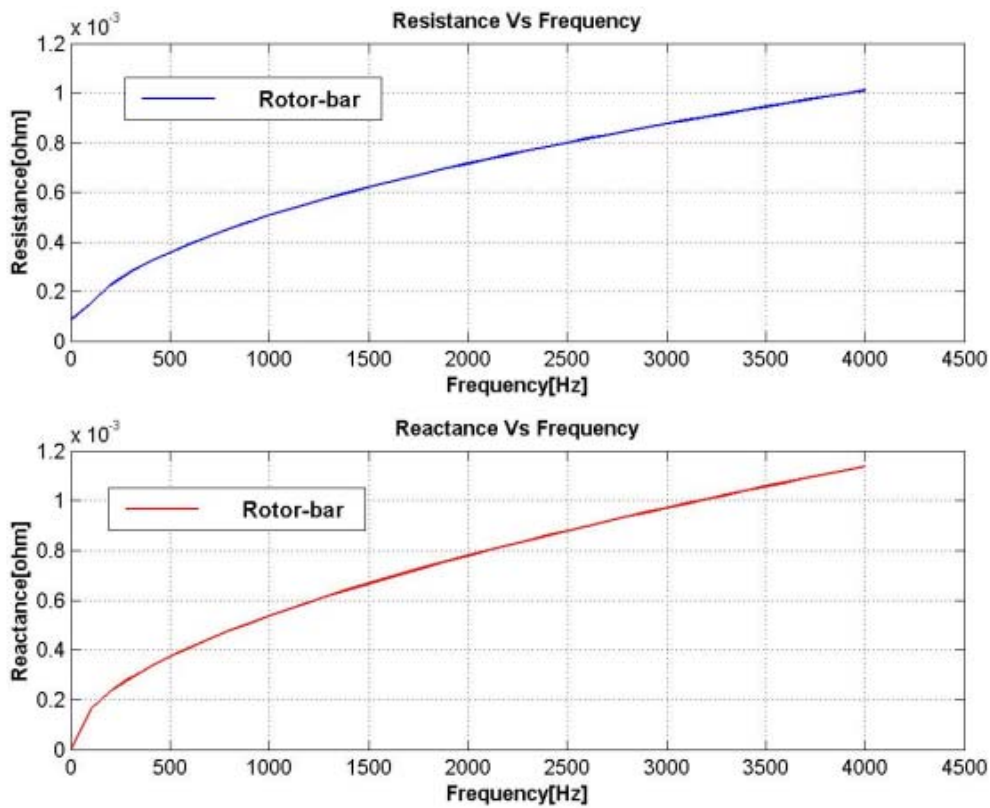


**Figure 3.5:** Rotor-bar plots for n=100.

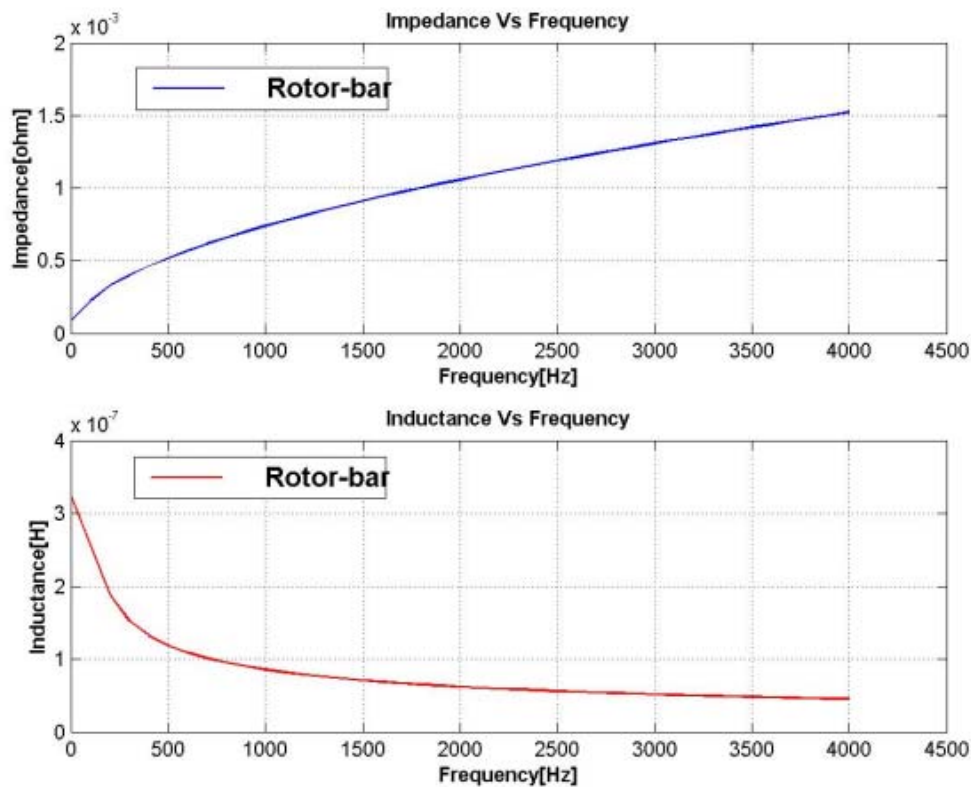


**Figure 3.6:** Rotor-bar plots for n=100.

### 3.3 Temperature effect

It has been observed that changes in temperature influence to a considerable extent the performance of induction machine[12]. This is so because as the rotor temperature changes, the secondary resistance also changes. The influence of change in the secondary resistance is twofold. First, the time constant for the transient phenomena is changed by a change in the secondary resistance. When the temperature rises, the rotor resistance increases and the time constant decreases. Second, the steady-state operation of the induction machine is also influenced to some extent by a change in the rotor resistance due to temperature changes. Again, the rotor bar equation for skin-effect as shown in section 3.2 also indicates that the bar impedance is dependent on resistivity( $\rho$ ) which in itself is dependent on temperature. It is therefore imperative for the effect of temperature to be included in the rotor bar model if accurate modelling of the machine is to be realised. The resistance of the rotor bar at any temperature  $\theta^{\circ}\text{C}$  is given by

$$R_{\theta} = R_{20} (1 + \alpha \Delta \theta) \quad (3.18)$$

where,

$$\Delta \theta = (\theta_t^{\circ}\text{C} - 20^{\circ}\text{C}) \quad (3.19)$$

$R_{\theta}$  = resistance at  $\theta^{\circ}\text{C}$

$R_{20}$ = resistance at  $20^{\circ}\text{C}$

$\alpha$  = temperature coefficient ( for copper,  $\alpha = 0.0039/\text{K}$ )

Figures 3.7 and 3.8 show the computed rotor-bar impedance at different temperature points.

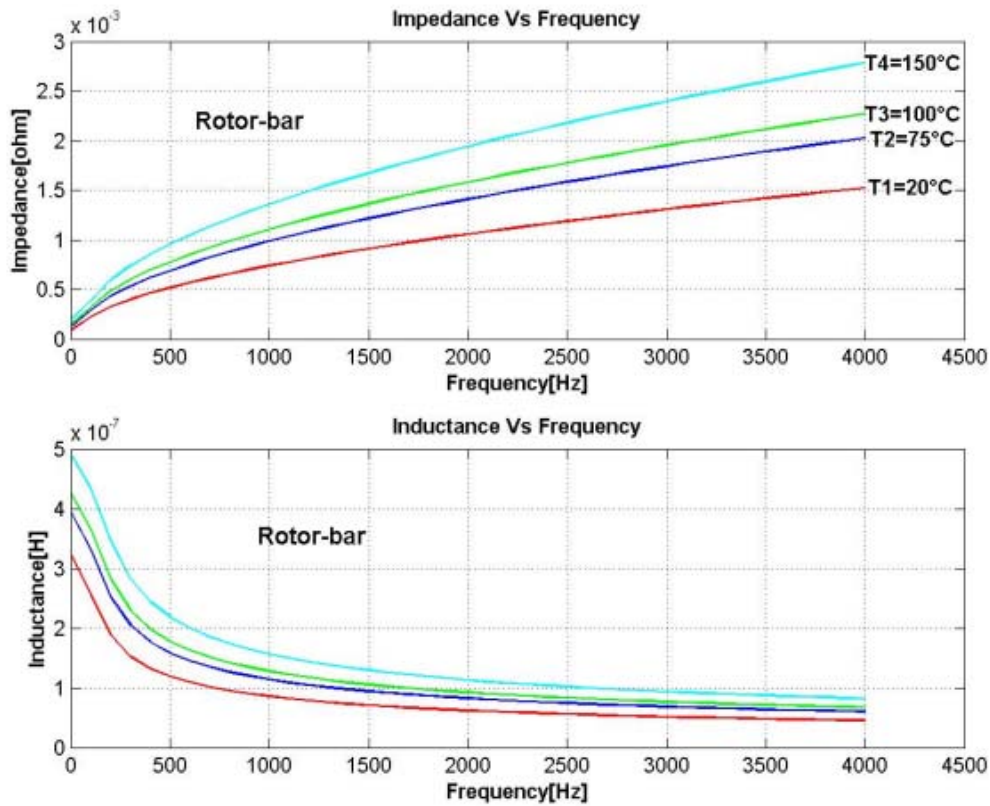


Figure 3.7: Rotor bar plots at different temperatures.

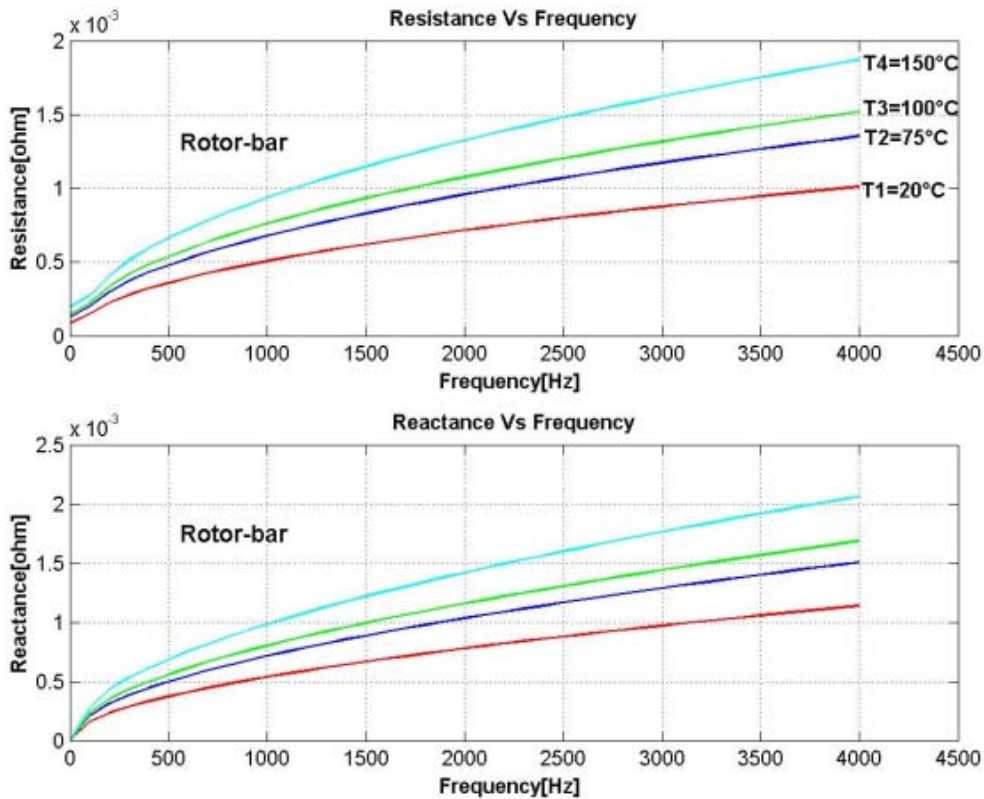
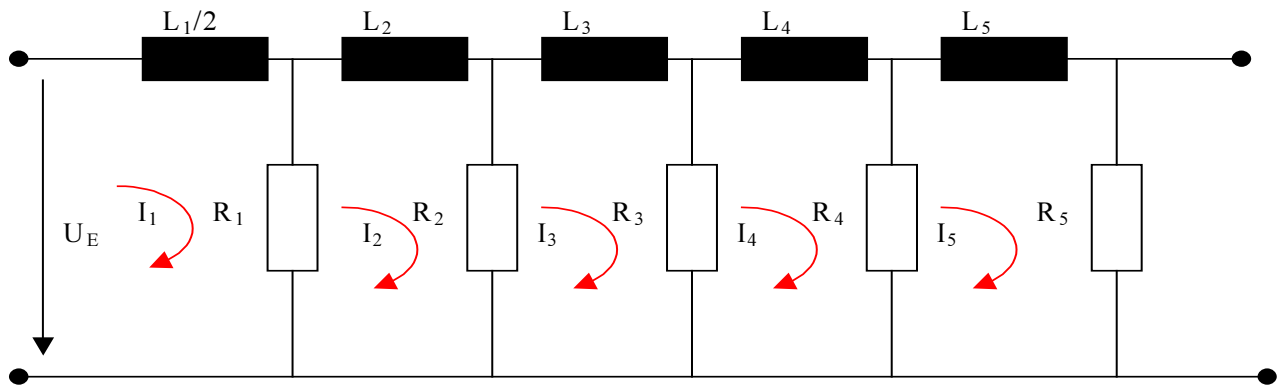


Figure 3.8: Rotor bar plots at different temperatures.

### 3.4 Derivation of the model impedance equation

The T-model network as shown in figure 3.9 is used in the modelling of the rotor bar. In figure 3.9 the rotor bar is divided into five sections. Suffice to say that although the program developed could be used to solve for the network impedance for n-number of divisions, the choice of five divisions is informed by the trends of the graphs shown in figures 3.10, 3.11 and figure 3.12. In these figures it is seen that for number of bar divisions greater than five, the model impedance, reactance and resistance do not change considerably with changes in frequency.



**Figure 3.9:** T -model rotor bar representation

From figure 3.9,

$L_1, L_2, L_3, L_4$  and  $L_5$  = model inductances

$R_1, R_2, R_3, R_4$  and  $R_5$  = model resistances

$I_1, I_2, I_3, I_4$  and  $I_5$  = loop currents

$U_E$  = input model voltage

Applying Kirchhoff's voltage law[28] in figure 3.9, the following loop voltage equations result.

$$U_E = \frac{L_1}{2} \frac{dI_1}{dt} + R_1 I_1 - R_1 I_2 \quad (3.20a)$$

$$0 = L_2 \frac{dI_2}{dt} - R_1 I_1 + R_1 I_2 + R_2 I_2 - R_2 I_3 \quad (3.20b)$$

$$0 = L_3 \frac{dI_3}{dt} - R_2 I_2 + R_3 I_3 + R_2 I_3 - R_3 I_4 \quad (3.20c)$$

$$0 = L_4 \frac{dI_4}{dt} - R_3 I_3 + R_3 I_4 + R_4 I_4 - R_4 I_5 \quad (3.20d)$$

$$0 = L_5 \frac{dI_5}{dt} - R_4 I_4 + R_4 I_5 + R_5 I_5 \quad (3.20e)$$

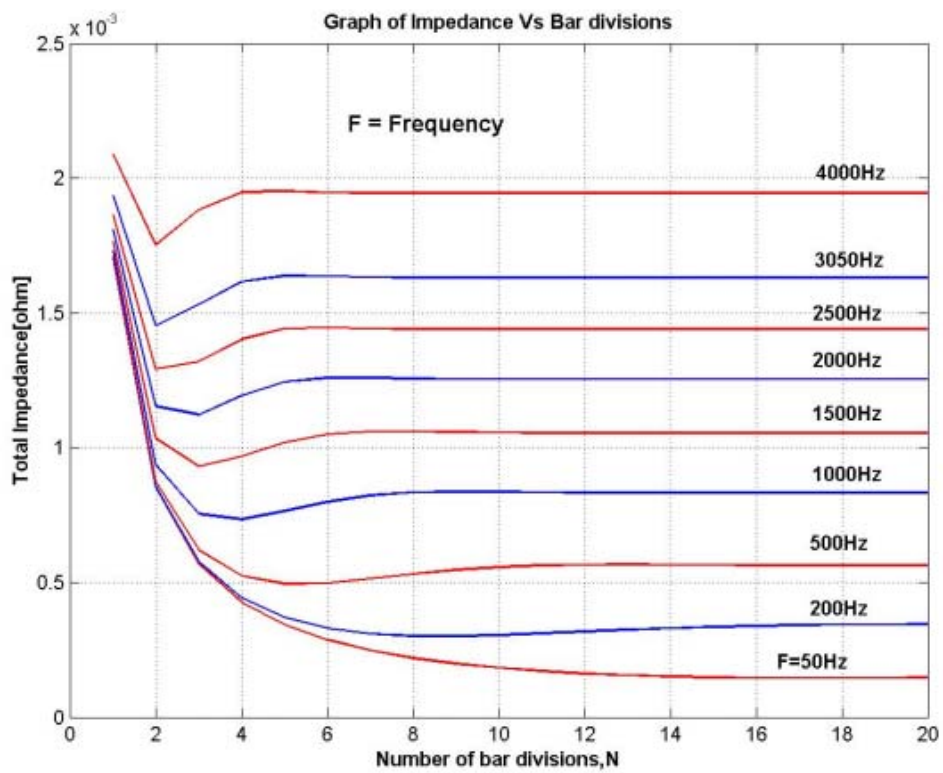


**Figure 3.10:** Graph of impedance against number of bar divisions for varying frequency.

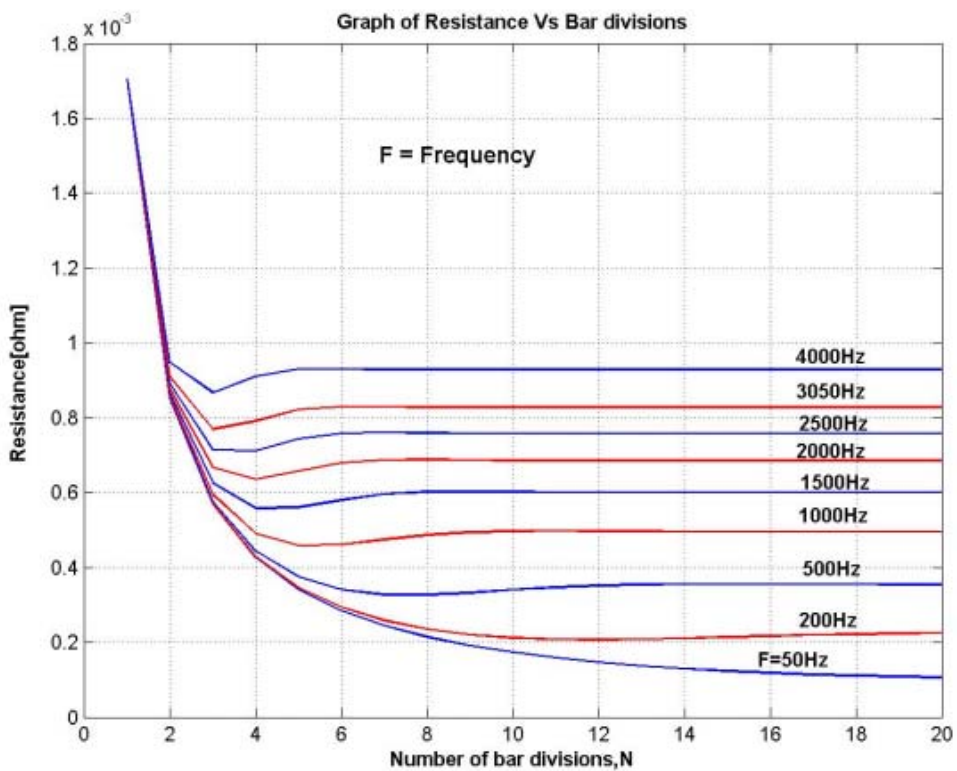


**Figure 3.11:** Graph of resistance against number of bar divisions for varying frequency.

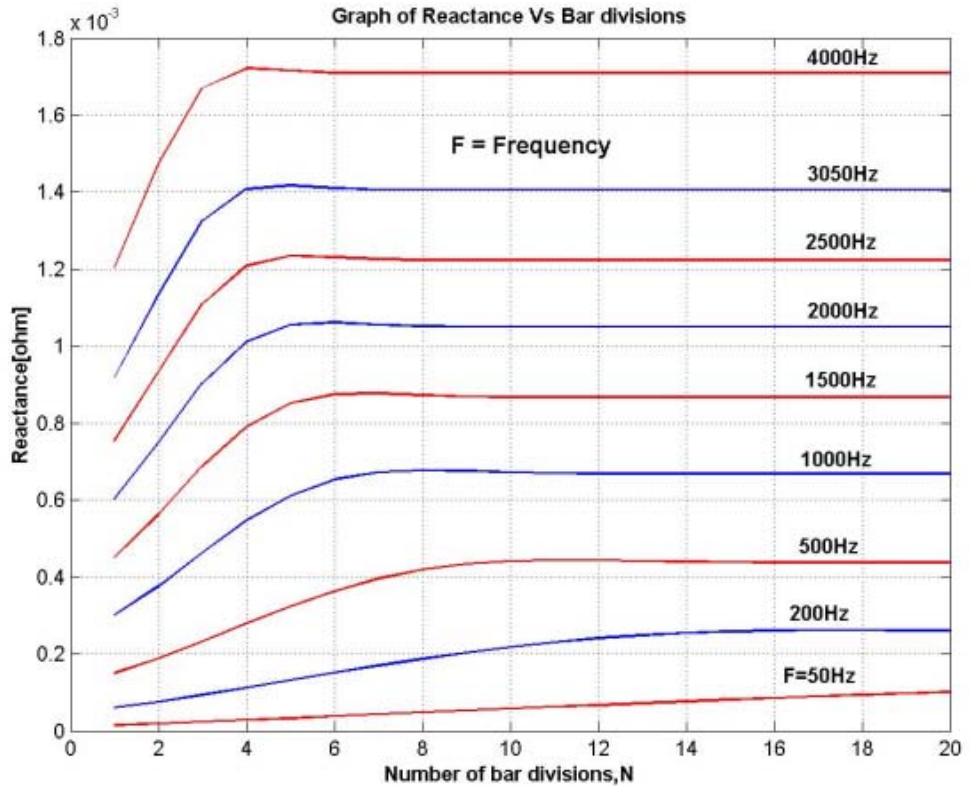


**Figure 3.12:** Graph of reactance against number of bar divisions for varying frequency.

Expressing equations(3.20a-3.20e) in Matrix form, we have

$$\begin{bmatrix} U_E \\ 0 \\ 0 \\ 0 \\ 0 \end{bmatrix} = \begin{bmatrix} R_1 & -R_1 & 0 & 0 & 0 \\ -R_1 & (R_1 + R_2) & -R_2 & 0 & 0 \\ 0 & -R_2 & (R_2 + R_3) & -R_3 & 0 \\ 0 & 0 & -R_3 & (R_3 + R_4) & -R_4 \\ 0 & 0 & 0 & -R_4 & (R_4 + R_5) \end{bmatrix} \begin{bmatrix} I_1 \\ I_2 \\ I_3 \\ I_4 \\ I_5 \end{bmatrix}$$

$$+ \begin{bmatrix} \frac{L_1}{2} & 0 & 0 & 0 & 0 \\ 0 & L_2 & 0 & 0 & 0 \\ 0 & 0 & L_3 & 0 & 0 \\ 0 & 0 & 0 & L_4 & 0 \\ 0 & 0 & 0 & 0 & L_5 \end{bmatrix} \begin{bmatrix} \dot{I}_1 \\ \dot{I}_2 \\ \dot{I}_3 \\ \dot{I}_4 \\ \dot{I}_5 \end{bmatrix} \quad (3.21)$$

Representing equation(3.21) in state variable form[13], we have

$$\dot{X} = \mathbf{AX} + \mathbf{BU} \quad (3.22)$$

$$y = \mathbf{CX} + \mathbf{DU} \quad (3.23)$$

$$\begin{aligned} \begin{bmatrix} \dot{I}_1 \\ \dot{I}_2 \\ \dot{I}_3 \\ \dot{I}_4 \\ \dot{I}_5 \end{bmatrix} &= - \begin{bmatrix} \frac{L_1}{2} & 0 & 0 & 0 & 0 \\ 0 & L_2 & 0 & 0 & 0 \\ 0 & 0 & L_3 & 0 & 0 \\ 0 & 0 & 0 & L_4 & 0 \\ 0 & 0 & 0 & 0 & L_5 \end{bmatrix}^{-1} \\ * \begin{bmatrix} R_1 & -R_1 & 0 & 0 & 0 \\ -R_1 & (R_1 + R_2) & -R_2 & 0 & 0 \\ 0 & -R_2 & (R_2 + R_3) & -R_3 & 0 \\ 0 & 0 & -R_3 & (R_3 + R_4) & -R_4 \\ 0 & 0 & 0 & -R_4 & (R_4 + R_5) \end{bmatrix} &\begin{bmatrix} I_1 \\ I_2 \\ I_3 \\ I_4 \\ I_5 \end{bmatrix} \\ + \begin{bmatrix} \frac{L_1}{2} & 0 & 0 & 0 & 0 \\ 0 & L_2 & 0 & 0 & 0 \\ 0 & 0 & L_3 & 0 & 0 \\ 0 & 0 & 0 & L_4 & 0 \\ 0 & 0 & 0 & 0 & L_5 \end{bmatrix}^{-1} \begin{bmatrix} U_E \\ 0 \\ 0 \\ 0 \\ 0 \end{bmatrix} \end{aligned} \quad (3.24)$$

where,

$$\mathbf{A} = - \begin{bmatrix} \frac{L_1}{2} & 0 & 0 & 0 & 0 \\ 0 & L_2 & 0 & 0 & 0 \\ 0 & 0 & L_3 & 0 & 0 \\ 0 & 0 & 0 & L_4 & 0 \\ 0 & 0 & 0 & 0 & L_5 \end{bmatrix}^{-1} \begin{bmatrix} R_1 & -R_1 & 0 & 0 & 0 \\ -R_1 & (R_1 + R_2) & -R_2 & 0 & 0 \\ 0 & -R_2 & (R_2 + R_3) & -R_3 & 0 \\ 0 & 0 & -R_3 & (R_3 + R_4) & -R_4 \\ 0 & 0 & 0 & -R_4 & (R_4 + R_5) \end{bmatrix} \quad (3.25a)$$

$$\mathbf{B} = \begin{bmatrix} \frac{L_1}{2} & 0 & 0 & 0 & 0 \\ 0 & L_2 & 0 & 0 & 0 \\ 0 & 0 & L_3 & 0 & 0 \\ 0 & 0 & 0 & L_4 & 0 \\ 0 & 0 & 0 & 0 & L_5 \end{bmatrix}^{-1} \quad (3.25b)$$

$$\mathbf{X} = [I_1 \ I_2 \ I_3 \ I_4 \ I_5]^\top \quad (3.25c)$$

$$\mathbf{D} = [0 \ 0 \ 0 \ 0 \ 0] \quad (3.25d)$$

$$\mathbf{C} = [1 \ 0 \ 0 \ 0 \ 0] \quad (3.25e)$$

In order to determine the rotor bar resistance and reactance, it is important to first of all determine the transfer function of the T-model network by taking the Laplace transform of equations(3.22) and (3.23).

Taking the Laplace transform of equations(3.22) and(3.23) we have,

$$\mathbf{SX}(S) = \mathbf{AX}(S) + \mathbf{BU}(S) \quad (3.26)$$

$$\mathbf{Y}(S) = \mathbf{CX}(S) + \mathbf{DU}(S) \quad (3.27)$$

From equation(3.26),

$$(\mathbf{SI} - \mathbf{A})\mathbf{X}(S) = \mathbf{BU}(S)$$

$$\mathbf{X}(S) = (\mathbf{SI} - \mathbf{A})^{-1}\mathbf{BU}(S) \quad (3.28)$$

Where,

$\mathbf{I}$  = identity matrix

Put equation(3.28) into equation(3.27) to get,

$$Y(S) = \mathbf{C}[(\mathbf{SI} - \mathbf{A})^{-1}\mathbf{BU}(S)] + \mathbf{DU}(S)$$

$$Y(S) = \mathbf{C}(\mathbf{SI} - \mathbf{A})^{-1}\mathbf{BU}(S) + \mathbf{DU}(S) \quad (3.29)$$

Equation(3.29) is the T-model output current. The network model transfer function,  $G(S)$  is,

$$G(S) = \frac{Y(S)}{U(S)} = \frac{\mathbf{C}(\mathbf{SI} - \mathbf{A})^{-1}\mathbf{BU}(S) + \mathbf{DU}(S)}{\mathbf{U}(S)}$$

$$G(S) = \mathbf{C}(S\mathbf{I} - \mathbf{A})^{-1} \mathbf{B} + \mathbf{D} \quad (3.30)$$

Equation(3.30) gives the model admittance.  
The model impedance is therefore,

$$Z(S) = \frac{1}{\mathbf{C}(S\mathbf{I} - \mathbf{A})^{-1} \mathbf{B} + \mathbf{D}} \quad (3.31)$$

where,

$S=j\omega$ , is the complex angular frequency in rad/s

$$S=j2\pi f \quad (3.32)$$

$f$  = frequency in Hertz

The values for  $\mathbf{A}$ ,  $\mathbf{B}$ ,  $\mathbf{C}$  and  $\mathbf{D}$  are as defined previously.

From equation(3.31),

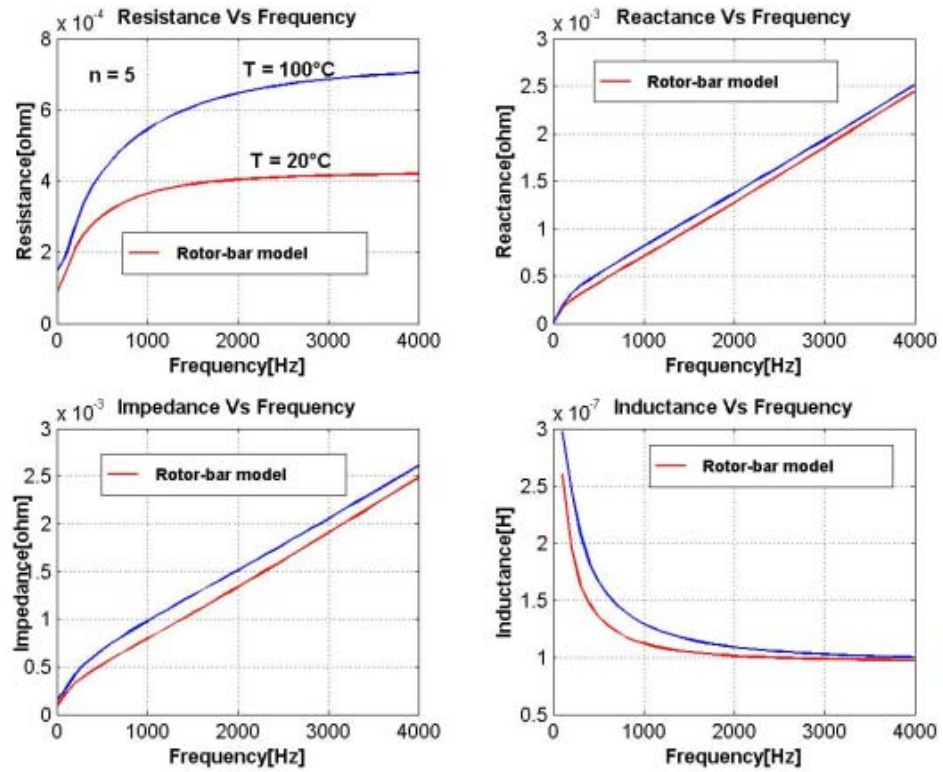
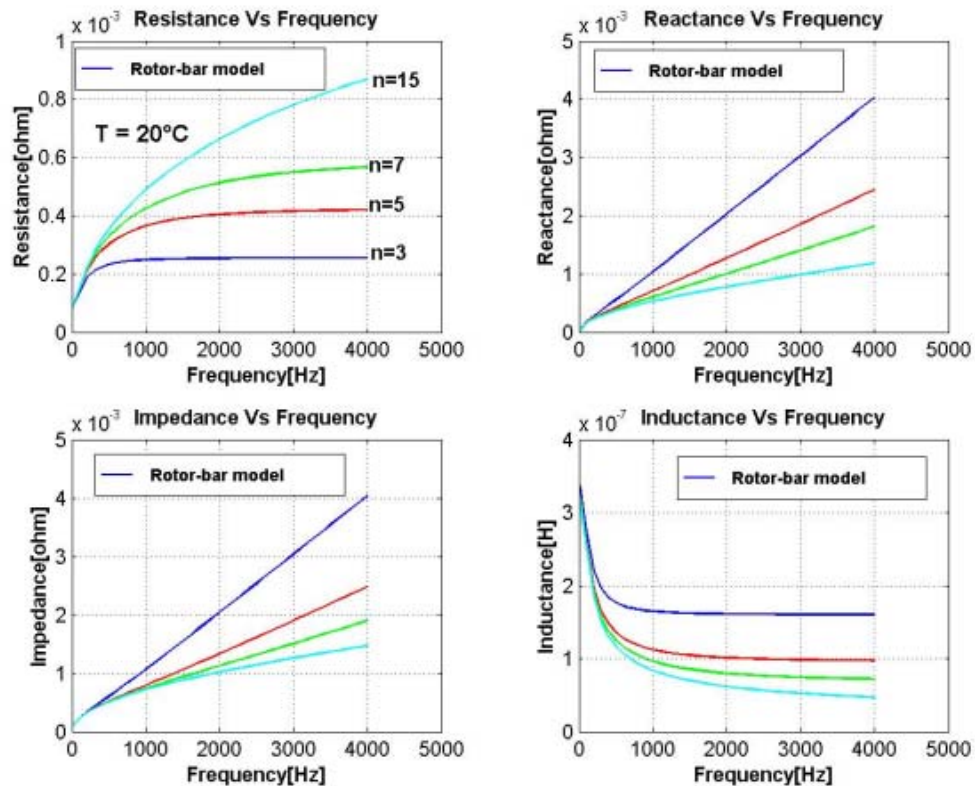
$$Z(j\omega) = R_T + jX_T \quad (3.33)$$

where,

$R_T$  = the T-model total resistance

$X_T$  = the T-model total reactance

MATLAB program is developed and used to solve equation(3.33). Figure 3.13 shows the computed results with the number of bar division equals five for two different temperatures, 20°C and 100°C. Figure 3.14 shows the model plots for different bar divisions at 20°C. The model impedance and height of each section at 20°C and 100°C are shown in Table 3.1.

**Figure 3.13:** Model plots for  $n = 5$ .**Figure 3.14:** Model plots for different bar divisions at  $20^\circ\text{C}$ .

Temperature [°C]	Number of bar sections,n	Height [mm] of bar sections		Resistance [mΩ] of each section		Inducatnce [μH] of each section	
20	5	h <sub>1</sub>	2.594	R <sub>1</sub>	0.4262	L <sub>1</sub>	0.192
		h <sub>2</sub>	2.594	R <sub>2</sub>	0.4262	L <sub>2</sub>	0.192
		h <sub>3</sub>	2.594	R <sub>3</sub>	0.4262	L <sub>3</sub>	0.192
		h <sub>4</sub>	2.594	R <sub>4</sub>	0.4262	L <sub>4</sub>	0.192
		h <sub>5</sub>	2.594	R <sub>5</sub>	0.4262	L <sub>5</sub>	0.192
100	5	h <sub>1</sub>	2.594	R <sub>1</sub>	0.734	L <sub>1</sub>	0.192
		h <sub>2</sub>	2.594	R <sub>2</sub>	0.734	L <sub>2</sub>	0.192
		h <sub>3</sub>	2.594	R <sub>3</sub>	0.734	L <sub>3</sub>	0.192
		h <sub>4</sub>	2.594	R <sub>4</sub>	0.734	L <sub>4</sub>	0.192
		h <sub>5</sub>	2.594	R <sub>5</sub>	0.734	L <sub>5</sub>	0.192

**Table 3.1:** Rotor-bar model height and impedance at 20°C and 100°C

## 4 Model modification, optimisation and computer simulation

### 4.1 Model modification

Figure 4.2 shows that the trend of the developed model in section 3.4 differs significantly without optimisation from that of the actual rotor bar. This difference necessitates in the optimisation of the developed model. In order for the model to accurately represent the actual rotor bar, the T-model described in chapter three(Section 3.4) has to be modified and subsequently optimised. Therefore the bar has to be divided into n-unequal number of sections. To adequately account for skin-effect, the bar division is done in such a way that the depth increases downward from the top of the bar. This is because the upper part of the rotor bar experiences more current flow as the bottom part. Again, since the lower part of the rotor bar experiences a higher inductance, this has to be accounted for by ensuring that the height of the first and the last sections are equal but very small compare to other remaining sections. Because the magnitude of the inductance and resistance varies differently along the bar depth, it is therefore necessary to select different heights for the calculation of the rotor resistance and inductance respectively as shown in figure 4.1.

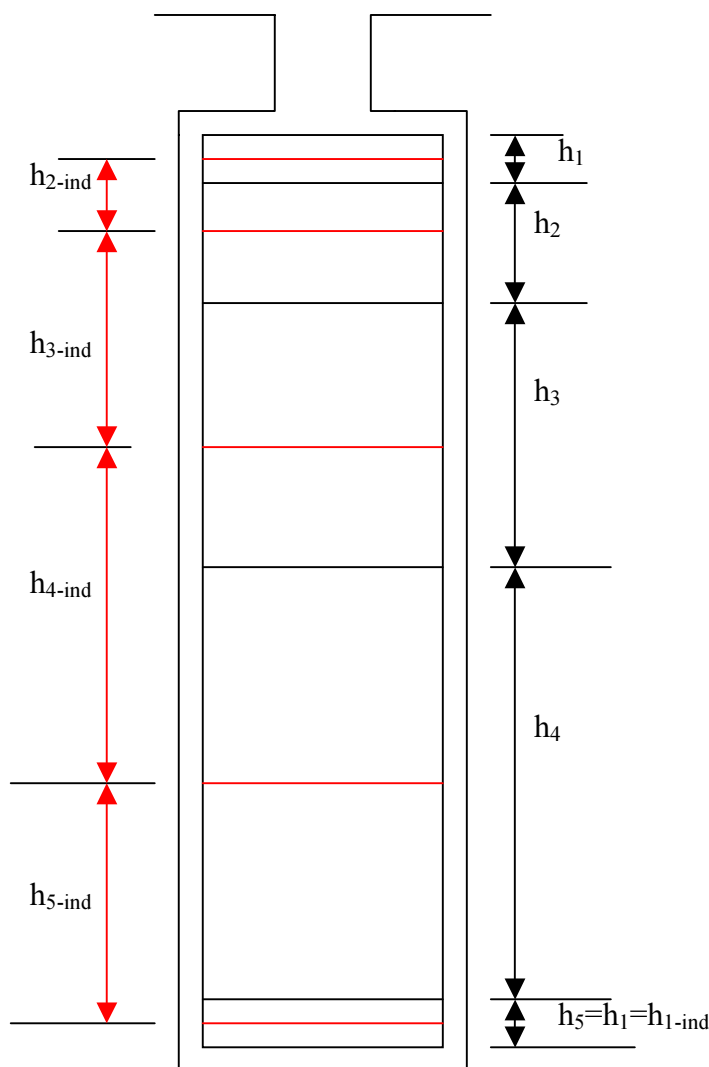


**Figure 4.1:** Rotor-bar division showing the respective depths used for the resistance and inductance calculations.

It could be seen from figure 4.1 that the section depths,  $h_1$ ,  $h_2$ ,  $h_3$ ,  $h_4$  and  $h_5$  were used for calculation of the resistance of each section respectively while the section depths,  $h_{1-ind}$ ,  $h_{2-ind}$ ,  $h_{3-ind}$ ,  $h_{4-ind}$  and  $h_{5-ind}$  were used for the calculation of the inductance of each section respectively.

$$h_{5-ind} = \frac{h_4}{2} + \frac{h_5}{2} \quad (4.1a)$$

$$h_{4-ind} = \frac{h_4}{2} + \frac{h_3}{2} \quad (4.1b)$$

$$h_{3-ind} = \frac{h_3}{2} + \frac{h_2}{2} \quad (4.1c)$$

$$h_{2-ind} = \frac{h_2}{2} + \frac{h_1}{2} \quad (4.1d)$$

$$h_{1-ind} = h_1 \quad (4.1e)$$

The inductance of each section is given by

$$L = \frac{\mu_o L_s h_{-ind}}{b_{Nut}} \quad (4.2)$$

where,

$h_{-ind}$  = the section depth as defined in equation(4.1a-4.1e).

and the resistance of each section,

$$R_L = \frac{L_s}{\chi_{cu} h b_L} \quad (4.3)$$

where,

$h$  = the section depth as shown in the right hand side of figure 4.1 .

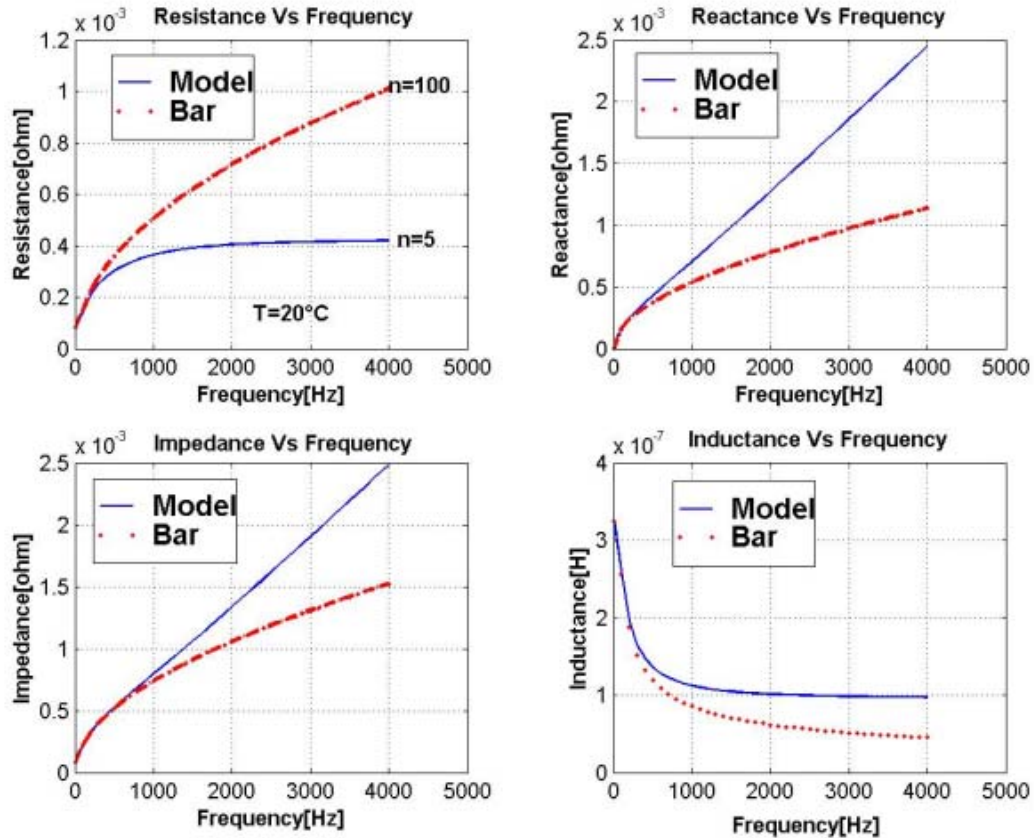


**Figure 4.2:** Comparison of actual bar impedance and model impedance

#### 4.2 Algorithm for model optimisation

In order to realise an optimal height for each bar section as well as the optimal model impedance that gives a close correlation with the actual rotor impedance of the test machine, an algorithm that accomplishes such optimal division is developed. The total height of the bar is assumed to be a geometrical sum of the individual height of the section given by

$$h_k = x_i (di)^{k-1} \quad (4.4)$$

where,

$h_k$  = height of each section

$x_i$  = fraction of the depth of the bar

$k$  = number of the section whose depth is being computed

$di$  = is the user-optimisation-index(UOI) which is equal to or greater than one( $di \geq 1$ ).

Note that:

1. When  $d_i = 1$ , we have a condition where the rotor bar is divided equally.
2. When  $d_i > 1$ , we have a condition where the rotor bar is divided unequally.

To illustrate this Algorithm, let consider a rectangular bar shown in figure 4.3 below.

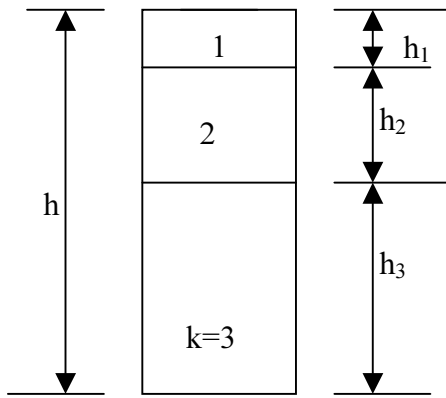


**Figure 4.3:** Rectangular bar showing 3 unequal sections.

Let assume,

$$h = 10\text{cm}$$

User-optimisation-index,  $d_i = 3.7$

From equation(4.4),

$$h_1 = x_i(3.7)^0 \quad \text{for } k = 1$$

$$h_1 = x_i \tag{4.5a}$$

$$h_2 = x_i(3.7)^1 \quad \text{for } k = 2 \tag{4.5b}$$

$$h_3 = x_i(3.7)^2 \quad \text{for } k = 3 \tag{4.5c}$$

But

$$h = h_1 + h_2 + h_3 \tag{4.5d}$$

Solving equations(4.5a-4.5d), we have

$$x_i = 0.5438$$

$$h_1 = 0.5438\text{cm}$$

$$h_2 = 2.0120\text{cm}$$

$$h_3 = 7.444\text{cm}$$

Note that if the UOI,  $d_i = 1.0$ , then

$$h_1 = h_2 = h_3 = 3.333\text{cm}.$$

In general therefore, a ‘for-loop’ algorithm is developed to accomplish the optimal division of the modified T-model. By carefully choosing appropriate value of the UOI,  $d_i$  the developed rotor model approaches to a very high level of accuracy the actual rotor bar impedance. However, in order to accurately determine UOI that results in optimal bar division, an error function is incorporated in the algorithm. The error function program therefore gives the value of UOI that corresponds to minimum error between the rotor bar and the rotor model impedance as shown in figures 4.5 and 4.7.

### 4.3 Method of solution and simulation results

The algorithm developed is incorporated into the MATLAB program of section 3.4. By so doing the rotor bar model can be divided into  $n$ -unequal sections. In order to optimise the model impedance so as to give a good correlation to the actual rotor bar impedance, an error function program is developed which automatically calculates the best estimate for the UOI. The optimised model as shown in figure 4.4 closely matches with the actual rotor bar characteristics of the machine. At approximately 4KHz frequency, the error in the developed model is about 6% as shown in figure 4.5.

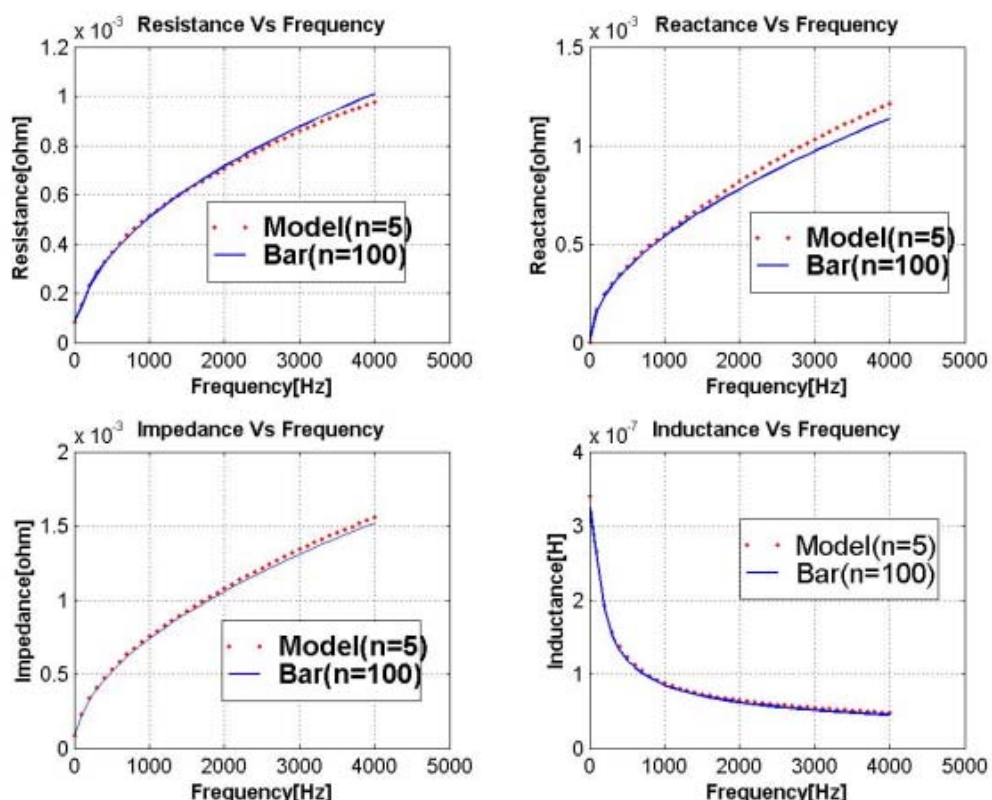


**Figure 4.4:** Bar-Model plots for bar sections(100) and model sections(5).

The optimised values of the model impedance as shown in Table 4.1 can therefore be used to represent accurately the actual machine in static and dynamic conditions with Skin-effect phenomenon included. Table 4.2 gives the computed heights for the various rotor sections that give rise to the optimised impedance at UOI equals 2.04.

<b>Resistance</b>	[mΩ]	<b>Inductance</b>	[μH]
R <sub>1</sub>	1.338	L <sub>1</sub>	6.1150e-2
R <sub>2</sub>	0.656	L <sub>2</sub>	9.2940e-2
R <sub>3</sub>	0.321	L <sub>3</sub>	0.1896
R <sub>4</sub>	0.179	L <sub>4</sub>	0.3562
R <sub>5</sub>	1.338	L <sub>5</sub>	0.2596

**Table 4.1:** Computed model impedance at 4KHz

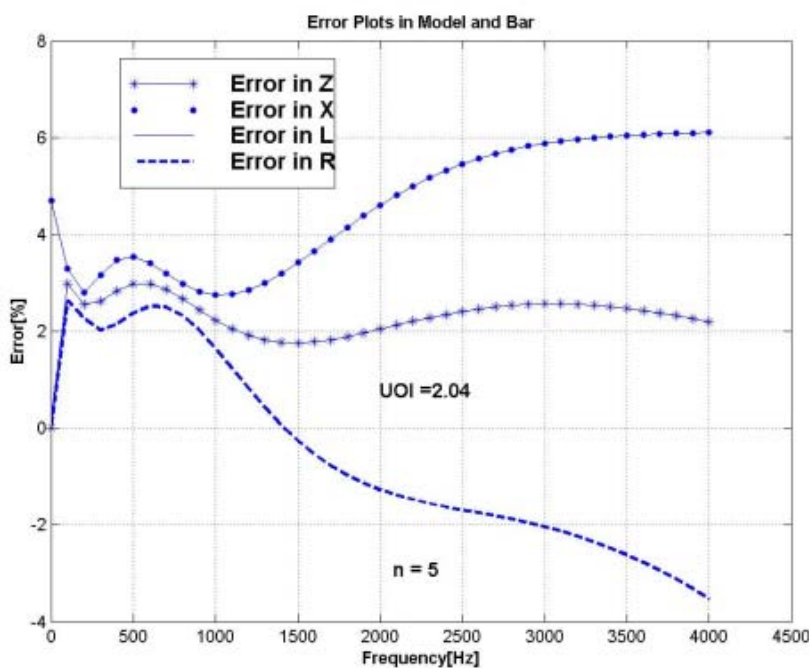


**Figure 4.5:** Error in the 5-section rotor-bar model.

<b>Section</b>	<b>h_resistance[mm]</b>	<b>h_inductance[mm]</b>
h <sub>1</sub>	0.827	0.827
h <sub>2</sub>	1.686	1.256
h <sub>3</sub>	3.440	2.563
h <sub>4</sub>	6.191	4.815
h <sub>5</sub>	0.827	3.509

**Table 4.2:** Computed model heights for each section.

To further increase the accuracy of the model, the number of bar divisions could be increased to, for instance six as shown in figure 4.6. By so doing the percentage error in the model impedance reduces to 5.2 as presented in figure 4.7. It must be pointed out here, however, that each additional rotor parallel branch introduces two further differential equations and resultantly increase in simulation time.

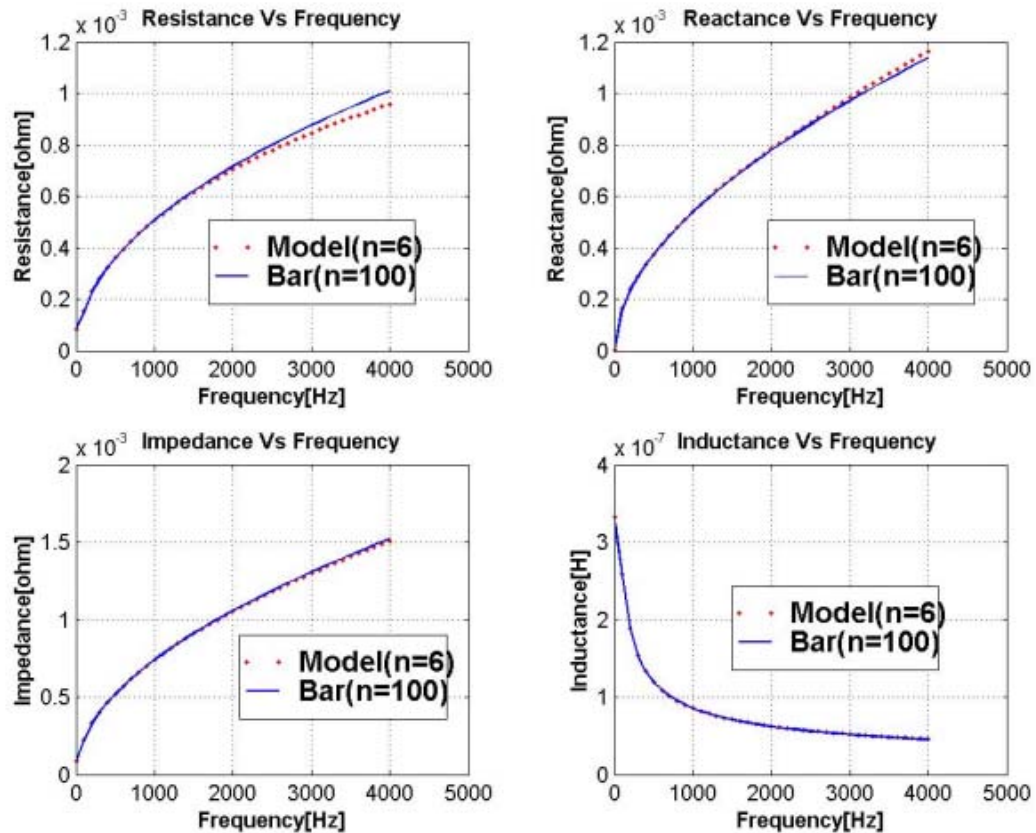


**Figure 4.6:** Bar-Model plots for bar sections(100) and model sections(6).

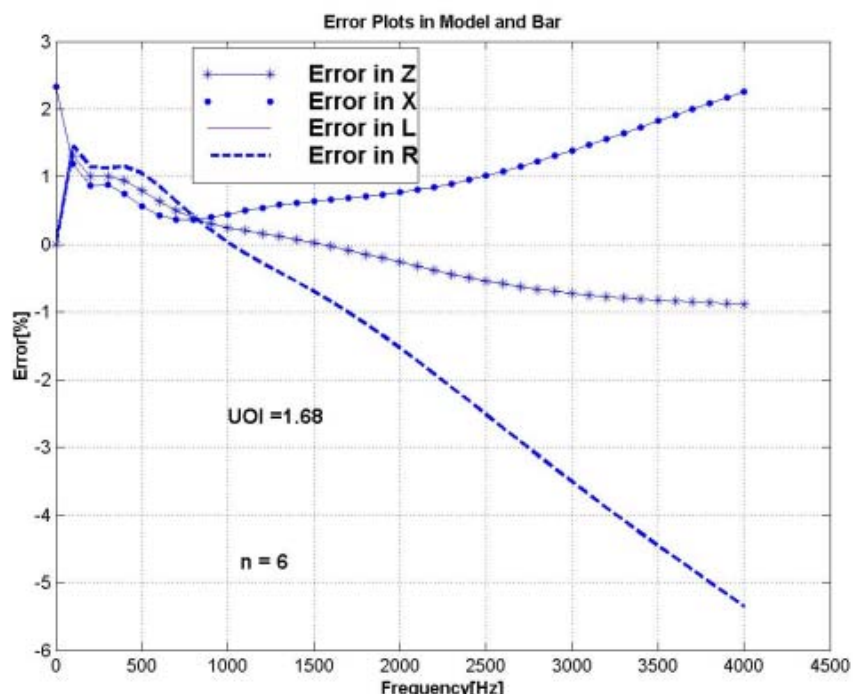


**Figure 4.7:** Error in the 6-section rotor-bar model.

## 5 Conventional machine model

### 5.1 D-Q axis transformation

The change of variables which replace the variables (currents, voltages, and flux linkages) associated with the stator windings of a synchronous machine with variables associated with fictitious windings rotating with the rotor was first investigated by Park[21]. This method was further extended by [22,23] to the application of the dynamic analysis of induction machine. By these methods therefore, a polyphase winding can be reduced to a set of two phase-windings with their magnetic axes aligned in quadrature as shown in figure 5.1.

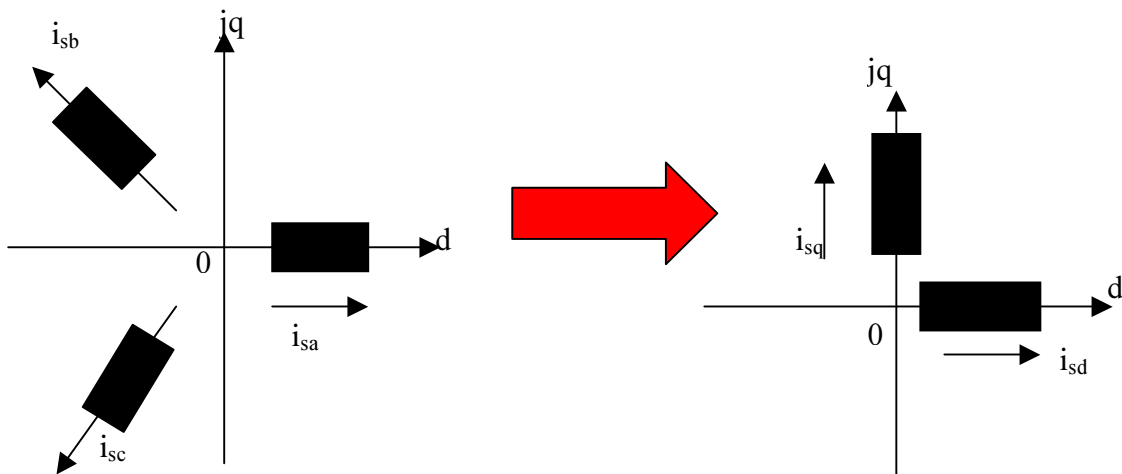


**Figure 5.1:** Polyphase winding and d-q equivalent.

The d-q axis transformation eliminates the mutual magnetic coupling of the phase-windings, thereby making the magnetic flux linkage of one winding to be independent on the current in the other winding. This system of transformation allows both polyphase windings in the stator and the rotor of an induction machine to be viewed from a common reference frame which may rotate at any angular speed or remain fixed to the stator. Generally, the reference frame can also be considered to be rotating at any arbitrary angular speed. The transformation from three phase system to a two phase system and vis-versa with the zero-sequence included is:

$$\begin{bmatrix} i_{sq} \\ i_{sd} \\ i_0 \end{bmatrix} = [C] \begin{bmatrix} i_{sa} \\ i_{sb} \\ i_{sc} \end{bmatrix} \quad (5.1)$$

$$\begin{bmatrix} i_{sa} \\ i_{sb} \\ i_{sc} \end{bmatrix} = [C]^{-1} \begin{bmatrix} i_{sq} \\ i_{sd} \\ i_0 \end{bmatrix} \quad (5.2)$$

where,

$$[\mathbf{C}] = \frac{2}{3} \begin{bmatrix} \cos\theta & \cos\left(\theta - \frac{2\pi}{3}\right) & \cos\left(\theta - \frac{4\pi}{3}\right) \\ \sin\theta & \sin\left(\theta - \frac{2\pi}{3}\right) & \sin\left(\theta - \frac{4\pi}{3}\right) \\ \frac{1}{2} & \frac{1}{2} & \frac{1}{2} \end{bmatrix} \quad (5.3)$$

$$[\mathbf{C}]^{-1} = \begin{bmatrix} \cos\theta & \sin\theta & 1 \\ \cos\left(\theta - \frac{2\pi}{3}\right) & \sin\left(\theta - \frac{2\pi}{3}\right) & 1 \\ \cos\left(\theta - \frac{4\pi}{3}\right) & \sin\left(\theta - \frac{4\pi}{3}\right) & 1 \end{bmatrix} \quad (5.4)$$

### 5.1.1 Reference frames voltages

Under balanced condition, the stator voltages of a three-phase induction machine may be considered as sinusoidal and expressed as

$$V_{as} = \sqrt{2}V \cos\omega_b t \quad (5.5)$$

$$V_{bs} = \sqrt{2}V \cos\left(\omega_b t - \frac{2\pi}{3}\right) \quad (5.6)$$

$$V_{cs} = \sqrt{2}V \cos\left(\omega_b t + \frac{2\pi}{3}\right) \quad (5.7)$$

These stator voltages are related to the d-q frame of reference by[1]

$$\begin{bmatrix} V_{sq} \\ V_{sd} \end{bmatrix} = [\mathbf{C}_1] \begin{bmatrix} V_{as} \\ V_{bs} \\ V_{cs} \end{bmatrix} \quad (5.8)$$

where,

$$[\mathbf{C}_1] = \frac{2}{3} \begin{bmatrix} \cos\theta & \cos\left(\theta - \frac{2\pi}{3}\right) & \cos\left(\theta - \frac{4\pi}{3}\right) \\ \sin\theta & \sin\left(\theta - \frac{2\pi}{3}\right) & \sin\left(\theta - \frac{4\pi}{3}\right) \end{bmatrix} \quad (5.9)$$

By application of trigonometric identities[70], equation(5.8) can be further simplified to give,

$$V_{sq} = \sqrt{2}V \cos(\theta - \omega_b t) \quad (5.10)$$

$$V_{sd} = \sqrt{2}V \sin(\theta - \omega_b t) \quad (5.11)$$

Equations(5.10-5.11) can be applied in any reference frame by making a suitable choice for theta( $\theta$ ):

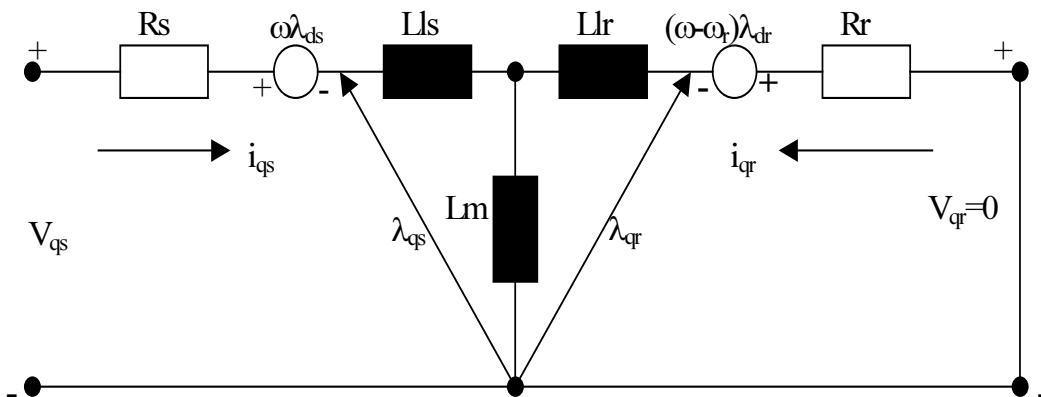
If theta equals  $\theta_r$ , then equations(5.10-5.11) lead to an expression for voltage in rotor reference frame. Also, if  $\theta$  equal to zero, the equations(5.10-5.11) apply to a frame of reference rigidly fixed in the stator(i.e. Stationary reference frame). Otherwise, for  $\theta$  equals  $\omega t$  in equations(5.10-5.11), a synchronously rotating reference frame results.

## 5.2. Conventional machine model development

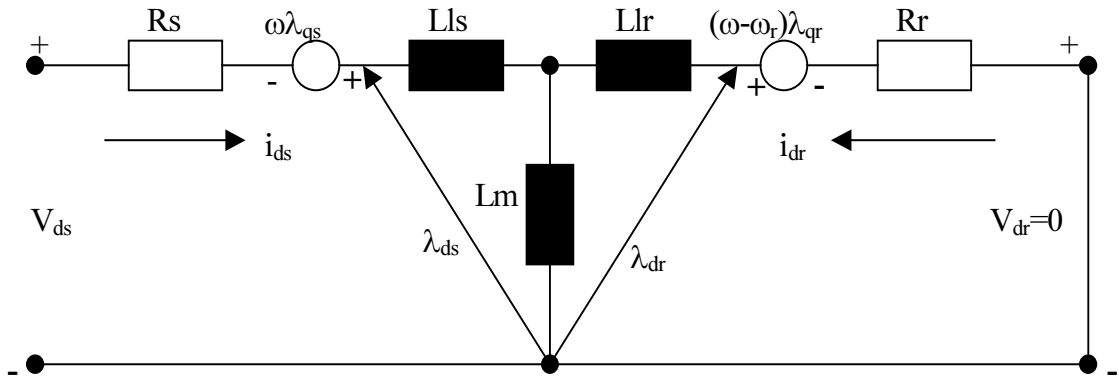
In the development of the transient equations for the conventional machine model, the following assumptions are made:

- (i) The machine is symmetrical with a linear air-gap and magnetic circuit.
- (ii) Saturation effect is neglected
- (iii) Skin-effect and temperature effect are neglected
- (iv) Harmonic content of the mmf wave is neglected
- (v) The stator voltages are balanced.

The differential equations governing the transient performance of the induction machine can be described in several ways and they only differ in detail and in their suitability for use in a given application. The conventional machine model is developed using the traditional method of reducing the machine to a two-axis coil(d-q axis) model on both the stator and the rotor as described by Krause and Thomas[1]. The d-q axis model of the motor provides a convenient way of modelling the machine and is most suitable for numerical solution. This is preferable to the space-vector machine model which describes the machine in terms of complex variables[24]. Figure 5.2 shows the d-q equivalent circuits for a 3-phase, symmetrical squirrel-cage induction machine in arbitrary-frame with the zero-sequence component neglected.



**Figure 5.2a**

**Figure 5.2b**

**Figure 5.2:** Squirrel-Cage Induction machine models in d-q axis: (a) q-axis model (b) d-axis model.

### 5.3. Electrical model of the machine

The non-linear differential equations which describe the dynamic performance of an ideal symmetrical Induction machine in an arbitrary reference frame could be derived from the d-q equivalent circuits as in [1].

$$\begin{bmatrix} V_{qs} \\ V_{ds} \\ 0 \\ 0 \end{bmatrix} = \begin{bmatrix} (R_s + L_s p) & \omega L_s & L_m p & \omega L_m \\ -\omega L_s & (R_s + L_s p) & -\omega L_m & L_m p \\ L_m p & (\omega - \omega_r) L_m & (R_r + L_r p) & (\omega - \omega_r) L_r \\ -(\omega - \omega_r) L_m & L_m p & -(\omega - \omega_r) L_r & (R_r + L_r p) \end{bmatrix} \begin{bmatrix} i_{qs} \\ i_{ds} \\ i_{qr} \\ i_{dr} \end{bmatrix} \quad (5.12)$$

where,

$$L_s = L_{ls} + L_m \quad (5.13)$$

$$L_r = L_{lr} + L_m \quad (5.14)$$

$$p = \frac{d}{dt} \quad (5.15)$$

In the analysis of induction machine, it is always advisable to transform equation(5.12) to d-q axis fixed either on the Stator[25], or the rotor[26],or rotating in synchronism with the supply voltages[29]. In[25], equation(5.12) is modified by setting  $\omega=0$  and in [26],  $\omega=\omega_r$  while in[29]  $\omega=\omega_e$ .

It is important to note that the choice of reference frame will affect the waveforms of all d-q variables and also the simulation speed as well as the accuracy of the results. However, the following guidelines as suggested in [30] are in order:

- Use the stationary reference frame if the stator voltages are either unbalanced or discontinuous and the rotor voltages are balanced(or zero).
- Apply the rotor reference frame if the rotor voltages are either unbalanced or discontinuous and the stator voltages are balanced
- Apply either the synchronous or stationary reference frames if all voltages are balanced and continuous.

Also for analysis involving saturation and deep bar effect, a reference frame fixed to the rotor is recommended[26,31].

Therefore, the electrical model of the squirrel-cage induction machine in rotor reference frame becomes,

$$\begin{bmatrix} V_{qs} \\ V_{ds} \\ 0 \\ 0 \end{bmatrix} = \begin{bmatrix} (R_s + L_s p) & \omega_r L_s & L_m p & \omega_r L_m \\ -\omega_r L_s & (R_s + L_s p) & -\omega_r L_m & L_m p \\ L_m p & 0 & (R_r + L_r p) & 0 \\ 0 & L_m p & 0 & (R_r + L_r p) \end{bmatrix} \begin{bmatrix} i_{qs} \\ i_{ds} \\ i_{qr} \\ i_{dr} \end{bmatrix} \quad (5.16)$$

For the purpose of digital simulation, equation(5.16) is represented in state variable form with currents as state variables.

$$p[\mathbf{i}] = -[\mathbf{L}]^{-1}([\mathbf{R}] + \omega_r [\mathbf{G}])[\mathbf{i}] + [\mathbf{L}]^{-1}[\mathbf{V}] \quad (5.17)$$

where,

$$[\mathbf{V}] = \begin{bmatrix} V_{qs} & V_{ds} & 0 & 0 \end{bmatrix} \quad (5.18)$$

$$[\mathbf{R}] = \begin{bmatrix} R_s & 0 & 0 & 0 \\ 0 & R_s & 0 & 0 \\ 0 & 0 & R_r & 0 \\ 0 & 0 & 0 & R_r \end{bmatrix} \quad (5.19)$$

$$[\mathbf{L}] = \begin{bmatrix} L_s & 0 & L_m & 0 \\ 0 & L_s & 0 & L_m \\ L_m & 0 & L_r & 0 \\ 0 & L_m & 0 & L_r \end{bmatrix} \quad (5.20)$$

$$[\mathbf{G}] = \begin{bmatrix} 0 & L_s & 0 & L_m \\ -L_s & 0 & -L_m & 0 \\ 0 & 0 & 0 & 0 \\ 0 & 0 & 0 & 0 \end{bmatrix} \quad (5.21)$$

$$[\mathbf{i}] = \begin{bmatrix} i_{qs} & i_{ds} & i_{qr} & i_{dr} \end{bmatrix}^t \quad (5.22)$$

Unlike in[32,33,67], where the authors preferred to invert the matrix,L at every integration step, in this work, in order to minimize the simulation time, a single symbolic inversion of L is carried out so as to obtain an analytical mathematical model of the machine(equation(5.17)). The symbolic matrix inversion is obtained by means of the software package “Mathematica”[34] as:

$$[\mathbf{L}]^{-1} = \frac{1}{L_s L_r - L_m^2} \begin{bmatrix} L_r & 0 & -L_m & 0 \\ 0 & L_r & 0 & -L_m \\ -L_m & 0 & L_s & 0 \\ 0 & -L_m & 0 & L_s \end{bmatrix} \quad (5.23)$$

The Electromagnetic torque,  $T_e$  is given by [30] as:

$$T_e = \frac{3}{2} P L_m (i_{qs} i_{dr} - i_{ds} i_{qr}) \quad (5.24)$$

where,  $P$ =Number of pole pairs.

## 5.4. Mechanical model of the machine

### 5.4.1. Mechanical model of the machine without coupling

The mechanical model of an induction motor comprises of the equations of motion of the motor and driven load as shown in figure 5.3a and is usually represented as a second-order differential equation[35].

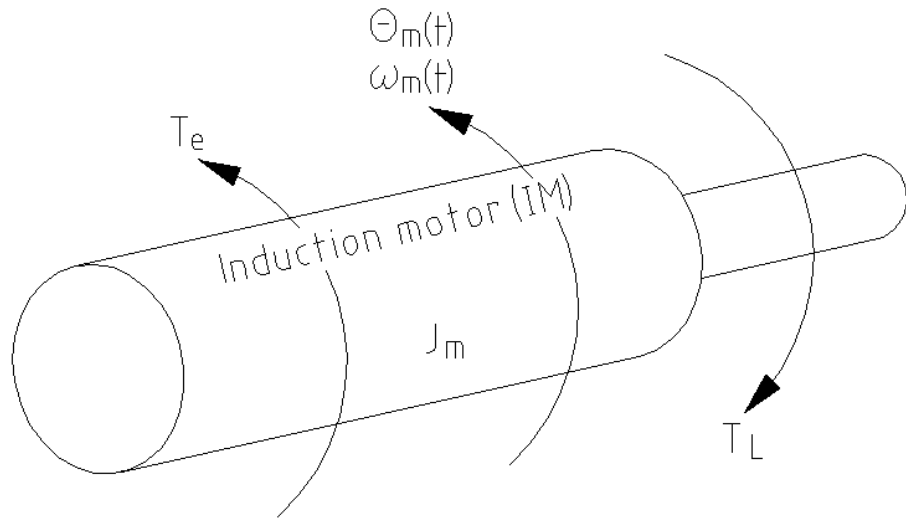


**Figure 5.3a.** Motor mechanical model schematic without coupling.

$$J_m P^2 \theta_m = T_e - T_L \quad (5.25)$$

Decomposing equation(5.25) into two first-order differential equations gives,

$$p\theta_m = \omega_m \quad (5.26)$$

$$J_m (p\omega_m) = (T_e - T_L) \quad (5.27)$$

But,

$$\omega_r = \omega_m P \quad (5.28)$$

$$\theta_r = \theta_m P \quad (5.29)$$

where,

$\omega_m$  = angular velocity of the rotor

$\theta_m$  = rotor angular position

$\theta_r$  = electrical rotor angular position

$\omega_r$  = electrical angular velocity

$J_m$  = combined rotor and load inertia coefficient

$T_L$  = applied load torque

The block diagram representing the mechanical model of the machine without coupling is shown in figure 5.3b.

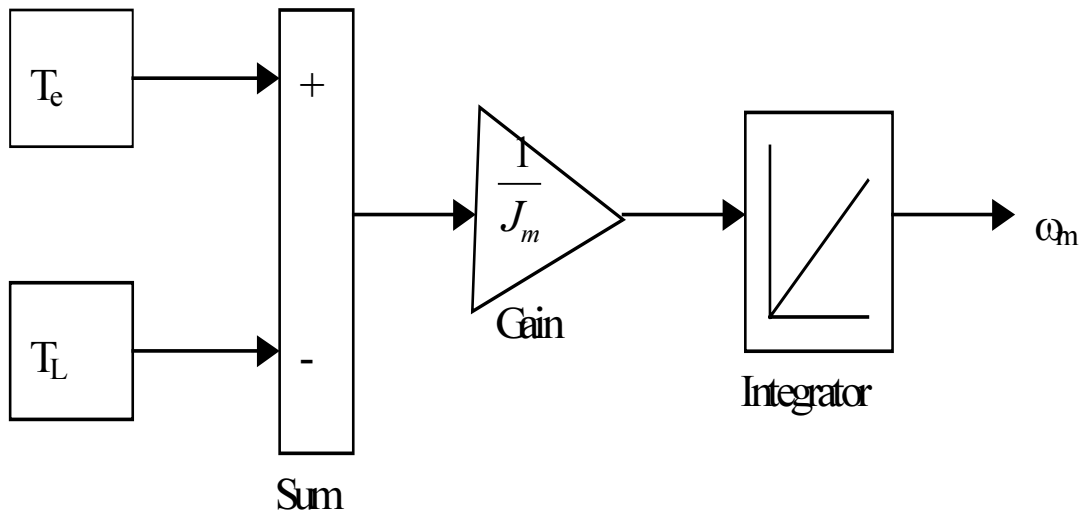


**Figure 5.3b.** Block diagram of the mechanical model without coupling.

### 5.4.2 Mechanical model of the machine with coupling

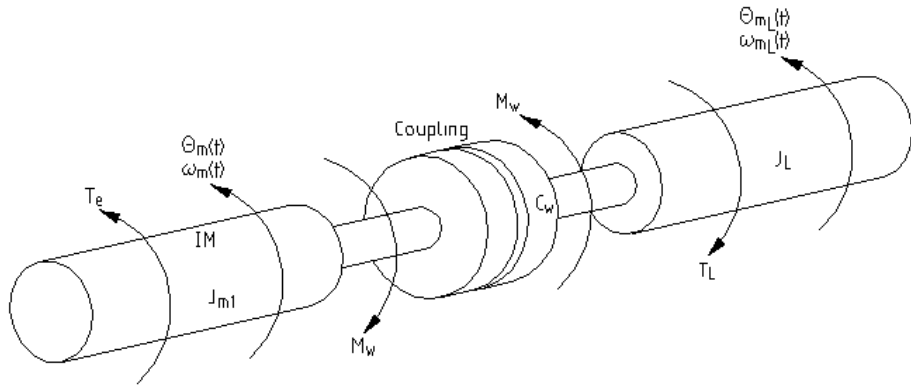


**Figure 5.3c:** Motor mechanical model schematic with coupling.

Figure 5.3c represents the motor mechanical model schematic for the motor-load connection.

The equation of motion of the motor and the coupling is given by

$$T_e - M_w = J_{m1} \frac{d^2\theta_m}{dt^2} \quad (5.30)$$

From equation(5.26),

$$\frac{d\omega_m}{dt} = \frac{d^2\theta_m}{dt^2} \quad (5.31)$$

Put equation(5.31) into equation(5.30), we have

$$T_e - M_w = J_{m1} \frac{d\omega_m}{dt} \quad (5.32)$$

Similarly, the equation of motion between the coupling and the driven load is related by

$$M_w - T_L = J_L \frac{d\omega_{mL}}{dt} \quad (5.33)$$

where,

$$\omega_{mL} = \frac{d\theta_{mL}}{dt} \quad (5.34)$$

By definition[85],

$$M_w = c_w (\theta_m - \theta_{mL}) \quad (5.35)$$

Taking the first derivative of equation(5.35), equation(5.36) results,

$$\frac{dM_w}{dt} = c_w \left( \frac{d\theta_m}{dt} - \frac{d\theta_{mL}}{dt} \right) \quad (5.36)$$

Substituting equations(5.26) and (5.34) into equation(5.36) we have,

$$\frac{dM_w}{dt} = c_w (\omega_m - \omega_{mL}) \quad (5.37)$$

Therefore, the general equation of the coupled system with damping factor( $d_w$ ) neglected can be expressed in matrix form as:

$$\begin{bmatrix} \dot{\omega}_m \\ \dot{\omega}_{mL} \\ \dot{M}_w \end{bmatrix} = \begin{bmatrix} 0 & 0 & -\frac{1}{J_{m1}} \\ 0 & 0 & \frac{1}{J_L} \\ c_w & -c_w & 0 \end{bmatrix} \begin{bmatrix} \omega_m \\ \omega_{mL} \\ M_w \end{bmatrix} + \begin{bmatrix} \frac{T_e}{J_{m1}} \\ -\frac{T_L}{J_L} \\ 0 \end{bmatrix} \quad (5.38)$$

where,

$J_{m1}$  = moment of inertia of induction motor

$M_w$  = shaft torque

$J_L$  = moment of inertia of the D.C. motor

$c_w$  = stiffness constant of the shaft system

$\omega_{mL}$  = mechanical speed of the D.C. motor

The block diagram of equation(5.38) is shown in figure 5.3d. Generally, with damping factor,  $d_w$  included, equation(5.37) becomes as defined in [36],

$$\frac{dM_w}{dt} = c_w (\omega_m - \omega_{mL}) - \left( \frac{d_w}{J_T} \right) M_w + d_w \left( \frac{T_e}{J_{m1}} - \frac{T_L}{J_L} \right) \quad (5.39)$$

where,

$$J_T = \frac{J_{m1}J_L}{(J_{m1} + J_L)} \quad (5.40)$$

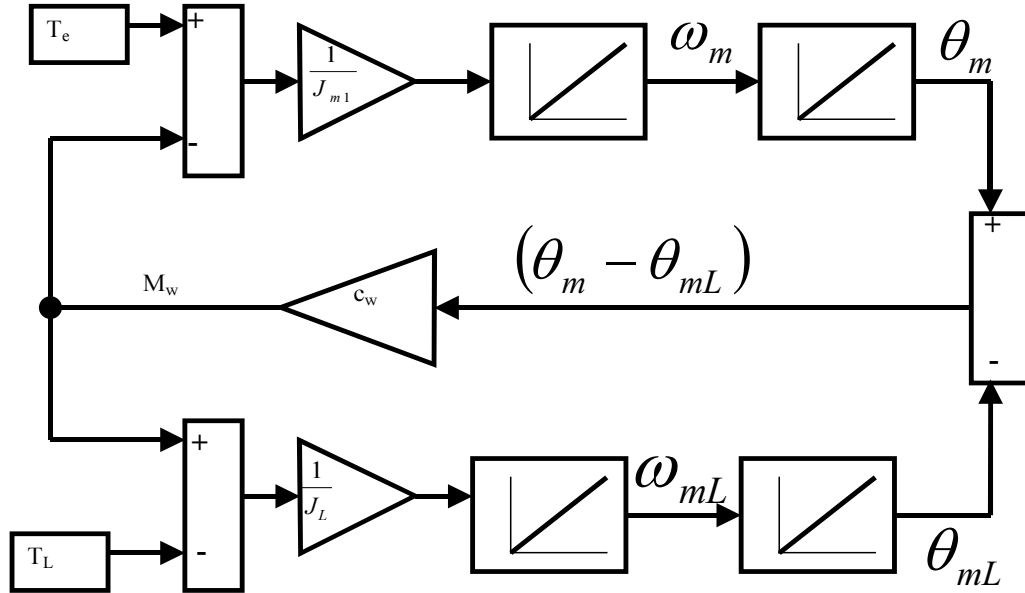


**Figure 5.3d.** Block diagram of motor mechanical model with coupling.

### 5.4.3 Determination of the shaft system stiffness constant, $c_w$

Since it is difficult to measure experimentally the electromagnetic torque developed by induction machine, effort is made to measure the shaft torque. To do this, the stiffness constant,  $c_w$  in equation(5.39)—which defines the time function of the shaft torque, needs to be determined.

Holzweißig and Dresig[85] give the relationship between the shaft undamped natural frequency,  $\omega_d$  and the shaft stiffness constant,  $c_w$  as,

$$\omega_d^2 = c_w \frac{(J_{m1} + J_L)}{(J_{m1}J_L)} \quad (5.41)$$

From equation(5.41), equation(5.42) results,

$$c_w = \frac{\omega_d^2 (J_{m1}J_L)}{(J_{m1} + J_L)} \quad (5.42)$$

Figure 5.3e shows the measured shaft system oscillation and from which the undamped natural frequency of the shaft system is estimated to be 80Hz(502.65rad/s). By substituting the experimental values of the moment of inertia of the motor( $J_{m1}$ ) and the load( $J_L$ ) together with the shaft undamped natural frequency in equation(5.42), the shaft stiffness constant,  $c_w$  becomes 14320Nm/rad.

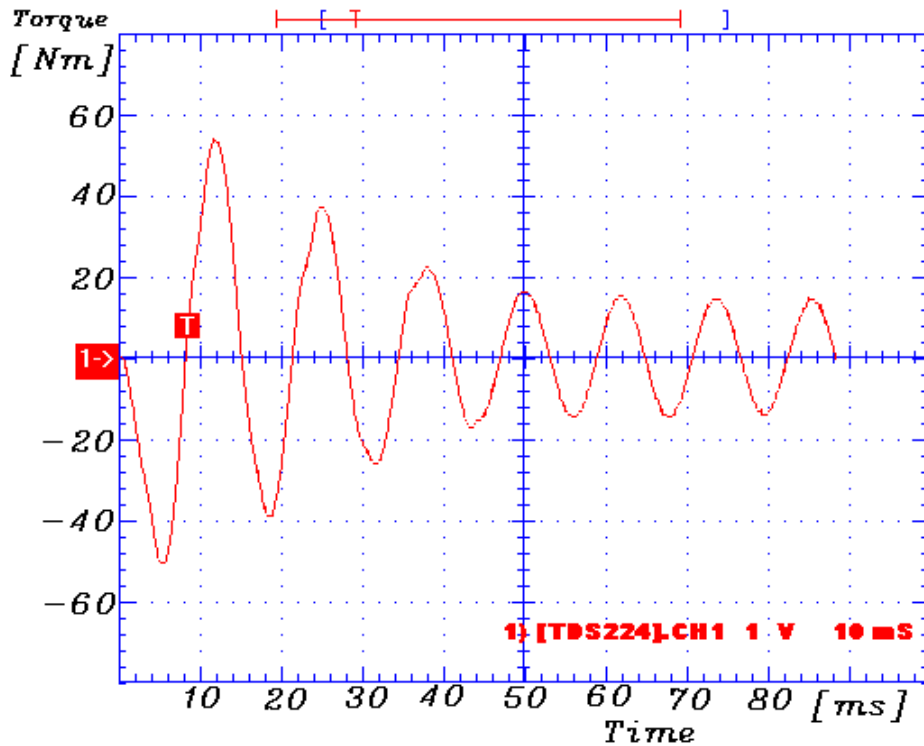


**Figure 5.3e.** Measured shaft system oscillation waveform.

### 5.5. Steady-state machine model

Under balanced operation of an induction machine, the zero quantities of the stator and rotor are zero. Also during balanced steady-state condition, the machine d- and q-voltages and currents referred to the synchronously rotating frame are constant. Therefore, in the development of the steady-state equations for the test machine, the time derivatives of all currents in equation(5.12) are set to zero for  $\omega_r$  equal to  $\omega_e$ (In synchronously rotating reference frame). This process results to the below steady-state equations:

$$\begin{bmatrix} V_{qso} \\ V_{dso} \\ 0 \\ 0 \end{bmatrix} = \begin{bmatrix} R_s & \omega_e L_s & 0 & \omega_e L_m \\ -\omega_e L_s & R_s & -\omega_e L_m & 0 \\ 0 & (\omega_e - \omega_r)L_m & R_r & (\omega_e - \omega_r)L_r \\ -(\omega_e - \omega_r)L_m & 0 & -(\omega_e - \omega_r)L_r & R_r \end{bmatrix} \begin{bmatrix} i_{qso} \\ i_{dso} \\ i_{qro} \\ i_{dro} \end{bmatrix} \quad (5.43)$$

Where,

$$\omega_e = 2\pi f \quad (5.44)$$

and

- $V_{qso}$  = Steady-state q-axis stator voltage
- $V_{dso}$  = Steady-state d-axis stator voltage
- $i_{qso}, i_{dso}$  = Steady-state q- and d-axis stator currents respectively
- $i_{qro}, i_{dro}$  = Steady-state q- and d-axis rotor currents respectively

The machine slip is defined as,

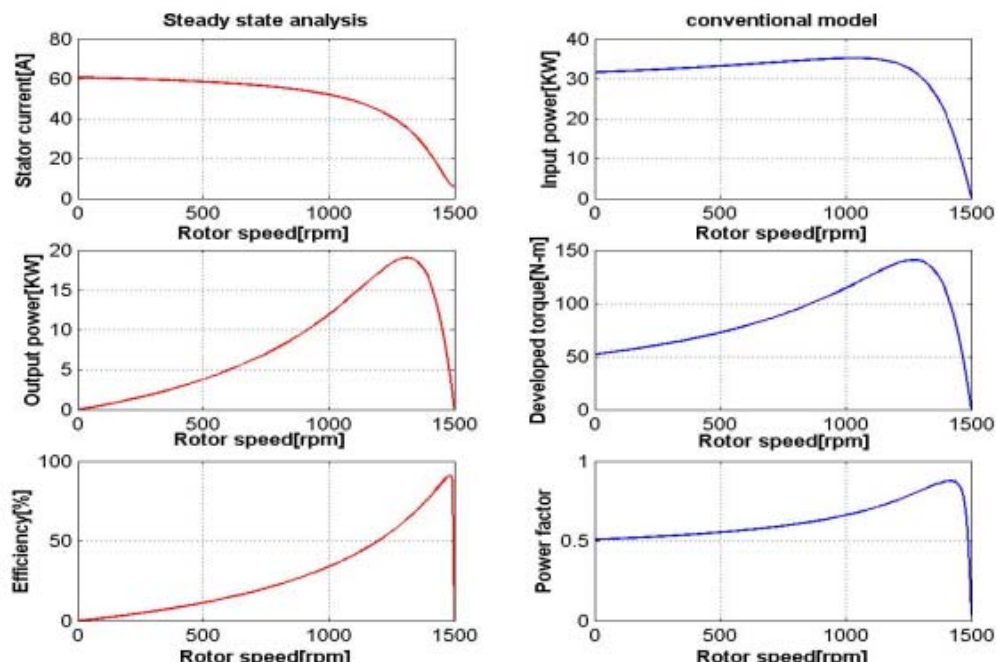
$$s = \frac{\omega_e - \omega_r}{\omega_e} \quad (5.45)$$

The electromagnetic behaviour of the machine under steady-state condition is described by the equation,

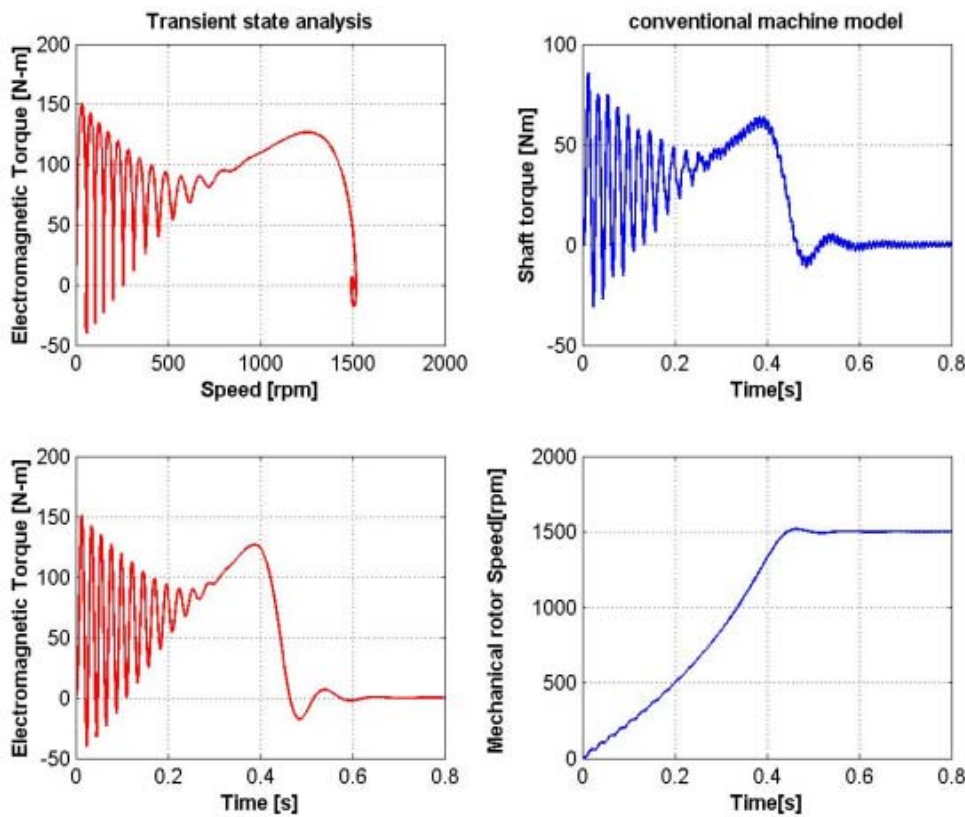
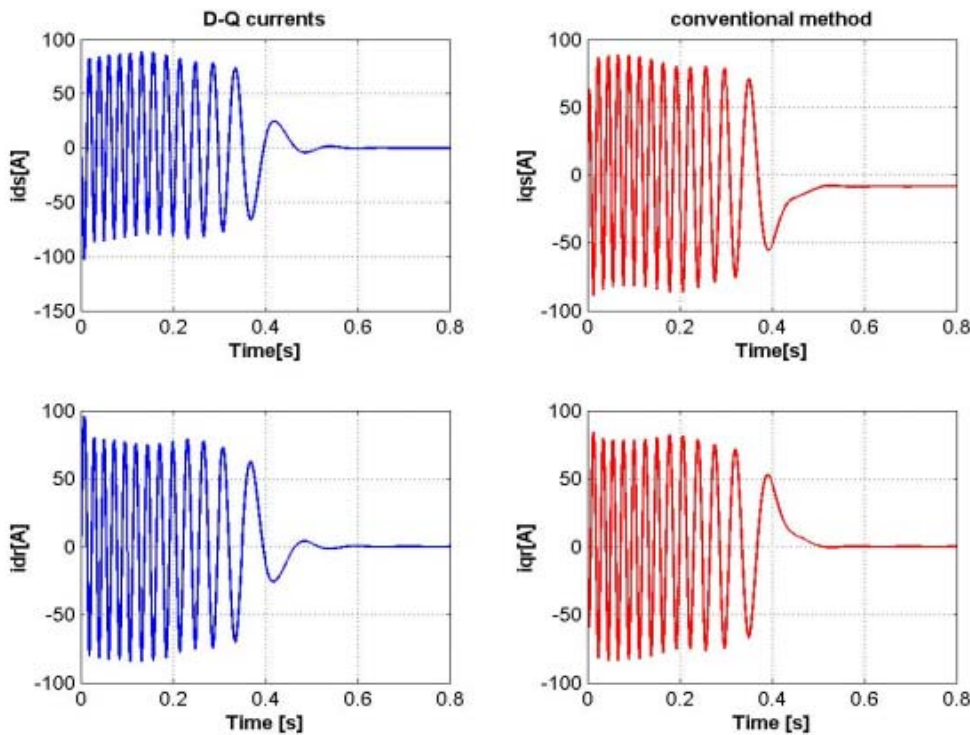
$$T_{eo} = 1.5PL_m(i_{qso}i_{dro} - i_{dso}i_{qro}) \quad (5.46)$$

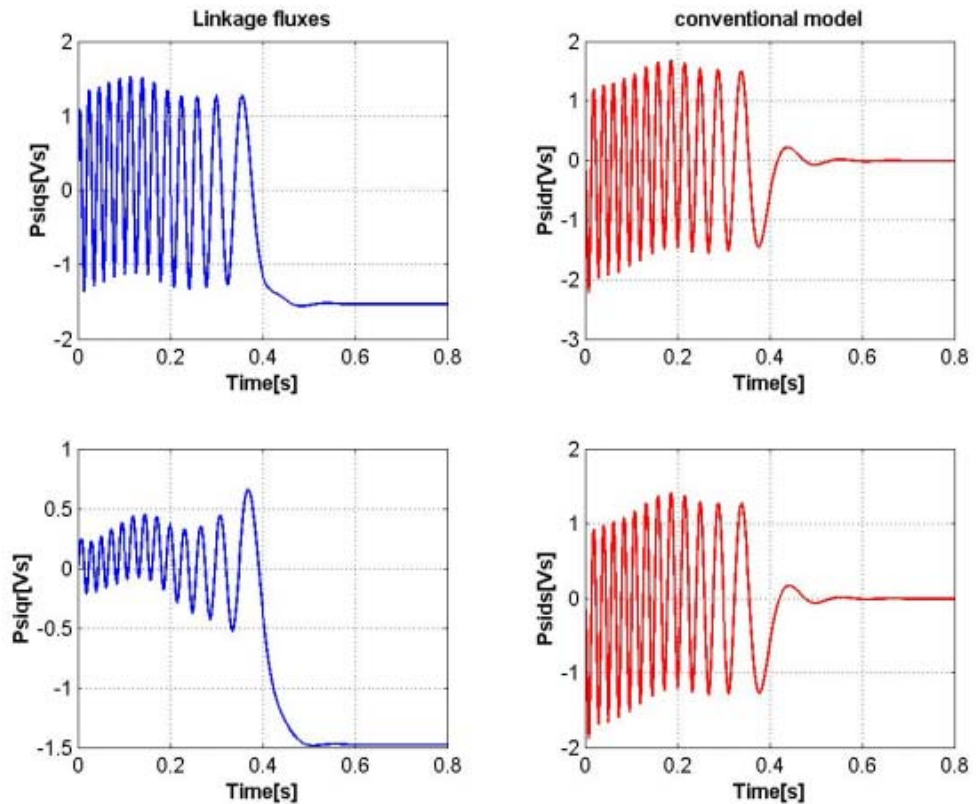
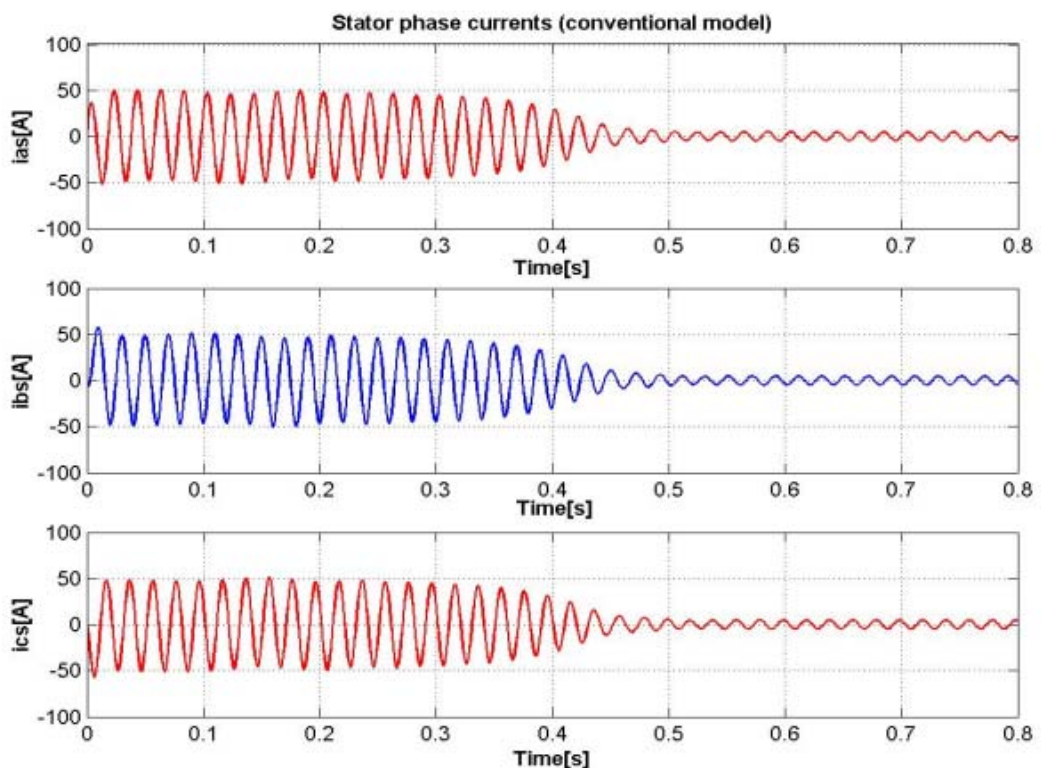
## 5.6. Computer simulation and results

MATLAB m-file is developed and used for solving equations(5.17),(5.24) and (5.27) for the dynamic model of the induction machine and equations(5.43-5.46) for the steady-state model of the machine. The developed program accepts constant stator and rotor quantities –such as resistances and inductances as inputs. These constant quantities are found through the open-circuit test, blocked-rotor test and the retardation test carried out on the 7.5KW Squirrel-cage induction machine. By supplying these input parameters, the steady-state and the dynamic behaviour of the machine can be predicted. The graphical representations for stator current, input power, output power, torque, efficiency and power factor as a function of rotor speed are shown in figure 5.4. Figure 5.5 shows the transient behaviours of the machine for the stator phase currents, torque, speed ,linkage fluxes and d-q currents as a function of time.



**Figure 5.4:** Conventional model steady-state characteristics.

**Figure 5.5a****Figure 5.5b**

**Figure 5.5c****Figure 5.5d**

**Figure 5.5.: Run-up characteristics of the simulated machine**

## 6 Machine models with skin-effect and saturation effect

### 6.1 Development of the equivalent circuit

In order to accurately represent the skin-effect phenomenon in a squirrel-cage induction machine, two distinct methods have been proposed. The quasi-static method in which the steady state values of resistance and inductance are first calculated for each speed within the operating range represents the first[36,37]. The second method represents the eddy-currents by additional circuit equations. The equations may be in the form of lumped-parameter networks which are effectively a crude finite difference approximation to the field equations describing the eddy-current distribution[5]. The first method produces unacceptable results at high frequencies. In this work, therefore, the lumped-parameter networks model is applied. In order to account for changes of the rotor inductance and resistance with changes in frequency, the rotor bar is divided into sections as shown in figure 3.2.

To model the rotor bar, a T-configuration network is used according to the method proposed by Babb and Williams[5]. From figure 3.2, the rotor bar resistance and inductance for each section is,

$$R_{\text{sec}} = \frac{L_s}{\chi_{cu} h_{\text{sec}} b_{\text{Nut}}} \quad (6.1)$$

$$L_{\text{sec}} = \frac{\mu_0 L_s h_{\text{sec}}}{b_{\text{Nut}}} \quad (6.2)$$

where,

$\mu_0$  = Permeability of free space

$b_{\text{Nut}}$  = Width of the rotor bar

It is important to note that equations(6.1) and (6.2) are modified to take account of all the bars and subsequently referred to the stator to give “ $R_r$ ” and “ $L_r$ ” as shown in the equivalent T-circuit of the induction motor, figure 6.1b and figure 6.1c.

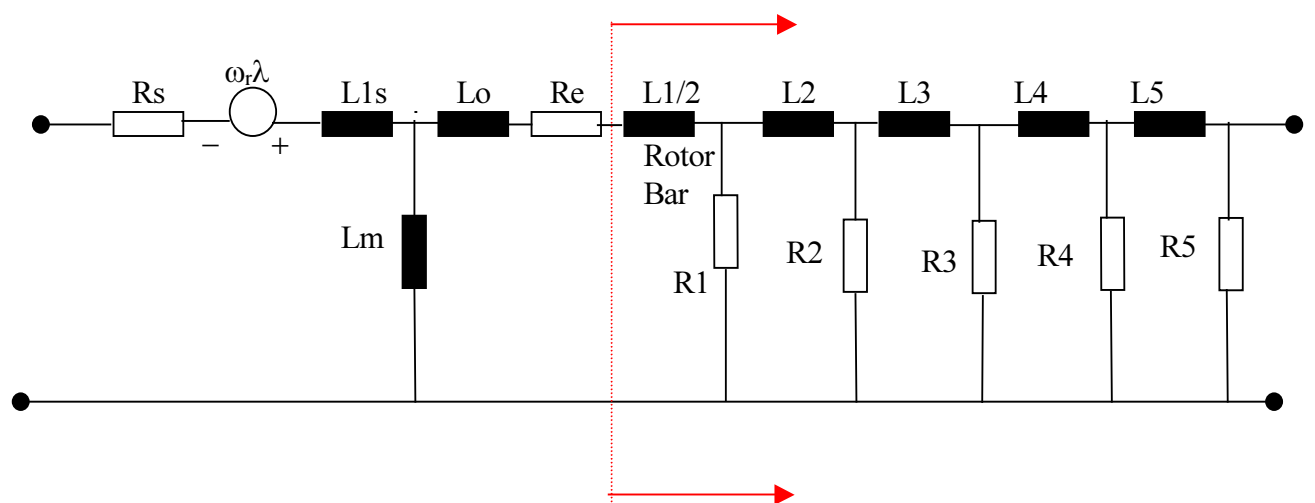


**Figure 6.1a:** Equivalent T-Circuit; Configuration for 5-section rotor bar.

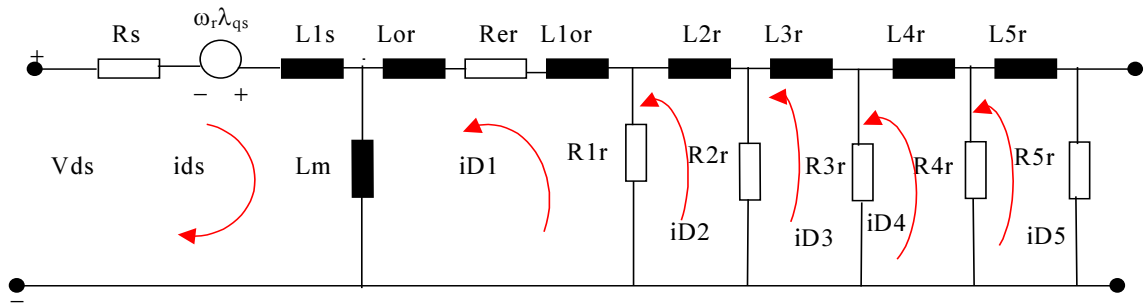


**Figure 6.1b:** Equivalent circuit for d-axis with rotor values referred to the stator

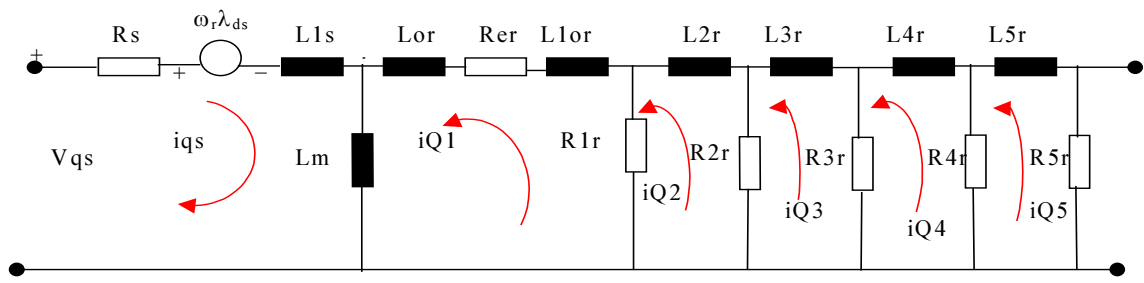


**Figure 6.1c:** Equivalent circuit for q-axis with rotor values referred to the stator

The rotor parameters of figure 6.1 are referred to the stator by using the transformation factor,  $k$  and the values defined mathematically by,

$$\begin{aligned}
 L1r &= k^2 L10 \\
 L2r &= k^2 L2 \\
 L3r &= k^2 L3 \\
 L4r &= k^2 L4 \\
 L5r &= k^2 L5 \\
 L10 &= Lor + L1or
 \end{aligned} \tag{6.3a}$$

$$\begin{aligned}
 Re_r &= k^2 Re \\
 R1r &= k^2 R1 \\
 R2r &= k^2 R2 \\
 R3r &= k^2 R3 \\
 R4r &= k^2 R4 \\
 R5r &= k^2 R5
 \end{aligned} \tag{6.3b}$$

where  $k_1$  is defined thus[38]:

$$k_1^2 = \frac{m1}{m2} \left( \frac{k_{w1} N1}{k_{w2} N2} \right)^2 \tag{6.3c}$$

where,

$m1$  = number of phases on the stator

$m2$  = number of phases on the rotor

$k_{w1}$  = stator winding factor

$k_{w2}$  = rotor winding factor

$N_1$  = number of series-connected turns per phase of the stator

$N_2$  = number of series-connected turns per phase of the rotor

But ,

$m_2 = (\text{number of rotor bars})/(\text{number of pairs of poles})$

$$m_2 = \frac{Q}{P} \quad (6.3d)$$

Seinsch[86] defines the relationship between the rotor bar resistance and the rotor resistance as:

$$R_2 = \frac{R_{bar}}{P} \quad (6.3e)$$

with the equivalent rotor referred resistance as,

$$R'^2 = k^2 R_{bar} \quad (6.3f)$$

where,

$$k^2 = \frac{k_1^2}{P} \quad (6.3g)$$

## 6.2 The machine D-Q model equations

The machine d-q model equations are derived by taken the Kirchhoff's voltage expressions for each loop in figure 6.1[28]. By using the reference frame fixed to the rotor, the voltage equations for each of the loops become:

### [A] Stator Equations—(fig.6.1b & fig.6.1c)

#### Loop1

$$V_{ds} = R_s i_{ds} - \omega_r \lambda_{qs} + L_{ls} \frac{di_{ds}}{dt} + L_m \frac{di_{ds}}{dt} + L_m \frac{di_{D1}}{dt} \quad (6.4)$$

$$V_{ds} = R_s i_{ds} + L_s \frac{di_{ds}}{dt} - L_s \omega_r i_{qs} - L_m \omega_r i_{Q1} + L_m \frac{di_{D1}}{dt} \quad (6.5)$$

where,

$$L_s = L_{ls} + L_m \quad (6.6)$$

$$V_{qs} = R_s i_{qs} + \omega_r \lambda_{ds} + L_{ls} \frac{di_{qs}}{dt} + L_m \frac{di_{qs}}{dt} + L_m \frac{di_{Q1}}{dt} \quad (6.7)$$

$$V_{qs} = R_s i_{qs} + L_s \frac{di_{qs}}{dt} + L_s \omega_r i_{ds} + L_m \frac{diQ1}{dt} + L_m \omega_r iD1 \quad (6.8)$$

**[B] Rotor Equations-(fig.6.1b & fig 6.1c)**

**Loop2**

$$VD1 = 0 = (Rer + R1r)iD1 - R1riD2 + L1r \frac{diD1}{dt} + Lm \frac{di_{ds}}{dt} + Lm \frac{diD1}{dt} \quad (6.9)$$

$$VQ1 = 0 = (Rer + R1r)iQ1 - R1riQ2 + L1r \frac{diQ1}{dt} + Lm \frac{di_{qs}}{dt} + Lm \frac{diQ1}{dt} \quad (6.10)$$

**Loop3**

$$VD2 = 0 = R1riD2 - R1riD1 + R2riD2 - R2riD3 + L2r \frac{diD2}{dt} \quad (6.11)$$

$$VQ2 = 0 = R1riQ2 - R1riQ1 + R2riQ2 - R2riQ3 + L2r \frac{diQ2}{dt} \quad (6.12)$$

**Loop4**

$$VD3 = 0 = R2riD3 + R3riD3 - R3riD4 - R2riD2 + L3r \frac{diD3}{dt} \quad (6.13)$$

$$VQ3 = 0 = R2riQ3 + R3riQ3 - R3riQ4 - R2riQ2 + L3r \frac{diQ3}{dt} \quad (6.14)$$

**Loop5**

$$VD4 = 0 = R4riD4 + R3riD4 - R3riD3 - R4riD5 + L4r \frac{diD4}{dt} \quad (6.15)$$

$$VQ4 = 0 = R4riQ4 + R3riQ4 - R3riQ3 - R4riQ5 + L4r \frac{diQ4}{dt} \quad (6.16)$$

**Loop6**

$$VD5 = 0 = R5riD5 + R4riD5 - R4riD4 + L5r \frac{diD5}{dt} \quad (6.17)$$

$$VQ5 = 0 = R5riQ5 + R4riQ5 - R4riQ4 + L5r \frac{diQ5}{dt} \quad (6.18)$$

**[C] FLUX LINKAGES[ $\lambda$ ] DEFINITIONS**

$$\lambda_{md} = Lm(i_{ds} + iD1) \quad (6.19)$$

$$\lambda_{mq} = Lm(i_{qs} + iQ1) \quad (6.20)$$

$$\lambda_{mq} = Lmq \left( \frac{\lambda_{qs}}{Lls} + \frac{\lambda Q1}{L1r} \right) \quad (6.21)$$

$$\lambda_{md} = Lmd \left( \frac{\lambda_{ds}}{Lls} + \frac{\lambda D1}{L1r} \right) \quad (6.22)$$

$$Lmq = Lmd = \frac{1}{\frac{1}{Lm} + \frac{1}{Lls} + \frac{1}{L1r}} \quad (6.23)$$

$$\lambda_{ds} = Lls i_{ds} + Lm(i_{ds} + iD1) \quad (6.24)$$

$$\lambda_{qs} = Lls i_{qs} + Lm(i_{qs} + iQ1) \quad (6.25)$$

$$\lambda D1 = L1riD1 + Lm(i_{ds} + iD1) \quad (6.26)$$

$$\lambda Q1 = L1riQ1 + Lm(i_{qs} + iQ1) \quad (6.27)$$

$$\lambda D2 = L2riD2 \quad (6.28)$$

$$\lambda Q2 = L2riQ2 \quad (6.29)$$

$$\lambda D3 = L3riD3 \quad (6.30)$$

$$\lambda Q3 = L3riQ3 \quad (6.31)$$

$$\lambda D4 = L4riD4 \quad (6.32)$$

$$\lambda Q4 = L4riQ4 \quad (6.33)$$

$$\lambda D5 = L5riD5 \quad (6.34)$$

$$\lambda Q5 = L5riQ5 \quad (6.35)$$

## [D] CURRENTS DEFINITIONS

The motor d-q currents are solved from the flux linkages expressions as:

$$i_{ds} = \frac{1}{L1s} (\lambda_{ds} - \lambda_{md}) \quad (6.36)$$

$$i_{qs} = \frac{1}{Lls} (\lambda_{qs} - \lambda_{mq}) \quad (6.37)$$

$$iD1 = \frac{1}{Llr} (\lambda D1 - \lambda_{md}) \quad (6.38)$$

$$iQ1 = \frac{1}{Llr} (\lambda Q1 - \lambda_{mq}) \quad (6.39)$$

$$iD2 = \frac{\lambda D2}{L2r} \quad (6.40)$$

$$iQ2 = \frac{\lambda Q2}{L2r} \quad (6.41)$$

$$iD3 = \frac{\lambda D3}{L3r} \quad (6.42)$$

$$iQ3 = \frac{\lambda Q3}{L3r} \quad (6.43)$$

$$iD4 = \frac{\lambda D4}{L4r} \quad (6.44)$$

$$iQ4 = \frac{\lambda Q4}{L4r} \quad (6.45)$$

$$iD5 = \frac{\lambda D5}{L5r} \quad (6.46)$$

$$iQ5 = \frac{\lambda Q5}{L5r} \quad (6.47)$$

### 6.3 Motor sets of differential equations

By substituting the d-q currents definitions into the stator and rotor voltage equations, below expressions are derived.

$$\frac{d\lambda_{ds}}{dt} = Vds + \frac{Rs}{Lls} [\lambda_{md} - \lambda_{ds}] + \omega_r \lambda_{qs} \quad (6.48)$$

$$\frac{d\lambda_{qs}}{dt} = Vqs + \frac{Rs}{Lls} [\lambda_{mq} - \lambda_{qs}] - \omega_r \lambda_{ds} \quad (6.49)$$

$$\frac{d\lambda D1}{dt} = \left( \frac{Re r + R1r}{L1r} \right) [\lambda_{md} - \lambda D1] + \frac{R1r}{L2r} \lambda D2 \quad (6.50)$$

$$\frac{d\lambda Q1}{dt} = \left( \frac{Re r + R1r}{L1r} \right) [\lambda_{mq} - \lambda Q1] + \frac{R1r}{L2r} \lambda Q2 \quad (6.51)$$

$$\frac{d\lambda D2}{dt} = - \left( \frac{R1r + R2r}{L2r} \right) \lambda D2 - \frac{R1r}{L1r} [\lambda_{md} - \lambda D1] + \frac{R2r}{L3r} \lambda D3 \quad (6.52)$$

$$\frac{d\lambda Q2}{dt} = - \left( \frac{R1r + R2r}{L2r} \right) \lambda Q2 - \frac{R1r}{L1r} [\lambda_{mq} - \lambda Q1] + \frac{R2r}{L3r} \lambda Q3 \quad (6.53)$$

$$\frac{d\lambda D3}{dt} = - \left( \frac{R2r + R3r}{L3r} \right) \lambda D3 + \frac{R2r}{L2r} \lambda D2 + \frac{R3r}{L4r} \lambda D4 \quad (6.54)$$

$$\frac{d\lambda Q3}{dt} = -\left(\frac{R2r + R3r}{L3r}\right)\lambda Q3 + \frac{R2r}{L2r}\lambda Q2 + \frac{R3r}{L4r}\lambda Q4 \quad (6.55)$$

$$\frac{d\lambda D4}{dt} = -\left(\frac{R3r + R4r}{L4r}\right)\lambda D4 + \frac{R3r}{L3r}\lambda D3 + \frac{R4r}{L5r}\lambda D5 \quad (6.56)$$

$$\frac{d\lambda Q4}{dt} = -\left(\frac{R3r + R4r}{L4r}\right)\lambda Q4 + \frac{R3r}{L3r}\lambda Q3 + \frac{R4r}{L5r}\lambda Q5 \quad (6.57)$$

$$\frac{d\lambda D5}{dt} = -\left(\frac{R4r + R5r}{L5r}\right)\lambda D5 + \frac{R4r}{L4r}\lambda D4 \quad (6.58)$$

$$\frac{d\lambda Q5}{dt} = -\left(\frac{R4r + R5r}{L5r}\right)\lambda Q5 + \frac{R4r}{L4r}\lambda Q4 \quad (6.59)$$

#### 6.4 Model equations in state variable form

In order to facilitate the digital computer simulation of the developed model, it is necessary to put the differential equations in its state variable form with currents as state variables:

$$[\mathbf{V}] = [\mathbf{R}][\mathbf{i}] + [\mathbf{L}] \frac{d[\mathbf{i}]}{dt} + \omega_r [\mathbf{G}][\mathbf{i}] \quad (6.60)$$

$$\text{But } \dot{\mathbf{X}} = \mathbf{AX} + \mathbf{BU} \quad (6.61)$$

Therefore, equation(6.60) can be rearranged to get

$$\frac{d[\mathbf{i}]}{dt} = -[\mathbf{L}]^{-1}([\mathbf{R}] + \omega_r [\mathbf{G}])[\mathbf{i}] + [\mathbf{L}]^{-1}[\mathbf{V}] \quad (6.62)$$

Comparing equation(6.61) and equation(6.62), we have

$$\mathbf{A} = -[\mathbf{L}]^{-1}([\mathbf{R}] + \omega_r [\mathbf{G}]) \quad (6.63)$$

$$\mathbf{B} = [\mathbf{L}]^{-1} \quad (6.64)$$

$$\mathbf{U} = [\mathbf{V}] \quad (6.65)$$

$$\mathbf{X} = [\mathbf{i}] \quad (6.66)$$

Where  $\mathbf{R}$ ,  $\mathbf{L}$ ,  $\mathbf{V}$ ,  $\mathbf{i}$  and  $\mathbf{G}$  are defined as:

$$[\mathbf{i}] = [i_{ds} \ i_{qs} \ iD1 \ iQ1 \ iD2 \ iQ2 \ iD3 \ iQ3 \ iD4 \ iQ4 \ iD5 \ iQ5]^T \quad (6.67)$$

$$[\mathbf{V}] = [V_{ds} \ V_{qs} \ 0 \ 0 \ 0 \ 0 \ 0 \ 0 \ 0 \ 0 \ 0 \ 0]^T \quad (6.68)$$

$$[\mathbf{G}] = \begin{bmatrix} 0 & -L_s & 0 & -L_m & 0 & 0 & 0 & 0 & 0 & 0 & 0 & 0 \\ L_s & 0 & L_m & 0 & 0 & 0 & 0 & 0 & 0 & 0 & 0 & 0 \\ 0 & 0 & 0 & 0 & 0 & 0 & 0 & 0 & 0 & 0 & 0 & 0 \\ 0 & 0 & 0 & 0 & 0 & 0 & 0 & 0 & 0 & 0 & 0 & 0 \\ 0 & 0 & 0 & 0 & 0 & 0 & 0 & 0 & 0 & 0 & 0 & 0 \\ 0 & 0 & 0 & 0 & 0 & 0 & 0 & 0 & 0 & 0 & 0 & 0 \\ 0 & 0 & 0 & 0 & 0 & 0 & 0 & 0 & 0 & 0 & 0 & 0 \\ 0 & 0 & 0 & 0 & 0 & 0 & 0 & 0 & 0 & 0 & 0 & 0 \\ 0 & 0 & 0 & 0 & 0 & 0 & 0 & 0 & 0 & 0 & 0 & 0 \\ 0 & 0 & 0 & 0 & 0 & 0 & 0 & 0 & 0 & 0 & 0 & 0 \\ 0 & 0 & 0 & 0 & 0 & 0 & 0 & 0 & 0 & 0 & 0 & 0 \\ 0 & 0 & 0 & 0 & 0 & 0 & 0 & 0 & 0 & 0 & 0 & 0 \end{bmatrix} \quad (6.69)$$

$$[\mathbf{R}] = \begin{bmatrix} R_s & 0 & 0 & 0 & 0 & 0 & 0 & 0 & 0 & 0 & 0 & 0 \\ 0 & R_s & 0 & 0 & 0 & 0 & 0 & 0 & 0 & 0 & 0 & 0 \\ 0 & 0 & R_{11} & 0 & -R_{1r} & 0 & 0 & 0 & 0 & 0 & 0 & 0 \\ 0 & 0 & 0 & R_{11} & 0 & -R_{1r} & 0 & 0 & 0 & 0 & 0 & 0 \\ 0 & 0 & -R_{1r} & 0 & R_{22} & 0 & -R_{2r} & 0 & 0 & 0 & 0 & 0 \\ 0 & 0 & 0 & -R_{1r} & 0 & R_{22} & 0 & -R_{2r} & 0 & 0 & 0 & 0 \\ 0 & 0 & 0 & 0 & -R_{2r} & 0 & R_{33} & 0 & -R_{3r} & 0 & 0 & 0 \\ 0 & 0 & 0 & 0 & 0 & -R_{2r} & 0 & R_{33} & 0 & -R_{3r} & 0 & 0 \\ 0 & 0 & 0 & 0 & 0 & 0 & -R_{3r} & 0 & R_{44} & 0 & -R_{4r} & 0 \\ 0 & 0 & 0 & 0 & 0 & 0 & 0 & -R_{3r} & 0 & R_{44} & 0 & -R_{4r} \\ 0 & 0 & 0 & 0 & 0 & 0 & 0 & 0 & -R_{4r} & 0 & R_{55} & 0 \\ 0 & 0 & 0 & 0 & 0 & 0 & 0 & 0 & 0 & -R_{4r} & 0 & R_{55} \end{bmatrix} \quad (6.70)$$

Where,

$$R_{11} = R_e r + R_{1r}$$

$$R_{22} = R_{1r} + R_{2r}$$

$$R_{33} = R_{2r} + R_{3r} \quad (6.71)$$

$$R_{44} = R_{3r} + R_{4r}$$

$$R_{55} = R_{4r} + R_{5r}$$

$$[\mathbf{L}] = \begin{bmatrix} L_s & 0 & L_m & 0 & 0 & 0 & 0 & 0 & 0 & 0 & 0 & 0 \\ 0 & L_s & 0 & L_m & 0 & 0 & 0 & 0 & 0 & 0 & 0 & 0 \\ L_m & 0 & L_{mr} & 0 & 0 & 0 & 0 & 0 & 0 & 0 & 0 & 0 \\ 0 & L_m & 0 & L_{mr} & 0 & 0 & 0 & 0 & 0 & 0 & 0 & 0 \\ 0 & 0 & 0 & 0 & L_{2r} & 0 & 0 & 0 & 0 & 0 & 0 & 0 \\ 0 & 0 & 0 & 0 & 0 & L_{2r} & 0 & 0 & 0 & 0 & 0 & 0 \\ 0 & 0 & 0 & 0 & 0 & 0 & L_{3r} & 0 & 0 & 0 & 0 & 0 \\ 0 & 0 & 0 & 0 & 0 & 0 & 0 & L_{3r} & 0 & 0 & 0 & 0 \\ 0 & 0 & 0 & 0 & 0 & 0 & 0 & 0 & L_{4r} & 0 & 0 & 0 \\ 0 & 0 & 0 & 0 & 0 & 0 & 0 & 0 & 0 & L_{4r} & 0 & 0 \\ 0 & 0 & 0 & 0 & 0 & 0 & 0 & 0 & 0 & 0 & L_{5r} & 0 \\ 0 & 0 & 0 & 0 & 0 & 0 & 0 & 0 & 0 & 0 & 0 & L_{5r} \end{bmatrix} \quad (6.72)$$

Where,

$$L_{mr} = L_{1r} + L_m \quad (6.73)$$

## 6.5 Model development with saturation effect

The values of the inductances used in the development of the dynamic equations for the classical and skin-effect induction machine models were assumed to be constant. By so doing, the models fail to take into consideration the saturation effects of the magnetizing field. It has been proved beyond doubts by several authors[71,72,73,74] that the stability and dynamic conditions of induction machine are highly affected by saturation. Several methods have been developed in modelling saturation effect in induction machines[74,75,76,77,78]-each differing in area of applications and of course, in the part of the machine inductances that are assumed to saturate. In[74,75], induction motor with saturable leakage reactances is modelled and simulated with the help of analog computer and IGSPICE respectively. In He[73] and Levi[77] the effect of considering the main flux saturation is investigated. A saturation model for leakage inductances presents a difficult task in terms of analysis and computer time[74,75,78]. It has been shown however, that the main magnetizing field contributes significantly to the disparity between induction machines computer simulation results and experiment[73]. Therefore, to a very high level of accuracy the effects of saturation in induction machines can be included by variation of the main flux inductance while assuming the leakage inductances to be constant. However, where the stator and rotor currents are expected to be very high values, inclusion of the leakage inductance saturation becomes imperative[74,75]. In this work, saturation due to the influence of the main flux inductance is considered. The application of this method requires that the no-load saturation curve of the machine be known. The saturation curve of the induction motor determined by taking the motor no-load current measurements with balanced 3-phase, 50Hz voltages applied to the stator windings without mechanical load on the motor is shown in figure 6.2

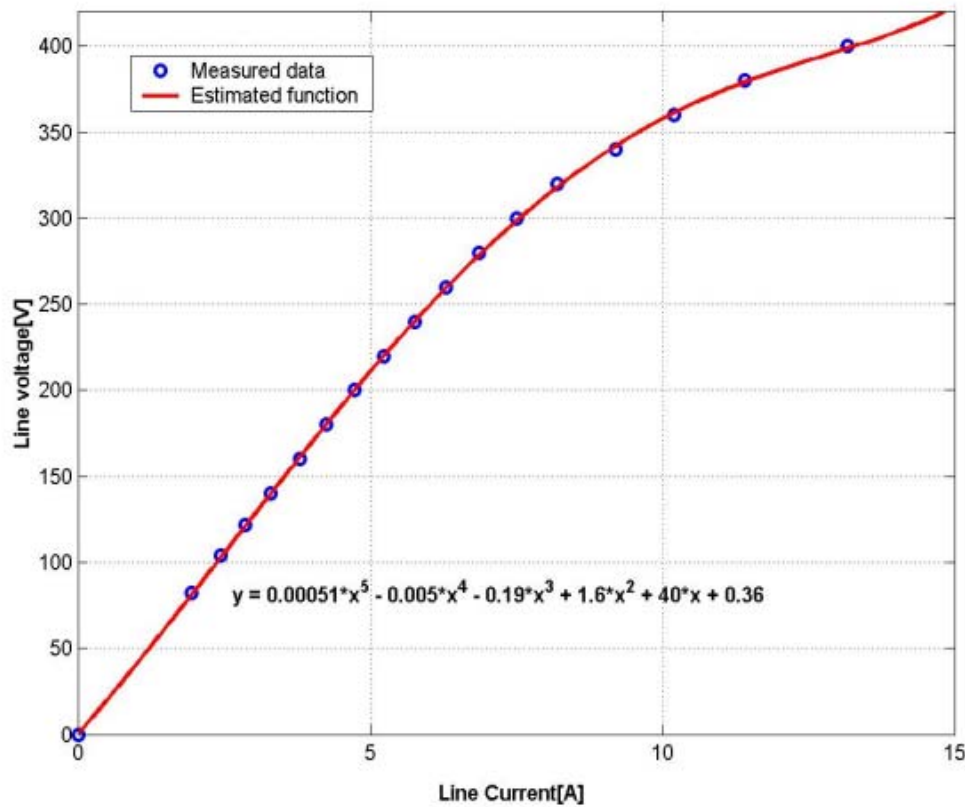


**Figure 6.2:** No-Load Saturation curve.

The voltage increments start below rated voltage on the linear portion of the curve and normally continue to somewhat above rated voltage well beyond the knee of the curve. It is important to add that measurements above rated voltage should be taken as quickly as possible to avoid over heating of the stator windings and consequent breakdown of the machine. Because the loss component of no-load current is very low compared to the magnetizing component, the measured no-load current values may be assumed to be all flux-producing currents without loss in accuracy. Due to very low slip at no-load, the secondary branch impedances become very high referred to the stator. This practically eliminates the participation of the rotor circuit leaving only the stator leakage( $L_{ls}$ ) and the magnetizing branch( $L_m$ ) to contribute to the no-load saturation curve shown in figure 6.2. Since the stator leakage inductance,  $L_{ls}$  is assumed constant, then the magnetizing inductance can be extracted from figure 6.2. By so doing, figure 6.3 results.

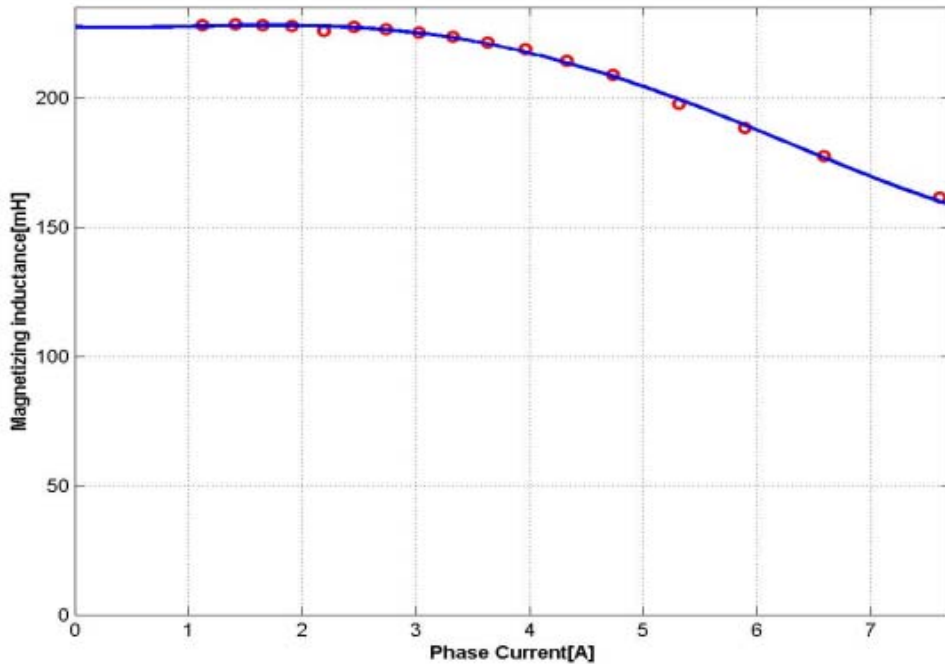


**Figure 6.3:** Saturation characteristic curve.

In order to find an analytical expression for the saturation characteristic curve of figure 6.3, a curve-fitting method which employs the algorithm of Marquardt[79] is employed. Figure 6.4 shows the approximated curve with the estimated function as:

$$L_m = 0.064i_m^4 - 0.94i_m^3 + 2.4i_m^2 - 1.4i_m + 230[mH] \quad (6.74)$$

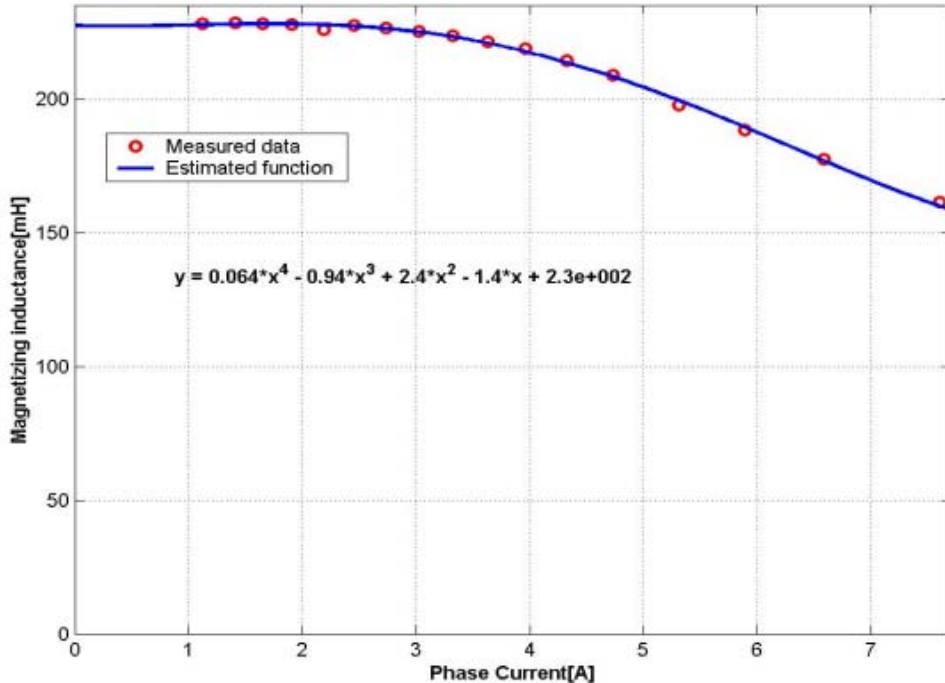


**Figure 6.4:** Saturation Curve and Polynomial approximation.

The magnetizing current,  $i_m$  is defined as,

$$i_m = \sqrt{i_{dt}^2 + i_{qt}^2} \quad (6.75)$$

and

$$i_{dt} = i_{ds} + i_{dr} \quad (6.76)$$

$$i_{qt} = i_{qs} + i_{qr} \quad (6.77)$$

By storing the analytical expression in the computer, the value of the magnetizing inductance in both the induction machine conventional and Skin-effect models can be updated at each integration step.

## 6.6 Steady-state machine model

In consideration of the steady-state equation of the induction machine with skin-effect, the time derivatives of current in equation(6.60) are set to zero with the rotor speed constant and the machine d- and q-voltages and currents referred to the synchronously rotating reference frame. By so doing, the resultant algebraic equation can be expressed in compact form as,

$$[\mathbf{V}_o] = [\mathbf{Z}_o] \mathbf{I}_o \quad (6.78a)$$

and

$$[\mathbf{I}_o] = [\mathbf{Z}_o]^{-1} [\mathbf{V}_o] \quad (6.78b)$$

where,

$$[\mathbf{I}_o] = [id_{so} \quad iq_{so} \quad iD1o \quad iQ1o \quad iD2o \quad iQ2o \quad iD3o \quad iQ3o \quad iD4o \quad iQ4o \quad iD5o \quad iQ5o]^T \quad (6.78c)$$

$$[\mathbf{V}_o] = [Vd_{so} \quad Vq_{so} \quad 0 \quad 0]^T \quad (6.78d)$$

and

$$[\mathbf{Z}_o] = \begin{bmatrix} R_s & -Ls\omega_b & 0 & -Lm\omega_b & 0 & 0 & 0 & 0 & 0 & 0 & 0 & 0 \\ Ls\omega_b & R_s & Lm\omega_b & 0 & 0 & 0 & 0 & 0 & 0 & 0 & 0 & 0 \\ 0 & (\omega_r - \omega_b)Lm & R11 & (\omega_r - \omega_b)Lr & -R1r & 0 & 0 & 0 & 0 & 0 & 0 & 0 \\ (\omega_b - \omega_r)Lm & 0 & (\omega_b - \omega_r)Lr & R11 & 0 & -R1r & 0 & 0 & 0 & 0 & 0 & 0 \\ 0 & 0 & -R1r & 0 & R22 & 0 & -R2r & 0 & 0 & 0 & 0 & 0 \\ 0 & 0 & 0 & -R1r & 0 & R22 & 0 & -R2r & 0 & 0 & 0 & 0 \\ 0 & 0 & 0 & 0 & -R2r & 0 & R33 & 0 & -R3r & 0 & 0 & 0 \\ 0 & 0 & 0 & 0 & 0 & -R2r & 0 & R33 & 0 & -R3r & 0 & 0 \\ 0 & 0 & 0 & 0 & 0 & 0 & -R3r & 0 & R44 & 0 & -R4r & 0 \\ 0 & 0 & 0 & 0 & 0 & 0 & 0 & -R3r & 0 & R44 & 0 & -R4r \\ 0 & 0 & 0 & 0 & 0 & 0 & 0 & 0 & -R4r & 0 & R55 & 0 \\ 0 & 0 & 0 & 0 & 0 & 0 & 0 & 0 & 0 & -R4r & 0 & R55 \end{bmatrix} \quad (6.78e)$$

where  $R_{11}$ ,  $R_{22}$ ,  $R_{33}$ ,  $R_{44}$  and  $R_{55}$  are as defined in equation(6.71). By solving equation(6.78b) together with equation(5.33), the steady-state with skin-effect performance as shown in figure 6.5 results.

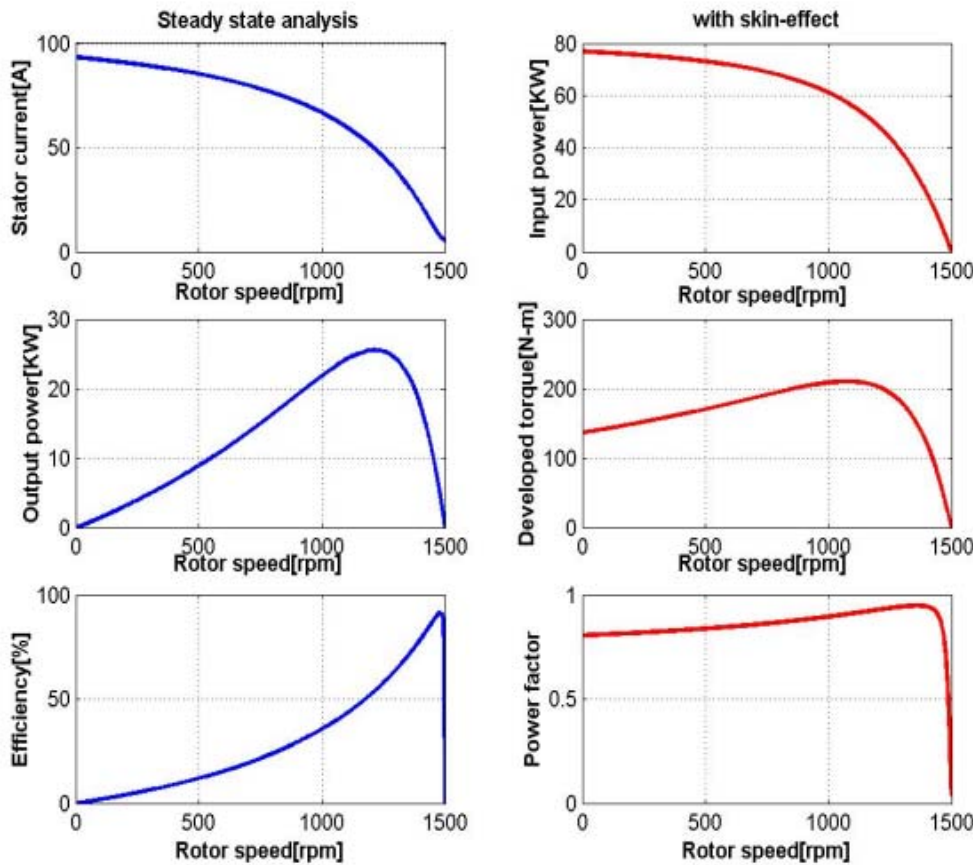


**Figure 6.5:** Steady-state performance curves with skin-effect.

In order to investigate the effect of saturation on the steady-state performance of the machine, the estimated function of the magnetizing inductance given in equation(6.74) is substituted in equations (5.30) and (6.78b)—thereby making the value of the magnetizing inductance in these equations to be varying. The steady-state magnitude of the rotor bar currents for each section as a function of rotor speed is shown in figure 6.6. Figure 6.7 depicts the rotor bar currents for each section as a function of rotor speed and with saturation effect included.

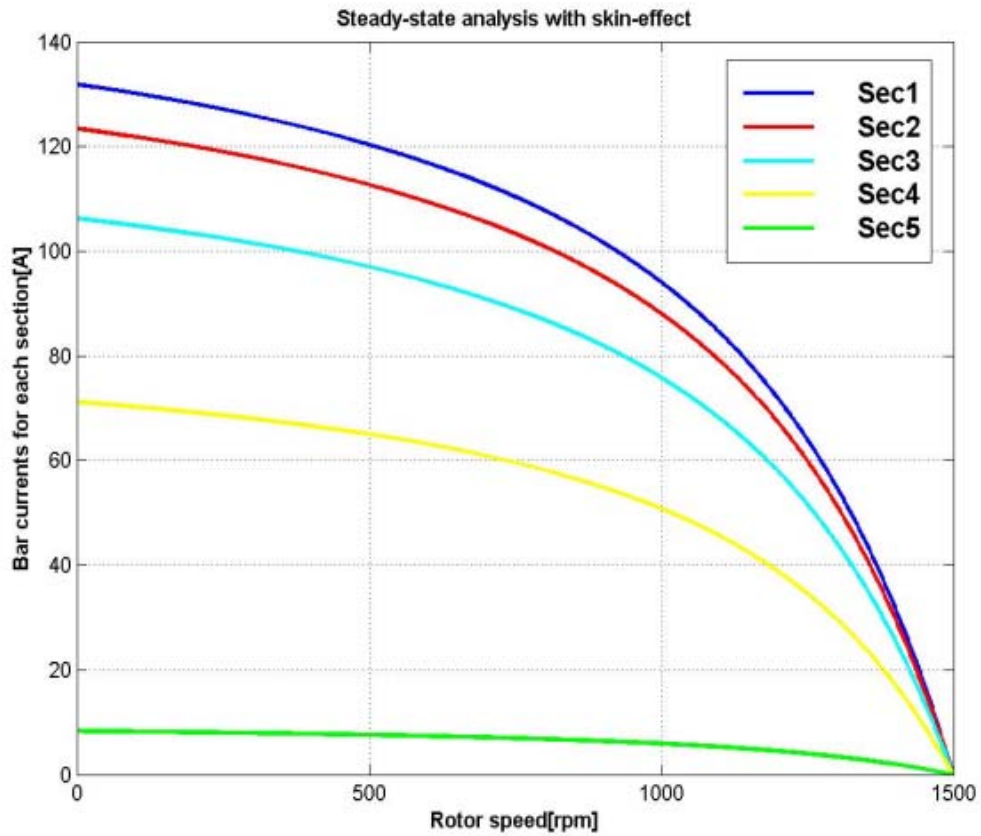


**Figure 6.6:** Rotor bar currents for each section with skin-effect.

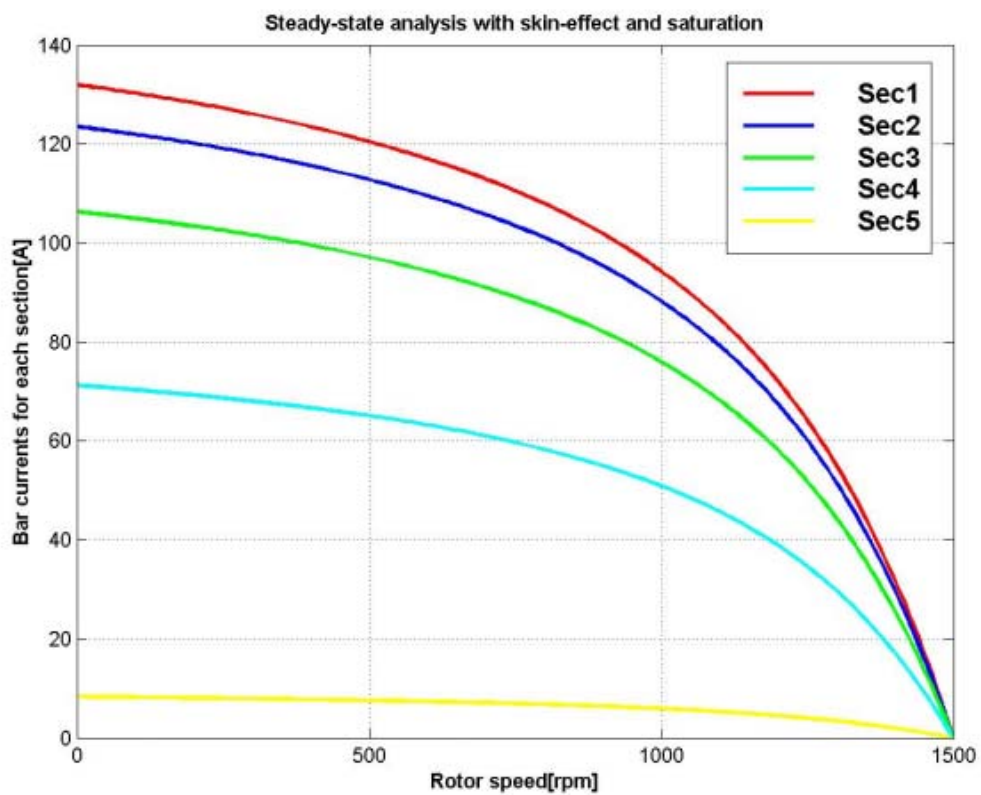


**Figure 6.7:** Rotor bar currents for each section with skin and saturation effects.

Figure 6.8 and figure 6.9 show the computed steady-state performances with saturation effect for conventional and skin-effect machine models respectively.

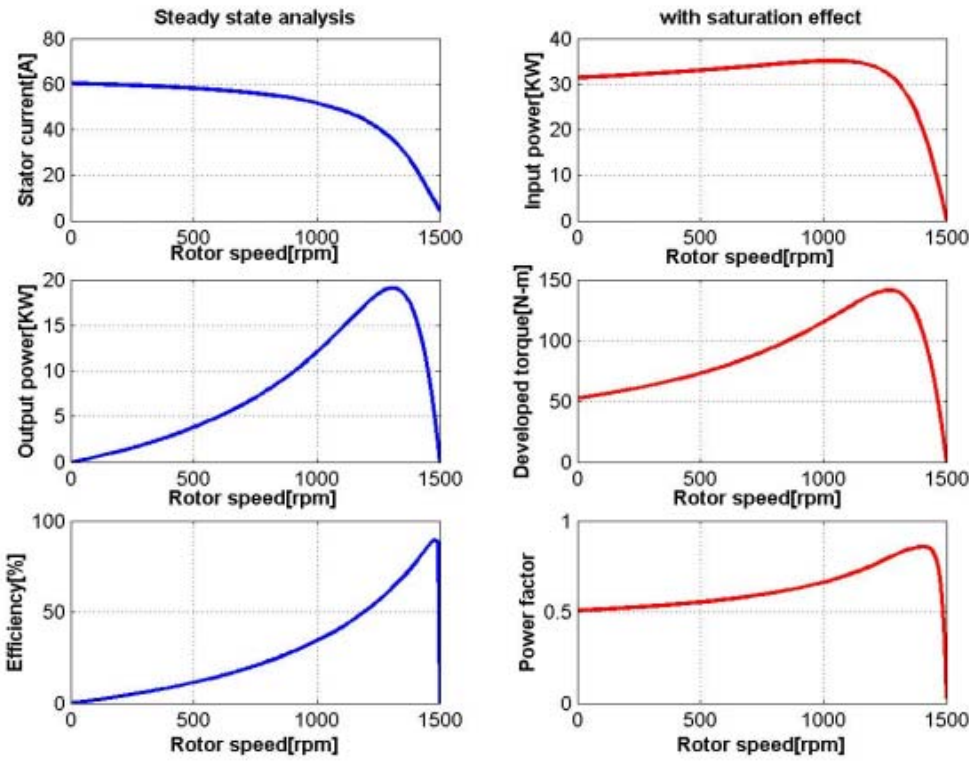


**Figure 6.8:** Steady-state performance curves with saturation effect.

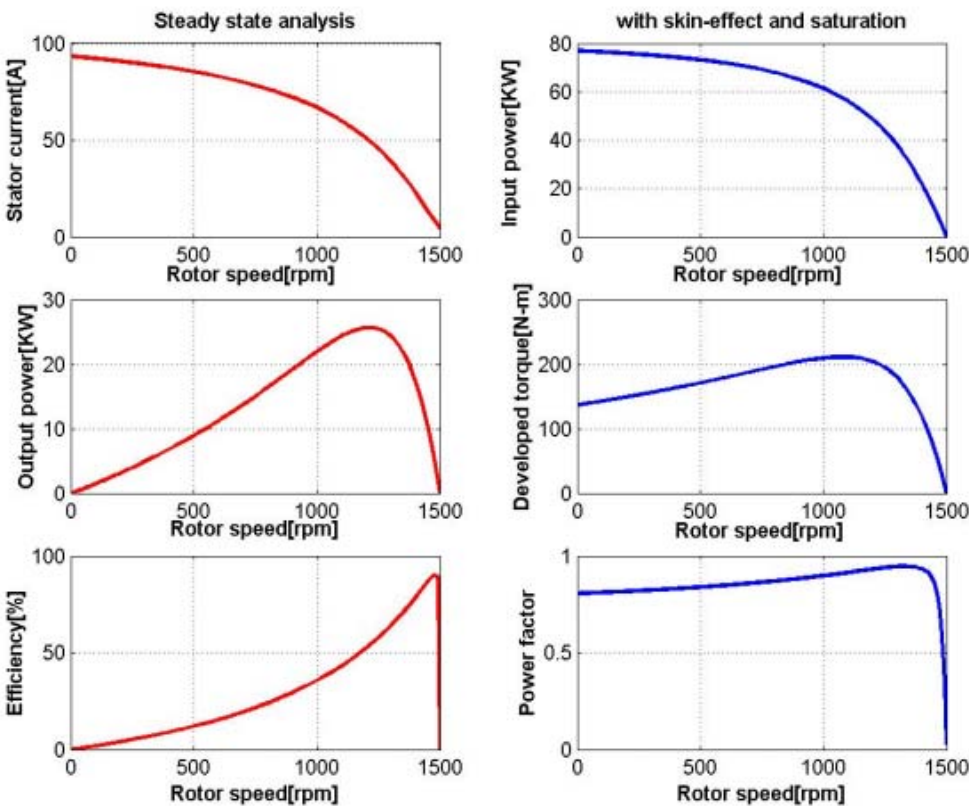


**Figure 6.9:** Steady-state performance curves with both skin and saturation effects.

## 6.7 Computer simulation and results

In order to predict the dynamic performances of the machine, the model equations in state variable form with currents as state variables are used. MATLAB function program which describes the differential equations of the machine in dynamic condition as discussed in section 6.4 is developed. Together with the mechanical model of the machine as shown in section 5.4, the transient behaviour of the induction machine at run-up can be simulated. It is assumed that the rotor and stator currents are initially at zero. The program also incorporates the analytical expression of the magnetizing inductance in order to investigate the effect of saturation on both steady-state and dynamic behaviours of the machine. The rotor circuit parameters as shown in table 4.1 are referred to the stator and subsequently used for the simulation involving skin-effect. The steady-state performance curves are shown in figures(6.5-6.9). Figure 6.10 and figure 6.11 show the transient behaviours of the simulated machine for the stator phase currents, torque, speed, linkage fluxes and d-q currents as a function of time with skin-effect and saturation effect included respectively. In figure 6.12, the transient behaviours of the simulated conventional machine model with saturation effect are presented.

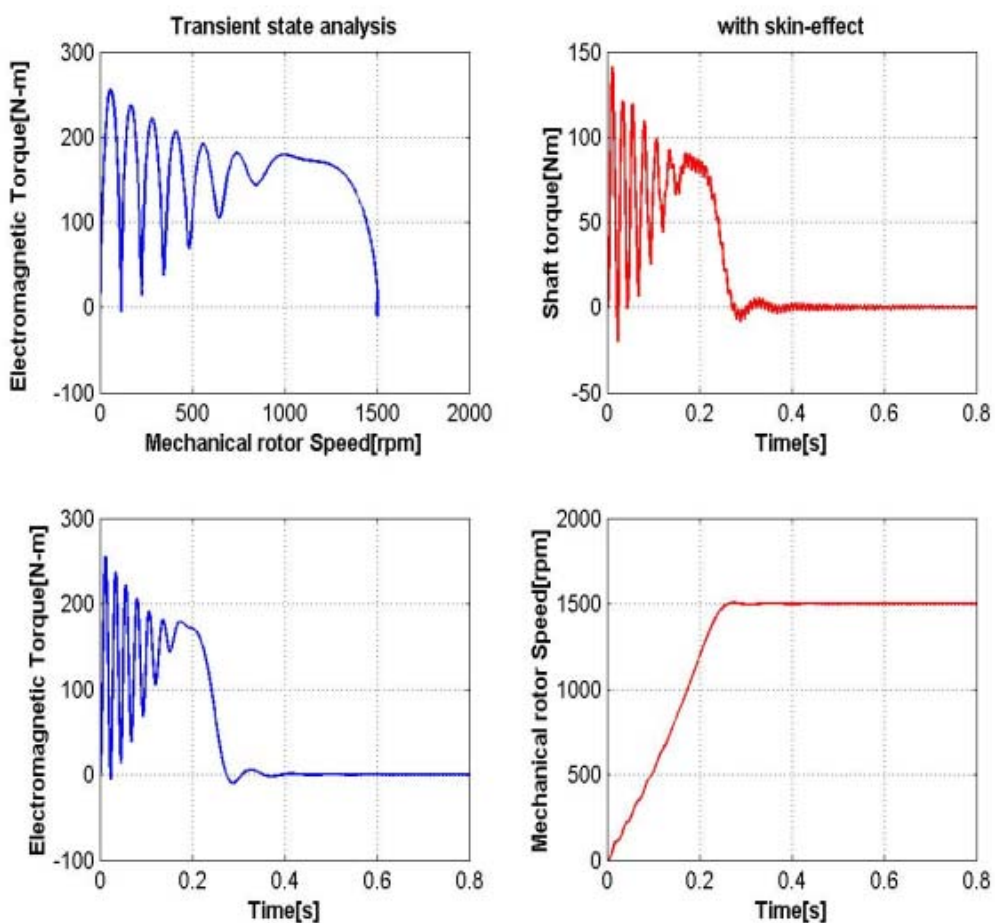


Figure 6.10a

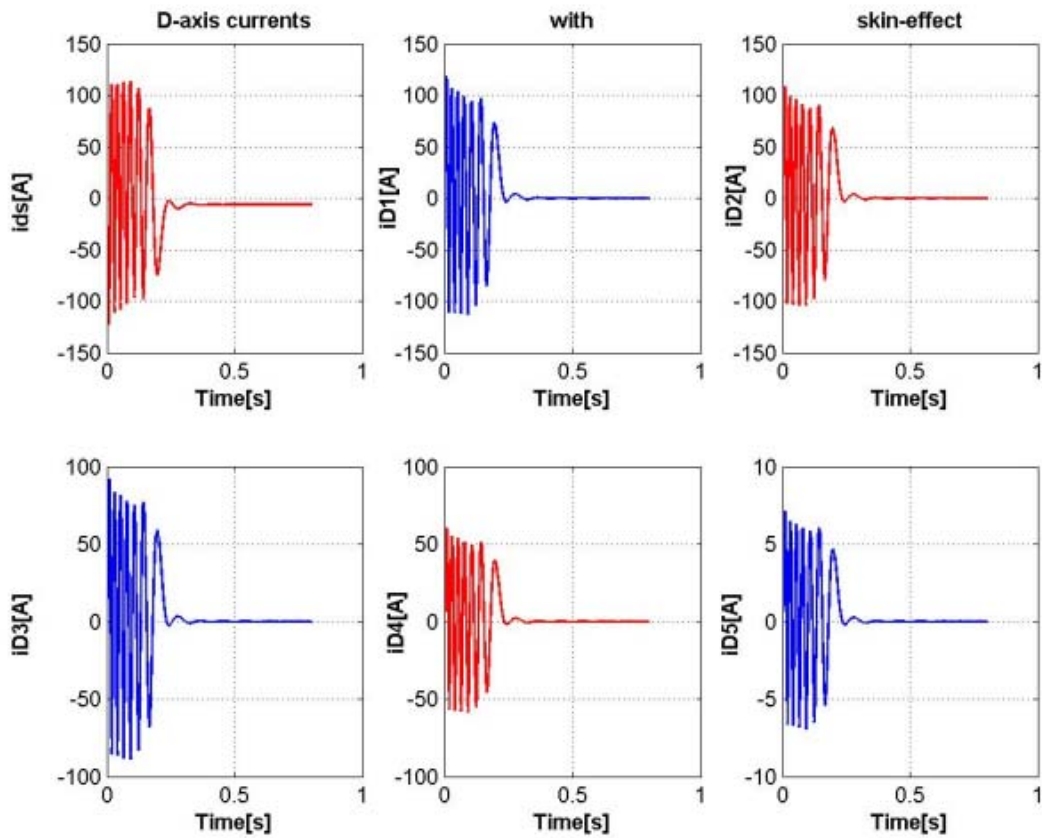


Figure 6.10b

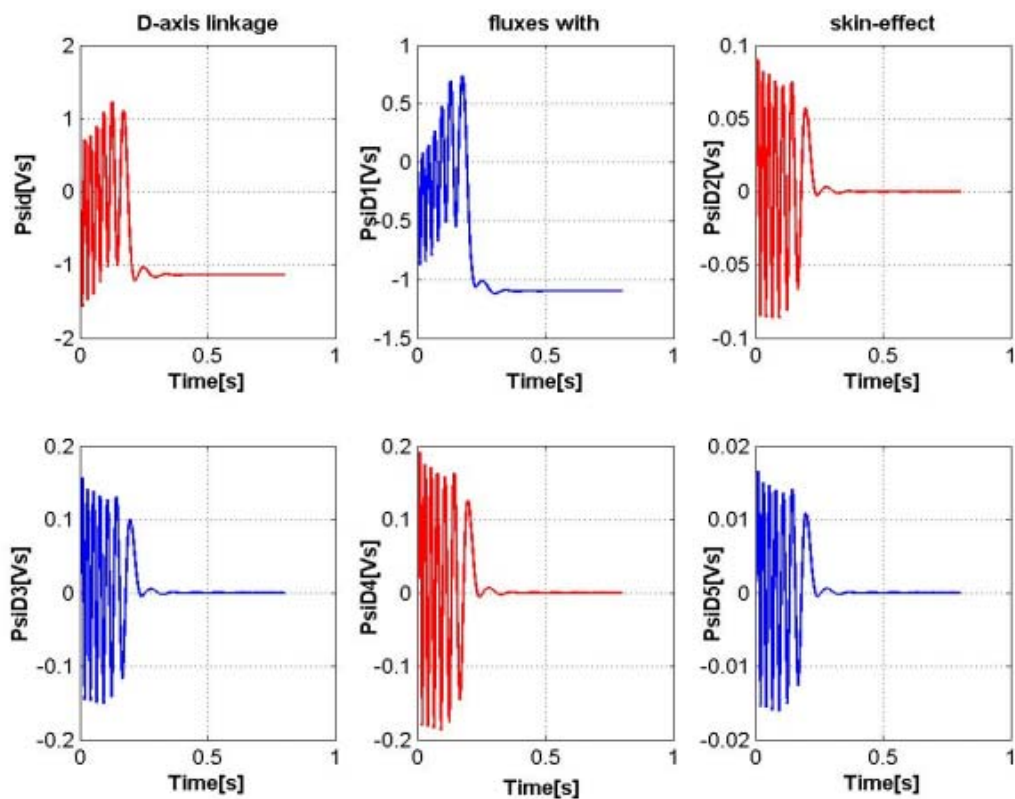


Figure 6.10c

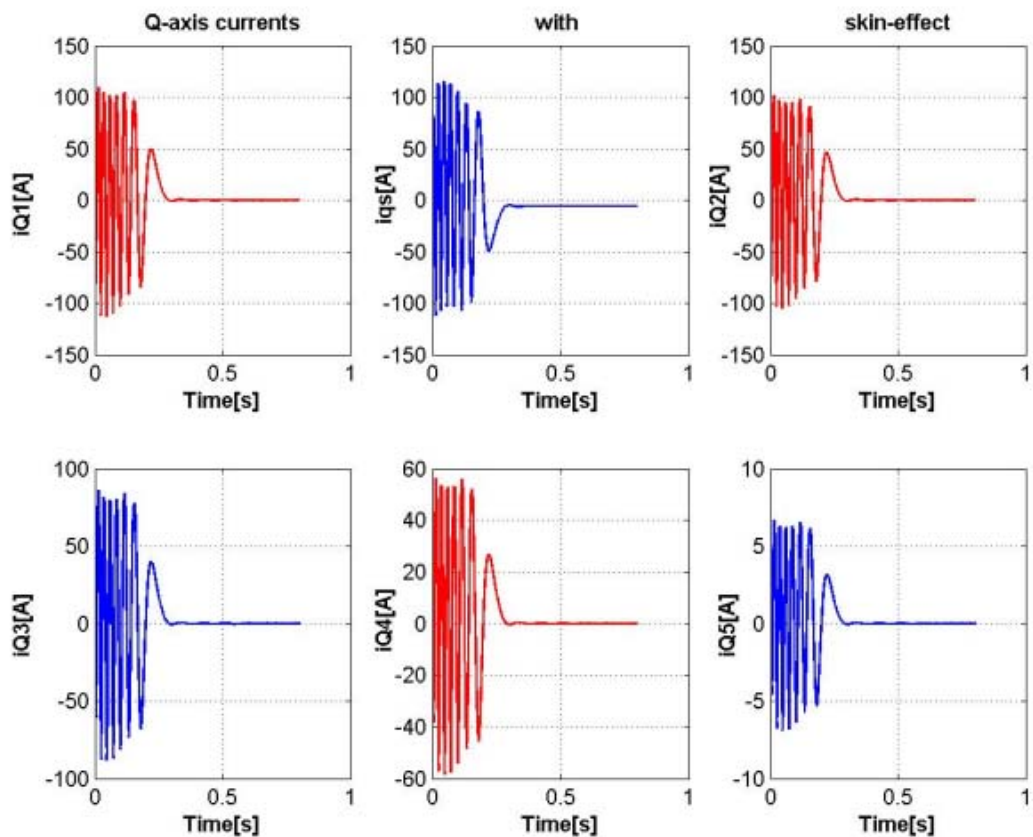


Figure 6.10d

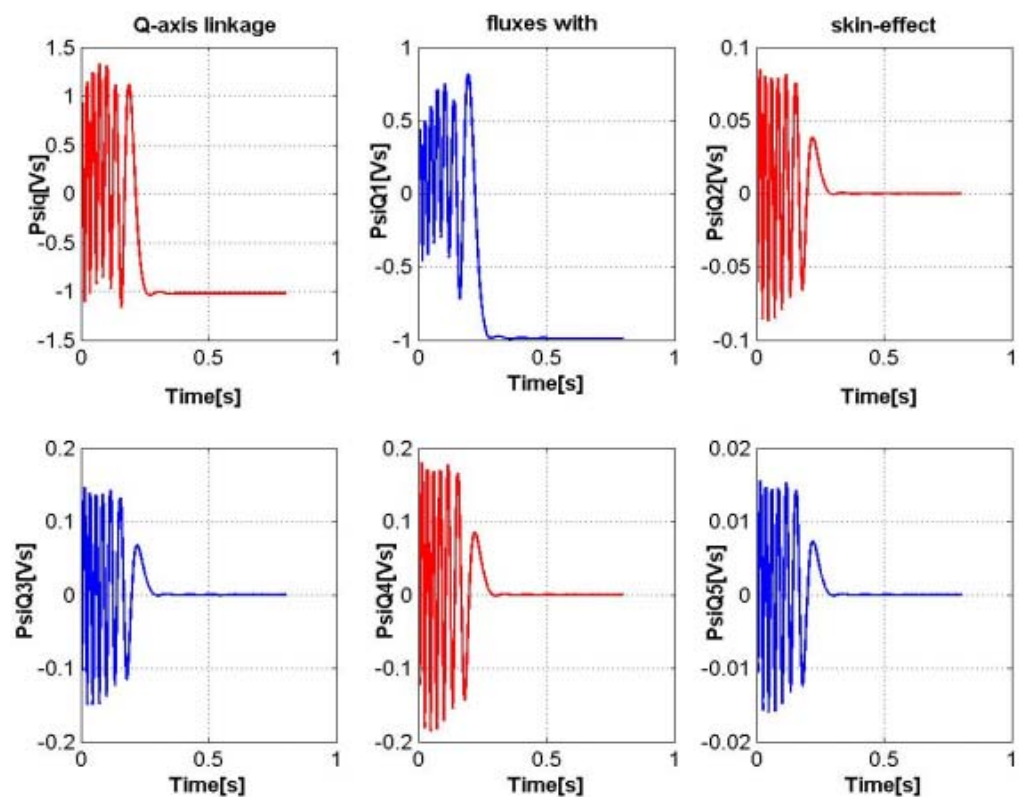
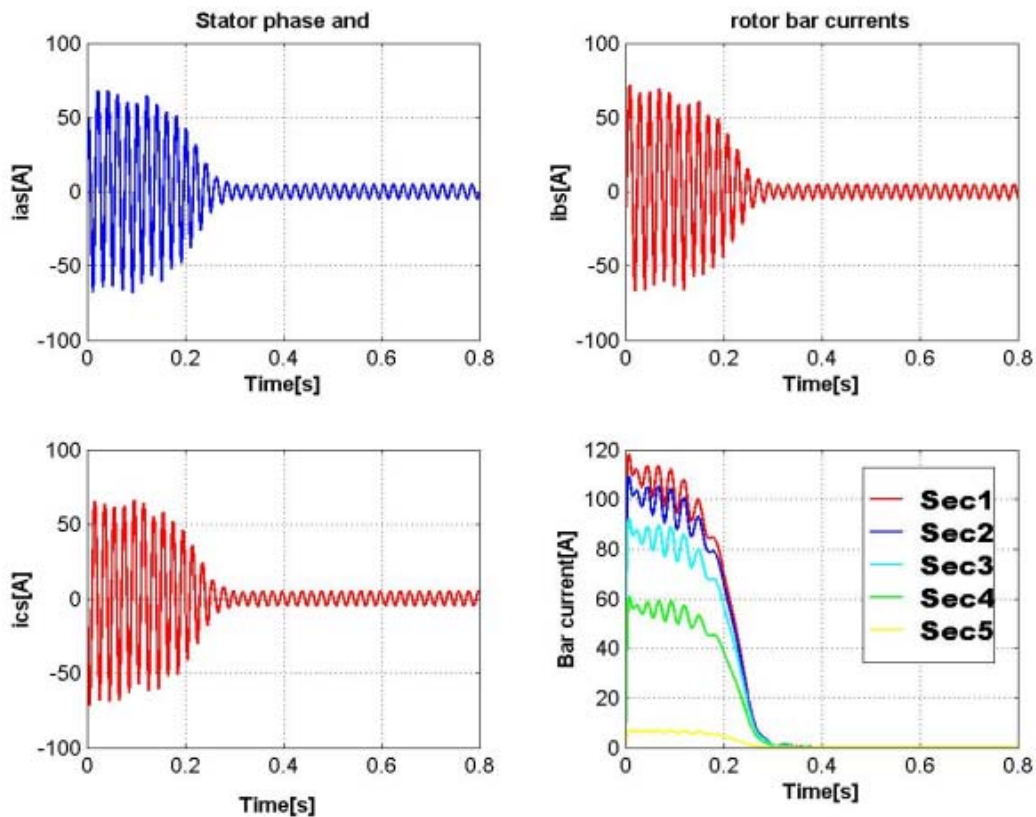
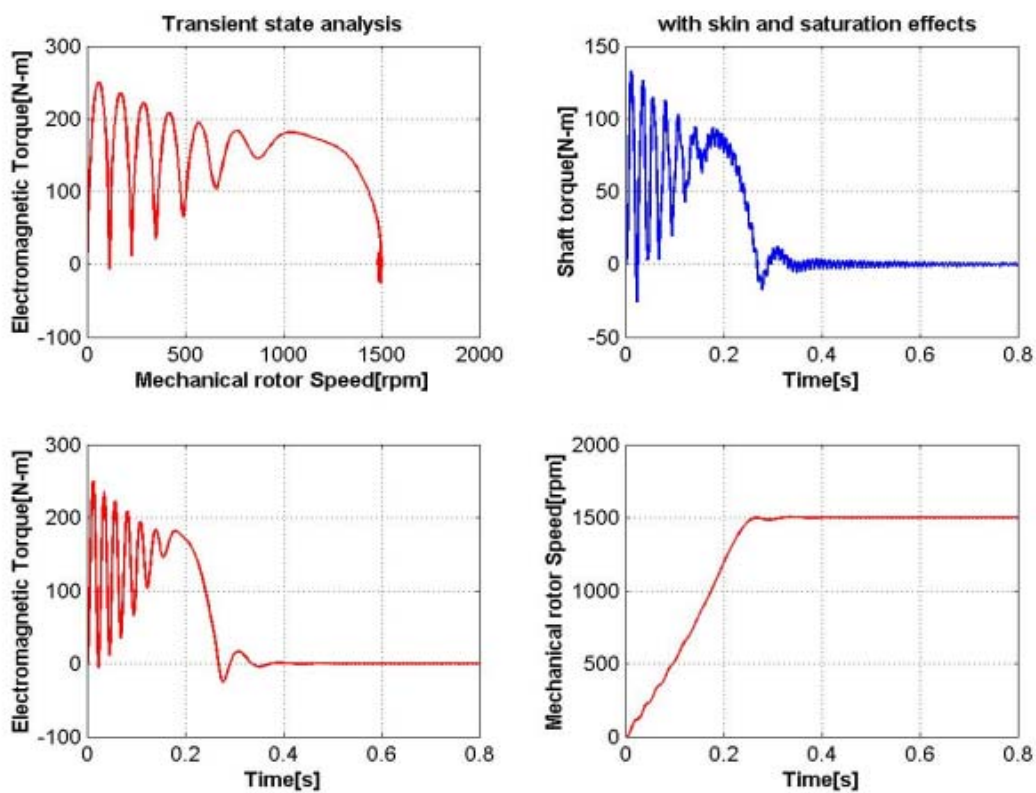
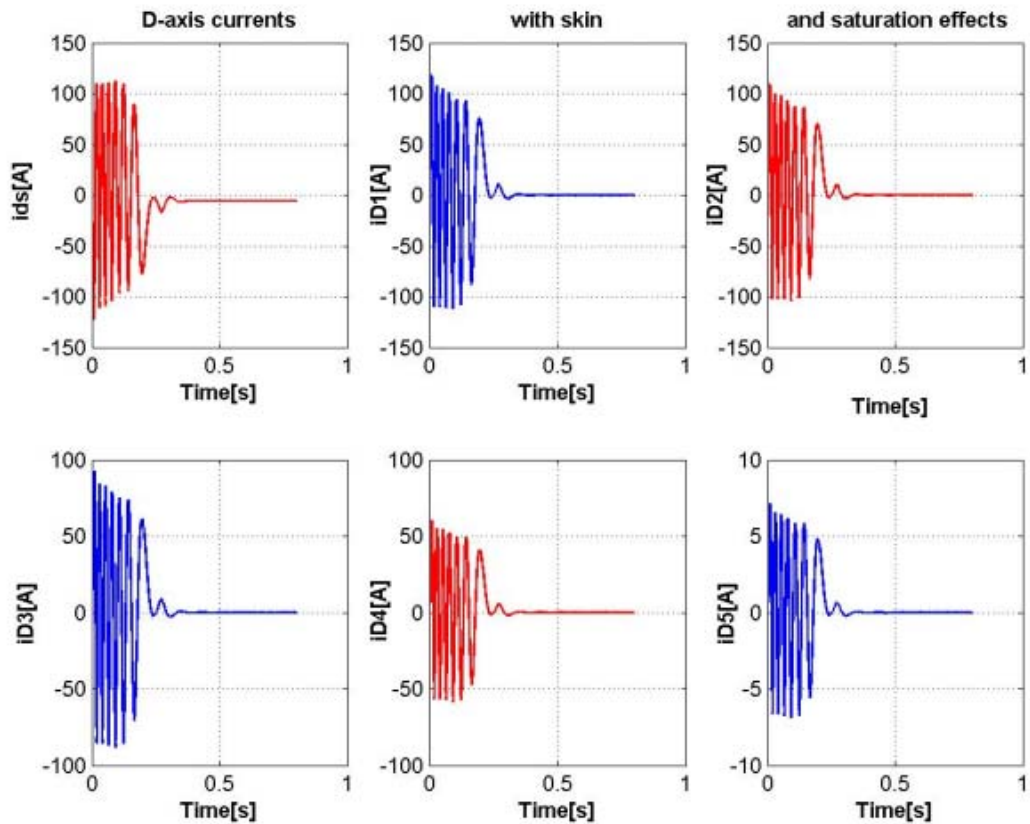
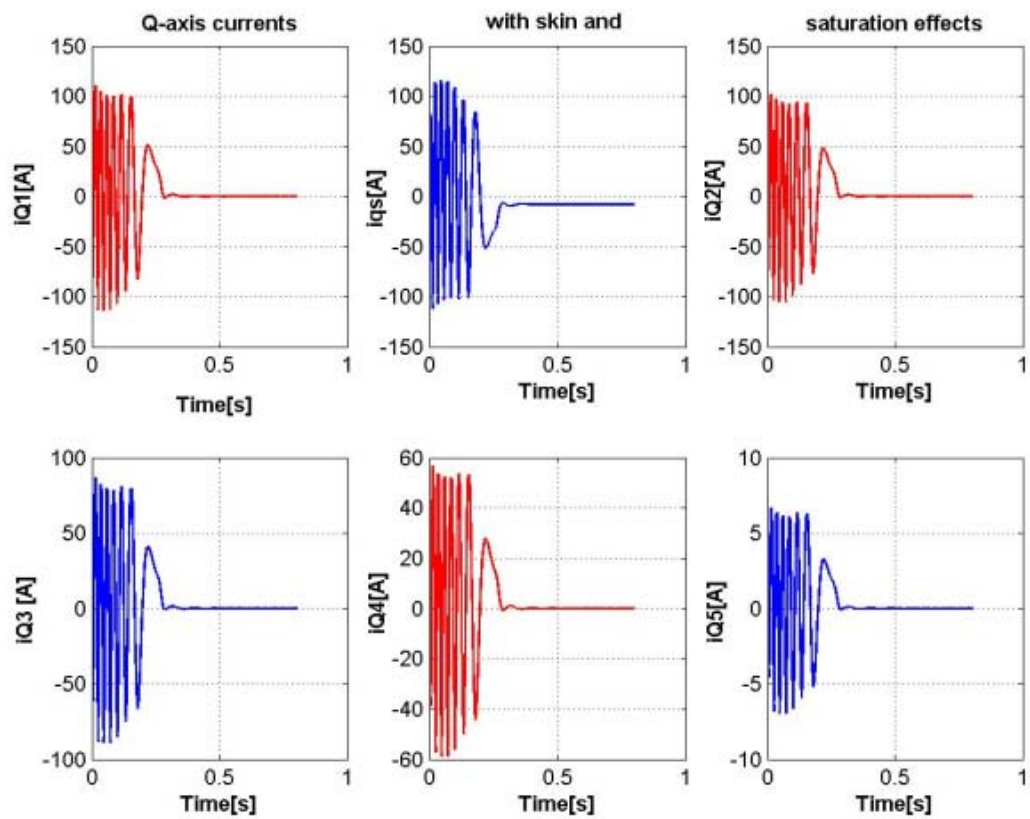


Figure 6.10e

**Figure 6.10f**

**Figure 6.10:** Transient state performances of induction machine with skin-effect.

**Figure 6.11a**

**Figure 6.11b****Figure 6.11c**

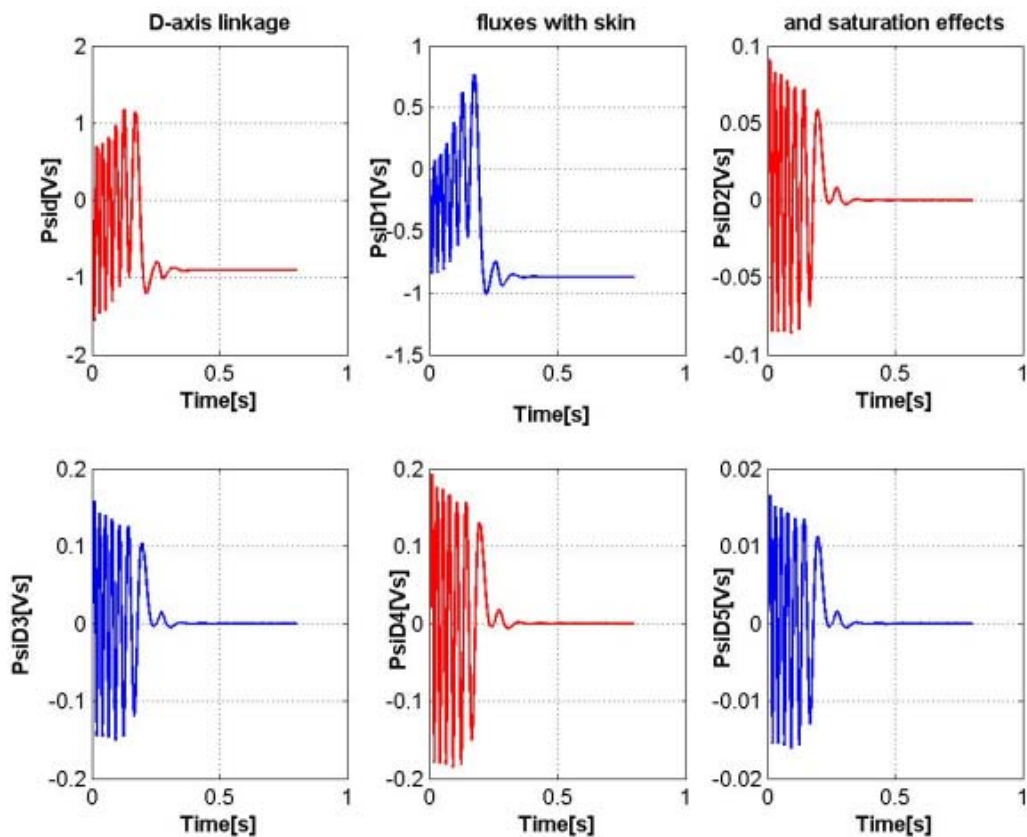


Figure 6.11d

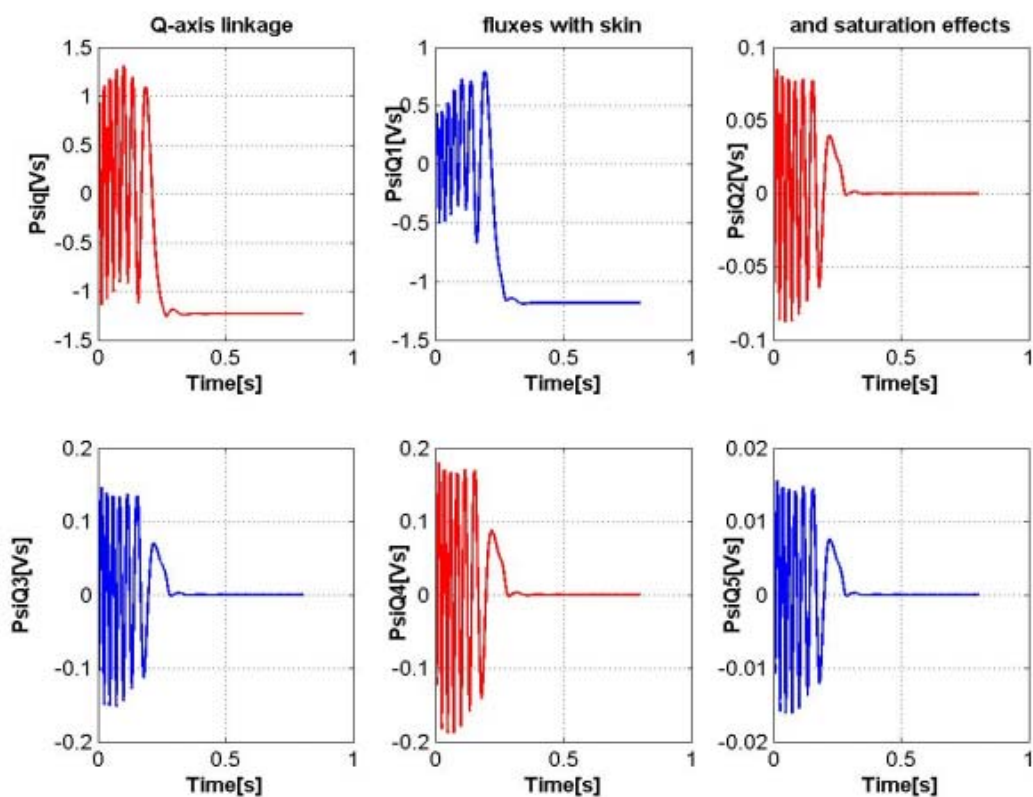
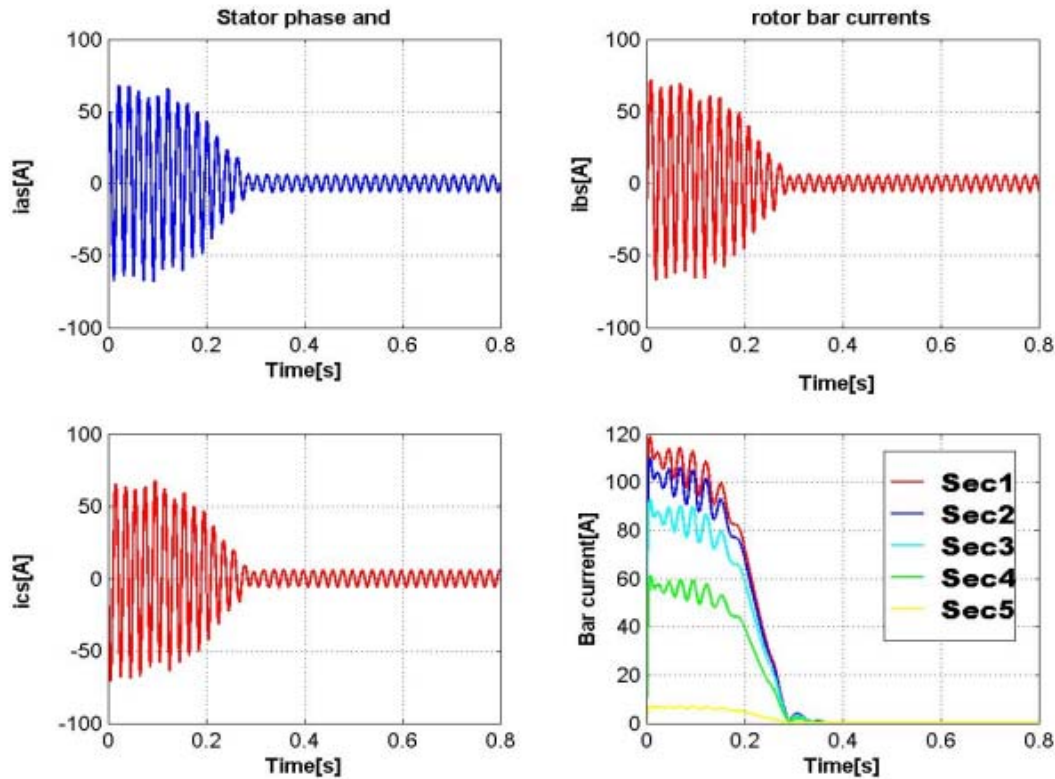
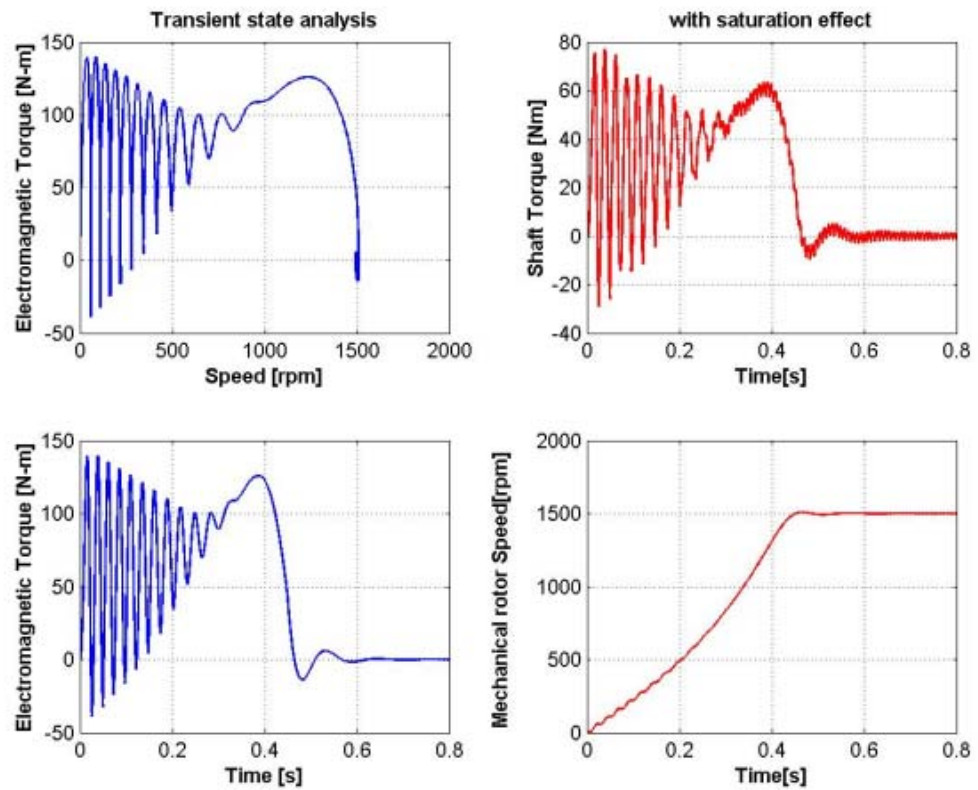


Figure 6.11e

**Figure 6.11f**

**Figure 6.11:** Transient state performances of induction machine with skin and saturation effects.

**Figure 6.12a**

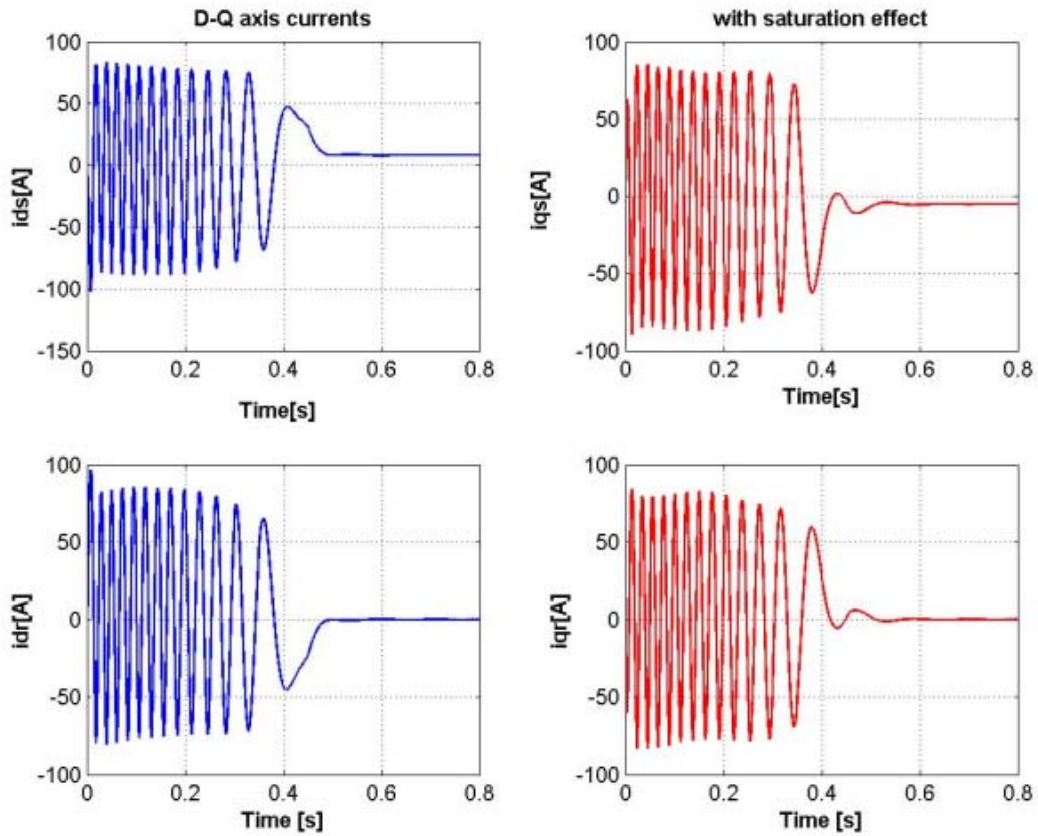


Figure 6.12b

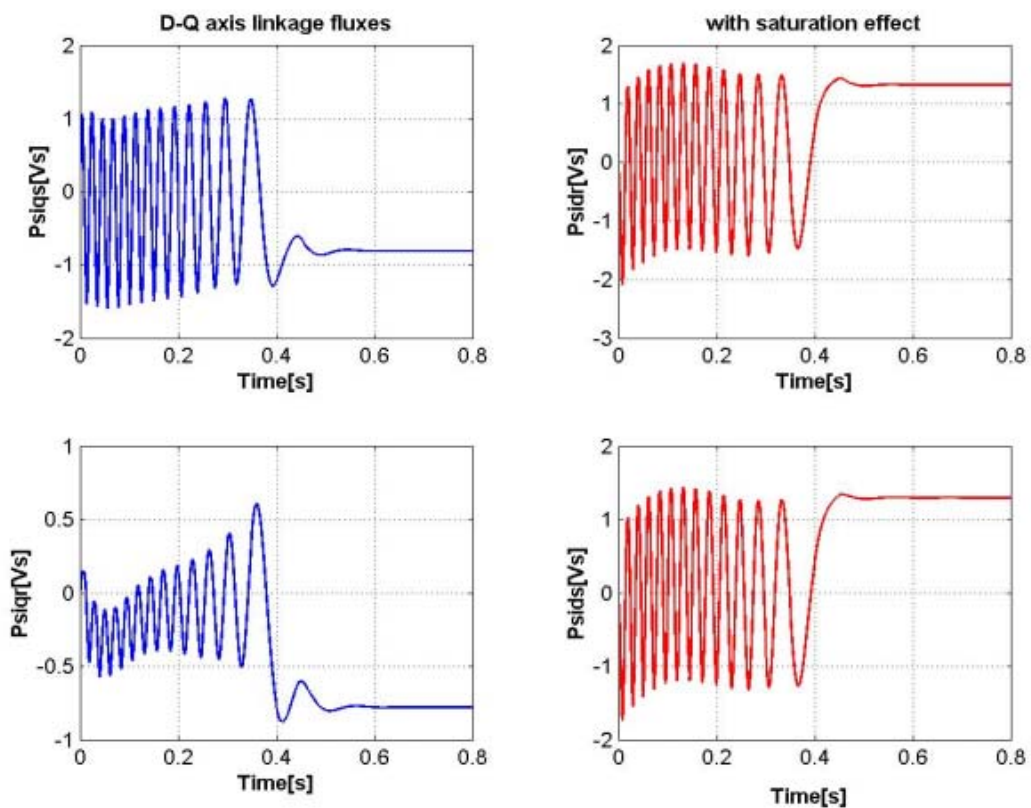
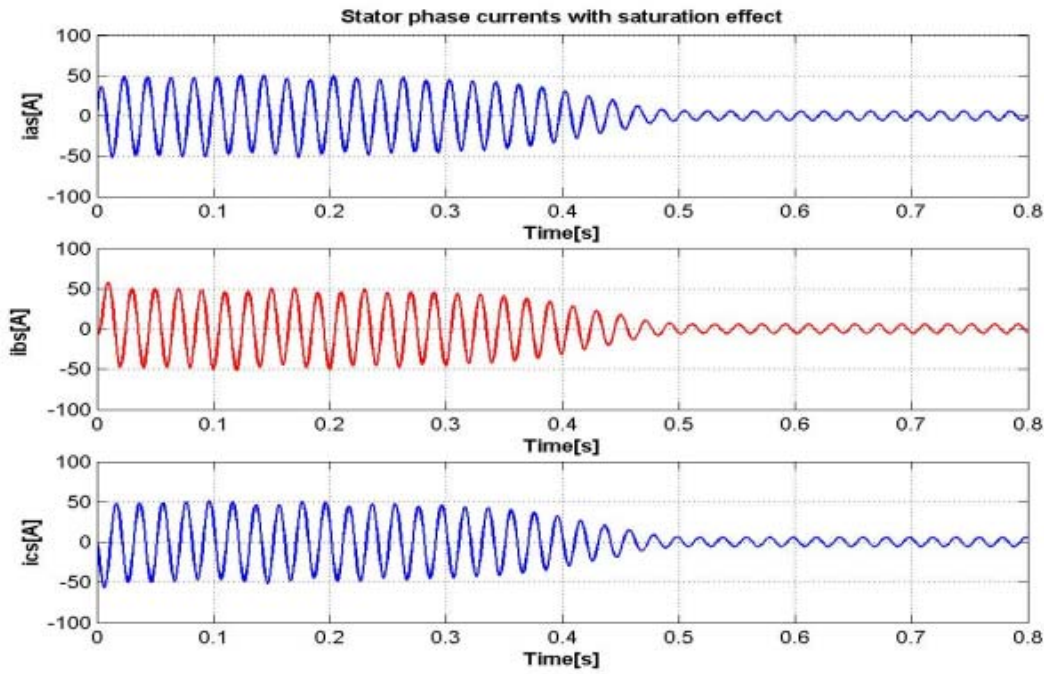


Figure 6.12c

**Figure 6.12d**

**Figure 6.12:** Transient state performances of conventional induction machine model with saturation effect.

### 6.8 Models simulation results comparison.

In order to visualise the effects of skin and /or saturation effects on the steady and transient states performances of induction machine, the results of the simulation involving skin-effect and saturation effect models have to be compared graphically with that from the conventional model. By so doing, figure 6.13 for the steady-state model and figure 6.14 for the transient state model result.

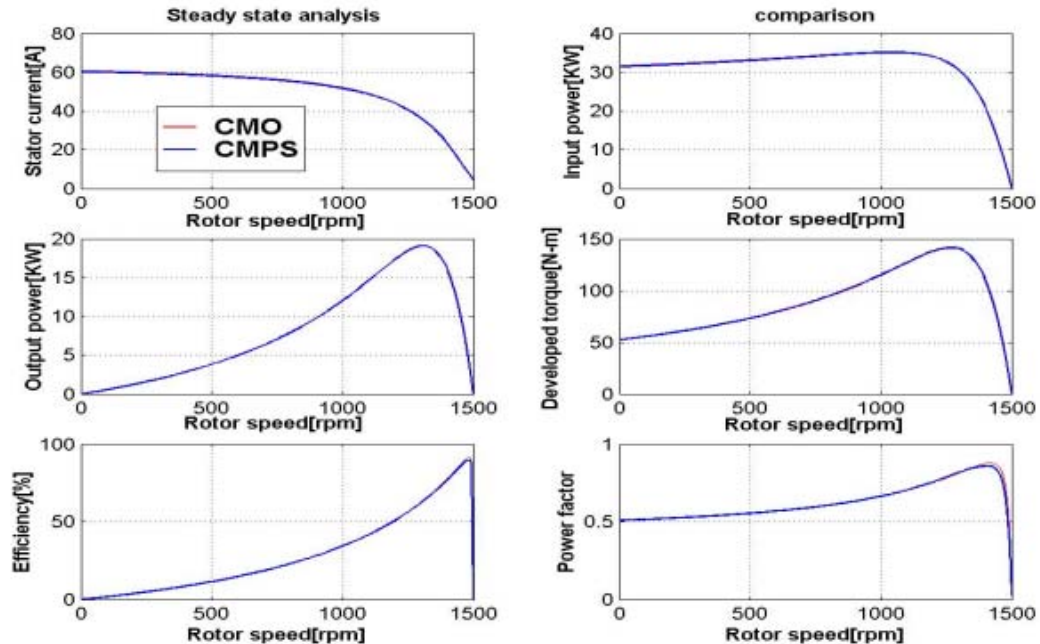


**Figure 6.13a**(Conventional model only(CMO),Conventional model plus saturation(CMPS))

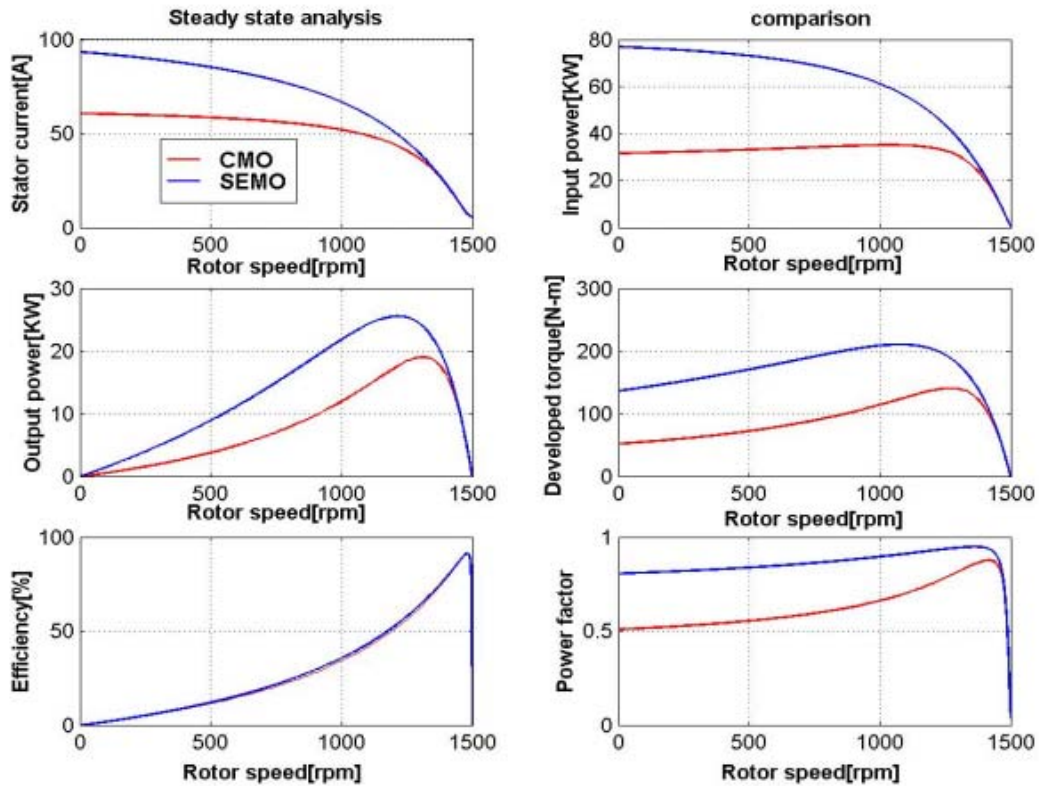


**Figure 6.13b**(Conventional model only(CMO),Skin-effect model only(SEMO))

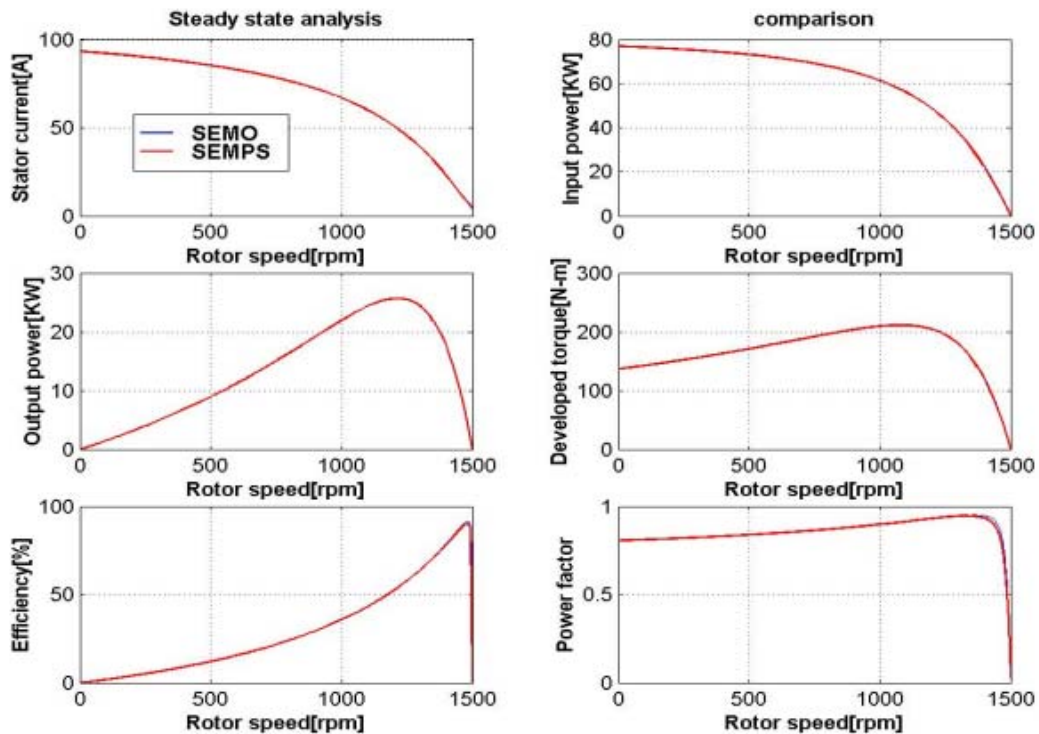


**Figure 6.13c**(Skin-effect model plus saturation(SEMPs),Skin-effect model only(SEMO))

**Figure 6.13:** Steady-state models comparisons.

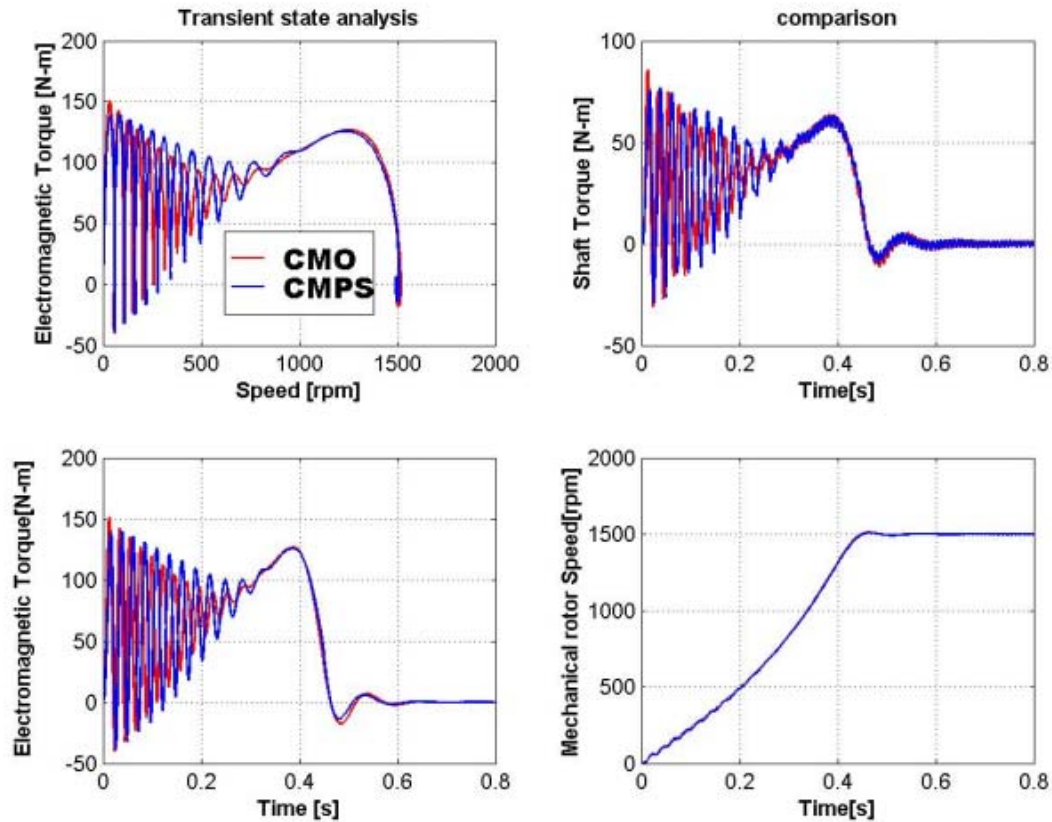


**Figure 6.14a**(Conventional model only(CMO),Conventional model plus saturation(CMPS))

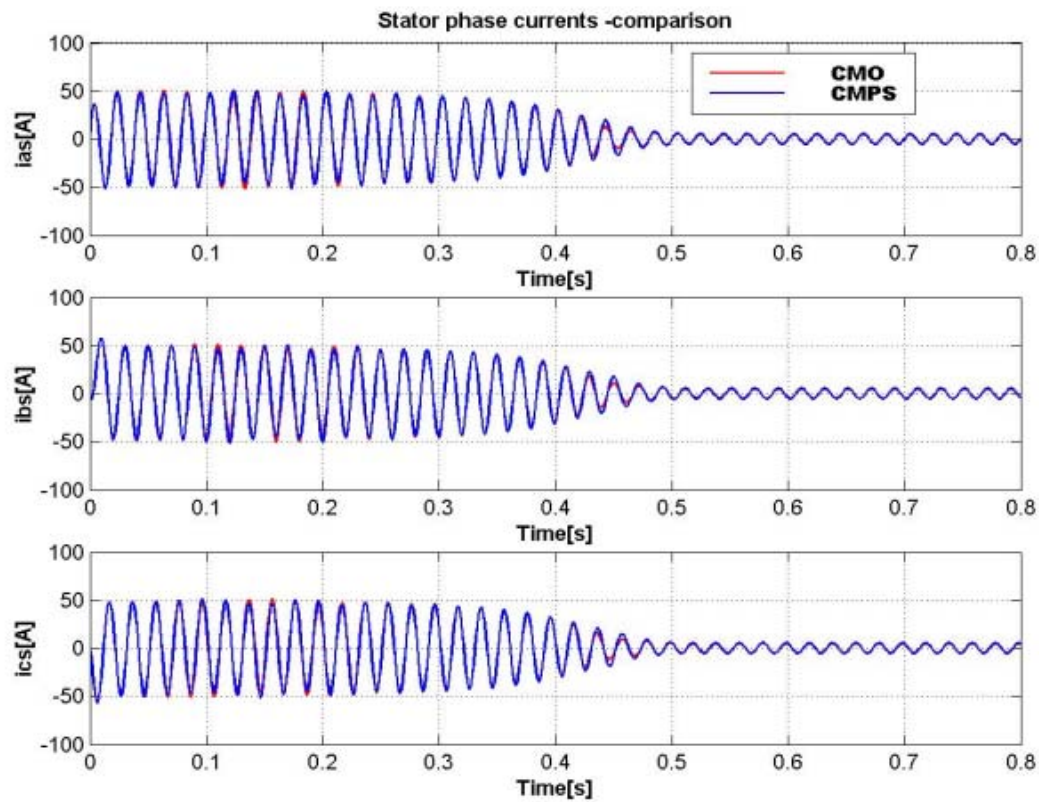


**Figure 6.14b**(Conventional model only(CMO),Conventional model plus saturation(CMPS))

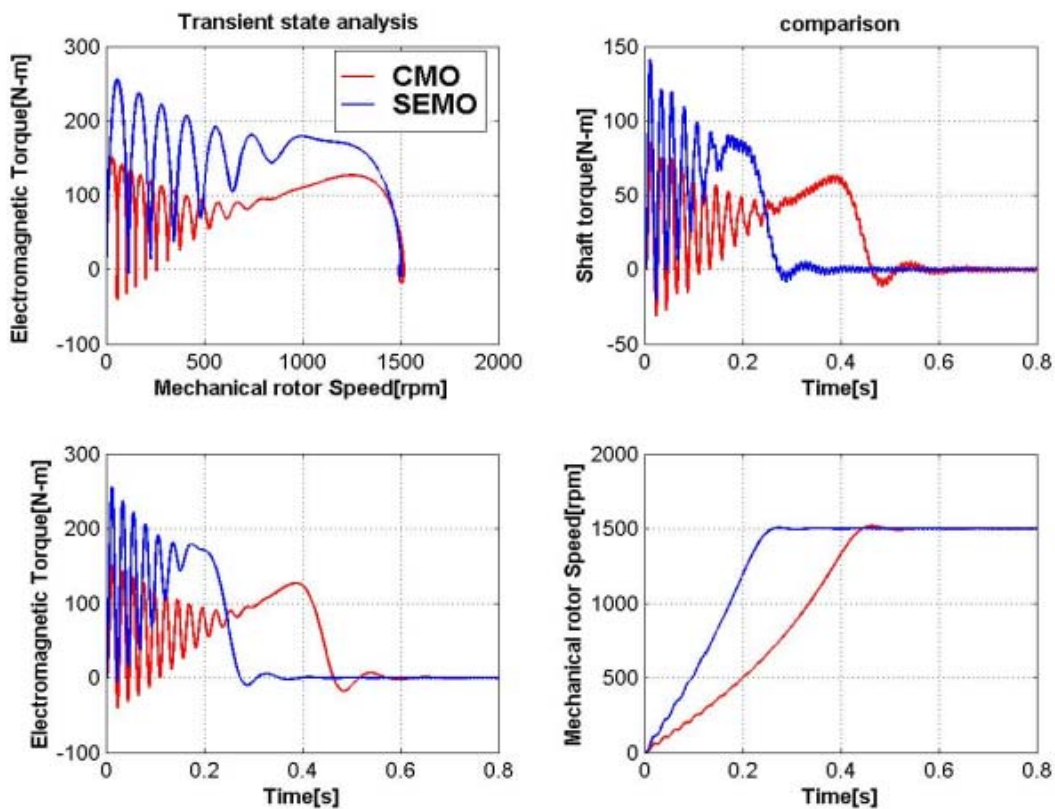


**Figure 6.14c**(Conventional model only(CMO),Skin-effect model only(SEMO))

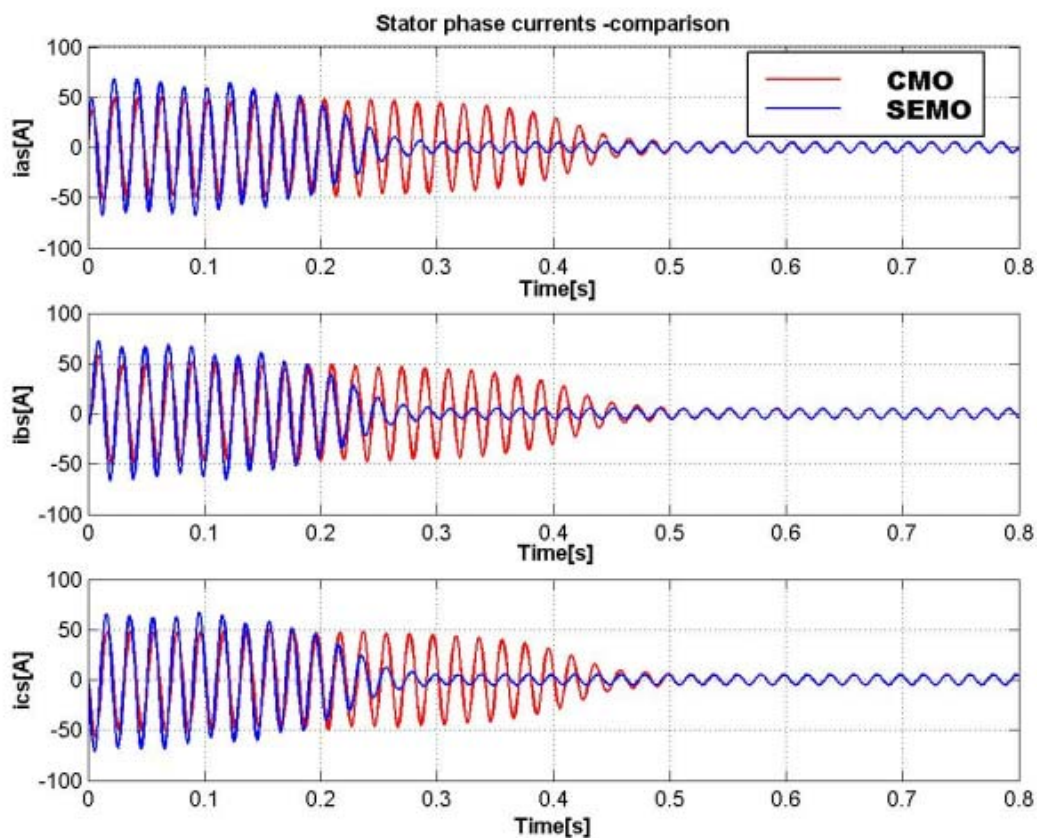


**Figure 6.14d**(Conventional model only(CMO),Skin-effect model only(SEMO))

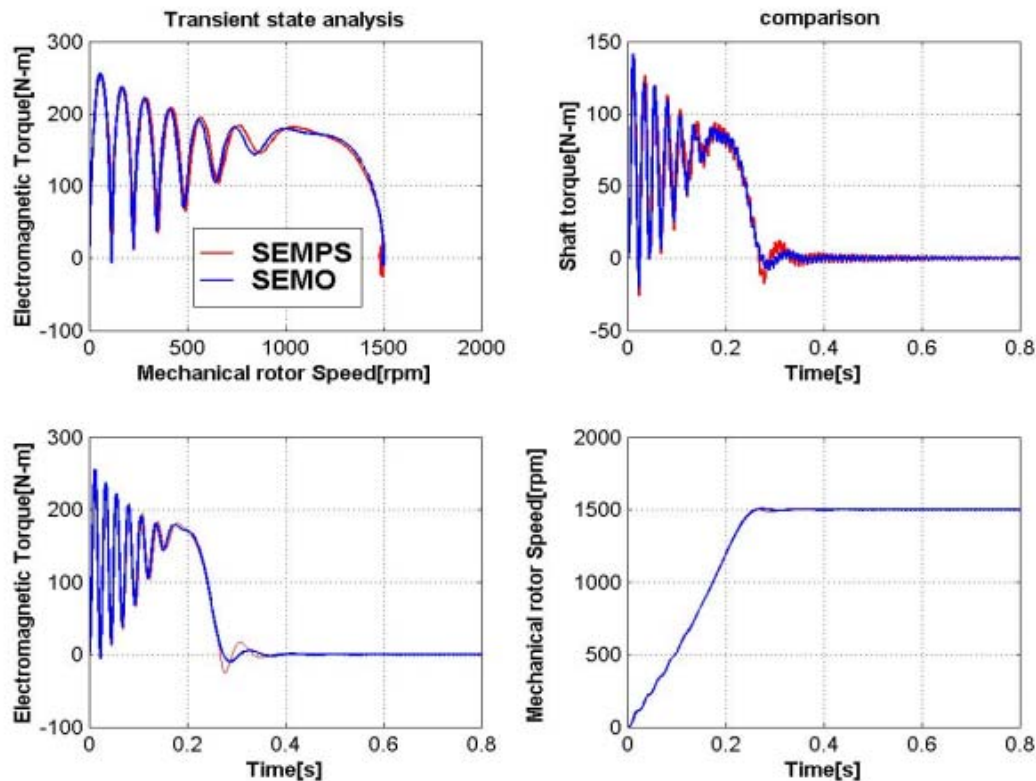


**Figure 6.14e**(Skin-effect model plus saturation(SEMPS),Skin-effect model only(SEMO))

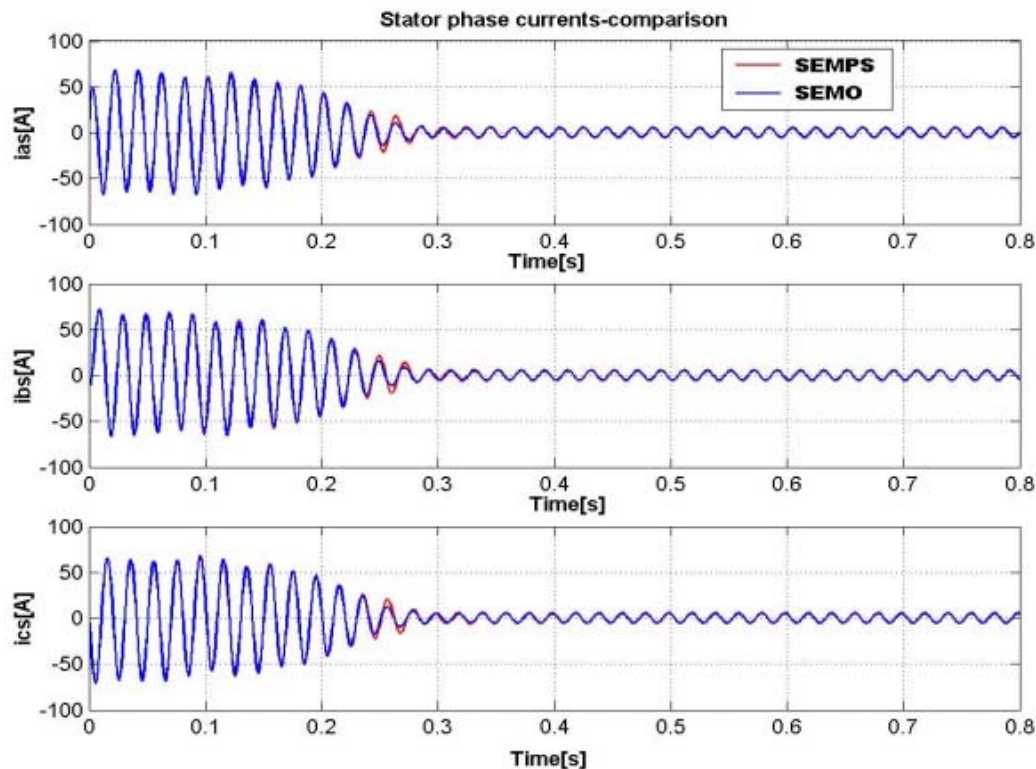


**Figure 6.14f**(Skin-effect model plus saturation(SEMPS),Skin-effect model only(SEMO))

**Figure 6.14:** Transient-state models comparisons.

## 7 Induction machine thermal modelling

### 7.1 Losses in induction machine

Consideration of losses in induction machine is important not only in the determination of the machine's efficiency but also in the heating of the machine and hence the rating or the obtainable power output without undue deterioration of the insulation. Losses in induction machines can be broadly classified into: Stator losses, Rotor losses and Rotational losses.

#### 7.1.1 Losses calculations

##### Ohmic Losses

Ohmic losses are load losses emanating from currents flowing through the stator and rotor windings. These losses are dependent approximately on the square of the load current. The ohmic losses of the stator and rotor are given mathematically by

$$P_{cu1} = 3R_s I_s^2 \quad (7.1)$$

$$P_{cu2} = 3R_r I_r^2 \quad (7.2)$$

Where,

$R_s$  = Stator resistance

$I_s$  = Stator current per phase

$R_r$  = Rotor resistance

$I_r$  = Rotor current per phase

The stator and rotor resistances are dependent on the motor temperature. Therefore, the measured resistance at room temperature( $\theta_0$ ) must be corrected to a specified temperature( $\theta$ ). The correction for the resistance change with temperature can be made by

$$R = R_{20} \frac{K + \theta}{K + \theta_0} \quad (7.3)$$

Where  $R$  is the corrected resistance at  $\theta$ , and  $K$  is equal to 245 for Aluminum and 235 for Copper.

##### Iron Losses

The iron losses consist of the eddy current losses and hysteresis losses. Iron Losses are dependent on the machine's flux which in turn is almost proportional to voltage. Iron losses in a Squirrel-cage machine can be broadly divided into three:

- Iron losses in the machine yoke,  $P_{Fe1Y}$
- Iron losses in the stator teeth,  $P_{Fe1T}$
- Iron losses in the rotor,  $P_{Fe2R}$

The hysteresis losses, according to Steinmetz law are proportional to frequency and to  $B_{max}^{(1.5-2.5)}$  depending on magnetic saturation. The eddy current losses are proportional to the square of the frequency and also to the square of the maximum value of flux density. The empirical form of these losses is given by Klamt[58] as:

$$P_H = \sigma_H \frac{f}{100} B^2 m \quad (7.4)$$

$$P_E = \sigma_E \left( \Delta_{Fe} \frac{f}{100} B \right)^2 m \quad (7.5)$$

$$P_{Fe} = P_H + P_E = \left[ \sigma_H \frac{100}{f} + \sigma_E \Delta_{Fe}^2 \right] \left( \frac{f}{100} \right)^2 B^2 m \quad (7.6)$$

where,

$\sigma_H$  =Hysteresis loss Coefficient

$\sigma_E$  =Eddy-current loss Coefficient

$\Delta_{Fe}$  =the thickness of the lamination sheet

m = mass

f = frequency

B = magnetic flux density

The total iron losses,  $P_{FeT}$  becomes,

$$P_{FeT} = P_{Fe1Y} + P_{Fe1T} + P_{Fe2R} \quad (7.7)$$

$$P_{FeT} = \underbrace{P_{FeHY} + P_{FeEY}}_{P_{Fe1Y}} + \underbrace{P_{FeHT} + P_{FeET}}_{P_{Fe1T}} + \underbrace{P_{FeHR} + P_{FeER}}_{P_{Fe2R}} \quad (7.8)$$

The parameters  $\sigma_H$ ,  $\sigma_E$  and m in equations(7.4-7.5) are material dependent and can be eliminated by normalizing the equations and expressing the iron losses as factors dependent only on magnetic flux and frequency.

$$\frac{P_H}{P_{NH}} = \frac{\sigma_H \frac{f}{100} B^2 m}{\sigma_H \frac{f_N}{100} B^2 N m} = \frac{f}{f_N} \left( \frac{\psi}{\psi_N} \right)^2 \quad (7.9)$$

$$\frac{P_E}{P_{NE}} = \frac{\sigma_E \left( \Delta_{Fe} \frac{f}{100} B \right)^2 m}{\sigma_E \left( \Delta_{Fe} \frac{f_N}{100} B_N \right)^2 m} = \left( \frac{f}{f_N} \right)^2 \left( \frac{\psi}{\psi_N} \right)^2 \quad (7.10)$$

where,

$$\frac{B}{B_N} = \frac{A_{eff}\psi}{A_{eff}\psi_N} = \frac{\psi}{\psi_N} \quad (7.11)$$

$\psi$  = magnetic flux

$\psi_N$  = rated magnetic flux

$A_{eff}$  = effective Area

$f_N$  = rated frequency

The magnetic flux in the stator and rotor can be expressed respectively as,

$$\psi_1 = \sqrt{\psi_{1d}^2 + \psi_{1q}^2} \quad (7.12)$$

$$\psi_2 = \sqrt{\psi_{2d}^2 + \psi_{2q}^2} \quad (7.13)$$

Application of equations(7.9-7.10) requires that the machine's rated stator and rotor frequency as well as the rated iron losses in equation(7.8) be determined. The determination of these rated losses of the machine can be achieved by subdividing the total rated iron losses in the manner reported by [82]:

1. A factor  $K_S$  is used to distribute the total iron losses between the stator and the rotor.

$$P_{Fe1} = K_S P_{FeT} \quad (7.14a)$$

$$P_{Fe2R} = P_{Fe2} = (1 - K_S) P_{FeT} \quad (7.14b)$$

2. The stator iron losses are further distributed between the teeth and the yoke with a factor  $K_T$ .

$$P_{Fe1Y} = K_T P_{Fe1} \quad (7.15a)$$

$$P_{Fe1T} = (1 - K_T) P_{Fe1} \quad (7.15b)$$

3. The calculated losses in (1) and (2) can now be shared between hysteresis and Eddy-current losses using the three constant factors,  $H_Y$ ,  $H_T$  and  $H_R$ .

$$P_{FeH1Y} = H_Y P_{Fe1Y} \quad (7.16a)$$

$$P_{FeE1Y} = (1 - H_Y) P_{Fe1Y} \quad (7.16b)$$

$$P_{FeH1T} = H_T P_{Fe1T} \quad (7.16c)$$

$$P_{FeE1T} = (1 - H_T) P_{Fe1T} \quad (7.16d)$$

$$P_{FeH2R} = H_R P_{Fe2R} \quad (7.16e)$$

$$P_{FeE2R} = (1 - H_R) P_{Fe2R} \quad (7.16f)$$

The rotor frequency is expressed as

$$f_2 = f_s = f_1 - f \quad (7.17)$$

By substituting equations (7.14), (7.15) and (7.16) into equations(7.9) and (7.10), the below equations result.

$$P_{FeH1Y} = H_Y K_T K_S P_{NFeT} \frac{f_1}{f_{1N}} \left( \frac{\psi_1}{\psi_{1N}} \right)^2 \quad (7.18a)$$

$$P_{FeE1Y} = (1 - H_Y) K_T K_S P_{NFeT} \left( \frac{f_1}{f_{1N}} \right)^2 \left( \frac{\psi_1}{\psi_{1N}} \right)^2 \quad (7.18b)$$

$$P_{FeH1T} = H_T (1 - H_T) K_S P_{NFeT} \frac{f_1}{f_{1N}} \left( \frac{\psi_1}{\psi_{1N}} \right)^2 \quad (7.18c)$$

$$P_{FeE1T} = (1 - H_T) (1 - K_T) K_S P_{NFeT} \left( \frac{f_1}{f_{1N}} \right)^2 \left( \frac{\psi_1}{\psi_{1N}} \right)^2 \quad (7.18d)$$

$$P_{FeH2R} = H_R (1 - K_S) P_{NFeT} \left( \frac{f_2}{f_{2N}} \right) \left( \frac{\psi_2}{\psi_{2N}} \right)^2 \quad (7.18e)$$

$$P_{FeE2R} = (1 - H_R) (1 - K_S) P_{NFeT} \left( \frac{f_2}{f_{2N}} \right)^2 \left( \frac{\psi^2}{\psi_{2N}} \right)^2 \quad (7.18f)$$

The loss distribution factors  $K_S$ ,  $K_T$ ,  $H_Y$ ,  $H_T$  and  $H_R$  differ for different machines depending on construction and the material used and can be gotten from the manufacturer's data or from experiment. For the test machine, these factors lie between 0.3 to 0.99.

### **Mechanical Losses**

The mechanical losses often referred as friction and windage losses consist of brush and bearing friction, windage, and the power required to circulate the air through the induction machine and ventilating system, if one is available. The total mechanical losses can be determined by carrying out the no-load test on the machine. By plotting the input power against the square of the phase voltage and then extrapolating to zero voltage, the intersection on the input power axis gives the total friction and windage losses. Figure 2.2 shows the total friction and windage losses of the test squirrel-cage induction motor conducted in this manner. However, the friction and windage losses have been noted to have very negligible effect on heating the machine.

### **Additional losses**

Additional losses in induction machines can be treated as stray losses. These losses are due to the non-uniform current distribution in the copper and the additional core losses produced in the iron by distortion of the magnetic flux by the load current. The stray load losses consist of the following components—especially when the motor is operated at high frequency[60]:

- Surface losses in the stator
- Surface losses in the rotor
- Pulsation losses in the stator teeth
- Pulsation losses in the rotor teeth
- Losses in the squirrel-cage winding
- Losses due to skewing with uninsulated cast aluminum squirrel-cage windings.

The additional losses are difficult to determine accurately. However, a considerable volume of work has been done and published on this subject and the causes of the losses and their determination are well established[61,62,63,84]. In this work, the stray load losses, which represent about 1.8% of the machine rated power as reported by [88], are taken into consideration and added to the rotor losses. The test machine power losses at No-load, rated load and blocked rotor operations at 50Hz were calculated by program based on finite-element analysis(FEA) of electromagnetic fields[87]. The distributions of these losses are presented in figure 7.1a, figure 7.1b and figure 7.1c for the various operating conditions.

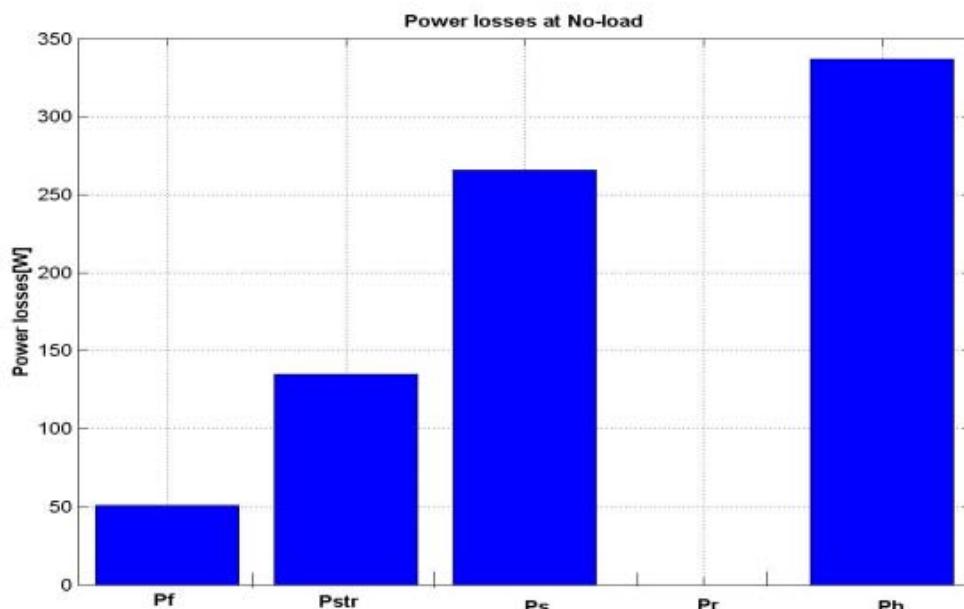


**Figure 7.1a:** Power losses of the 7.5KW motor at No-load.

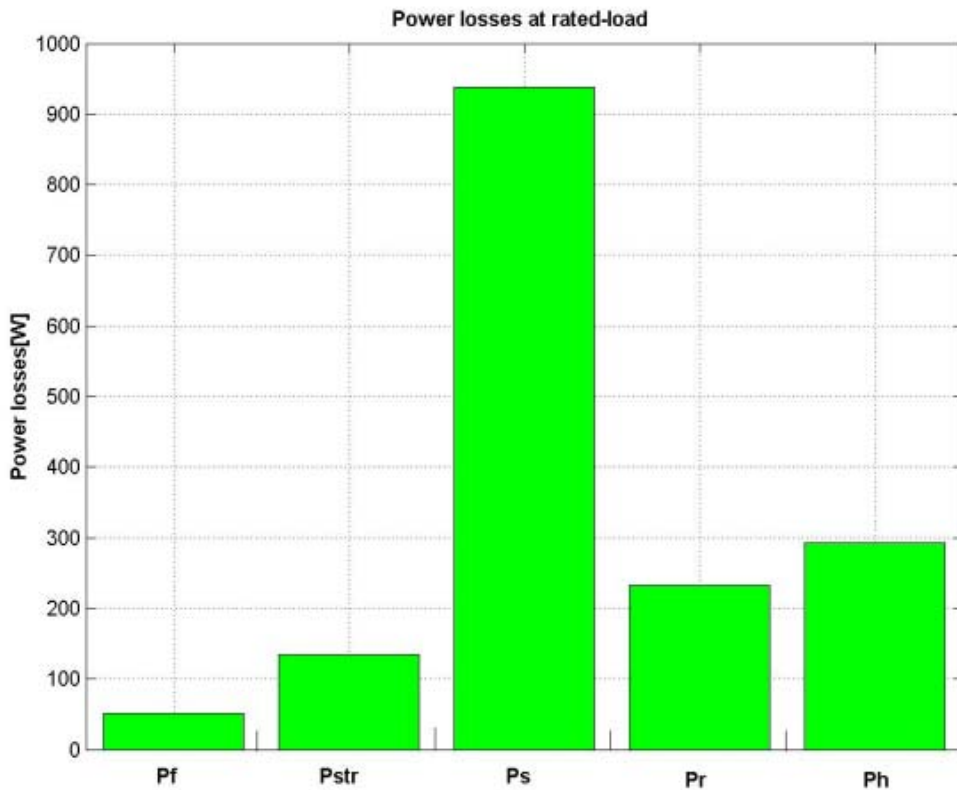


**Figure 7.1b:** Power losses of the 7.5KW motor at rated load.

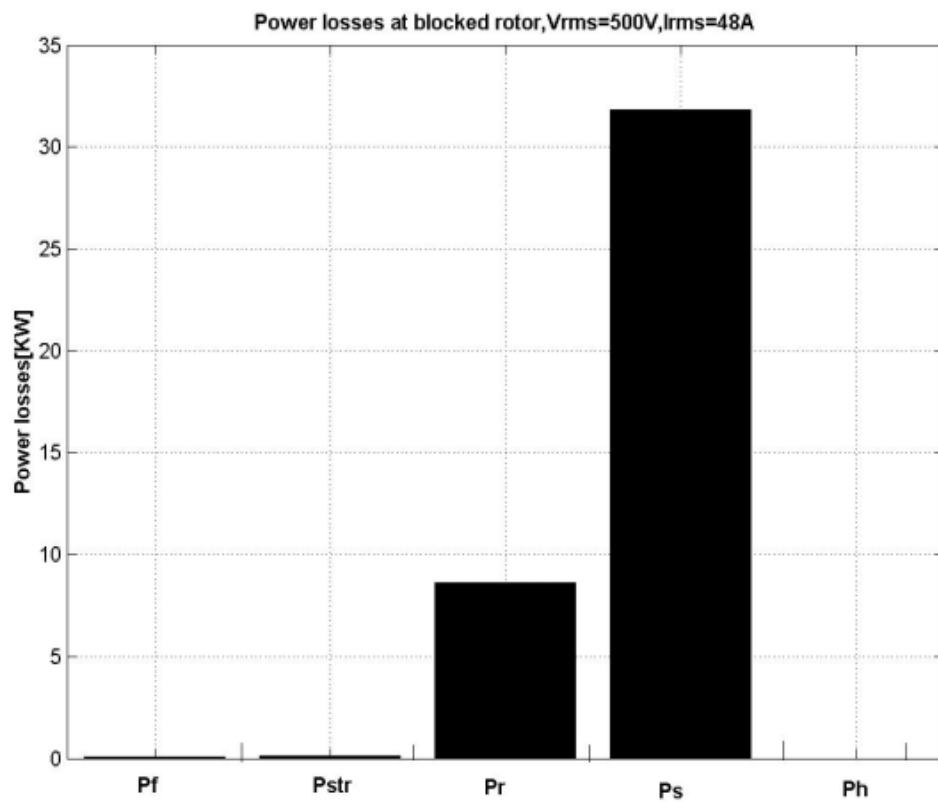


**Figure 7.1c:** Power losses of the 7.5KW motor at blocked rotor.

Where,

$P_f$  = friction and windage losses  
 $P_{str}$  = stray losses  
 $P_s$  = stator winding losses  
 $P_r$  = rotor winding losses  
 $P_h$  = iron core losses

## 7.2 Heat transfer theory

In order to calculate the thermal resistances of a thermal network, a background knowledge of heat transfer is appropriate. Three modes of heat transfer are considered for the calculation of the thermal resistances: Conduction, Convection and Radiation.

### Conduction

The general equation governing heat conduction in rectangular coordinate system(x,y,z) is given by[64]:

$$\frac{1}{\alpha} \frac{\partial \theta}{\partial t} = \frac{\partial^2 \theta}{\partial x^2} + \frac{\partial^2 \theta}{\partial y^2} + \frac{\partial^2 \theta}{\partial z^2} + \frac{1}{K} Q \quad (7.19)$$

and

$$\alpha = \frac{K}{\rho c_p} \quad (7.20)$$

Where,

$c_p$  = Specific heat of material,[J/(Kg.°C)]  
 $Q$  = heat generation rate, [W/m<sup>3</sup>]  
 $\rho$  = density of material,[kg/m<sup>3</sup>]  
 $K$  = thermal conductivity, [W/(m.°C)]  
 $\theta$  = temperature, [°C]

For one-dimensional analysis, which is applied in this work, the general expression for the conductive heat transfer is given by Fourier's law as:

$$q = -K \frac{\partial \theta}{\partial x} \quad (7.21)$$

where,

$q$ = heat flux, [W/m<sup>2</sup>]  
 $x$ = distance,[m]

Therefore, the thermal resistance between two points becomes,

$$R_{th} = \frac{x_2 - x_1}{kA} \quad (7.22)$$

Where A is the cross-sectional area,[m<sup>2</sup>].

Thermal conductivity of most solid bodies varies very little with temperature. Pertinently, for a one-dimensional analysis, thermal resistance of a solid body can be taken to be constant. Table 7.1 shows the values of thermal conductivities of some materials used in the test machine.

Material	Part	K[W/m.K]
Al-Si 20	Frame	161
Steel(0.5 % C)	Shaft	54
Aluminum	Rotor cage	240
Carbon Steel(1.5 % C)	Stator core and Rotor core	36
Copper	Stator winding	386
Unsaturated polyester	Stator winding impregnation and slot insulation	0.2
Air at 300K	Airgap, Ambient air	0.02624

**Table 7.1:** Thermal conductivities of the machine parts.

### Convection

Heat transfer as a result of convection is described by

$$q = h_c (\theta_w - \theta_f) \quad (7.23)$$

Where,

$\theta_w$  = the temperature of the surface

$\theta_f$  = the temperature at a distant point from the surface

The coefficient of heat transfer,  $h_c$  is dependent on:

- the nature of flow(laminar or turbulent)
- the body geometry
- the average temperature and physical characteristics of the fluid
- the nature of the heat transfer (natural or forced)

These dependencies can be expressed as a function of dimensionless numbers:

$$h_c = f(Nu, Pr, Gr, Re) \quad (7.24)$$

The first term in equation(7.24) is the Nusselt number and is related to heat transfer coefficient by

$$Nu = \frac{h_c x}{k_f} \quad (7.25)$$

Where x is a characteristic length and  $k_f$  is the thermal conductivity of the fluid. The second term in equation (7.24) is the Prandtl number expressed as,

$$Pr = \frac{C_f \mu}{k_f} \quad (7.26)$$

Where,

$c_f$  = fluid specific heat,[J/Kg°C]

$\mu$  = fluid dynamic viscosity, [kg/ms]

The third variable in equation (7.24) is the Grashof number which expresses the ratio of buoyancy to viscous forces:

$$G_r = \frac{g\beta(\theta_w - \theta_f)x^3}{v^2} \quad (7.27)$$

Where,

$v$  = kinematic viscosity, [m<sup>2</sup>/s]

$g$  = acceleration due to gravity,[9.81m/s<sup>2</sup> ]

$\beta$  = thermal expansion coefficient, [1/°C]

The last variable in equation(7.24) is the Reynolds number,Re given by

$$R_e = \frac{\rho U_f x}{\mu} \quad (7.28)$$

Where,

$\rho$ =fluid density,[kg/m<sup>3</sup>]

$U_f$ =fluid velocity,[m/s]

In free convection, the fluid motion is sustained by the buoyancy forces while in forced convection the motion is maintained by external means such as fan, pump or rotating element. The ratio of the Grashof number to the square of the Reynolds number gives an important factor that distinguishes the mode of convection mechanism in a given medium.

That is,

$$K_{gr} = \frac{G_r}{R_e^2} \quad (7.29)$$

if  $K_{gr} \gg 1$ , free convection dominates

if  $K_{gr} \ll 1$ , forced convection dominates

However, in electrical machines forced convection dominates. For air-cooled electrical machines, the empirical formula for the heat-transfer coefficient given by[59] is in order.

$$h_{c-free} = 6.5 + 0.05(\theta_w - \theta_f) \quad (7.30)$$

Equation(7.30) is used to estimate the heat transfer from the machine frame to ambient air for the test machine. The thermal resistance due to convection is estimated by

$$R_{th} = \frac{1}{h_c A} \quad (7.31)$$

### Radiation

The net heat transfer by radiation between two real bodies is derived from the Stefan-Boltzmann's law and given by[64] as,

$$q_r = A_1 \varepsilon_1 \delta (\theta_w^4 - \theta_f^4) \quad (7.32)$$

where,

$A_1$  = area of surface one

$\varepsilon_1$ =emissivity of surface one,  $[0 \leq \varepsilon \leq 1]$ . For Iron,  $\varepsilon = 0.96$  and for Aluminum,  $\varepsilon = 0.08$ .

$\delta$  = Stefan-Boltzmann constant,  $[5.6697 \times 10^{-8} \text{ W}/(\text{m}^2 \cdot \text{K}^4)]$

The thermal resistance to the surroundings due to radiation is given by

$$R_{th} = \frac{\theta_w - \theta_f}{A_1 \varepsilon_1 \delta (\theta_w^4 - \theta_f^4)} \quad (7.33)$$

The heat transfer mechanism in the 7.5KW Squirrel-cage induction machine is shown in figure 7.2.

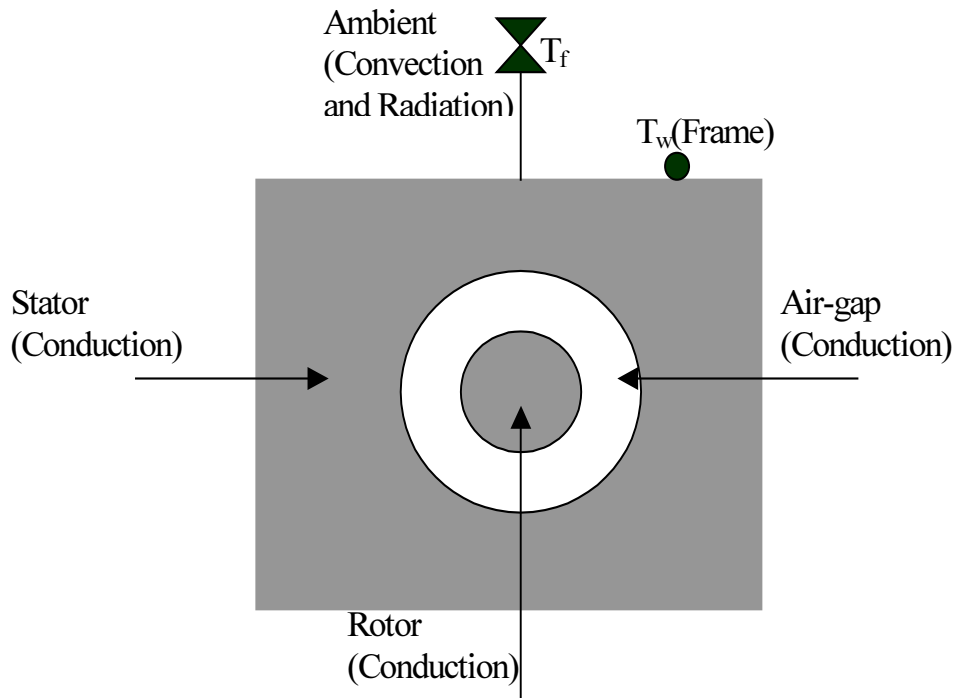


**Figure 7.2:** SCIM heat transfer mechanism.

### 7.3 Thermal network model theory

In a thermal network model, it is assumed that all the heat generation in the component is concentrated in one point—usually referred as the node. A node connotes the mean temperature of the component. In a thermal network model as shown in figure 7.3, each node is assigned a thermal capacitance,  $C_{th}$  and heat flowing between nodes and represented as current source,  $P_G$  is passed through thermal resistance,  $R_{th}$ .

Thermal network models as applicable to electrical machines range from one dimensional to three dimensional. However, a two dimensional or three dimensional thermal network models

can be developed by connecting several one-dimensional models together in the point of the mean temperature. A detailed analysis on this principle is given by Mellor[39].

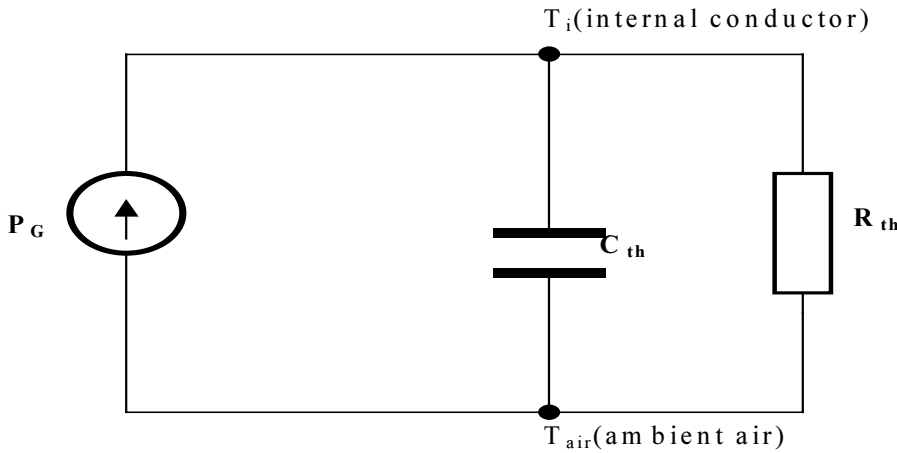


**Figure 7.3:** Thermal network model.

For small induction machines, the machine elements are represented by the temperature rise with the ambient air temperature taken as a thermal reference. The heat generation,  $P_G$  as in electrical machines represents the losses in the machine parts(e.g Stator, Rotor,etc). The thermal capacitance,  $C_{th}$  of an element is usually calculated from the geometry and material data of the element. It is expressed as,

$$C_{th} = \rho C_p V \quad (7.34)$$

Where,

$V$ =volume of the element

$\rho$  = material density

$C_p$  = specific heat capacity of the material

Thermal network model offers both steady and transient states solutions for the temperature difference between the element and the ambient air temperature. The general transient equation for a thermal network with  $n$  nodes and each linked to the others through thermal resistances,  $R_{ij}$  is expressed thus:

$$C_i \frac{d\theta_i}{dt} = P_i - \sum_{j=1}^n \frac{\theta_i - \theta_j}{R_{ij}} \quad (7.35)$$

Where,

$i = 1, \dots, n$

$C_i$  = node thermal capacitance

$\theta_i$  = node temperature rise

$R_{ij}$  = thermal resistance between adjoining nodes  $i,j$

$P_i$  = heat generation at node  $i$

In matrix form, equation(7.35) can be expressed as,

$$\frac{d\theta_t}{dt} = [\mathbf{C}_t]^{-1}[\mathbf{P}_t] - [\mathbf{C}_t]^{-1}[\mathbf{G}_t]\boldsymbol{\theta}_t \quad (7.36)$$

Where the thermal capacitance matrix ( $\mathbf{C}_t$ ), the loss matrix ( $\mathbf{P}_t$ ), the temperature rise matrix ( $\boldsymbol{\theta}_t$ ) and the conductance matrix ( $\mathbf{G}_t$ ) are defined as,

$$[\mathbf{C}_t] = \begin{bmatrix} C_1 & 0 & 0 & - & - & - & 0 \\ 0 & C_2 & 0 & - & - & - & 0 \\ 0 & 0 & C_3 & - & - & - & 0 \\ - & - & - & - & - & - & - \\ - & - & - & - & - & - & - \\ - & - & - & - & - & - & - \\ 0 & 0 & 0 & 0 & 0 & 0 & C_n \end{bmatrix} \quad (7.37)$$

$$[\mathbf{P}_t] = \begin{bmatrix} P_1 \\ P_2 \\ P_3 \\ - \\ - \\ - \\ P_n \end{bmatrix} \quad (7.38)$$

$$[\boldsymbol{\theta}_t] = \begin{bmatrix} \theta_1 \\ \theta_2 \\ \theta_3 \\ - \\ - \\ - \\ \theta_n \end{bmatrix} \quad (7.39)$$

$$[\mathbf{G}_t] = \begin{bmatrix} \sum_{i=1}^n G_{1,i} & -G_{1,2} & -G_{1,3} & - & - & - & -G_{1,n} \\ -G_{2,1} & \sum_{i=1}^n G_{2,i} & -G_{2,3} & - & - & - & -G_{2,n} \\ -G_{3,1} & -G_{3,2} & \sum_{i=1}^n G_{3,i} & - & - & - & -G_{3,n} \\ - & - & - & - & - & - & - \\ - & - & - & - & - & - & - \\ - & - & - & - & - & - & - \\ -G_{n,1} & -G_{n,2} & -G_{n,3} & - & - & - & \sum_{i=1}^n G_{n,i} \end{bmatrix} \quad (7.40)$$

In equation (7.40),

$$G_{1,i} = \frac{1}{R_{1,i}} \text{, etc} \quad (7.41)$$

Also due to symmetry,

$G_{1,2} = G_{2,1}$  and

$G_{1,3} = G_{3,1}$  etc.

Under steady-state conditions, the thermal capacitance can be considered at full

capacity  $\left[ \frac{d\theta_i}{dt} = 0 \right]$ , and therefore disappears from the transient state equation. By so doing, equation (7.42) results,

$$P_i = \sum_{j=1}^n \frac{\theta_i - \theta_j}{R_{i,j}} \quad i = 1 \dots n \quad (7.42)$$

In matrix form, equation (7.42) becomes,

$$[\mathbf{P}_t] = [\mathbf{G}_t] [\boldsymbol{\theta}_t] \quad (7.43)$$

and

$$[\boldsymbol{\theta}_t] = [\mathbf{G}_t]^{-1} [\mathbf{P}_t] \quad (7.44)$$

#### 7.4 Developed thermal model for the test machine

The thermal network model for the squirrel-cage induction machine is developed according to the principles reported by Kessler[43]. Figure 7.4 shows the typical construction of a Squirrel-Cage induction machine. In developing the thermal network model, the machine geometry is divided into basic elements and each element being identified by a node in the thermal network with its corresponding thermal capacitance and heat source. The choice of subdividing a machine into elementary components remains a compromise between the simplicity of the model and the accuracy required of the results[65]. It has been shown by Kylander[40] that high level of accuracy could be achieved by modest subdivision of the induction machines geometrical parts. The developed thermal network model is shown in figure 7.5. The model consists of 11 nodes and 15 thermal resistances. In the model, the stator of the machine has networks for the stator iron, stator winding and the end windings. It is assumed that the heat transfer from the rotor winding through the air-gap goes directly to the stator winding with negligible impact on the stator teeth. The rotor part of the machine is divided into the rotor iron, rotor winding and the end rings. By connecting the networks for the rotor, stator and frame together, the thermal network model for the machine is realised. In the model, the electromagnetic losses are given as input values. These losses are as shown in section 7.1. The values of the thermal resistances and capacitances were calculated with the equations presented in section 7.2 and the values presented in the appendix.

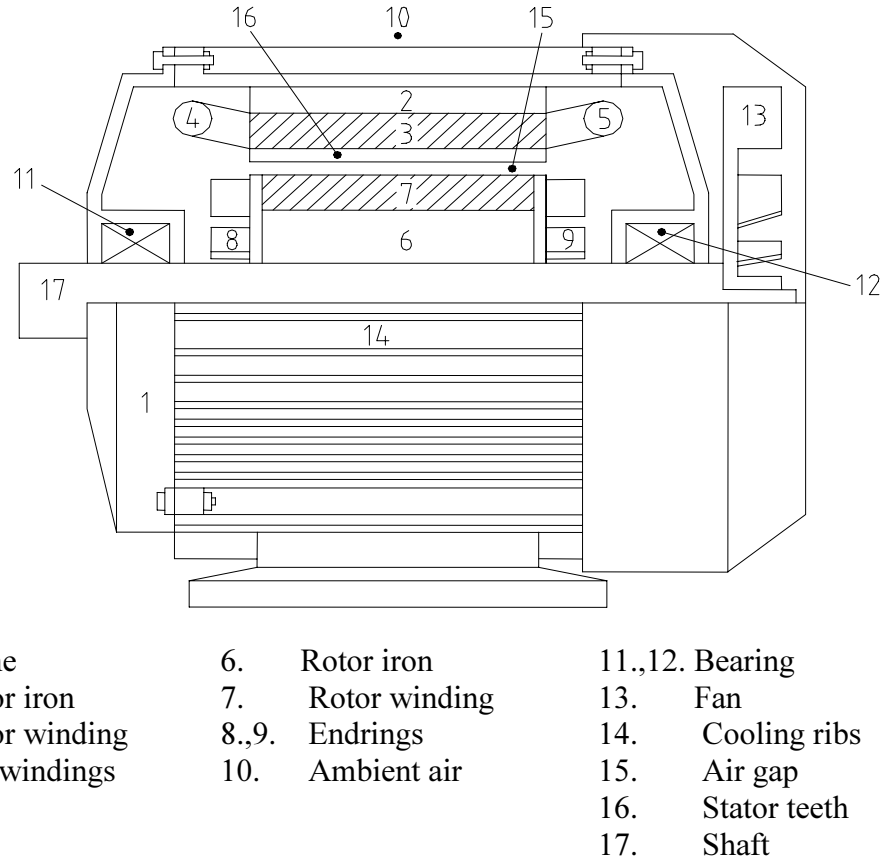


**Figure 7.4:** Typical Construction of Squirrel-Cage Induction Machine.

## 7.5 Mathematical representation of the proposed thermal model.

The system of algebraic and differential equations which describes the thermal behaviour of the developed thermal network model under steady and transient conditions respectively are presented.

### 7.5.1 Transient state thermal model equations

The transient thermal network equation presented in section 7.3 is used to develop the transient state thermal model equations for the induction machine thermal model of figure 7.5. The equations taken node by node give:

$$P_1 = C_1 \frac{d\theta_1}{dt} + \frac{1}{R_{1b}} (\theta_1 - \theta_{kb}) + \frac{1}{R_{12}} (\theta_1 - \theta_2) \quad (7.45a)$$

$$P_2 = C_2 \frac{d\theta_2}{dt} + \frac{1}{R_{12}} (\theta_2 - \theta_1) + \frac{1}{R_{23}} (\theta_2 - \theta_3) + \frac{1}{R_{26}} (\theta_2 - \theta_6) \quad (7.45b)$$

$$P_3 = C_3 \frac{d\theta_3}{dt} + \frac{1}{R_{23}} (\theta_3 - \theta_2) + \frac{1}{R_{35}} (\theta_3 - \theta_5) + \frac{1}{R_{34}} (\theta_3 - \theta_4) \quad (7.45c)$$

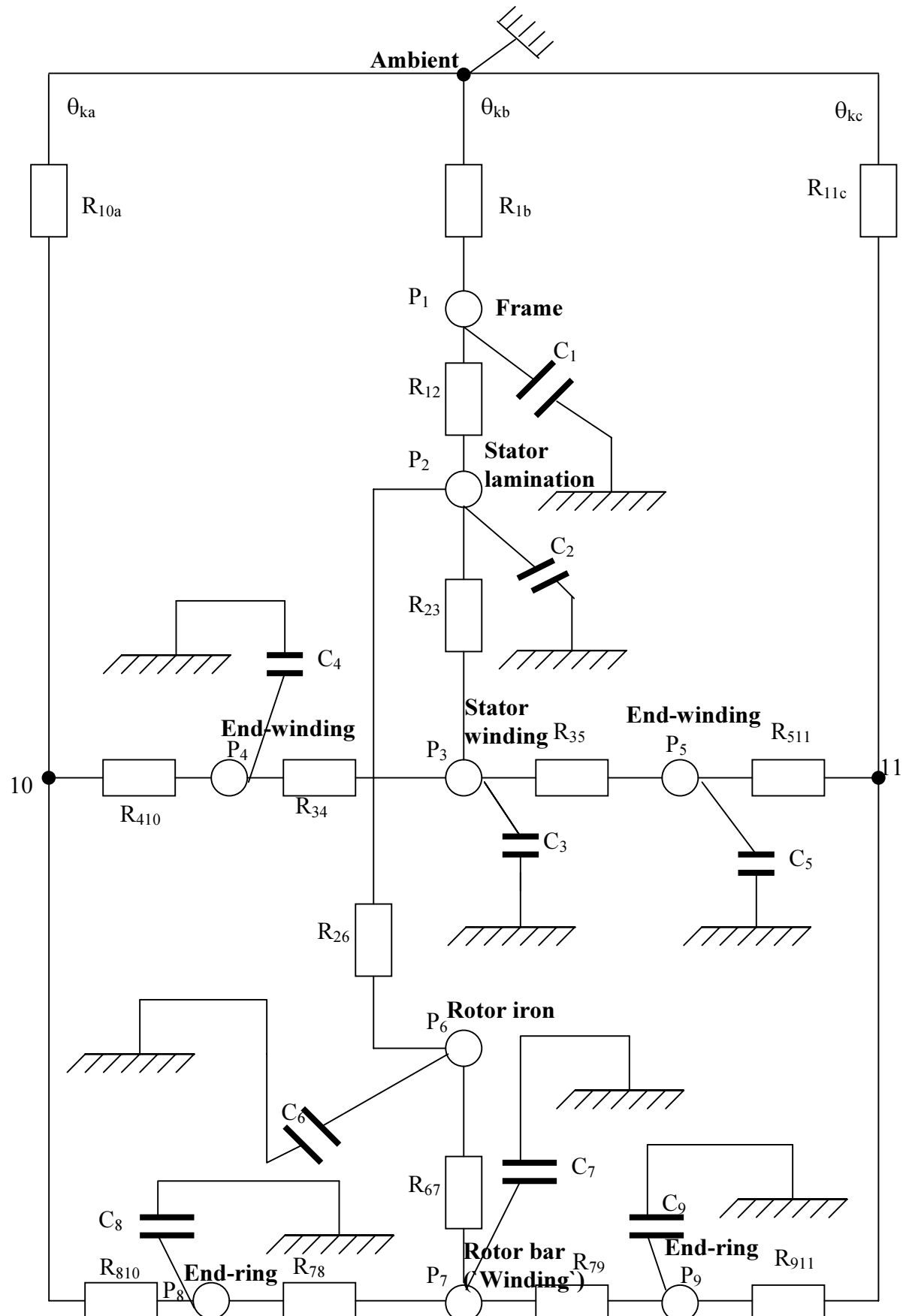


Figure 7.5: Thermal network model representation for the 7.5kW induction machine

$$P_4 = C_4 \frac{d\theta_4}{dt} + \frac{1}{R_{34}}(\theta_4 - \theta_3) + \frac{1}{R_{410}}(\theta_4 - \theta_{10}) \quad (7.45\text{d})$$

$$P_5 = C_5 \frac{d\theta_5}{dt} + \frac{1}{R_{511}}(\theta_5 - \theta_{11}) + \frac{1}{R_{35}}(\theta_5 - \theta_3) \quad (7.45\text{e})$$

$$P_6 = C_6 \frac{d\theta_6}{dt} + \frac{1}{R_{26}}(\theta_6 - \theta_2) + \frac{1}{R_{67}}(\theta_6 - \theta_7) \quad (7.45\text{f})$$

$$P_7 = C_7 \frac{d\theta_7}{dt} + \frac{1}{R_{79}}(\theta_7 - \theta_9) + \frac{1}{R_{78}}(\theta_7 - \theta_8) + \frac{1}{R_{67}}(\theta_7 - \theta_6) \quad (7.45\text{g})$$

$$P_8 = C_8 \frac{d\theta_8}{dt} + \frac{1}{R_{78}}(\theta_8 - \theta_7) + \frac{1}{R_{810}}(\theta_8 - \theta_{10}) \quad (7.45\text{h})$$

$$P_9 = C_9 \frac{d\theta_9}{dt} + \frac{1}{R_{911}}(\theta_9 - \theta_{11}) + \frac{1}{R_{79}}(\theta_9 - \theta_7) \quad (7.45\text{i})$$

$$P_{10} = C_{10} \frac{d\theta_{10}}{dt} + \frac{1}{R_{410}}(\theta_{10} - \theta_4) + \frac{1}{R_{810}}(\theta_{10} - \theta_8) + \frac{1}{R_{10a}}(\theta_{10} - \theta_{ka}) \quad (7.45\text{j})$$

$$P_{11} = C_{11} \frac{d\theta_{11}}{dt} + \frac{1}{R_{511}}(\theta_{11} - \theta_5) + \frac{1}{R_{911}}(\theta_{11} - \theta_9) + \frac{1}{R_{11c}}(\theta_{11} - \theta_{kc}) \quad (7.45\text{k})$$

Re-arranging equations(7.45a-k) in a form amenable to computer simulation, we have

$$\frac{d\theta_1}{dt} = \frac{1}{C_1} \left( P_1 - \frac{1}{R_{1b}}(\theta_1 - \theta_{kb}) - \frac{1}{R_{12}}(\theta_1 - \theta_2) \right) \quad (7.46\text{a})$$

$$\frac{d\theta_2}{dt} = \frac{1}{C_2} \left( P_2 - \frac{1}{R_{12}}(\theta_2 - \theta_1) - \frac{1}{R_{23}}(\theta_2 - \theta_3) - \frac{1}{R_{26}}(\theta_2 - \theta_6) \right) \quad (7.46\text{b})$$

$$\frac{d\theta_3}{dt} = \frac{1}{C_3} \left( P_3 - \frac{1}{R_{23}}(\theta_3 - \theta_2) - \frac{1}{R_{35}}(\theta_3 - \theta_5) - \frac{1}{R_{34}}(\theta_3 - \theta_4) \right) \quad (7.46\text{c})$$

$$\frac{d\theta_4}{dt} = \frac{1}{C_4} \left( P_4 - \frac{1}{R_{34}}(\theta_4 - \theta_3) - \frac{1}{R_{410}}(\theta_4 - \theta_{10}) \right) \quad (7.46\text{d})$$

$$\frac{d\theta_5}{dt} = \frac{1}{C_5} \left( P_5 - \frac{1}{R_{511}}(\theta_5 - \theta_{11}) - \frac{1}{R_{35}}(\theta_5 - \theta_3) \right) \quad (7.46\text{e})$$

$$\frac{d\theta_6}{dt} = \frac{1}{C_6} \left( P_6 - \frac{1}{R_{26}}(\theta_6 - \theta_2) - \frac{1}{R_{67}}(\theta_6 - \theta_7) \right) \quad (7.46f)$$

$$\frac{d\theta_7}{dt} = \frac{1}{C_7} \left( P_7 - \frac{1}{R_{79}}(\theta_7 - \theta_9) - \frac{1}{R_{78}}(\theta_7 - \theta_8) - \frac{1}{R_{67}}(\theta_7 - \theta_6) \right) \quad (7.46g)$$

$$\frac{d\theta_8}{dt} = \frac{1}{C_8} \left( P_8 - \frac{1}{R_{78}}(\theta_8 - \theta_7) - \frac{1}{R_{810}}(\theta_8 - \theta_{10}) \right) \quad (7.46h)$$

$$\frac{d\theta_9}{dt} = \frac{1}{C_9} \left( P_9 - \frac{1}{R_{911}}(\theta_9 - \theta_{11}) - \frac{1}{R_{79}}(\theta_9 - \theta_7) \right) \quad (7.46i)$$

$$\frac{d\theta_{10}}{dt} = \frac{1}{C_{10}} \left( P_{10} - \frac{1}{R_{410}}(\theta_{10} - \theta_4) - \frac{1}{R_{810}}(\theta_{10} - \theta_8) - \frac{1}{R_{10a}}(\theta_{10} - \theta_{ka}) \right) \quad (7.46j)$$

$$\frac{d\theta_{11}}{dt} = \frac{1}{C_{11}} \left( P_{11} - \frac{1}{R_{511}}(\theta_{11} - \theta_5) - \frac{1}{R_{911}}(\theta_{11} - \theta_9) - \frac{1}{R_{11c}}(\theta_{11} - \theta_{kc}) \right) \quad (7.46k)$$

In matrix form, equations(7.46a-7.46k) become,

$$\begin{bmatrix} \dot{\theta}_1 \\ \dot{\theta}_2 \\ \dot{\theta}_3 \\ \dot{\theta}_4 \\ \dot{\theta}_5 \\ \dot{\theta}_6 \\ \dot{\theta}_7 \\ \dot{\theta}_8 \\ \dot{\theta}_9 \\ \dot{\theta}_{10} \\ \dot{\theta}_{11} \end{bmatrix} = \begin{bmatrix} C_1 & 0 & 0 & 0 & 0 & 0 & 0 & 0 & 0 & 0 & 0 \\ 0 & C_2 & 0 & 0 & 0 & 0 & 0 & 0 & 0 & 0 & 0 \\ 0 & 0 & C_3 & 0 & 0 & 0 & 0 & 0 & 0 & 0 & 0 \\ 0 & 0 & 0 & C_4 & 0 & 0 & 0 & 0 & 0 & 0 & 0 \\ 0 & 0 & 0 & 0 & C_5 & 0 & 0 & 0 & 0 & 0 & 0 \\ 0 & 0 & 0 & 0 & 0 & C_6 & 0 & 0 & 0 & 0 & 0 \\ 0 & 0 & 0 & 0 & 0 & 0 & C_7 & 0 & 0 & 0 & 0 \\ 0 & 0 & 0 & 0 & 0 & 0 & 0 & C_8 & 0 & 0 & 0 \\ 0 & 0 & 0 & 0 & 0 & 0 & 0 & 0 & C_9 & 0 & 0 \\ 0 & 0 & 0 & 0 & 0 & 0 & 0 & 0 & 0 & C_{10} & 0 \\ 0 & 0 & 0 & 0 & 0 & 0 & 0 & 0 & 0 & 0 & C_{11} \end{bmatrix}^{-1} \begin{bmatrix} P_1 + \theta_{kb} * G_{1b} \\ P_2 \\ P_3 \\ P_4 \\ P_5 \\ P_6 \\ P_7 \\ P_8 \\ P_9 \\ \theta_{ka} * G_{10a} \\ \theta_{kc} * G_{11c} \end{bmatrix} - [C_t]^{-1} *$$

$\uparrow C_t$

$\uparrow P_t$



Where,

$$G_{11} = G_{1b} + G_{12} \quad (7.49a)$$

$$G_{22} = G_{21} + G_{23} + G_{26} \quad (7.49b)$$

$$G_{33} = G_{32} + G_{35} + G_{34} \quad (7.49c)$$

$$G_{44} = G_{43} + G_{410} \quad (7.49d)$$

$$G_{55} = G_{53} + G_{511} \quad (7.49e)$$

$$G_{66} = G_{62} + G_{67} \quad (7.49f)$$

$$G_{77} = G_{78} + G_{79} + G_{76} \quad (7.49g)$$

$$G_{88} = G_{87} + G_{810} \quad (7.49h)$$

$$G_{99} = G_{97} + G_{911} \quad (7.49i)$$

$$G_{1010} = G_{104} + G_{10a} + G_{108} \quad (7.49j)$$

$$G_{1111} = G_{115} + G_{11c} + G_{119} \quad (7.49k)$$

## 7.6 Computer simulation and results

The developed thermal model gives rise to a set of algebraic and differential equations which describe the thermal behaviour of the machine under steady and transient conditions respectively. MATLAB m-files are developed for half of the machine in order to determine the average temperature rise in the various parts of the machine. This reduces the set of differential equations to eight. Temperature rise of the machine parts is computed from the state equations using Runge-Kutta numerical method[68,69]. By incorporating the ambient temperature, rotor iron, rotor winding, end ring, stator lamination, frame, stator winding and end winding temperatures under steady and transient conditions are then computed. Table 7.2 shows the computed and measured steady temperatures for the test machine at No-load, rated load and blocked rotor conditions. Figure 7.6, figure 7.7 and figure 7.8 show the simulated temperatures of the test machine under No-load, rated load and blocked rotor operations respectively.

Model component	Predicted temperature[°C] (Steady state)	Measured temperature[°C] (Steady state)
Frame	40.12	44.80
Stator lamination	47.60	-
Stator winding	51.72	50.13
End winding	52.91	51.81
Rotor iron	53.04	-
Rotor winding	53.17	-
End ring	53.75	52.1*

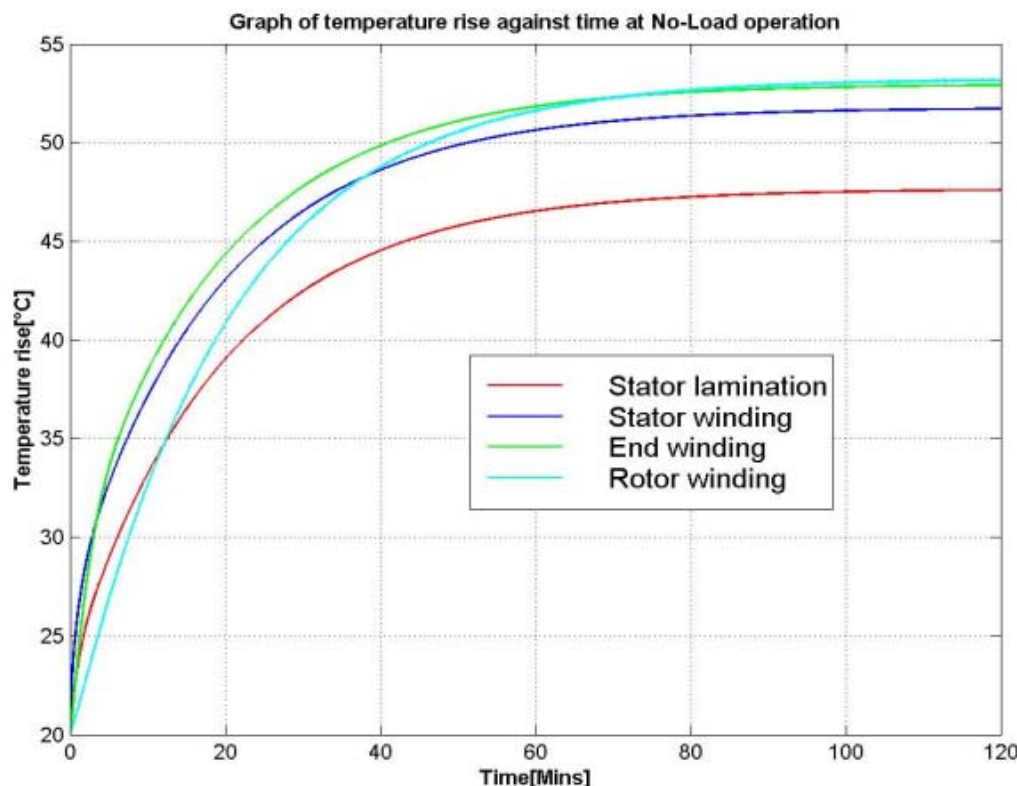
**Table 7.2a:** Measured and predicted steady state temperatures at No-load

Model component	Predicted temperature[°C] (Steady state)	Measured temperature[°C] (Steady state)
Frame	54.71	56.30
Stator lamination	67.60	-
Stator winding	82.96	82.13
End winding	91.26	85.93
Rotor iron	83.67	-
Rotor winding	84.12	-
End ring	88.30	84.5*

**Table 7.2b:** Measured and predicted steady state temperatures at rated load

Model component	Predicted temperature[°C] (Steady state)	Measured temperature[°C] (Steady state)
Frame	24.41	23.1*
Stator iron	37.08	42.25
End winding	88.78	88.43
Rotor iron	30.94	-
Rotor winding	32.86	46.30
End ring	84.45	95.35

\* measurement done with the infra-red instrument.

**Table 7.2c:** Measured and predicted steady state temperatures at blocked rotor**Figure 7.6a:** Predicted temperatures at No-load

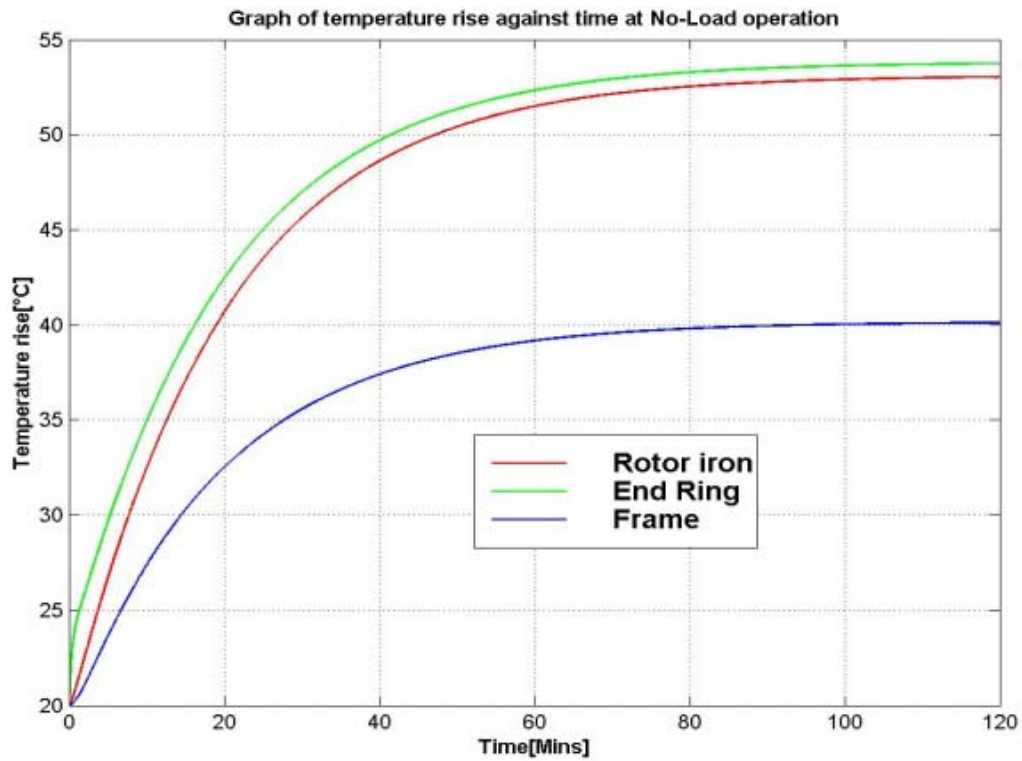


**Figure 7.6b:** Predicted temperatures at No-load

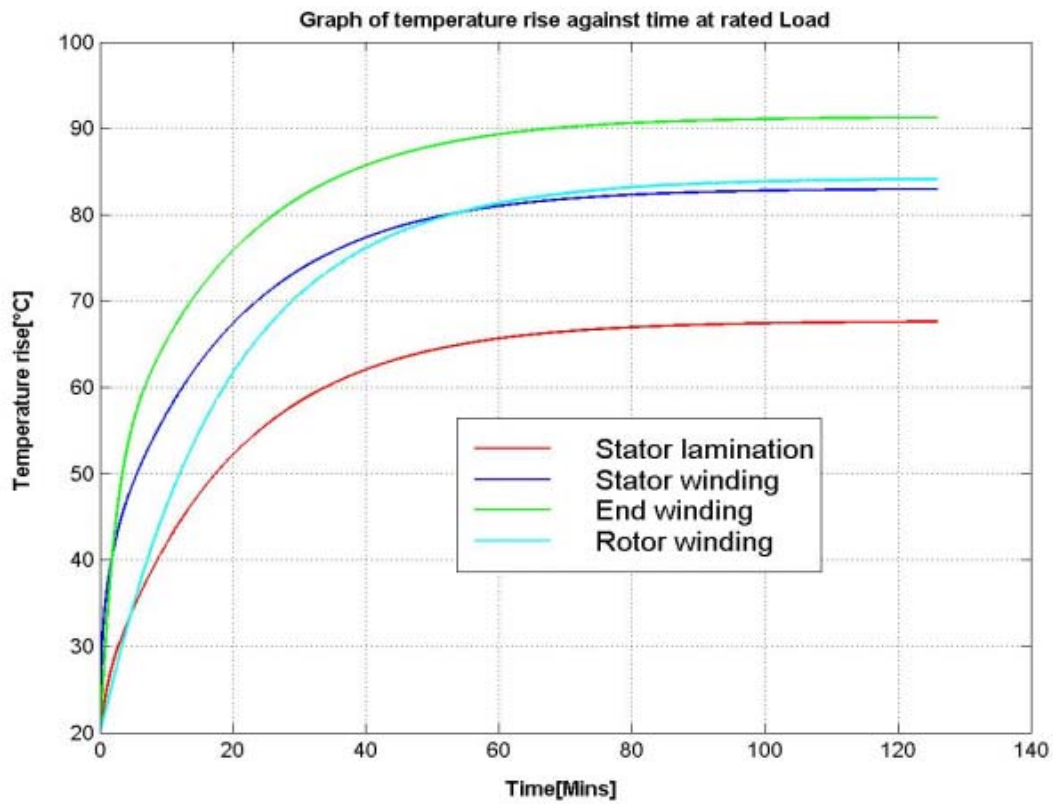


**Figure 7.7a:** Predicted temperatures at rated load

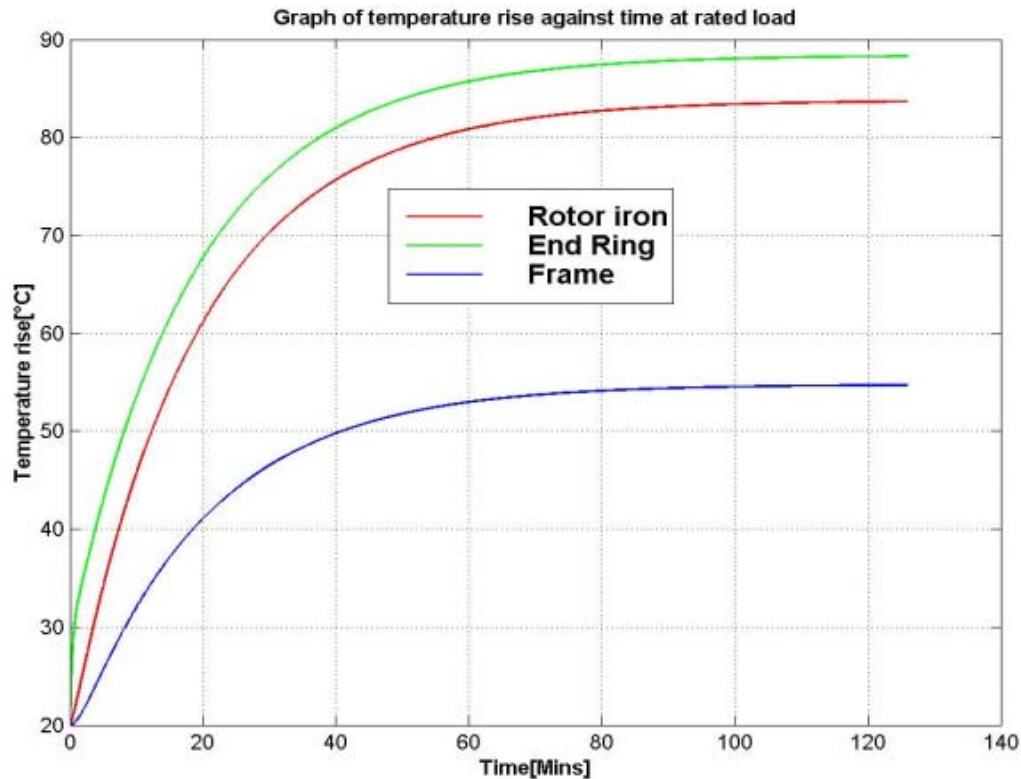


**Figure 7.7b:** Predicted temperatures at rated load

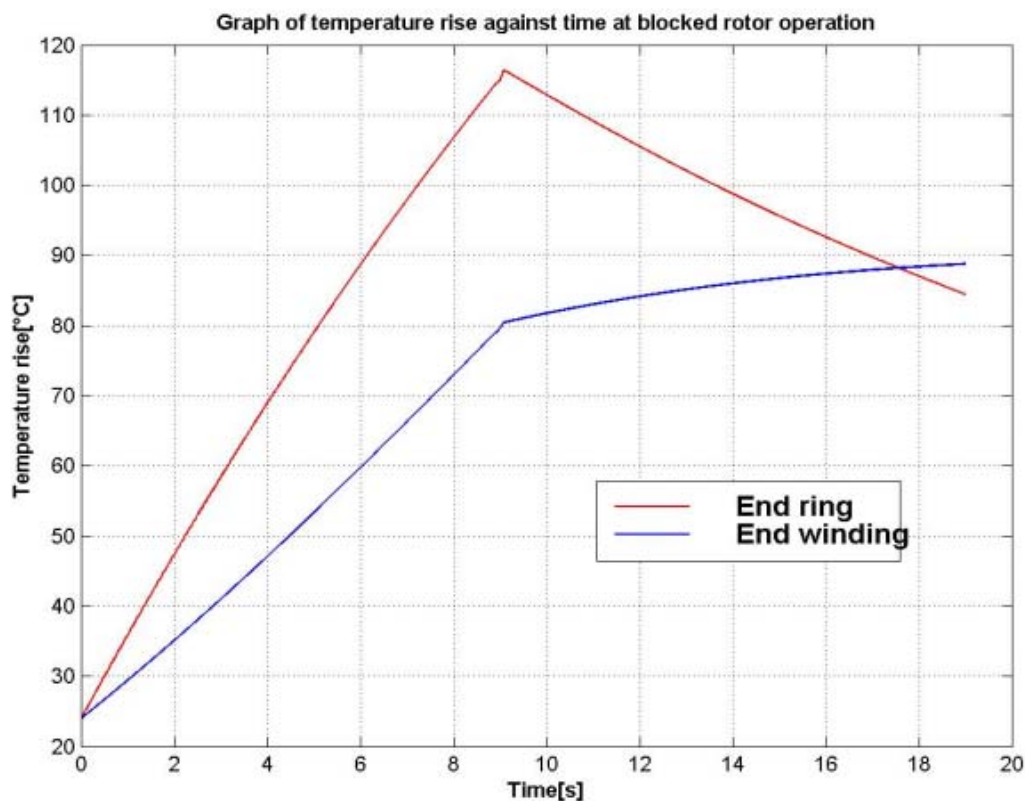


**Figure 7.8a:** Predicted temperatures at blocked rotor.

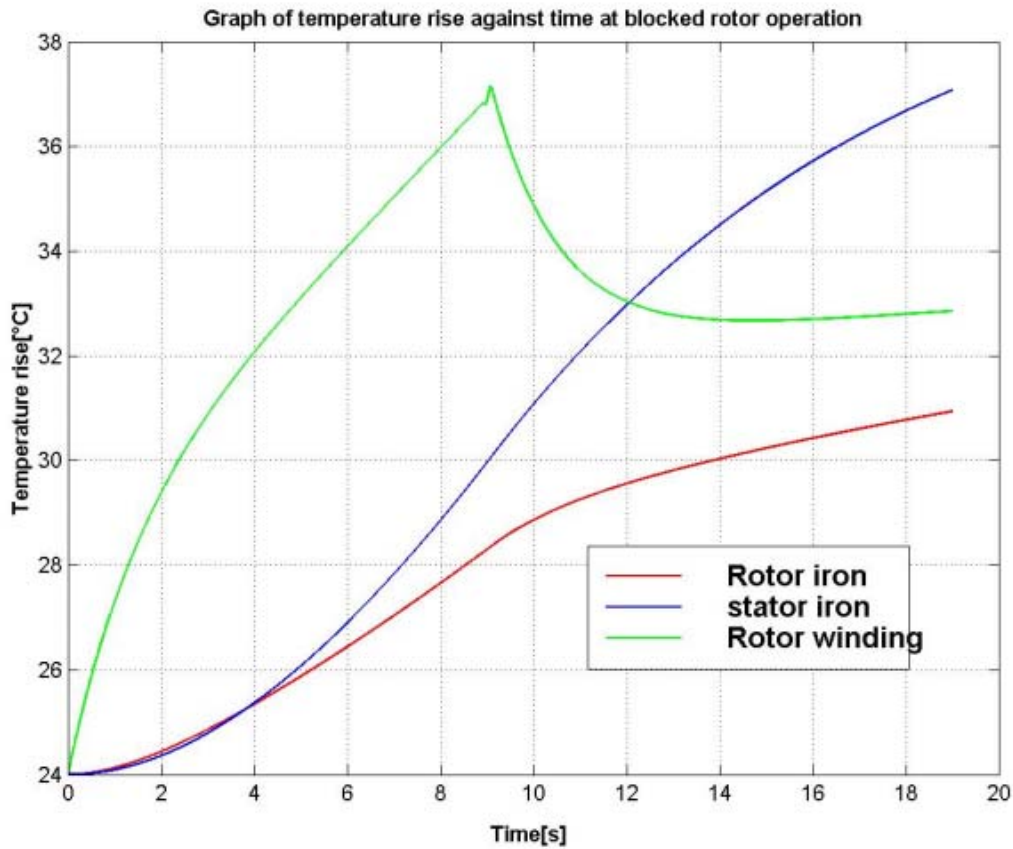


**Figure 7.8b:** Predicted temperatures at blocked rotor.

## 8 Measurements

### 8.1 Test Machine

The test machine is a **KATT VDE 0530**, Class F insulation, surfaced-cooled squirrel-cage induction motor. The rated power, speed, and current are 7.5KW, 1400rpm and 19.2A respectively. The test machine is a four-pole motor with 50Hz rated frequency and 340V rated voltage. Figure 8.1 shows the test machine.

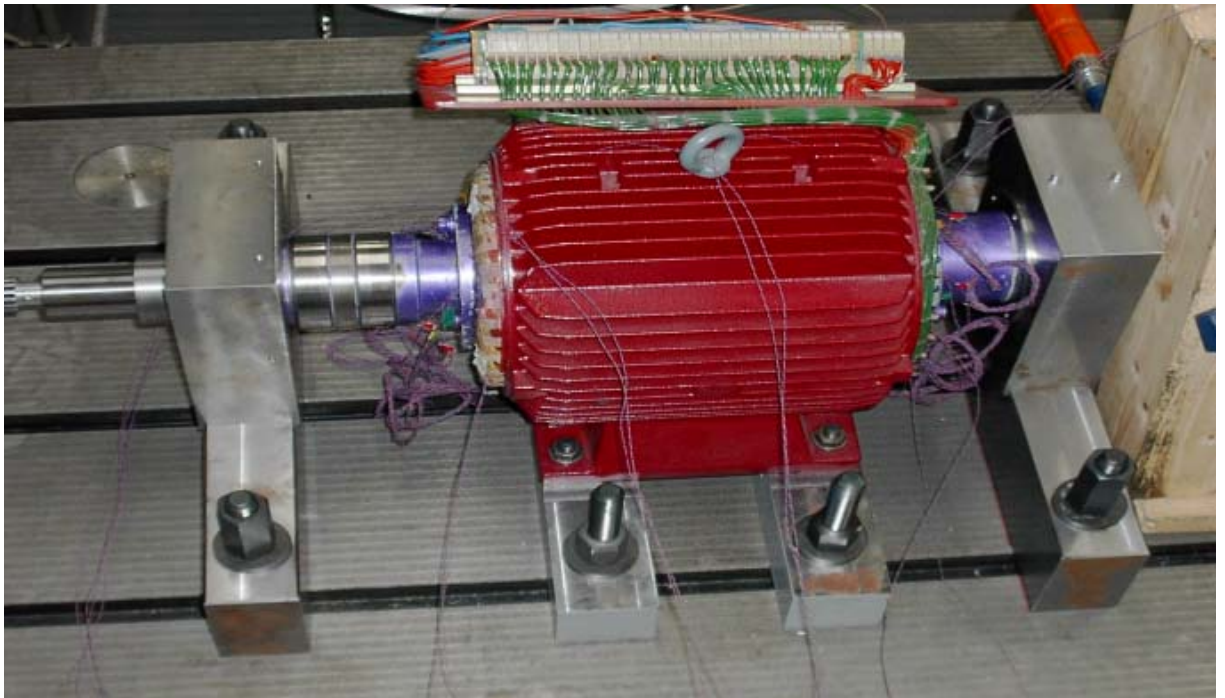


**Figure 8.1:** The 7.5kW test motor.

The slot geometries and the schematic diagram of the stator winding of the test motor are shown in figure 8.2 and figure 8.3 respectively. The parameters of the test machine's equivalent circuit together with the geometrical and winding data are given in table 2.1.

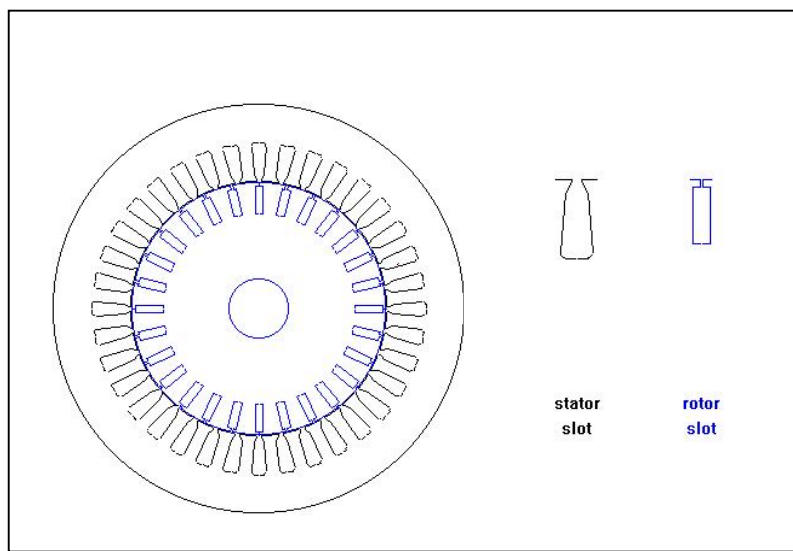


**Figure 8.2:** Slot geometry of the test machine.

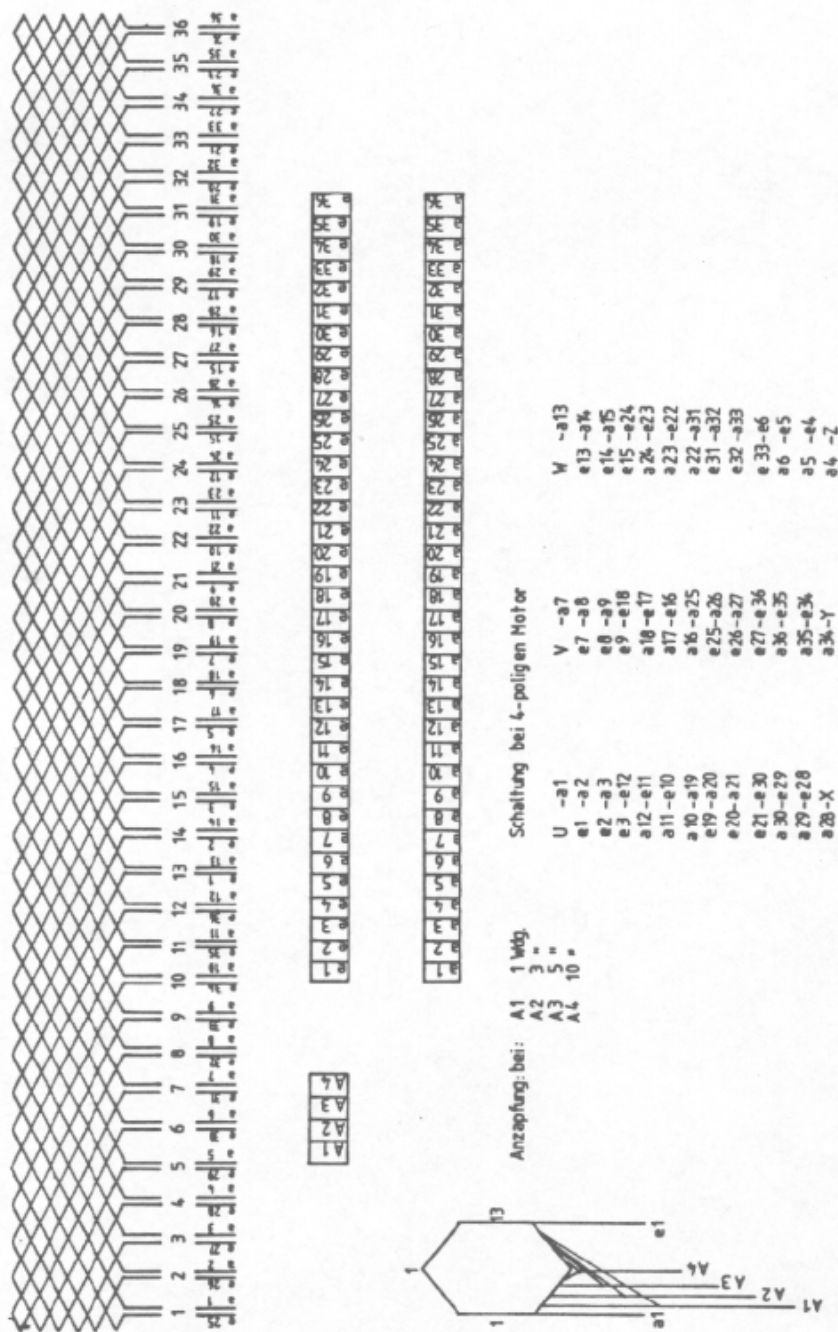


**Figure 8.3:** Schematic diagram of the stator winding of the test machine.

## 8.2 Measurement of electrical and mechanical quantities of the motor

Several experiments were carried out on the test machine. The No-load test was carried out at rated frequency and with balanced polyphase voltages applied to the stator terminals. Readings for current, voltage, electrical power and speed were taken after the motor has been running for a considerable long period of time necessary for the bearings to be properly lubricated. Locked-rotor test and test with the injection of D.C. current in the stator windings were made at standstill. The retardation test was carried out at No-load with and without additional standard mass. The load test was carried out with constant load and frequency at a sinusoidal stator windings voltage. The test machine is star-delta connected, operated as motor and was loaded by 7.6KW D.C. machine as shown in figure 8.4.

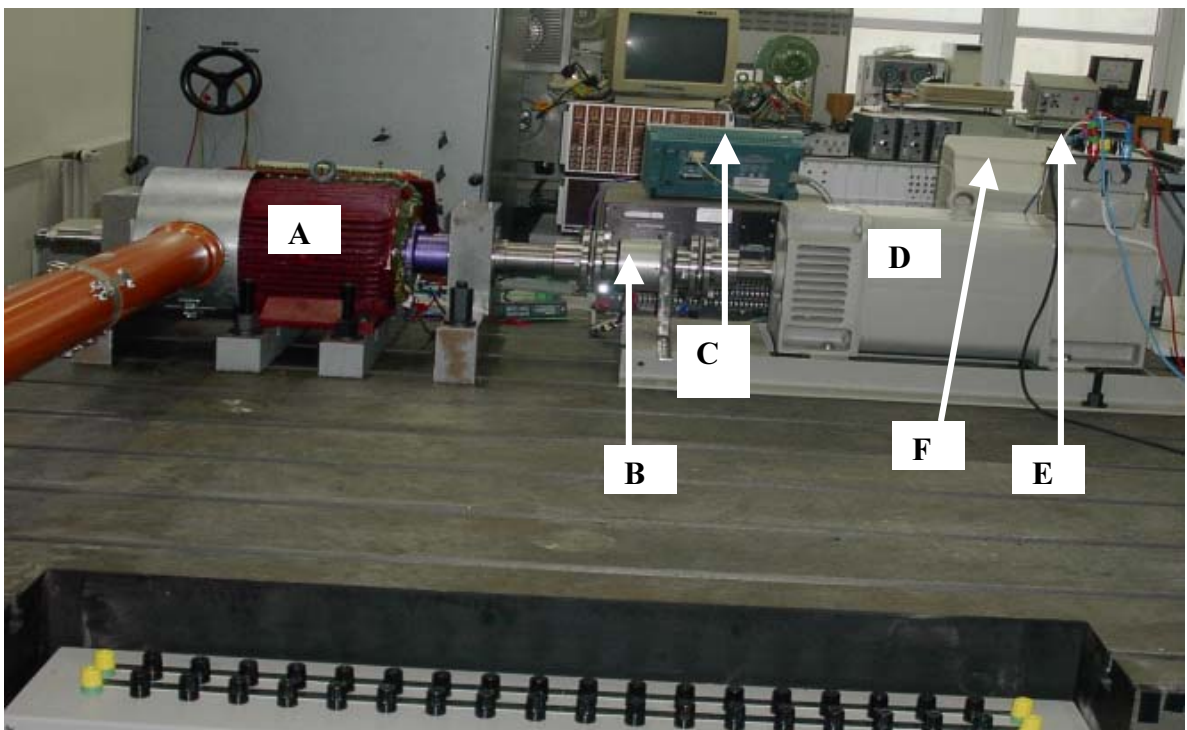


**Figure 8.4:** Test machine experimental set-up during rated load operation.  
Test machine(A),Coupling system(B),Digital-Real-Time Oscilloscope(C),Load D.C.machine(D),Mechanical speed leads(E),Computer(F).

Measurements of the test machine's transient stator currents, stator voltages, shaft torque and speed were made during run-up of the machine. The mechanical speed leads(E) as shown in figure 8.4 were taken through the speed terminals of the tacho-generator and connected to one of the channels of Digital Real-Time Oscilloscope,DRTO(C). The tacho-generator analog output is 20V per 1000rpm. The shaft torque was measured by using the 22/100 DATAFLEX torque measuring instrument connected together with the coupling system(B). The torque measuring instrument has as its output, voltage which was read through the DRTO. Three FLUKE current probes but with the same setting were used to measure the transient stator phase currents at run-up operation. All the run-up operation measurements were recorded in real time via a four-channel TS 200-series DRTO with RS232 output terminal. The RS232 output terminal enables the output from the DRTO to be monitored through a computer(F).

### 8.3 Temperature measurements

Temperature measurements on the test machine were carried out at No-load, rated load and blocked rotor operations. Iron-constantan, usually called Type J thermocouples were used for the measurements. These types of thermocouples are very popular due to their high Seebeck coefficient and low price. Thermocouples are generally more economical than PRTs and their temperature range is greater than thermistors. The main demerit of thermocouples is their relatively weak signal which makes their reading sensitive to corruption from electrical signal. During blocked rotor operation, 20 and 12 thermoelements were installed in the rotor and stator parts of the test machine respectively as shown in figure 8.5 and figure 8.6.



**Figure 8.5:** Rotor part of the test machine showing the installed J-type thermoelements.



**Figure 8.6:** Stator part of the test machine showing the installed J-type thermoelements.

All the thermocouples were connected to a 32-channel programmable recorder(see label E in figure 8.7) which combines the functions of a recorder with that of a datalogger and a data acquisition system. Measuring signals are printed with the built-in-inkjet printer on paper as values(with date and time). The time interval between print-outs is selectable. The printout shows the physical units of the measuring values, for example degree Centigrade. Through the built-in RS232 interface the measured data can be sent to a connected computer(See label F in figure 8.7). The computer stores and evaluates the measured data. The RS232 interface can transmit up to 40 values per second per channel. During the blocked rotor operation, the machine was star-connected and its rotor blocked. A 500V rms voltage was supplied to the machine with a stator current of 48A for about 9s and the temperature readings of the thermocouples recorded for every one second interval. It was observed that some of the thermocouples stopped working, probably because the soldering loosened.

The set-up for the No-load and rated load operations is as shown in figure 8.7. At No-load operation, the machine was delta-connected with a rated voltage of 340V.

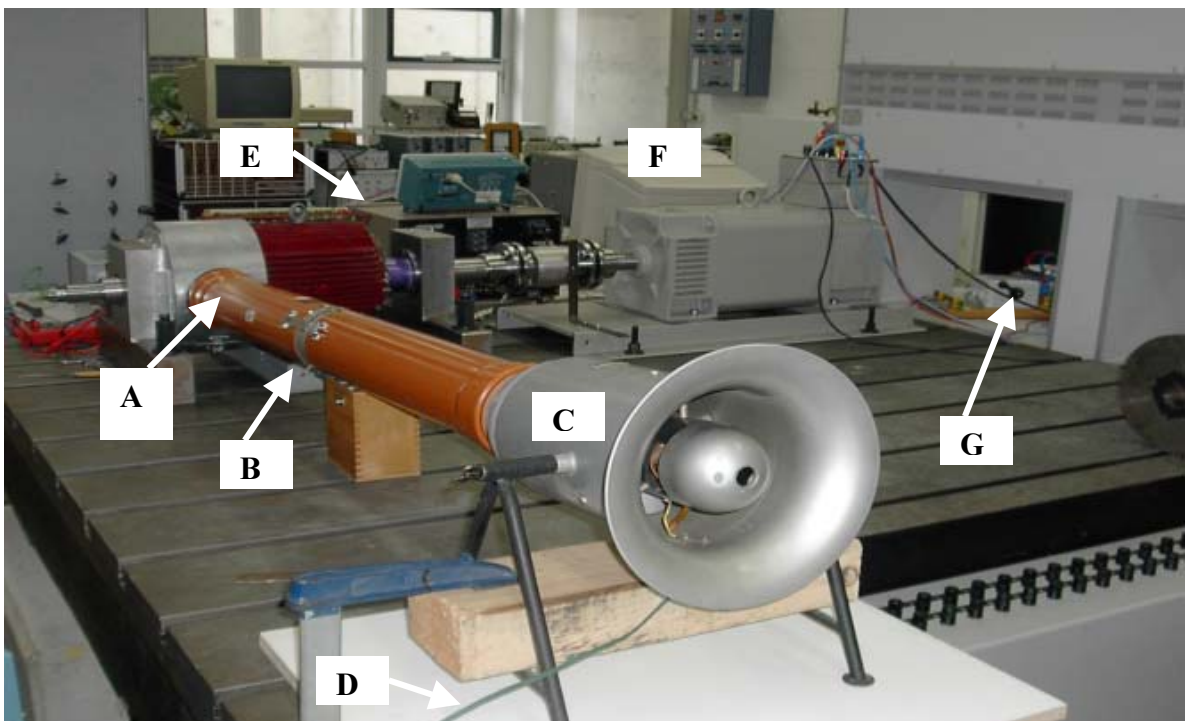


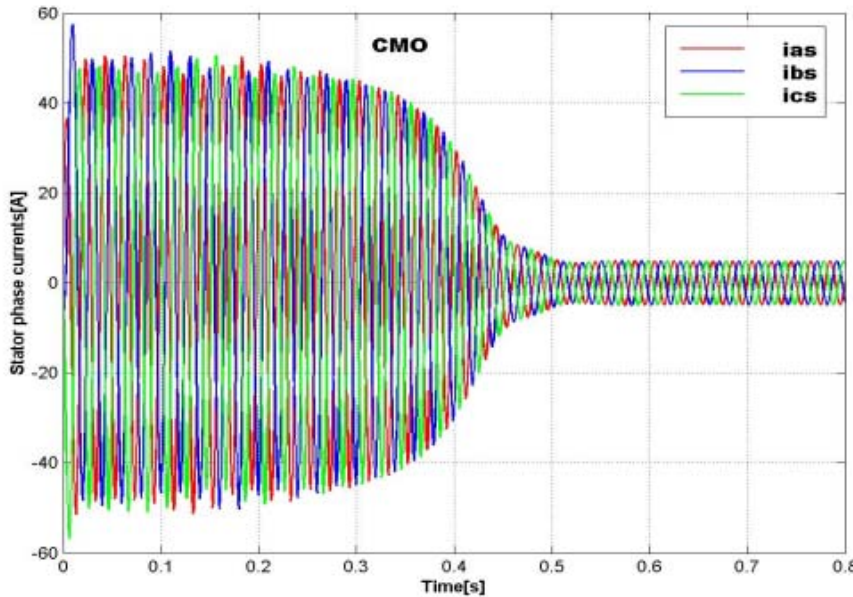
**Figure 8.7:** Experimental set-up for the heat runs at No-load and rated load operations. Air channel pipe(A), Anemometer On-Off switch(B), Ventilator(C), Leads to the voltage regulator(D), 32-channel programmable recorder(E), Computer(F), Star-Delta switch(G).

The machine was allowed to run at No-load for two hours until thermal equilibrium was attained. Temperature readings for every two minutes intervals were recorded. It is important to add that only the temperatures of the stator parts were recorded since the rotor parts were inaccessible during motor operation. The steady-state temperature of the drive side end-ring was however measured with the help of Infra-red instrument two hours after the machine has reached thermal equilibrium. The load test was carried out the same way as the No-load test but with the machine operated at rated full load until thermal equilibrium was reached. Measurements were recorded for every two minutes intervals. In both operations, the air flow rate into the test machine was kept constant and measured with the help of Anemometer(See label B in figure 8.7).

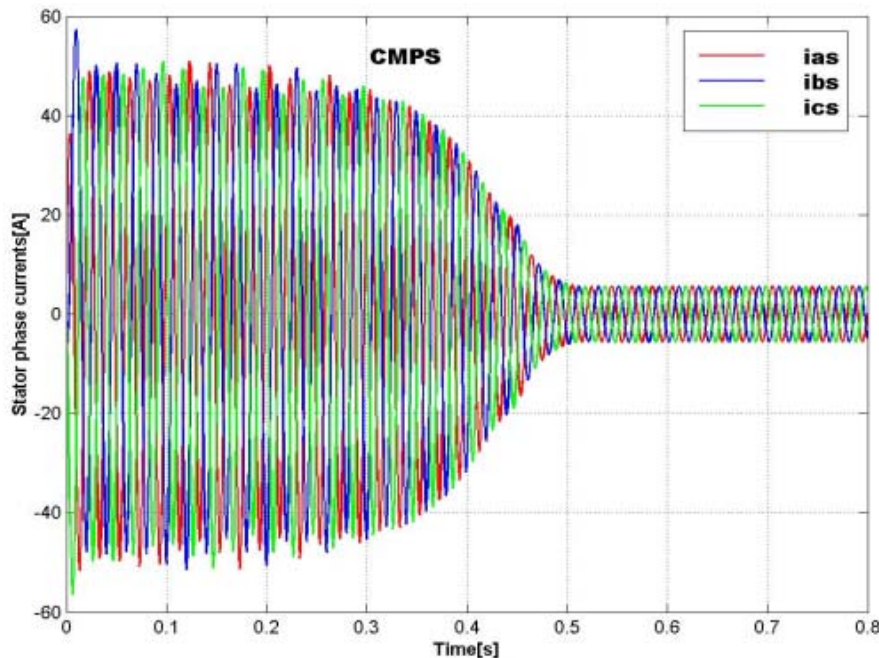
## 8.4 Simulation and experimental results

### 8.4.1. Run-up transient measurements and simulation results.

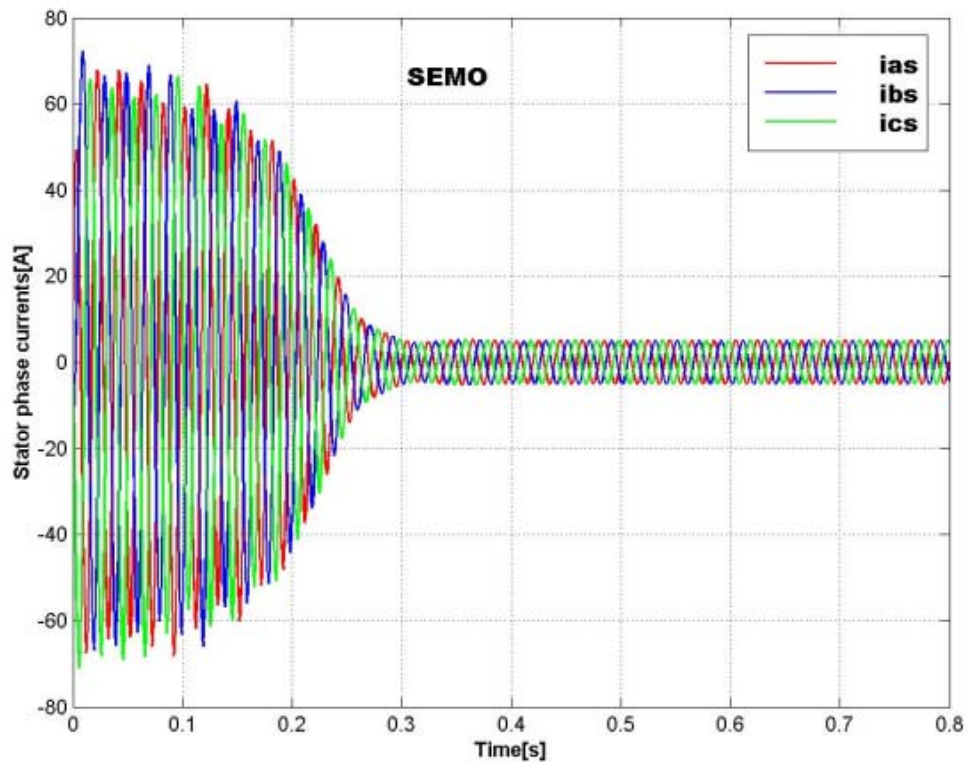
It is important to show how the measured parameters such as stator phase currents, mechanical rotor speed and the shaft torque compare with the developed models at run-up conditions. Therefore, simulated results for all the developed models shown in figures (8.8a-8.8m), are compared with the measurement results, shown in figures (8.9a-8.9c), respectively.



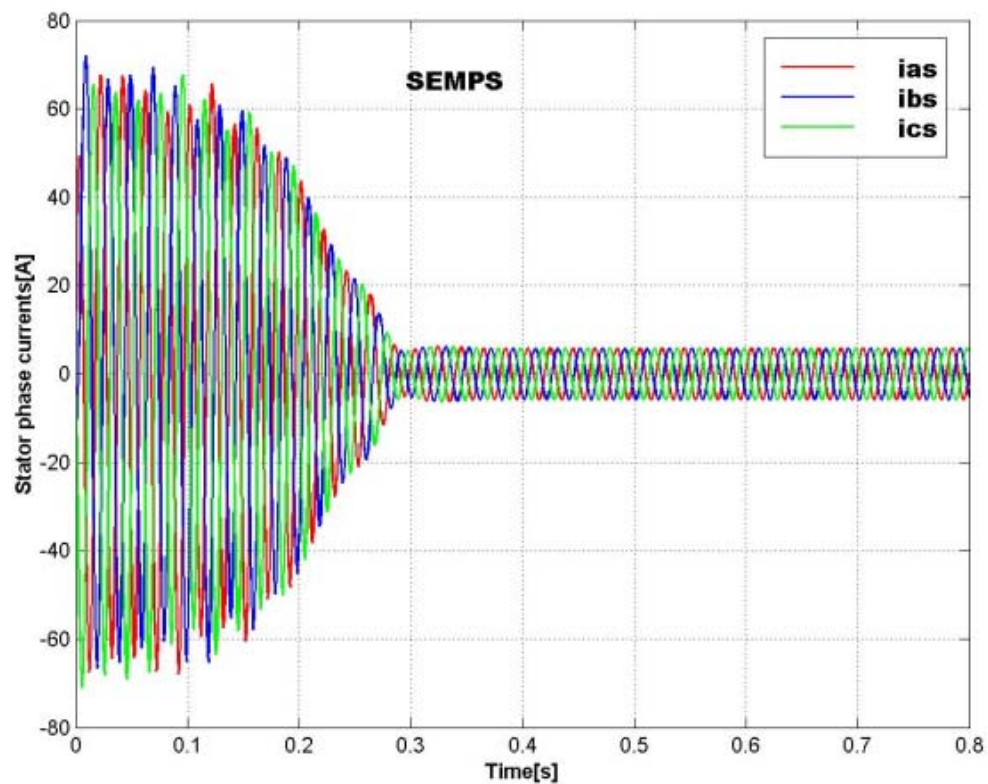
**Figure 8.8a:** Conventional model only(CMO) simulation: Stator phase currents at run-up.



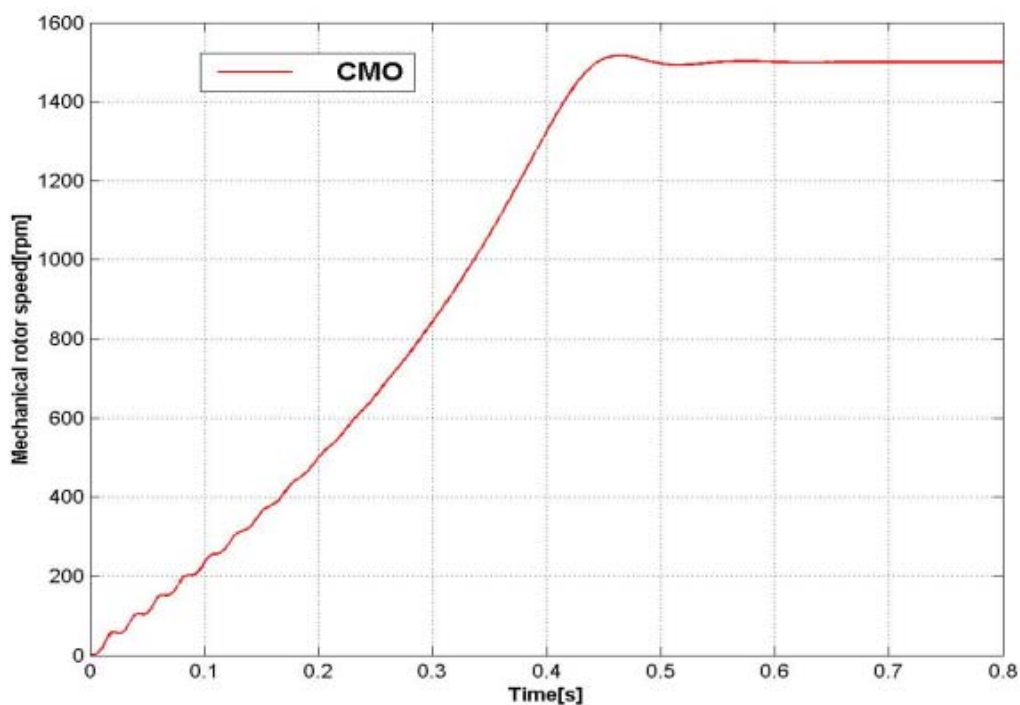
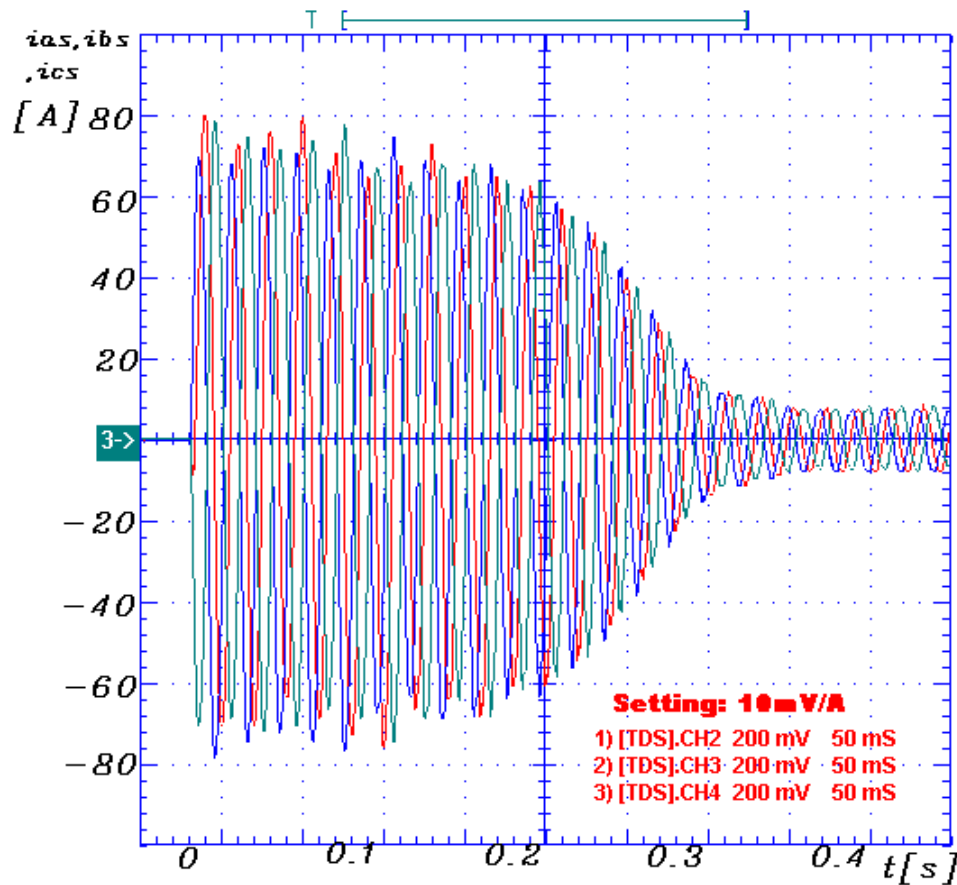
**Figure 8.8b:** Conventional model plus saturation(CMPS) simulation: Stator phase currents at run-up.



**Figure 8.8c:** Skin-effect model only(**SEMO**) simulation: Stator phase currents at run-up.



**Figure 8.8d:** Skin-effect model plus saturation(**SEMPS**) simulation: Stator phase currents at run-up.



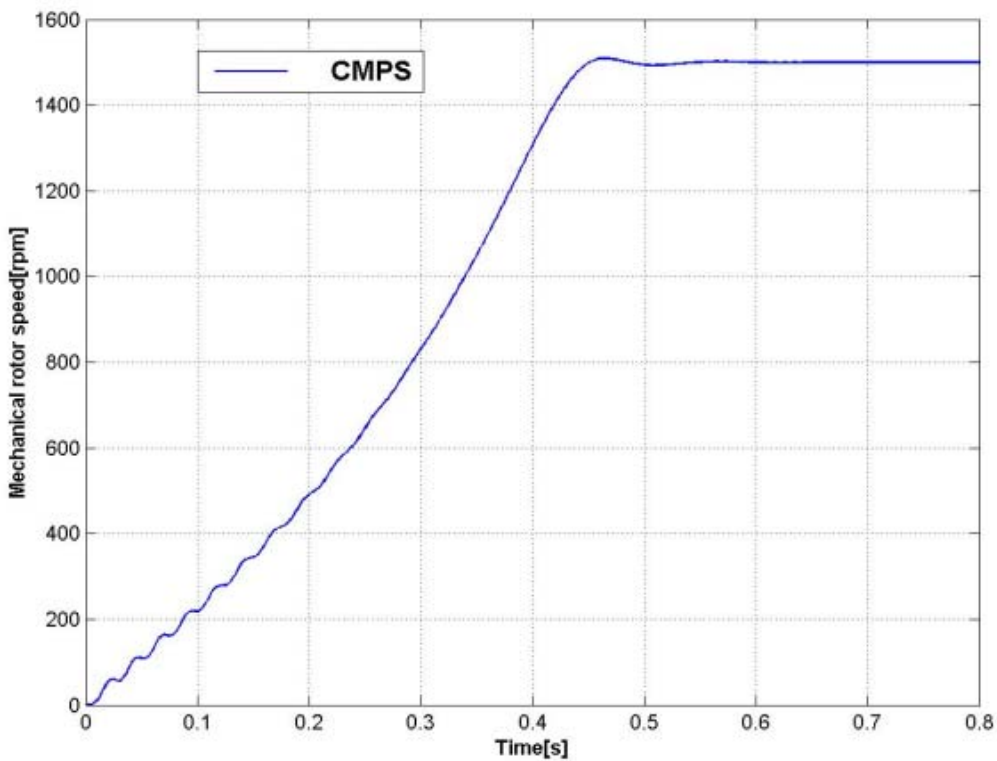


**Figure 8.8f:** Conventional model plus saturation(CMPS) simulation: Mechanical rotor speed at run-up.

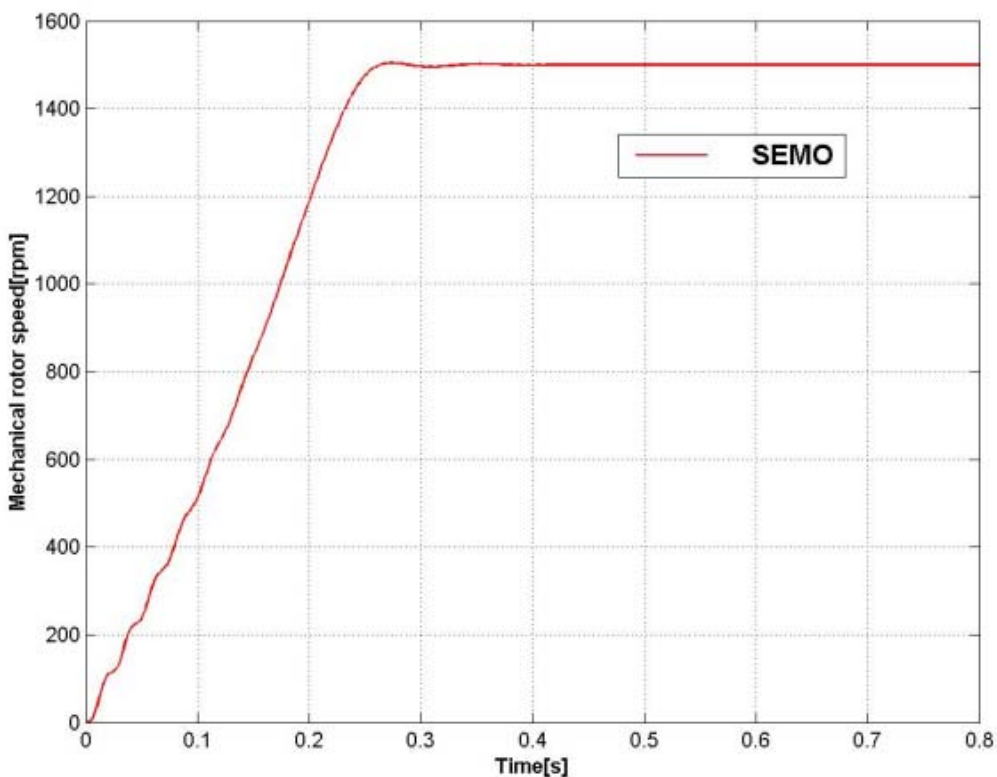


**Figure 8.8g:** Skin-effect model only(SEMO) simulation: Mechanical rotor speed at run-up.

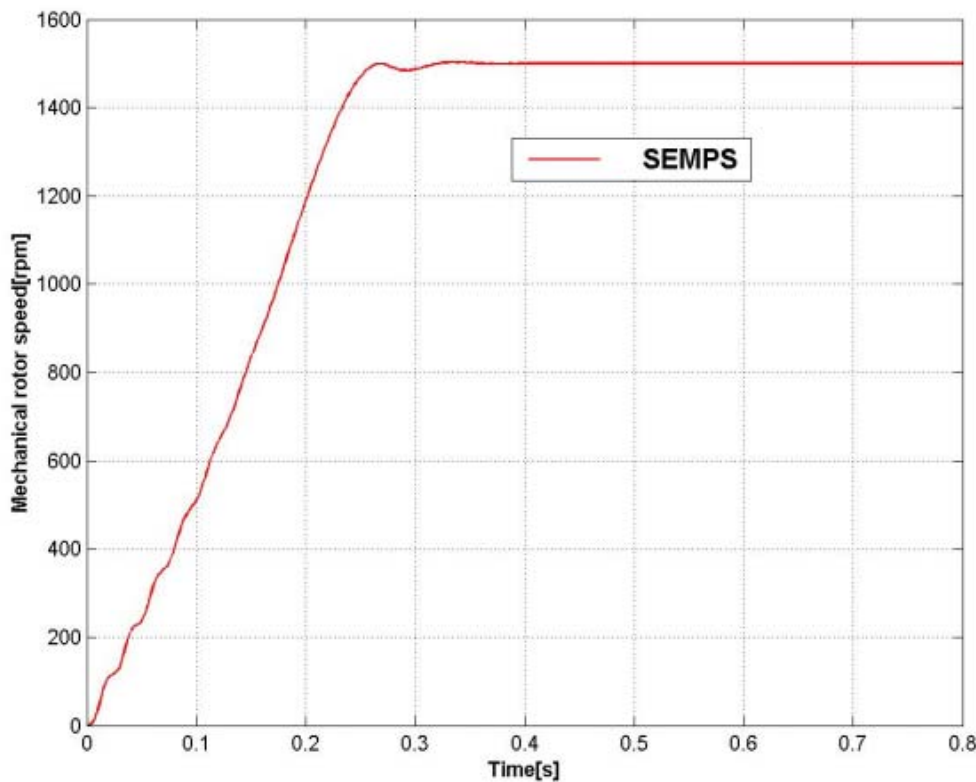


**Figure 8.8h:** Skin-effect model plus saturation(SEMPS) simulation: Mechanical rotor speed at run-up.

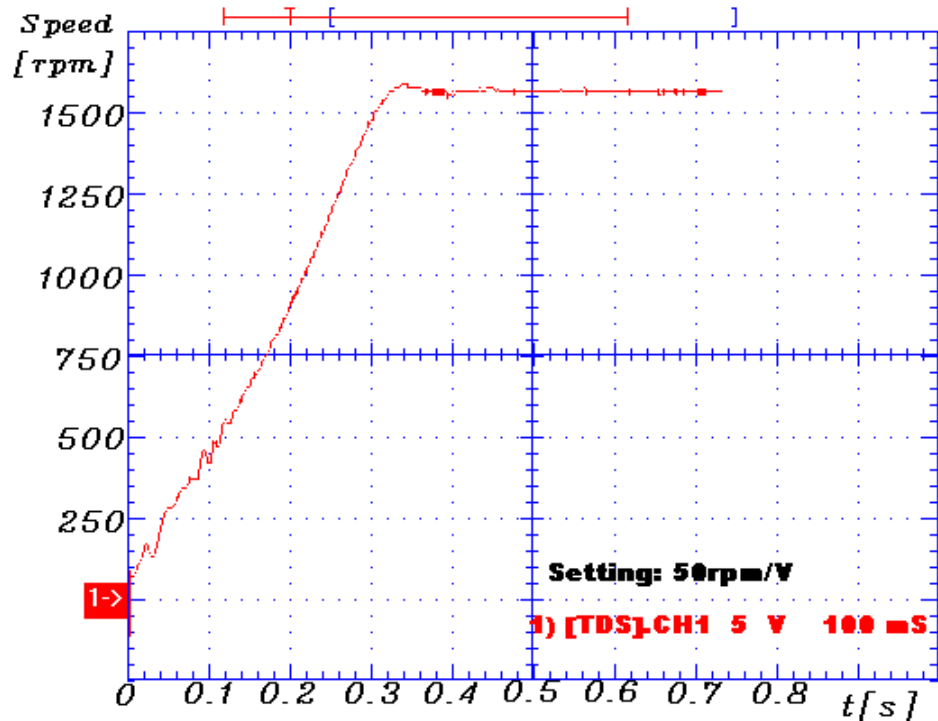


**Figure 8.9b:** Measurement: Mechanical rotor speed at run-up(Delta connected,Vrms=340V).

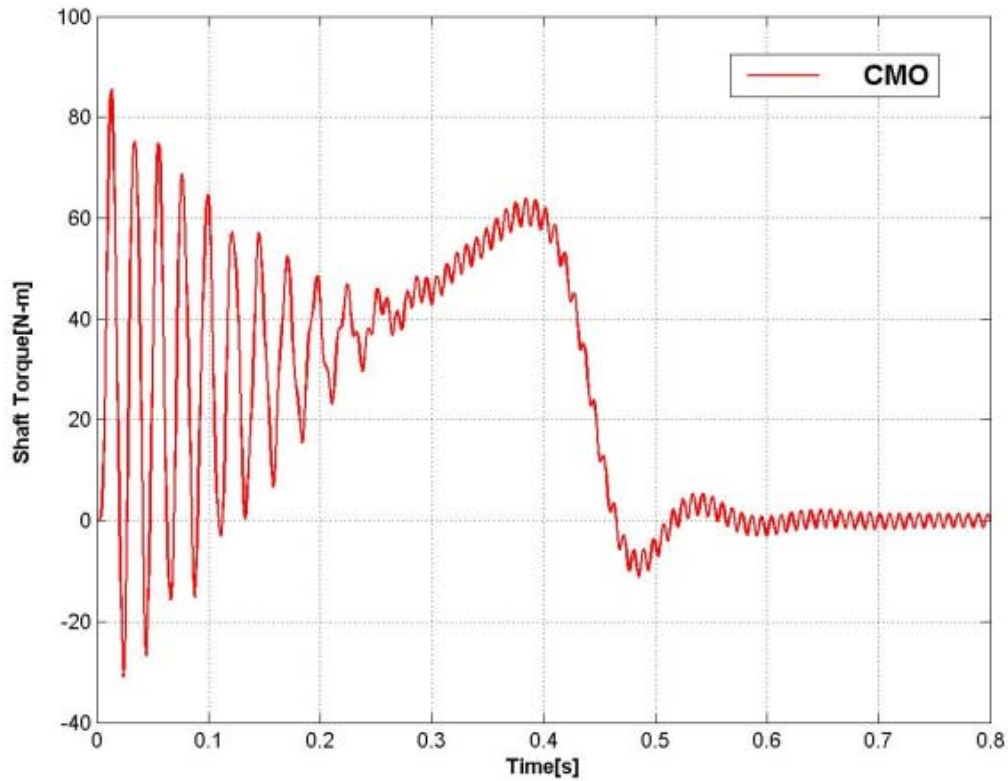


**Figure 8.8i:** Conventional model only(CMO) simulation: Shaft torque at run-up.

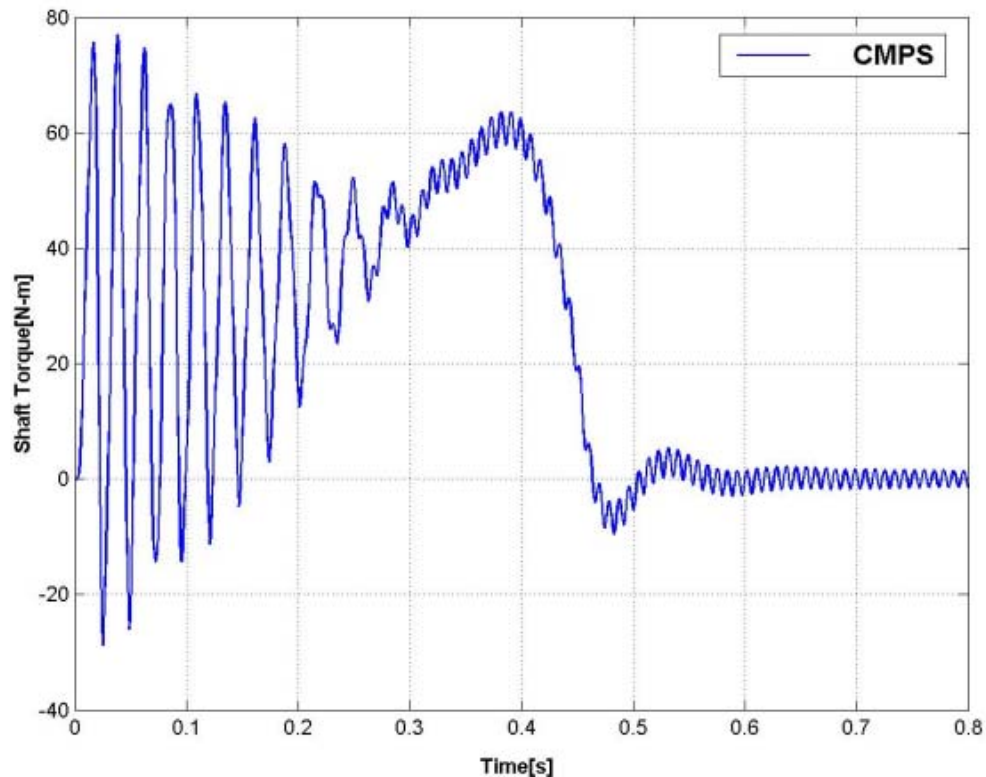


**Figure 8.8j:** Conventional model plus saturation(CMPS) simulation: Shaft torque at run-up.

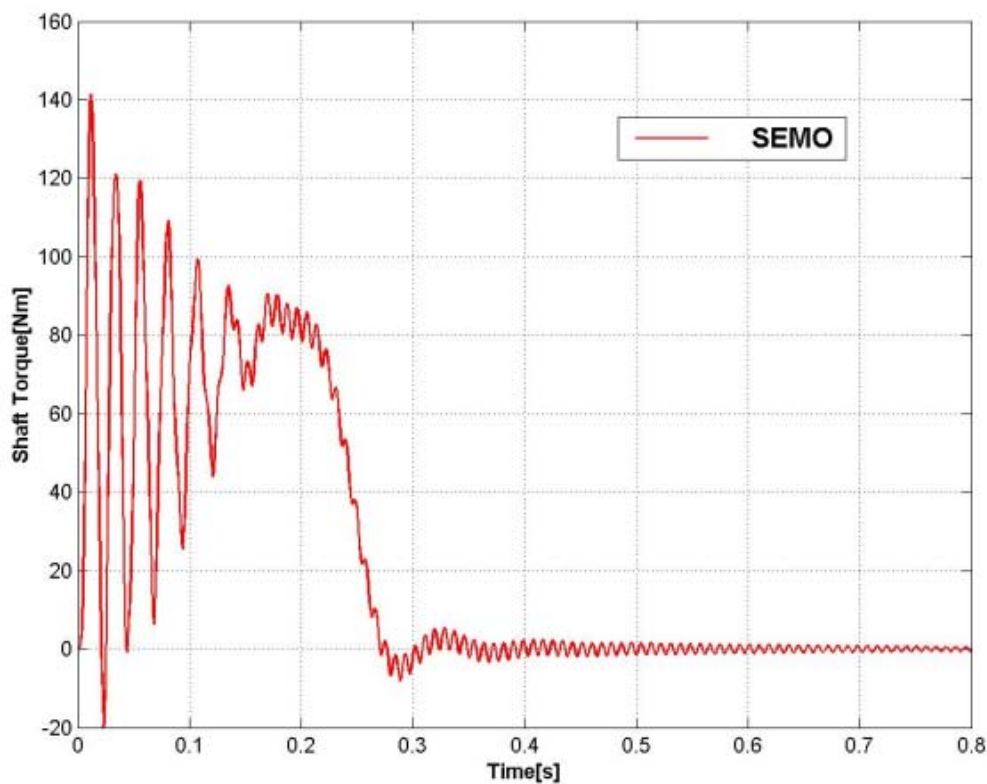


**Figure 8.8k:** Skin- effect model only(SEMO) simulation: Shaft torque at run-up.

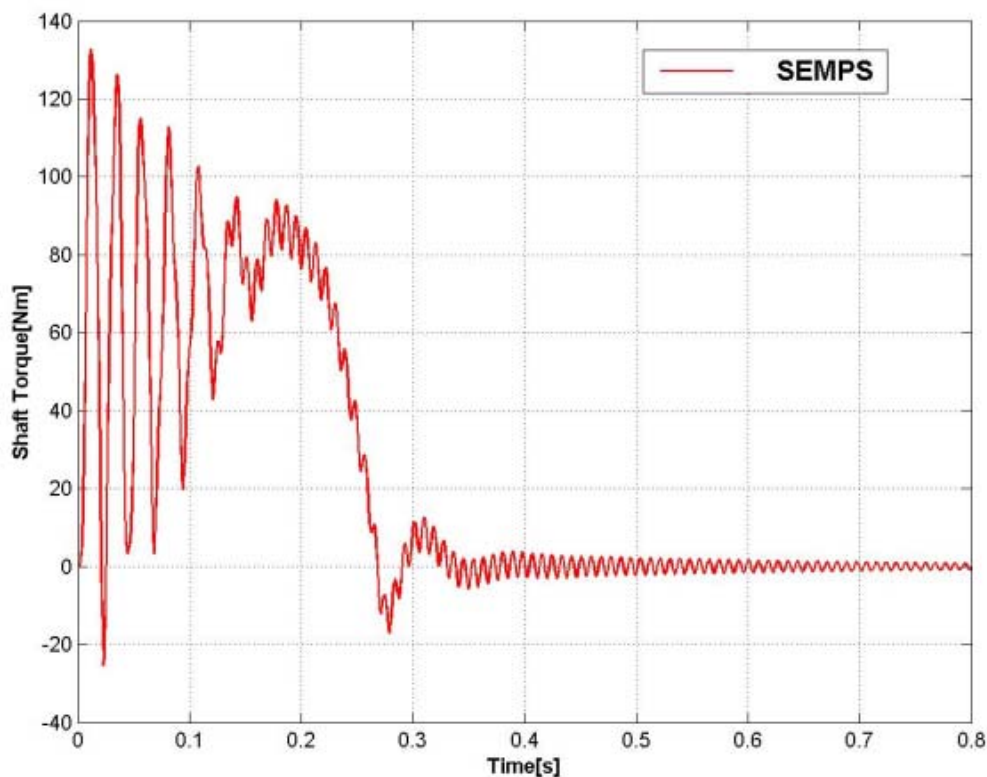


**Figure 8.8m:** Skin-effect model plus saturation(SEMPS) simulation: Shaft torque at run-up.

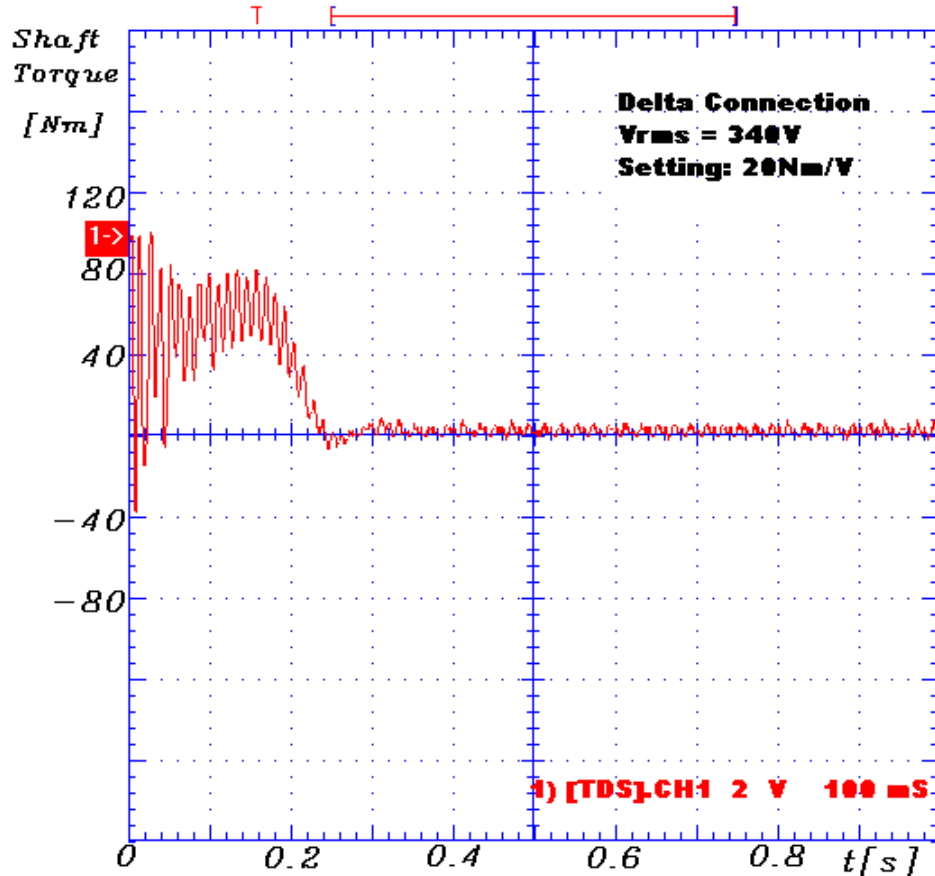


**Figure 8.9c:** Measurement: Shaft torque at run-up(Delta connected,  $V_{rms} = 340V$ , Setting:20Nm/V).

#### 8.4.2. Temperature measurements and simulation results.

The readings of the three thermocouples installed at the stator winding at No-load are shown in figure 8.10. Figure 8.11a and figure 8.11b show the measured temperatures of the stator end-winding at drive side and the non-drive side of the test machine respectively. The average of these temperatures were used to compare the simulated thermal model. The measured and predicted stator winding temperature is shown in figure 8.10a while that of stator end-winding is shown in figure 8.11c. Figure 8.12 shows the measured and predicted frame temperature.

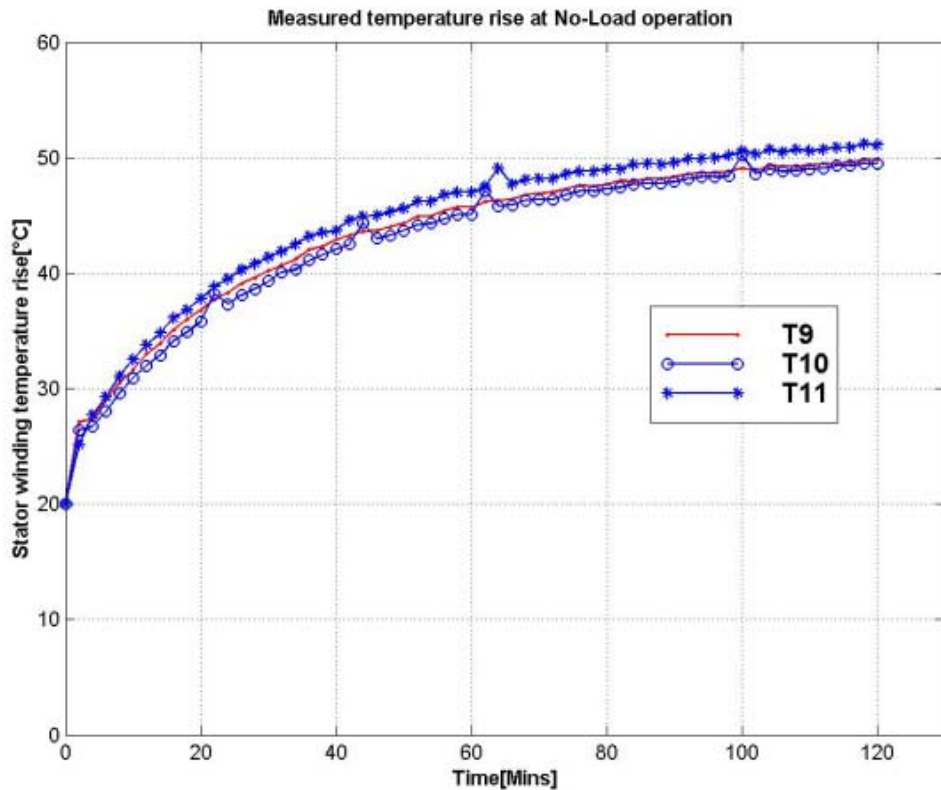


**Figure 8.10:** Measurement at No-load: Measured stator winding temperature.

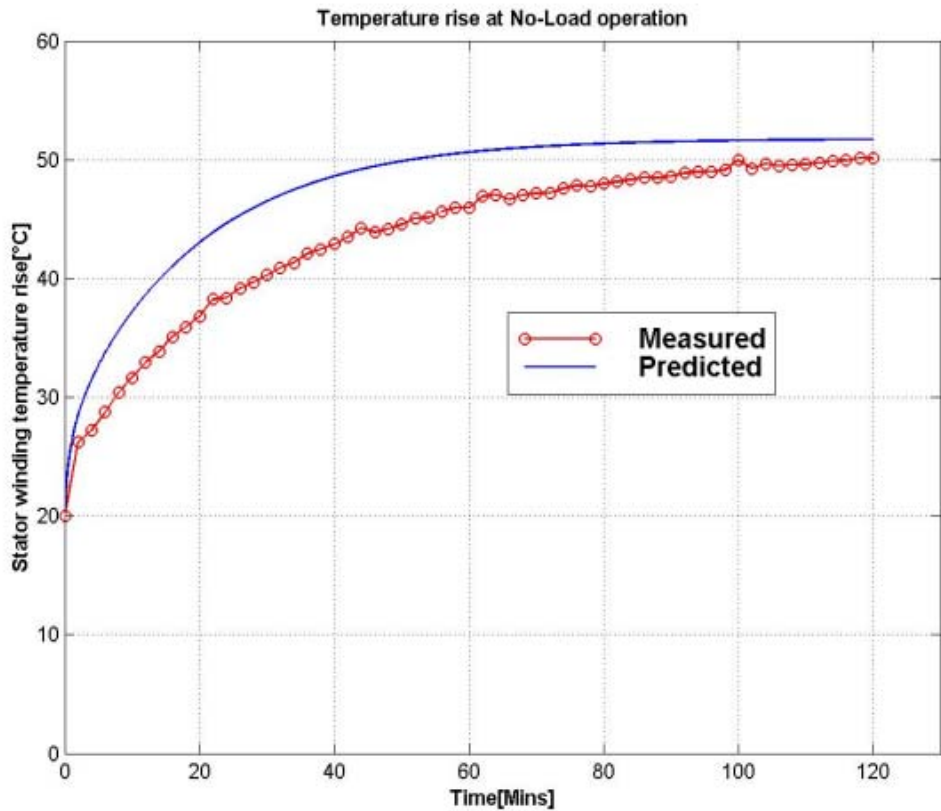


**Figure 8.10a:** Measured(Average) and predicted stator winding temperature at No-load.

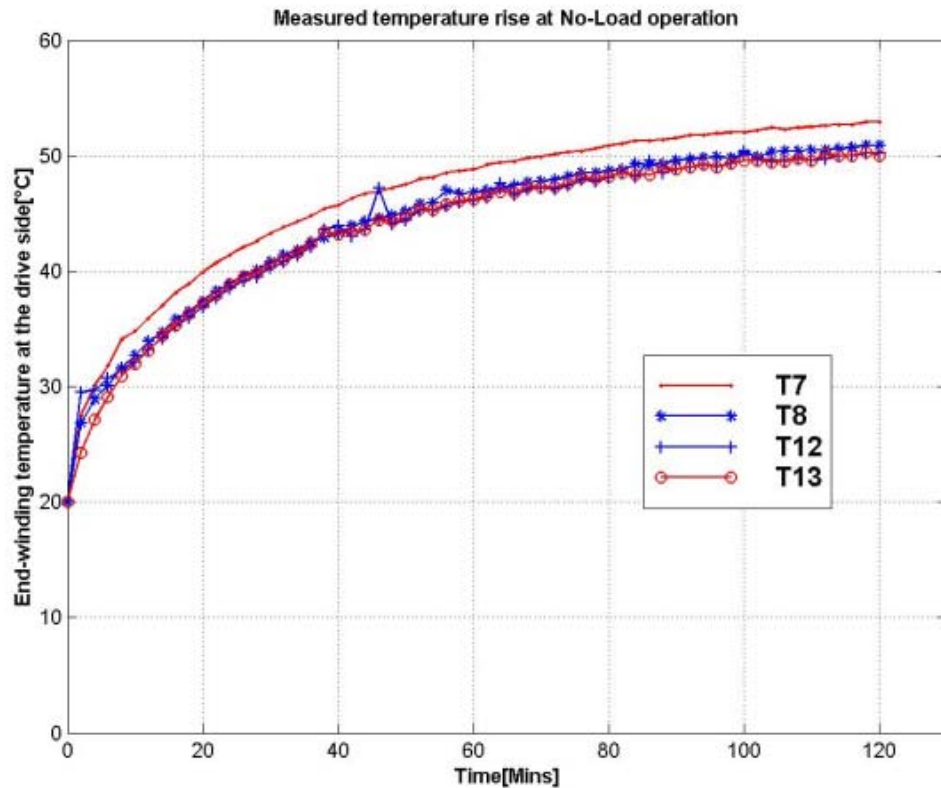


**Figure 8.11a:** Measurement at No-load: Measured end-winding temperature at the drive side.

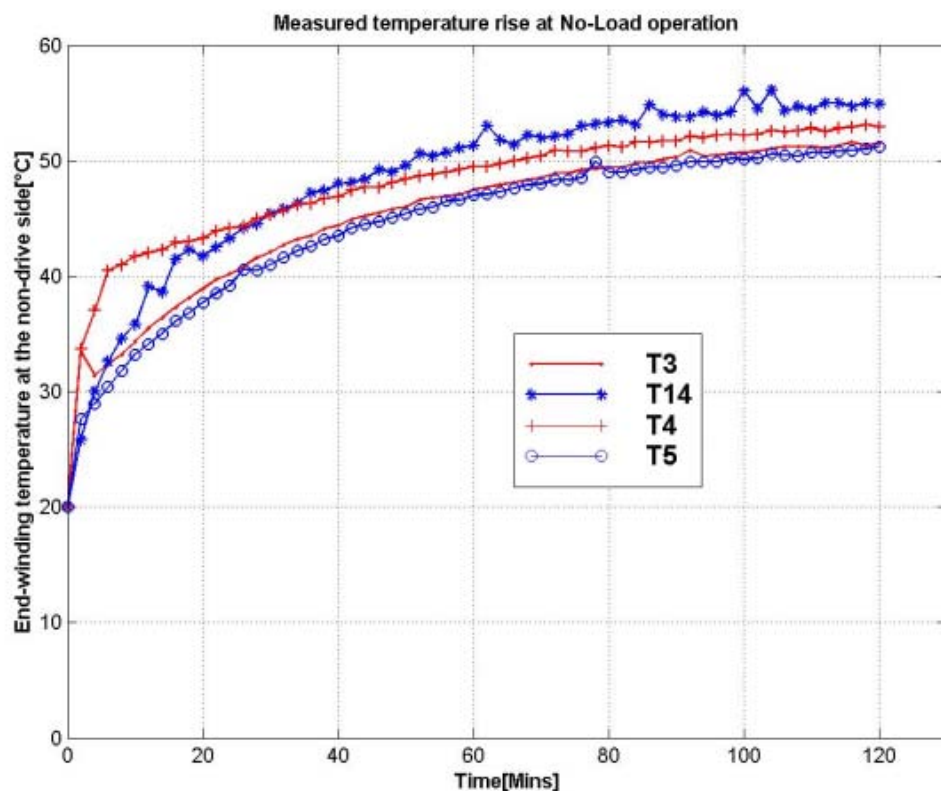


**Figure 8.11b:** Measurement at No-load: Measured end-winding temperature at the non-drive side.

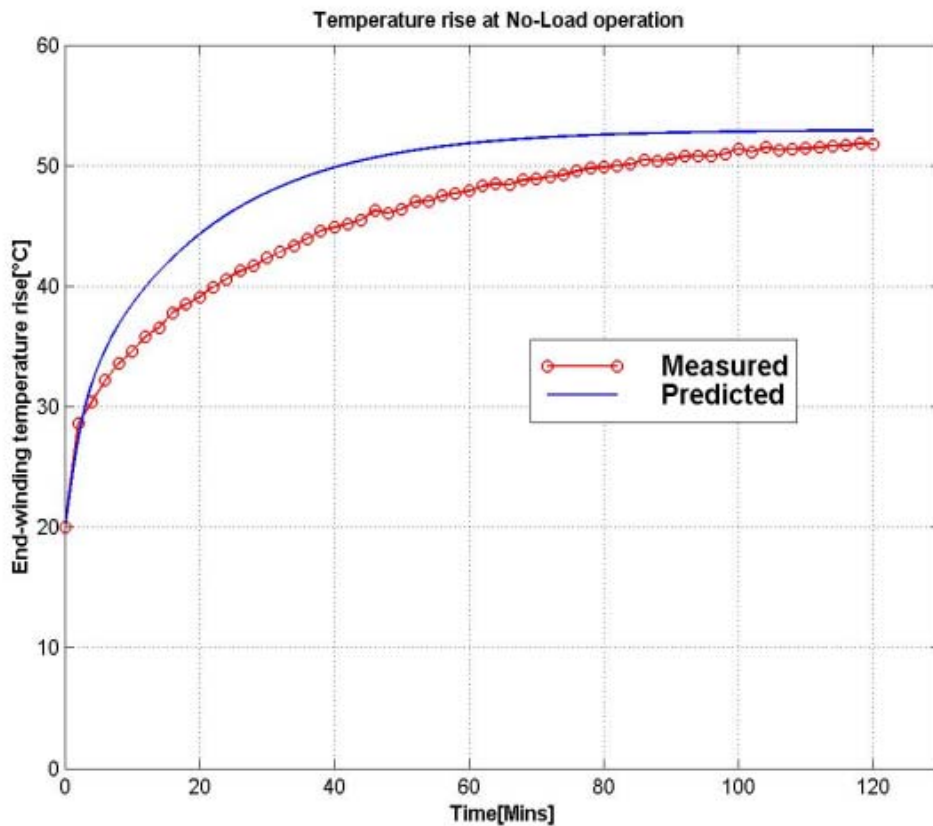


**Figure 8.11c:** Measured(Average)and predicted end-winding temperature at No-load.

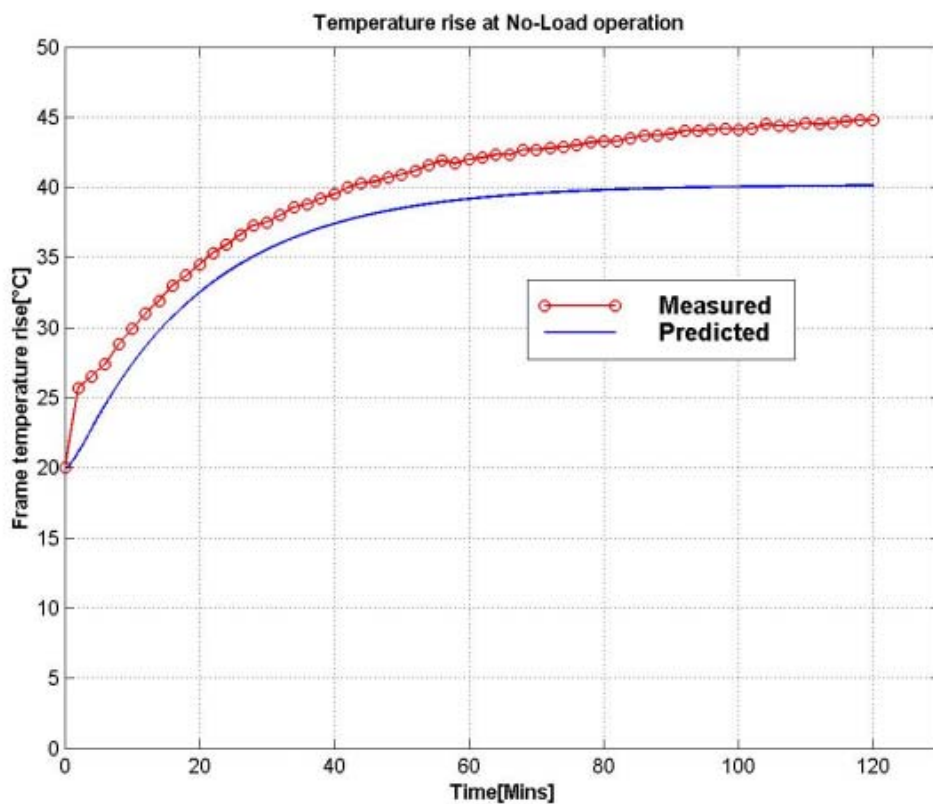


**Figure 8.12:** Measured and predicted frame temperature at No-load.

At rated load operation, the measured and computed temperatures of the various parts of the test machine are shown in figure 8.13, figure 8.14 and figure 8.15.

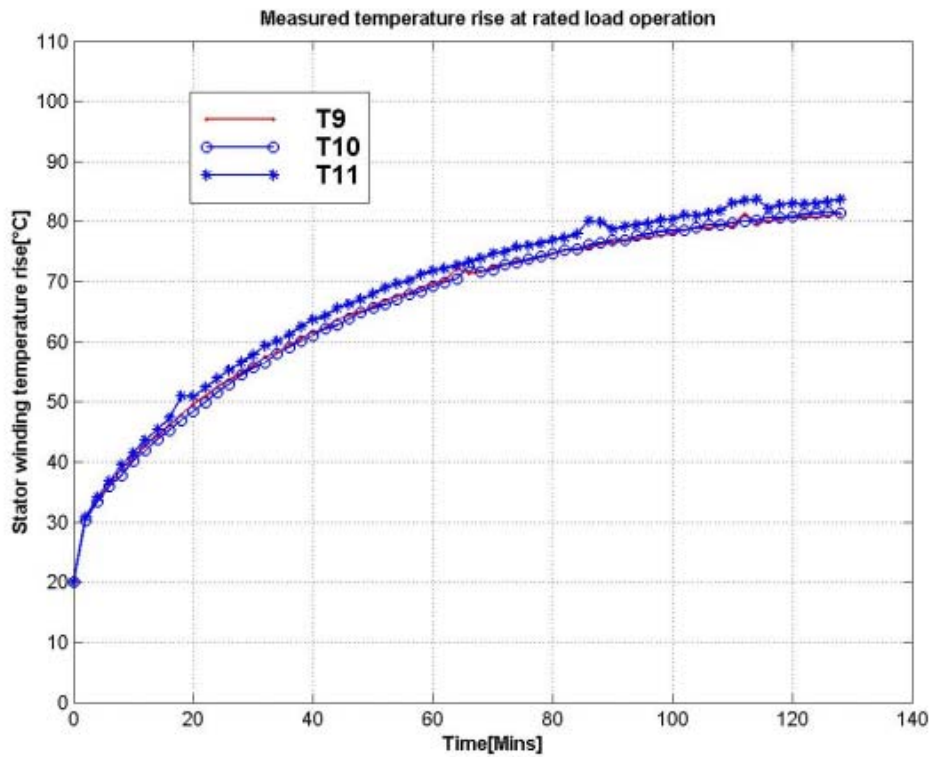


**Figure 8.13a:** Measurement at rated load: Measured stator winding temperature.

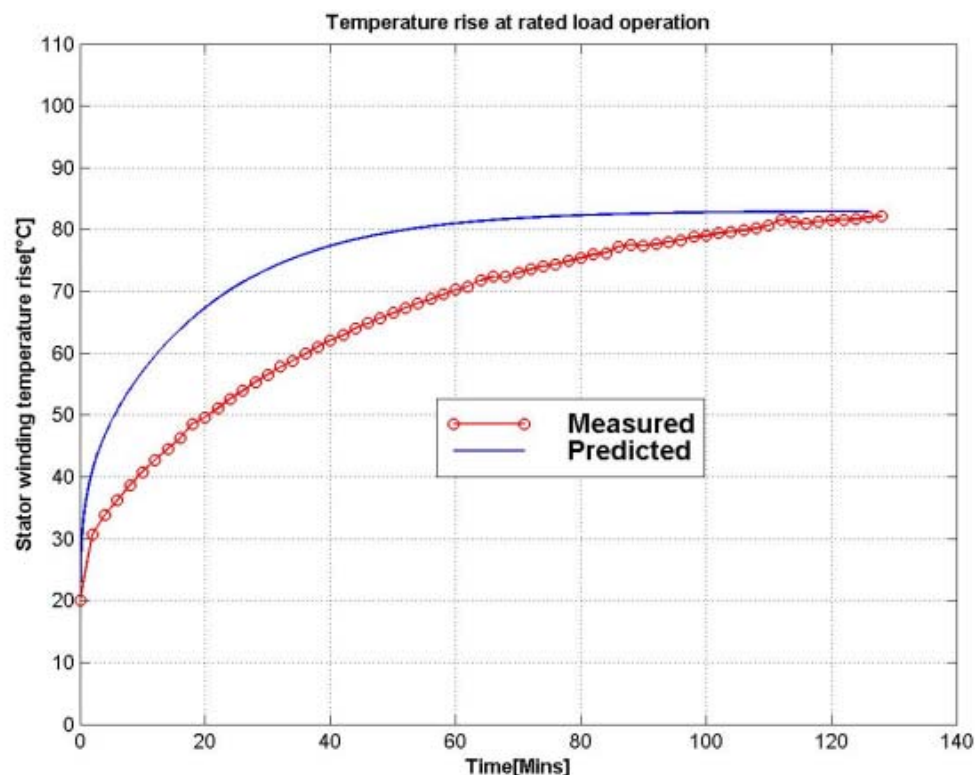


**Figure 8.13b:** Measured(Average) and predicted stator winding temperature at rated load.

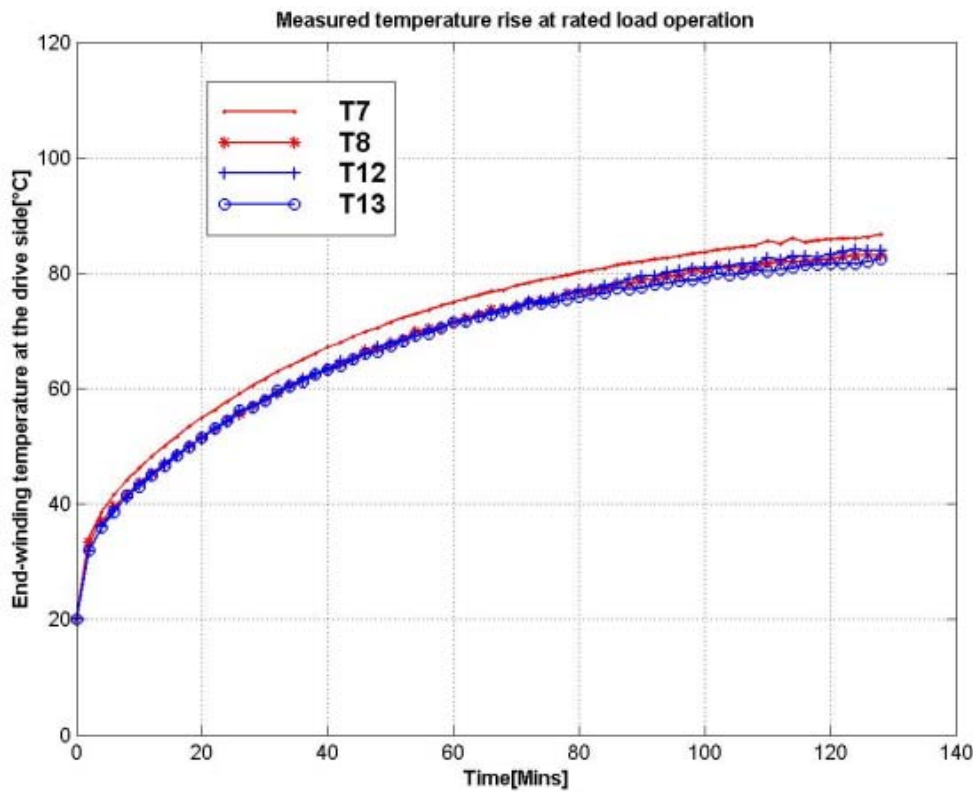


**Figure 8.14a:** Measurement at rated load: Measured end-winding temperature at the drive side.

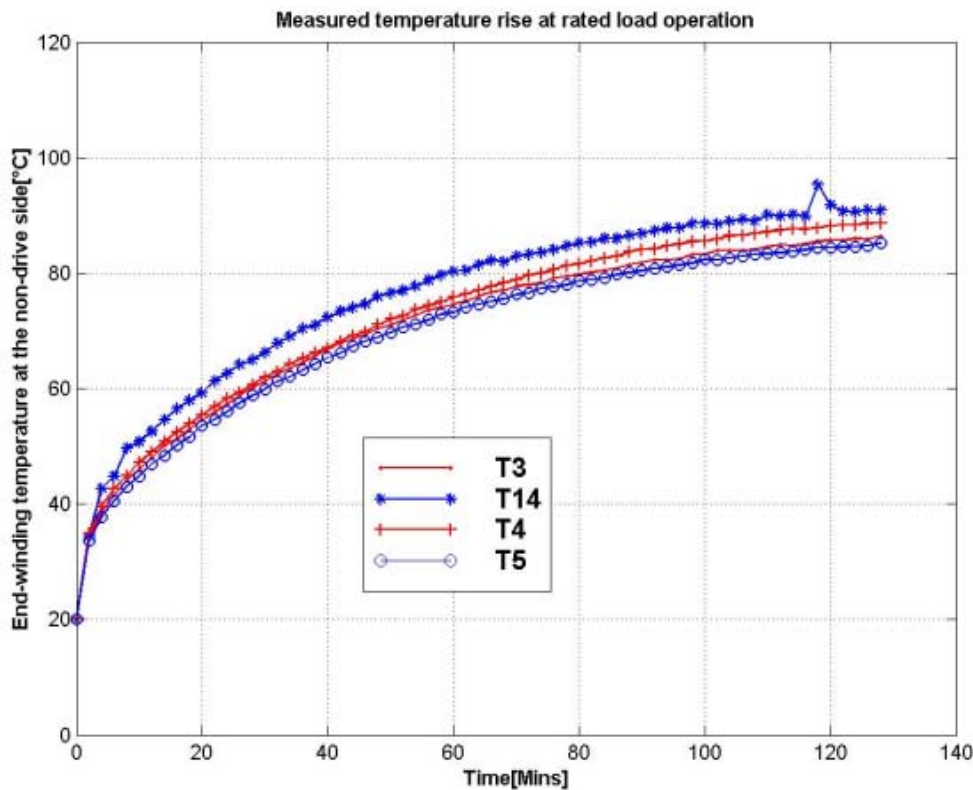


**Figure 8.14b:** Measurement at rated load: Measured end-winding temperature at the non-drive side.

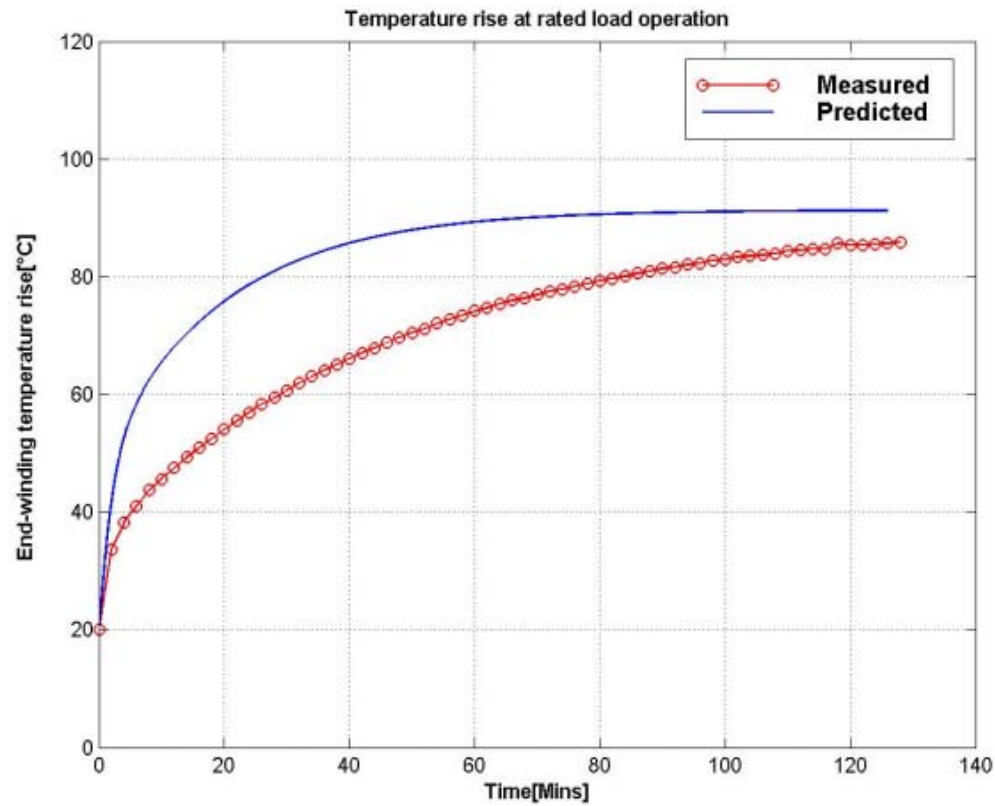


**Figure 8.14c:** Measured(Average)and predicted end-winding temperature at rated load.

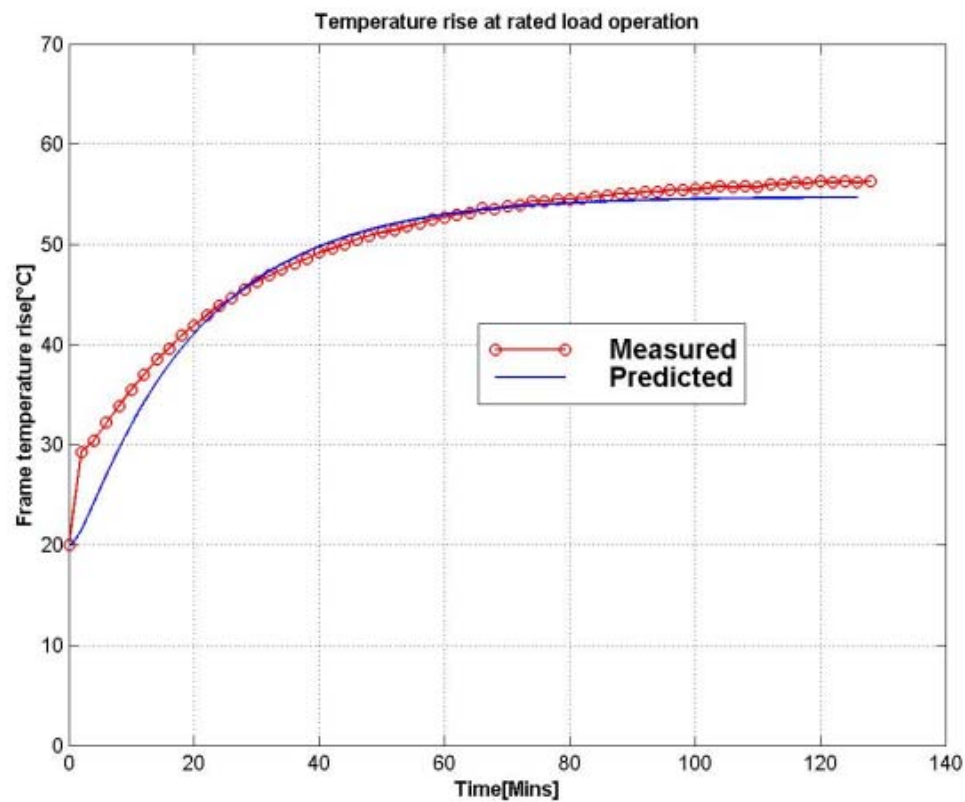


**Figure 8.15:** Measured and predicted frame temperature at rated load.

The measured and predicted temperatures of the various parts of the test machine at blocked rotor operation are presented in figure 8.16, figure 8.17, figure 8.18, and figure 8.19.

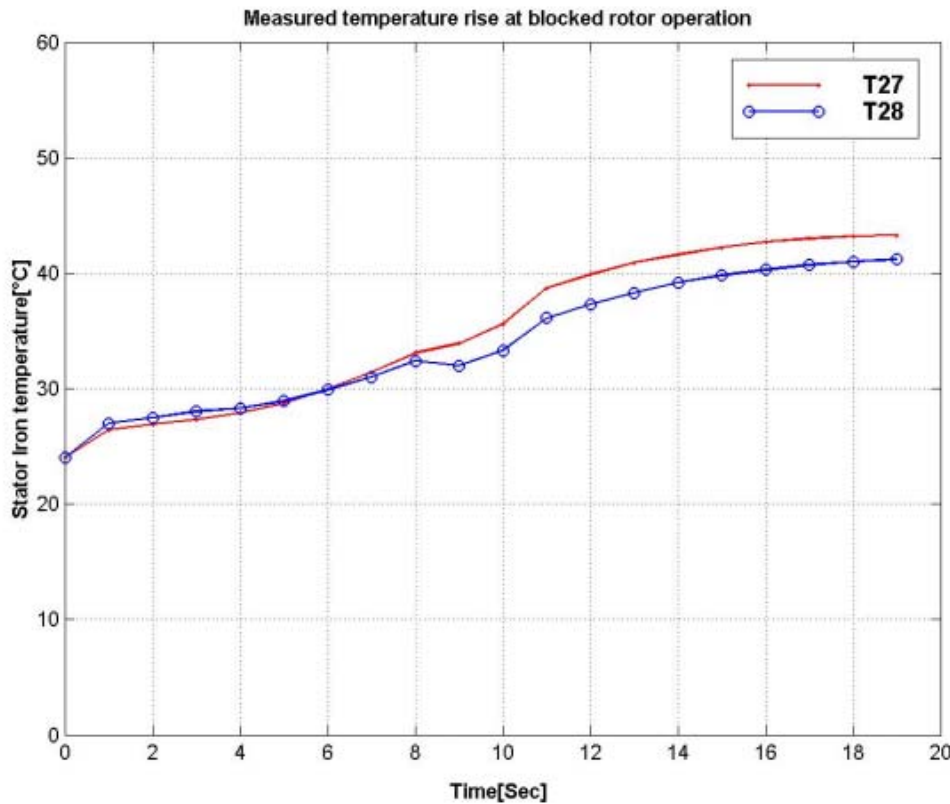


**Figure 8.16a:** Measurement at blocked rotor:Measured stator iron temperature.  
0...9s: Irms = 48A, Vrms = 500V, Star-connected; 9...20s: Irms = 0A, Vrms = 0V.

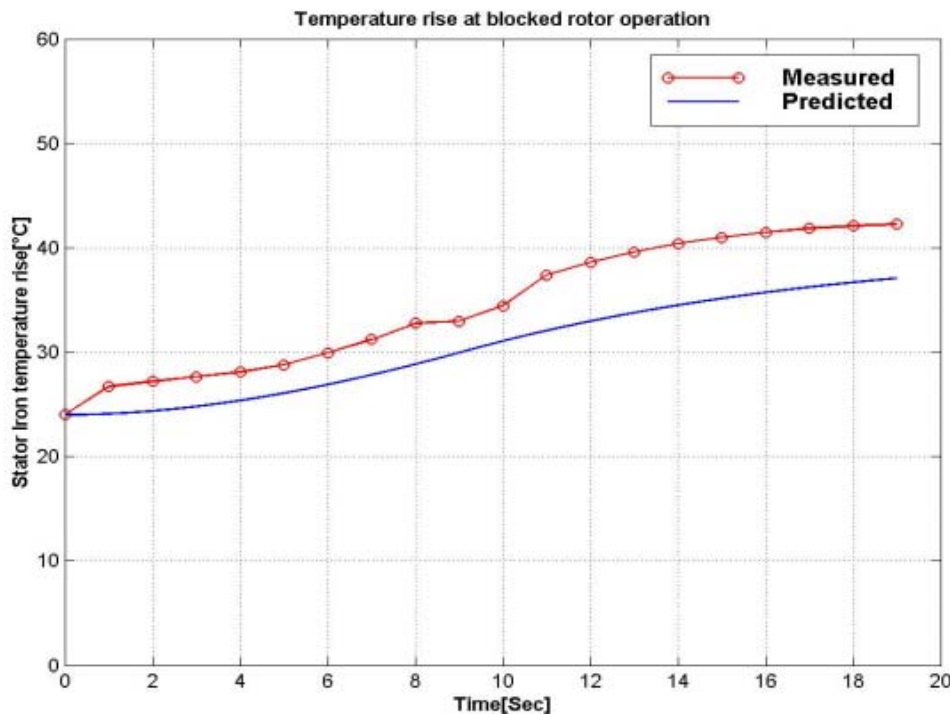


**Figure 8.16b:** Measured(Average) and predicted stator iron temperature at blocked rotor.

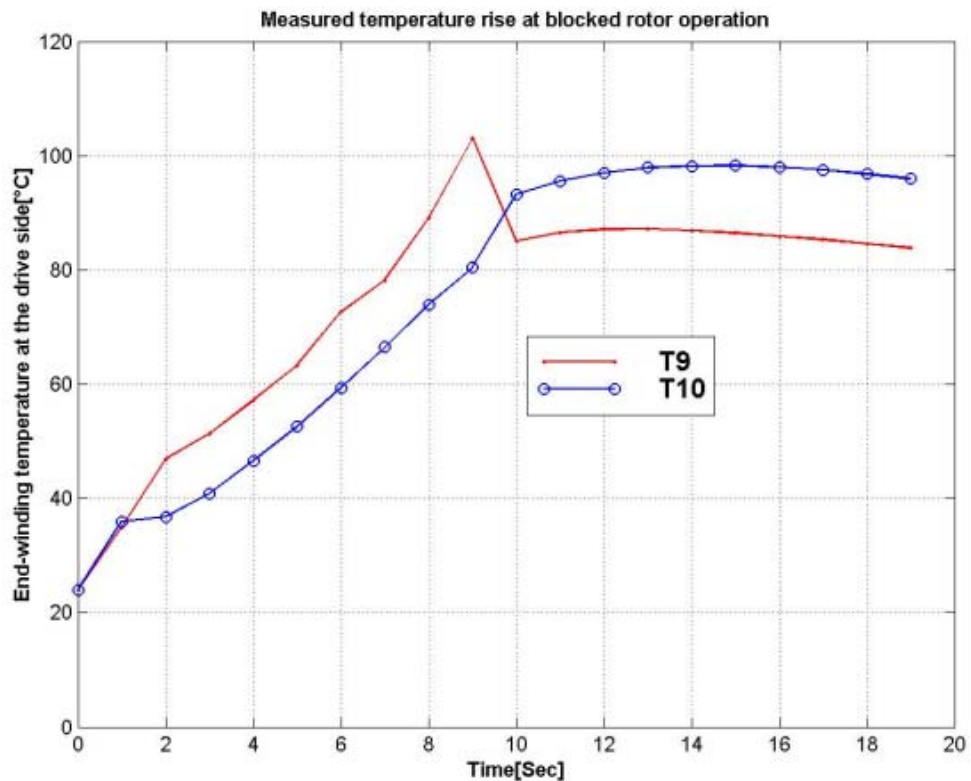


**Figure 8.17a:** Measurement at blocked rotor:Measured stator end-winding temperature at the drive side. 0...9s:  $I_{rms} = 48A$ ,  $V_{rms} = 500V$ , Star-connected; 9...20s:  $I_{rms} = 0A$ ,  $V_{rms} = 0V$ .

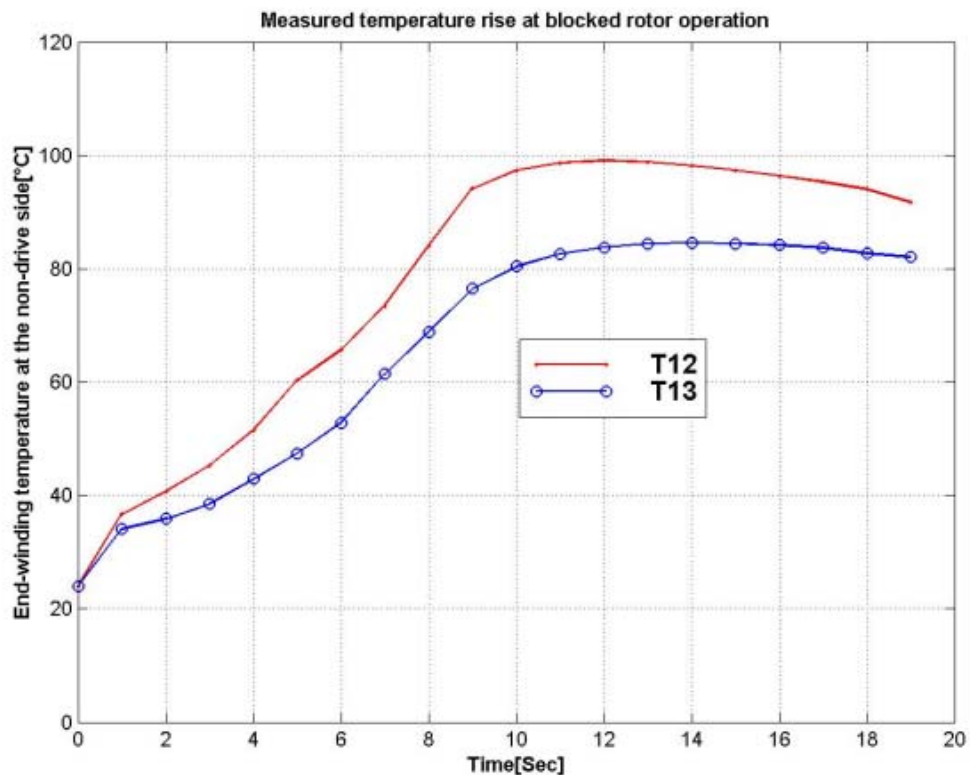


**Figure 8.17b:** Measurement at blocked rotor:Measured stator end-winding temperature at the non-drive side. 0...9s:  $I_{rms} = 48A$ ,  $V_{rms} = 500V$ , Star-connected; 9...20s:  $I_{rms} = 0A$ ,  $V_{rms} = 0V$ .

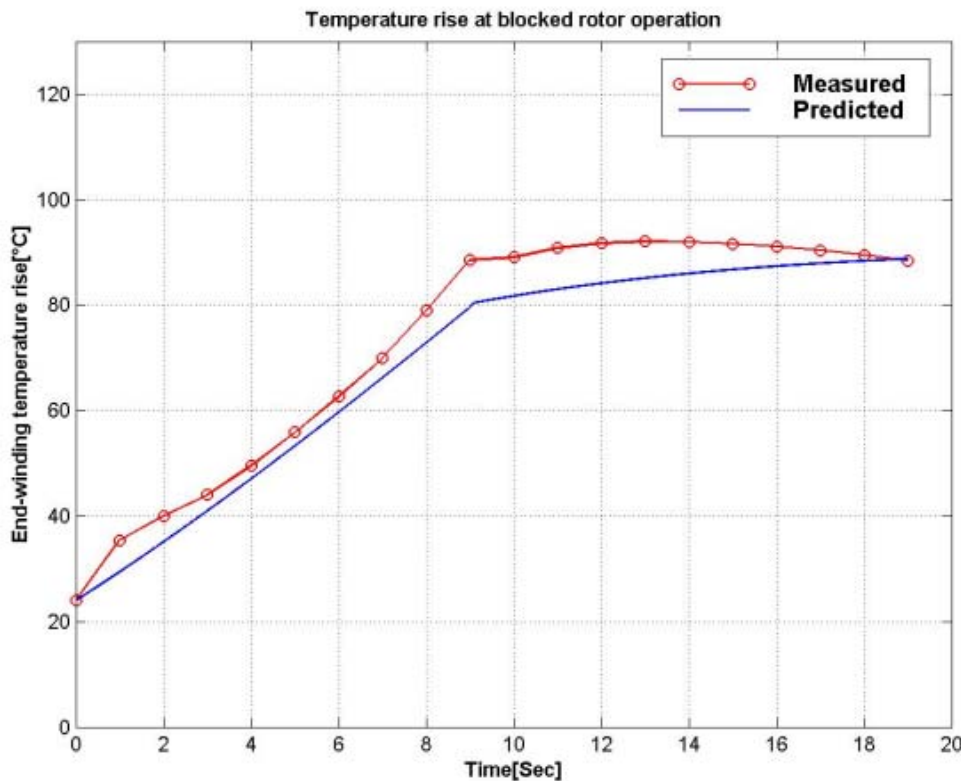


**Figure 8.17c:** Measured(Average) and predicted stator end-winding temperature at blocked rotor.

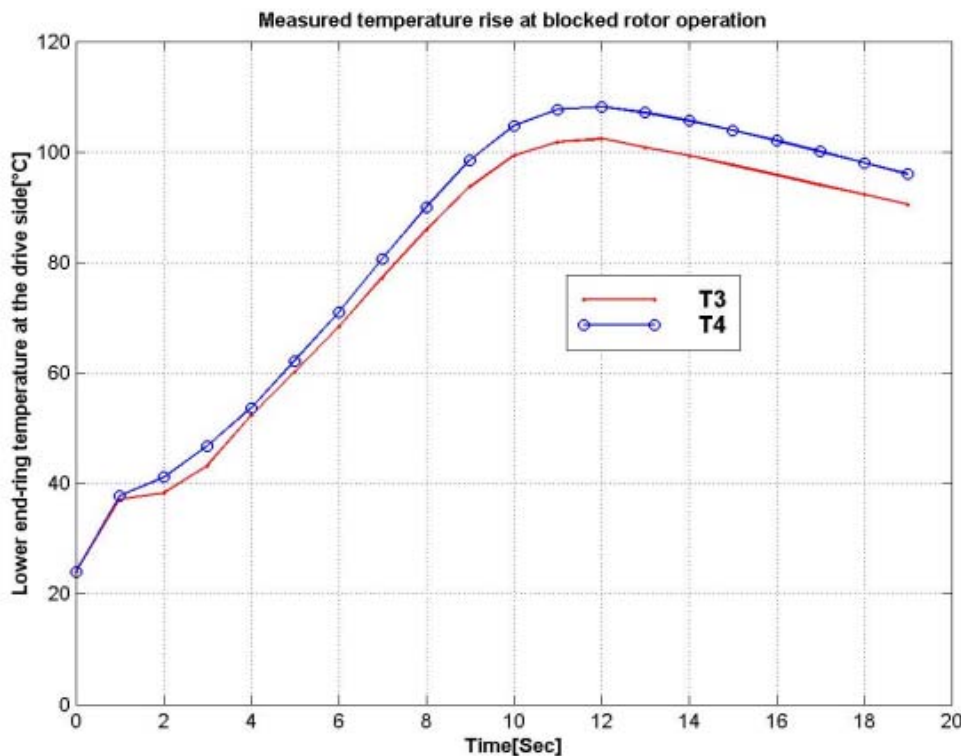


**Figure 8.18a:** Measurement at blocked rotor:Measured lower end-ring temperature at the drive side. 0...9s:  $I_{rms} = 48A$ ,  $V_{rms} = 500V$ , Star-connected; 9...20s:  $I_{rms} = 0A$ ,  $V_{rms} = 0V$ .

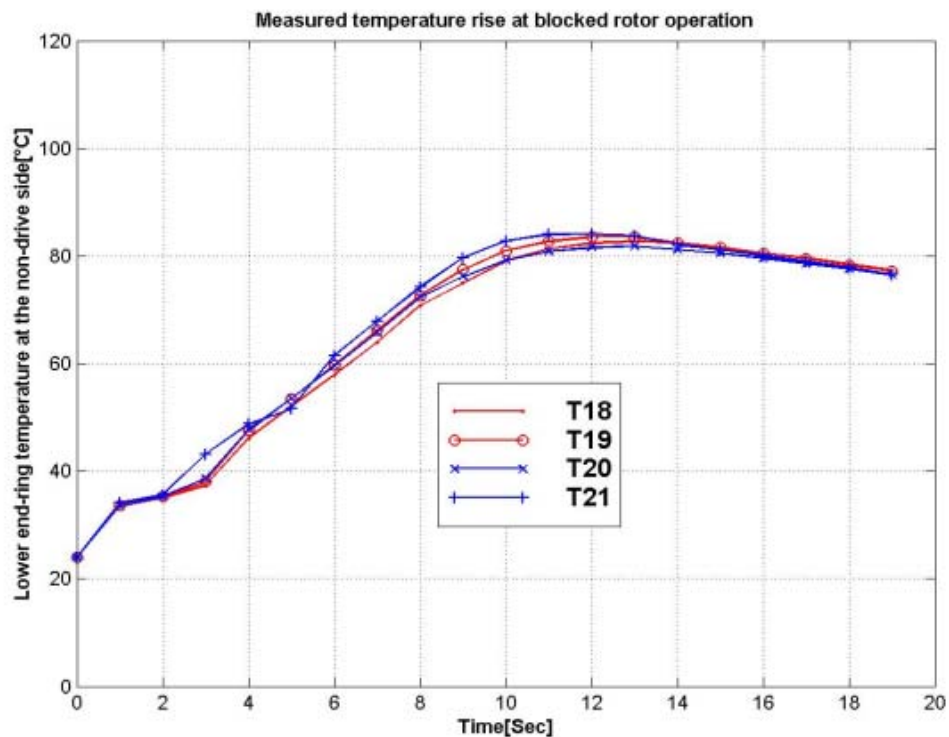


**Figure 8.18b:** Measurement at blocked rotor:Measured lower end-ring temperature at the non-drive side. 0...9s:  $I_{rms} = 48A$ ,  $V_{rms} = 500V$ , Star-connected; 9...20s:  $I_{rms} = 0A$ ,  $V_{rms} = 0V$ .

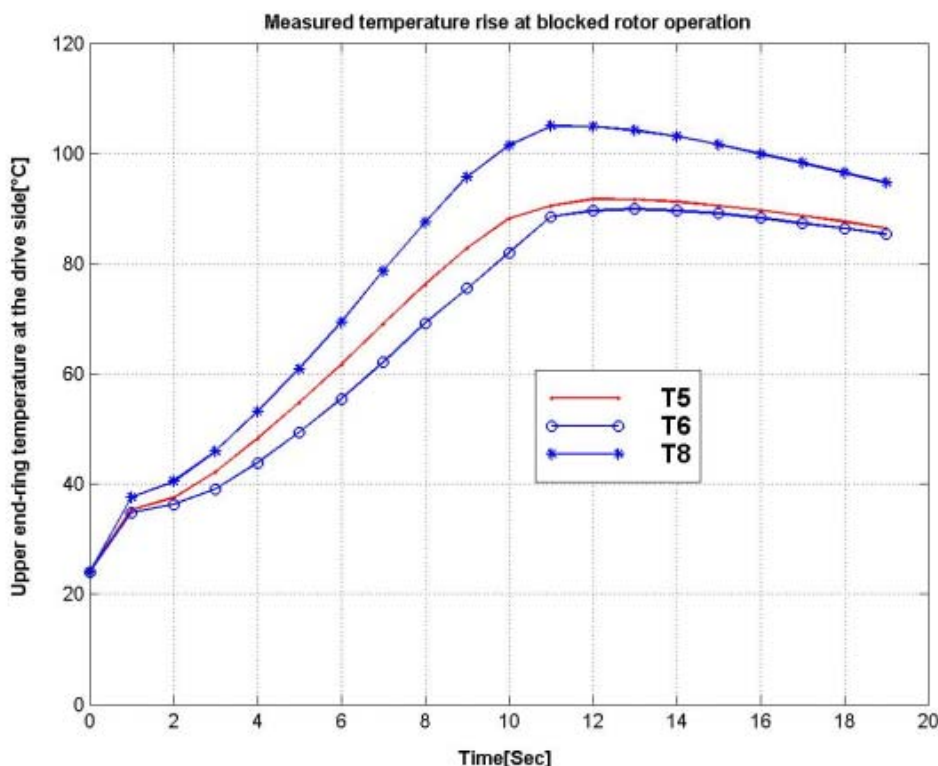


**Figure 8.18c:** Measurement at blocked rotor:Measured upper end-ring temperature at the drive side. 0...9s:  $I_{rms} = 48A$ ,  $V_{rms} = 500V$ , Star-connected; 9...20s:  $I_{rms} = 0A$ ,  $V_{rms} = 0V$ .

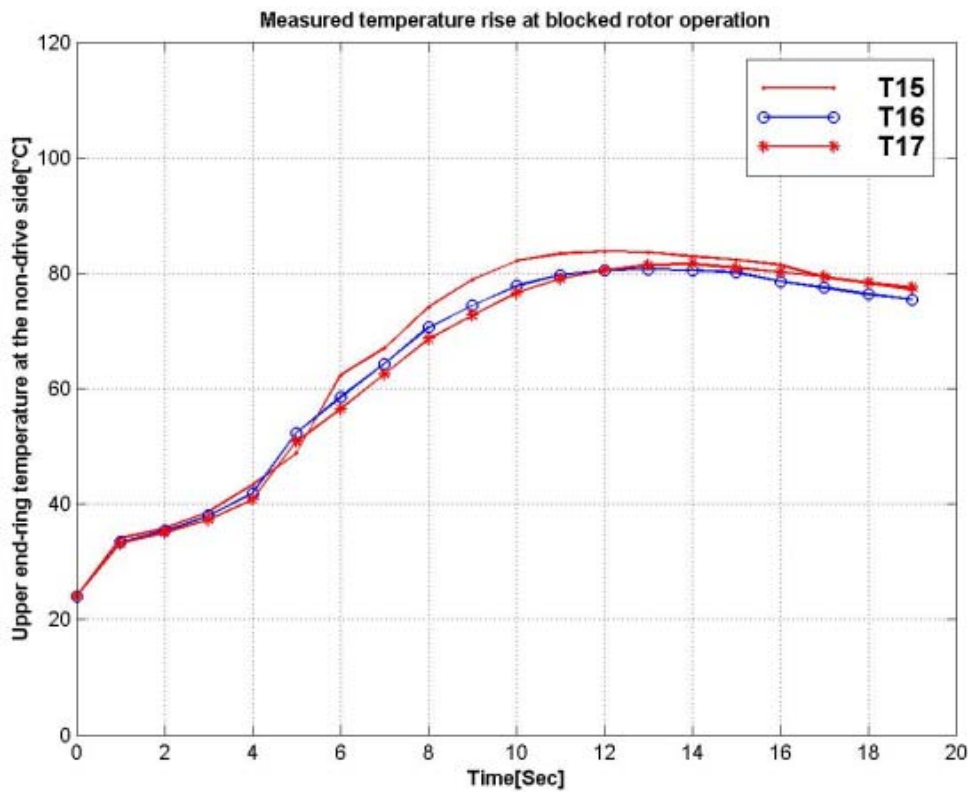


**Figure 8.18d:** Measurement at blocked rotor:Measured upper end-ring temperature at the non-drive side. 0...9s: Irms = 48A, Vrms = 500V, Star-connected; 9...20s: Irms = 0A, Vrms = 0V.

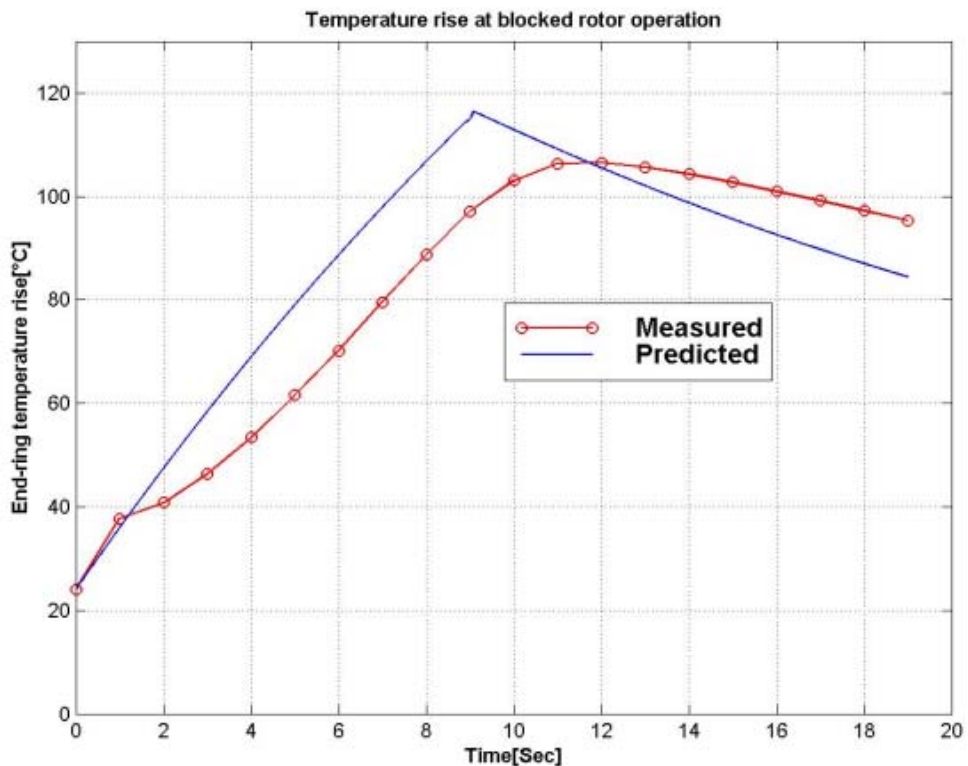


**Figure 8.18e:** Measured(Average(drive-end)) and predicted end-ring temperature at blocked rotor.

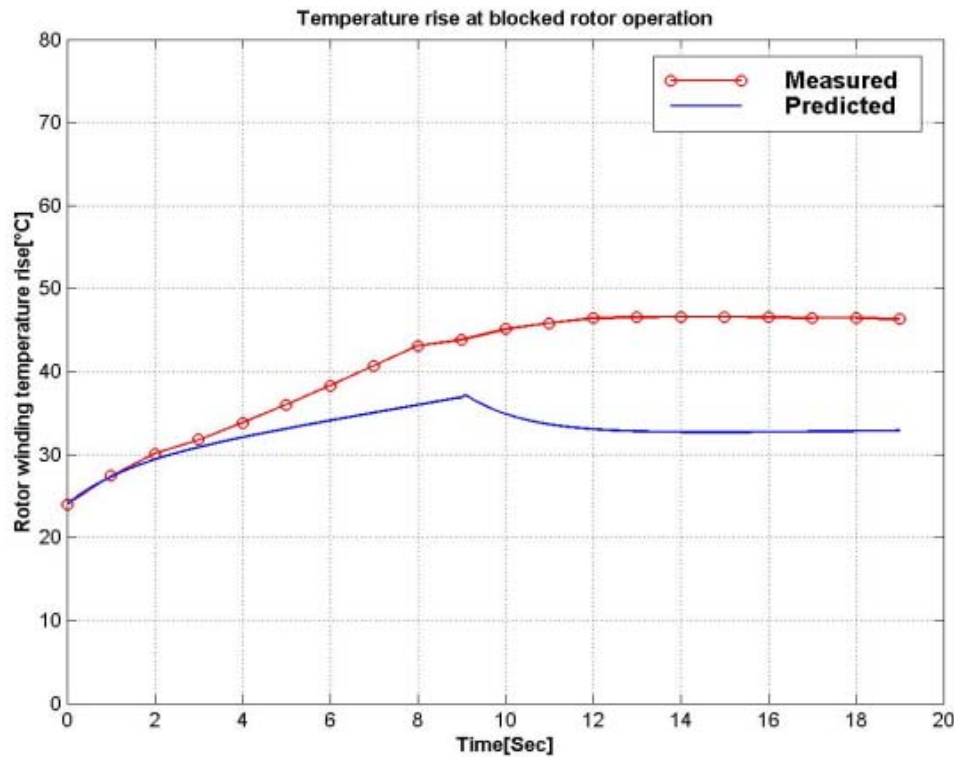


**Figure 8.19:** Measured and predicted rotor winding temperature at blocked rotor.

#### 8.4.3. Comments on the results.

The comparison of the simulated run-up transient characteristics of the induction motor with the actual motor performances shows that the conventional model fails to meet the machine's physical behaviours.

On the other hand, the simulated machine model with both skin-effect and saturation effect included gives a better result which can be conveniently used to predict the actual machine performances.

The thermal measurements carried out show that the proposed thermal model is capable of calculating the temperatures in the machines with good accuracy during No-load, rated load and blocked rotor operations. Differences of about 5°C at No-load, about 9°C at rated load and about 10°C at blocked rotor operations were observed between the measured and the predicted temperatures. These errors may be probably as a result of the fact that the developed thermal model calculates the average temperatures inside the stator and rotor windings whereas the installed thermoelements measure only the outside temperature of the stator and rotor windings. Probable error may also be due to the errors emanating from the calculation of the model's thermal resistances and capacitances which are dependent on the material properties of the machine—to which accurate information from the manufacturer on same is highly necessary. Thirdly, the power losses of the machine used in the simulation were assumed to be constant throughout the machine operation. This is not always correct as the copper losses are dependent on resistance which in itself is temperature dependent.

Where more than one thermoelements were used to represent a particular point in the test machine(for instance, end-winding, end-ring, stator winding,etc), the mean readings of the thermoelements were used to check the validity of the developed thermal model. However, the temperature readings of all the thermoelements have been included here in order to give an overview of temperature variations within the machine parts.

## 9 Conclusion

The main objective of this work was to develop models that accurately represent the dynamic and thermal behaviours of a squirrel-cage induction motor with non-linear effects. In order to realize this objective, four approaches have been adopted: Identification of the machine parameters by carrying out D.C. measurement test, No-load test, Blocked-rotor test and Retardation test on the machine; development of the machine models to include skin-effect, saturation effect and thermal effect; development of a computer program using a commercial available software package, MATLAB and validation of simulated results with measurements on the test machine.

On the modelling of the machine for skin-effect, it has been assumed that only the rotor part is affected by the phenomenon. A T-network lumped parameter model was used to model the the rotor bar. An optimisation algorithm which incorporates an error function was developed and used to optimise the rotor model. At approximately 4KHz frequency, the error in the developed rotor model to that of the actual bar was 6%. This error could be further reduced by increasing the number of the T-network lumped parameter model circuit but with a sacrifice in computer time.

The results of the No-Load, Blocked-rotor, D.C. measurement and Retardation tests were used to simulate the conventional and saturation models in order to study the behaviour of the test machine under steady-state and dynamic conditions. A comparison of the results indicated a sharp difference in the torque developed by the machine in transient state. The conventional machine model has a higher starting torque than the model with saturation effect. Little difference was observed under steady-state operation. That the effect is not very noticeable may probably due to the level of saturation considered and the part of the machine that is assumed to saturate. The effect on the steady-state performance of the machine will definitely be pronounced in highly saturated conditions.

On the other hand, a significant difference exists between the conventional steady-state model and the steady-state model with skin-effect. The developed torque in the skin-effect machine model was about three times higher than that of the conventional machine model at starting. At starting also, the magnitude of the stator current, power factor and input power of the skin-effect model was observed to be higher than that of the conventional model. Comparisons between the proposed skin-effect model and the conventional model under transient condition showed large errors in the predicted torque and speed. The first peak of torque in the skin-effect model was about 40% higher than the conventional model. The predicted speed-time curve increased faster to synchronous speed in the skin-effect model than that of the conventional model. Prolonged initial level of oscillations have been observed in the phase currents of the conventional model which differs considerably from the measured one. The simulated machine model with both skin-effect and saturation effect included gives a better result than the other models when compared with the measured machine transient performances at run-up condition and can therefore be conveniently used to predict the actual machine performances. The predicted time function of the bar currents in each rotor section showed that the current magnitude decreases as the bar section increases.

The proposed thermal model is based on thermal networks. Thermal networks are very effective in the thermal modelling of electrical machines. Different machine constructions are easy to model and the calculation does not require high capacity computers.

The input for the thermal-network MATLAB program is the geometry, material constants and the electromagnetic heat losses of the machine. As an output, the program gives the temperature distribution of the test machine. Due to assumed thermal symmetry of the motor, half of the machine was simulated. This method however, introduces large error if applied in large induction motor where thermal asymmetry is common feature. The calculated steady-state temperature rises of the machine parts were observed to compare favourably well with the measured results at No-load, rated load and blocked rotor conditions. Temperature errors of less than 10°C were achieved for frame, stator winding, end-winding and end-ring temperatures in both transient and steady-state conditions. These errors may probably be as a result of the fact that the developed thermal model calculates the average temperatures inside the stator and rotor windings whereas the installed thermoelements measure only the outside temperatures of the stator and rotor windings.

Hence, this work has contributed to the field of induction machine modelling by providing:

- An increased understanding of the rotor-bar modelling to include skin-effect.
- An increased understanding of which phenomena influence the operation of induction machine in both steady-state and dynamic conditions.
- Mathematical methods of modelling saturation which accounts for the magnetizing reactance variation.
- Thermal network model which presents a reliable solution in the estimation of average temperature of the machine parts, and
- An interactive MATLAB program which effectively and efficiently stimulates the developed models and validation of the models with measured results.

The developed non-linear machine model can also be favourably applied in the design of speed and torque controllers—For example in the control of induction machine by constant rotor flux linkage.

**Appendix: Calculated thermal resistances and capacitances**

<b>Thermal capacitances</b>	<b>Values[J/K]</b>	<b>Thermal resistances</b>	<b>Values[K/W]</b>
C <sub>1</sub>	18446.55	R <sub>1b</sub>	0.0416
C <sub>2</sub>	4450.625	R <sub>12</sub>	15.44e-3
C <sub>3</sub>	423.388	R <sub>23</sub>	35.58e-3
C <sub>4</sub>	539.92	R <sub>26</sub>	0.135
C <sub>5</sub>	3204.08	R <sub>35</sub>	0.1751
C <sub>6</sub>	408.267	R <sub>511</sub>	1.886
C <sub>7</sub>	218.785	R <sub>67</sub>	4.115e-3
C <sub>8</sub>	1006	R <sub>79</sub>	0.1055
		R <sub>911</sub>	0.932
		R <sub>11c</sub>	0.015

## References

**[1] Krause, P. C.; Thomas, C. H.**

Simulation of Symmetrical induction machinery. Transactions IEEE, PAS-84, Vol.11,1965, PP.1038-1053.

**[2] Jordan, H. E.**

Digital Computer Analysis of induction machines in dynamic systems. IEEE Transactions on Power Apparatus and Systems, Vol. PAS-86, N0.6, June 1967,PP. 722-728.

**[3] Leonhard, W.**

Control of Electrical Drives, Springer Verlag, Berlin, 1996.

**[4] Cochran, P. L.**

Polyphase induction motors: Analysis, Design, and Application, Marcel Dekker, Inc, New York, 1989.

**[5] Babb, D. S.; Williams, J. E.**

Network analysis of A-C machine conductors. AIEE Transactions Vol.70, 1951, PP. 2001-2005.

**[6] Babb, D. S.; Williams, J. E.**

Circuit analysis method for determination of A-C impedances of machine conductors. AIEE Transactions Vol.70, 1951, PP. 661-666.

**[7] Liwschitz-Garik, M. M.**

Computation of Skin Effect in Bars of Squirrel-Cage Rotors. AIEE Transactions, Vol.74, 1955, PP.768-771.

**[8] Weidemann, B.**

Hilfsblätter Zur Vorlesung Elektrische Maschinen, Universität GH Kassel, 1991.

**[9] Steube, Ulrich**

Modelbildung von Stromverdrängungseffekten in elektrischen Maschinen. Diplomarbeit, Universität GH Kassel, 1993.

[10] "The MATLAB compiler user's guide", in *Mathworks handbook*.

Math Works, April 1997

[11] **Alger, P. L.**

Induction machines: Their behaviour and uses. Gordon and Breach Science Publishers SA, USA, 1995.

[12] **Yamamura, S.**

AC motors for High-performance Applications: Analysis and control. Marcel Dekker, Inc, New York, 1986.

[13] **Perdikaris, G. A.**

Computer Controlled Systems: Theory and Applications. Kluwer Academic publishers, Netherlands, 1996.

[14] **Fürsich, H.**

Zur Theorie des dynamischen Betriebs von Drehstrommotoren mit Stromverdrängungsläufer. Archiv für Elektrotechnik 57, 1975, PP. 273-280.

[15] **Pollack, J. J.**

Some Guidelines for the Application of Adjustable-speed AC Drives. IEEE Transactions on industry Applications, Vol. IA-9, N0.6, Nov/Dec. 1973, PP. 704-710.

[16] **Chattopadhyay, A. K.**

Digital Computer Simulation of an Adjustable-speed induction motor Drive with a cycloconverter-type thyristor-commutator in the Rotor. IEEE Transactions on industrial Electronics and control Instrumentation, Feb; 1976, PP. 86-92.

[17] **Krause, P. C.; Lipo, T. A.**

Analysis and simplified Representations of a rectifier- inverter induction motor drive. IEEE Transactions on Power Apparatus and Systems, Vol. PAS-88, N0.5, May 1969, PP. 588-596.

**[18] Jordan, H. E.**

Analysis of induction machines in dynamic systems. IEEE Transactions on Power Apparatus and Systems, Vol. PAS-84, N0.11,Nov; 1965, PP. 1080-1088.

**[19] Krause, P. C.**

Simulation of unsymmetrical 2-phase induction machines. IEEE Transactions on Power Apparatus and Systems, Vol. PAS-84, N0.11, Nov; 1965, PP.1025-1037.

**[20] Ramamoorthy, M.; Arunachalam, M.**

Dynamic performance of closed loop induction motor speed control system with phase controlled SCRs in the Rotor. Conference Record of Industry Applications Society IEEE/IAS Annual meeting, 1978.

**[21] Park,R.H.**

Two-reaction theory of synchronous machines. AIEE Transactions,1929, PP717-727.

**[22] Kron, G.**

A short course in tensor Analysis for Electrical Engineers, John Wiley and sons, New York, 1942.

**[23] Stanley,H.C.**

An analysis of the induction machine. AIEE Transactions, Vol.57,1938, PP.751-757.

**[24] Vas,Peter**

Electrical machines and Drives-A space-vector theory approach. Oxford, Clarendon press,1992.

**[25] Lipo,T.A.**

The analysis of induction motors with voltage control by symmetrically triggered thyristor. IEEE Transactions on Power Apparatus and Systems, Vol. PAS-90,No.2, March/April 1971,  
PP.515-525.

**[26] Levy,W; Landy,C.F. and McCulloch,M.D.**

Improved models for the simulation of deep bar induction motors. IEEE Transactions on Energy Conversion, Vol.5,No.2, June 1990, PP393-400.

**[27] Adkins, Bernard and Harley, R.G.**

The General theory of Alternating current machines: Application to practical problems. Chapman and Hall, London,1975.

**[28] Guiliemin, E.A.**

Introductory Circuit Theory. Wiley, New-York, 1953

**[29] Cornell, E.P. and Lipo,T.A.**

Modeling and Design of Controlled current induction motor drive systems. IEEE Transactions on Industry Applications, Vol.IA-13, No.4, July/August 1977, PP.321-330.

**[30] Krause, P.C.**

Analysis of Electric Machinery, New York, McGraw-Hill, 1986.

**[31] Smith,A.C.**

A transient induction motor model including saturation and deep bar effect. IEEE Transactions on Energy Conversion, Vol.11,No.1, March 1996, PP.8-15.

**[32] Smith,J.R. and Sriharan,S.**

Transient performance of the induction motor. Proc. IEE, 113, (7), 1966, PP.1173-1181.

**[33] Nath, Gautam and Berg, G.J.**

Transient Analysis of three-phase SCR controlled induction motors. IEEE Transactions on Industry Applications, Vol.IA-17,No.2, March/April 1981, PP.133-142.

**[34] Wolfram,S.**

Mathematica, 2<sup>nd</sup> Ed; New-York/USA, Addison-Wesley Publishing company Inc; 1988.

**[35] Smith,J.R.**

Response analysis of A.C. Electrical machines-Computer models and simulation. New York, John Wiley and Sons, 1990.

**[36] Haun, Andreas**

Vergleich von Steuerverfahren für Spannungseinprägende Umrichter Zur Speisung von Käfigläufermotoren. Darmstädter Dissertation, Juli 1991.

**[37] Humpage, W.D.; Durrani,K.E. and Carvallo,V.F.**

Dynamic response analysis of interconnected synchronous-asynchronous machine groups. Proc. IEE, 116, (2), 1969, PP.2015-2027.

**[38] Nasar,S.A. and Unnewehr, L.E.**

Electromechanics and Electric machines. John Wiley and Sons, New-York, 1979.

**[39] Mellor,P.H.; Roberts,D. and Turner, D.R.**

Lumped parameter thermal model for electrical machines of TEFC design. IEE Proc.B,138, (5), 1995, PP.205-218.

**[40] Kylander,G.**

Thermal modelling of small cage induction motors. Doctor of Technology Thesis, Chalmers University of Technology, Gothenburg, Sweden, 1995.

**[41] Hak,J.**

Möglichkeiten und Aussichten einer Unbeschränkten Lösung des Wärmpproblems von Elektrischen Maschinen. Elektrotechnik und Maschinenbau, 74,(14), 1957, PP.305-311.

**[42] Boys,J.T. and Miles,M.J.**

Empirical thermal model for inverter-driven cage induction machines. IEE Proc.-Electrical Power Application, Vol.141,No.6, November 1994, PP.360-372.

**[43] Kessler,A.**

Versuch einer genaueren Vorausberechnung des zeitlichen Erwärmungsverlaufes Elektrischer Maschinen mittels Wärmequellennetzen. Archiv für Elektrotechnik, Vol.45 No.1, 1960, PP.59-76.

**[44] Champenois, G.; Roye, D. and Zhu, D .S.**

Thermal performance predictions in inverter fed Squirrel-Cage induction motor drives. Electric machines and Power systems, 22,3, 1994, PP.355-369.

**[45] Griffith,J.W.; McCoy,R.M. and Sharma, D.K.**

Induction motor Squirrel Cage Rotor winding thermal analysis. IEEE Transactions on Energy Conversion, Vol. EC-1,No.3, September 1986, PP.22-25.

**[46] Sarker, D.; Mukherjee,P.K. and Sen, S.K.**

Approximate Analysis of Steady state heat conduction in an Induction motor. IEEE Transactions on Energy Conversion, Vol.8,No.1, March 1993, PP. 78-84.

**[47] Chan,C.C.; Yan,Lietong ; Chen, Pizhang; Wang, Zezhong and Chau,K.T.**

Analysis of Electromagnetic and thermal fields for induction motors during starting. IEEE Transactions on Energy Conversion, Vol.9, No.1, March 1994, PP.53-58.

**[48] Soderberg,R.**

Steady flow of heat in large turbine-generators. AIEE, 50, 1931, PP. 782-802.

**[49] Hak, J.**

Wärmequellen-Netze elektrischer Maschinen. Elektrotechnik und Maschinenbau, 76, (11), 1959, PP. 236-243.

**[50] Hak, J.**

Die Inneren axialen Wärmewiderstände einer elektrischen Maschine. Archiv für Elektrotechnik, 43, 1957, PP.58-76.

**[51] Weidemann, B.**

Wärmerohrgekühlter Asynchronmotor mit Stromrichterspeisung als Bahnantrieb. Dissertation, Technischen Hochschule Aachen, 1979.

**[52] Feyzi,M.R. and Parker, A. M.**

Heating in deep-bar rotor cages. IEE Proc.-Electrical Power Application, Vol.144, No.4, July 1997, PP. 271-276.

- [53] Bastos, J.P.; Cabreira,M.F.R.R.; Sadowski, N. and Arruda, S.R.**  
A thermal Analysis of Induction motors using a weak coupled modeling. IEEE Transactions on Magnetics, Vol.33, No.2, March 1997, PP.1714-1717.
- [54] Lee, Yangsoo; Lee, Hyang-beom and Hahn, Song-Yop**  
Temperature Analysis of Induction motor with distributed heat sources by Finite Element Method. IEEE Transactions on Magnetics, Vol.33, No.2, March 1997, PP.1718-1721.
- [55] Jokinen,T. and Saari, J.**  
Modelling of the Coolant flow with heat flow controlled temperature sources in thermal Networks. IEE Proc.-Electrical Power Application, Vol. 144, No.5, September 1997, PP. 338-342.
- [56] De Doncker, R.; Vandenput, A. and Geysen,W.**  
Thermal models of Inverter fed Asynchronous machines suited for Adaptive temperature Compensation of field oriented controllers. Conference Record of Ind. Appl. Society, IEEE 86 CH 2272-3, Denver Colorado, September 1986, PP.132-138.
- [57] Rajagopal,M.S; Seetharamu,K.N. and Ashwathnarayana,P.A.**  
Transient thermal analysis of Induction motors. IEEE Transactions on Energy Conversion,Vol.13, No.1, March 1998, PP.62-69.
- [58] Klamt, J.**  
Berechnung und Bemessung elektrischer Maschinen. Springer Verlag, 1962.
- [59] Richter, R.**  
Elektrische Maschinen. Vol.1,2nd ed. Basel, Birkhauser Verlag,1951.
- [60] Heller,N. and Hamata, V.**  
Harmonic field effects in induction machines. Elsevier Scientific Publishing Company, Amsterdam, 1977.
- [61] Christofides,N. and Adkins, B.**  
Determination of load losses and Torques in Squirrel-cage induction motors.  
Proc. IEE, Vol.113, No.12, December 1966, PP.1995-2005.
- [62] Rao, Subba V. and Butler, O.I.**  
Stray Losses of polyphase Cage-induction motors with particular reference to the condition Of imperfect rotor bar-iron insulation. Proc. IEE, Vol.116, No.5, May 1969, PP.737-751.
- [63] Chalmers,B.J. and Richardson, J.**  
Investigation of high-frequency no-load losses in induction motors with open stator slots. Proceedings IEE, Vol.113, No.10, October 1966, PP1597-1605.
- [64] Özisik, M. N.**  
Heat Transfer—A basic Approach. McGraw-Hill Book Company, New York, 1985.
- [65] Bousbaine, A.; McCormick, M. and Low, W. F.**  
In-situ determination of thermal coefficients for electrical machines. IEEE Transactions on Energy Conversion, Vol.10, No.3, September 1995, PP.385-391.

**[66] Rahman,M.A. and Little,T.A.**

Dynamic performance of permanent magnet synchronous motors. IEEE Transactions on Power Apparatus and Systems, Vol. PAS-103, N0.6, June 1984, PP.1277-1282.

**[67] Smith,J.R. and Sriharan,S.**

Induction-motor reswitching transients. Proc. IEE, Vol.4, 114, April 1967, PP.503-509.

**[68] Gerald,C.F.**

Applied numerical analysis. Addison-Wesley publishing company, London,1978.

**[69] Press,W.H; Teukolsky,S.A; Vetterling,W.T. and Flannery,B.P.**

Numerical Recipes in C---The Art of Scientific computing. Second Edition, Cambridge University Press, London, 1992.

**[70] Stroud,K.A.**

Engineering Mathematics, 2<sup>nd</sup> ed.; Macmillan press Ltd, London, 1982.

**[71] Melkebeek, J.A.A.**

Magnetizing-field saturation and dynamic behaviour of induction machines. Part1: Improved Calculation method for induction-machine dynamics. IEE Proc.,Vol.130, Pt.B,No.1, January 1983, PP.1-9.

**[72] de Mello, F.P. and Walsh, G.W.**

Reclosing Transients in induction motors with Terminal Capacitors. AIEE Transactions, Feb.1961, PP.1206-1213.

**[73] He, Yi-Kang and Lipo, T.A.**

Computer simulation of an induction machine with spatially dependent saturation. IEEE Transactions on Power Apparatus and Systems, Vol. PAS-103, No.4, April 1984, PP 707-714.

**[74] Keyhani,A. and Tsai, H.**

IGSPICE simulation of induction machines with saturable inductances. IEEE Transactions on Energy Conversion, Vol.4, No.1, March 1989, PP.118-125.

**[75] Lipo, T.A. and Consoli, A.**

Modeling and simulation of induction motors with saturable leakage reactances. IEEE Transactions on Industry applications, Vol.IA-20, No.1, January/February 1984, PP.180-189.

**[76] Boldea,I. and Nasar, S.A.**

A general Equivalent Circuit(GEC) of Electric machines including crosscoupling saturation and frequency effects. IEEE Transactions on Energy conversion, Vol.3, September 1988,  
PP.689-695.

**[77] Levi,E.**

A unified approach to main flux saturation modelling in D-Q Axis models of induction machines. IEEE Transactions on Energy conversion, Vol.10,No.3, Sept.1995, PP.455-460.

**[78] Slemmon,G.R.**

Modelling of induction machines for electric drives. IEEE Transactions on Industry Applications, Vol.25, No.6, Nov./Dec. 1989, PP.1126-1131.

**[79] Marquardt, D.W.**

An Algorithm for Least-square estimation of non-linear parameters. J.Soc.Ind.Appl. Math; Vol.11, No.2, June 1963, PP.431-441.

**[80] Discussions on Transient effects in induction motors, Proc. IEE, 115, 1968, PP.128-135.****[81] Smith, J. R; Rogers,G.J. and Buckley,G.W.**

Application of induction motor simulation models to power station auxiliary pump drives. IEEE Transactions on Power Apparatus and Systems, Vol. PAS-98, No.5, Sept./Oct. 1979, PP. 1824-1831.

**[82] Rohrmoser, Andreas**

Entwurf einer feldorientierten Regelung für einen doppeltgespeisten Asynchronmotor unter Berücksichtigung nichtlinearer Effekte. Diplomarbeit II, Universität Kassel, August 1998.

**[83] Richter, Steffen**

Analyse and Bewertung von Steuerverfahren für Pulsumrichtergespeiste Asynchronmaschinen, Reihe 21, Elektrotechnik, No.207, 1996.

**[84] Bousbaine, A.; Low, W.F. and McCormick, M.**

Novel approach to the measurement of iron and stray load losses in induction motors. IEE Pro.-Electr. Power Application Vol. 143, No.16, Jan.1996, PP. 78-86.

**[85] Holzweißig,F. and Dresig,H.**

Lehrbuch der Maschinendynamik: Maschinendynamische Probleme und ihre Praktische Lösung. Zweite Auflage, Springer-Verlag, Wien, 1982.

**[86].Seinsch, H.O.**

Grundlagen elektrischer Maschinen und Antriebe. Teubner, Stuttgart, 1988.

**[87] ANSOFT:** Maxwell 2D/RMxprt FEA—Simulation Program. Ansoft corporation, Munich.**[88] IEEE standard Test procedure for polyphase induction motors and generators, IEEE standard 112-1991, 1991.**